Identification of new regulators of the mitochondrial unfolded protein response in *Caenorhabditis elegans* mutants with defects in mitochondrial dynamics

Dissertation an der Fakultät für Biologie der Ludwig-Maximilians-Universität München

Simon Häußler

München, 16.12.2020

Diese Dissertation wurde unter der Leitung von Prof. Dr. Barbara Conradt im Bereich Zell- und Entwicklungsbiologie an der Ludwig-Maximilians-Universität München angefertigt.

Erstgutachterin:	Prof. Dr. Barbara Conradt
Zweitgutachter:	Prof. Dr. Christof Osman
Tag der Abgabe:	16.12.2020
Tag der mündlichen Prüfung:	16.06.2021

Eidesstattliche Erklärung

Ich versichere hiermit an Eides statt, dass meine Dissertation selbständig und ohne unerlaubte Hilfsmittel angefertigt worden ist.

München, den 16.12.2020 _____

Simon Häußler

Erklärung

Die vorliegende Dissertation wurde weder ganz, noch teilweise bei einer anderen Prüfungskommission vorgelegt. Ich habe noch zu keinem früheren Zeitpunkt versucht, eine Dissertation einzureichen oder an einer Doktorprüfung teilzunehmen.

München, den 16.12.2020 _____

Simon Häußler

Table of content

List of publications

Stéphane G. Rolland, Sandra Schneid, Melanie Schwarz, Elisabeth Rackles, Christian Fischer, **Simon Haeussler**, Saroj G. Regmi, Assa Yeroslaviz, Bianca Habermann, Dejana Mokranjac, Eric Lambie and Barbara Conradt (2019). Compromised mitochondrial protein import acts as a signal for UPR^{mt}. Cell Reports 28(7). https://doi.org/10.1016/j.celrep.2019.07.049

Simon Haeussler, Fabian Köhler, Michael Witting, Madeleine F. Premm, Stéphane G. Rolland, Christian Fischer, Laetitia Chauve, Olivia Casanueva, Barbara Conradt (2020). Autophagy compensates for defects in mitochondrial dynamics. PLOS Genetics 16(3). https://doi.org/10.1371/journal.pgen.1008638

Christian A. Fischer, Laura Besora-Casals, Stéphane G. Rolland, **Simon Haeussler**, Kritarth Singh, Michael Duchen, Barbara Conradt, Carsten Marr (2020). MitoSegNet: easy to use deep learning segmentation for analysing mitochondrial morphology. iScience 23(10). https://doi.org/10.1016/j.isci.2020.101601

Submitted manuscripts

Simon Haeussler, Assa Yeroslaviz, Stéphane G. Rolland, Sebastian Luehr, Eric Lambie and Barbara Conradt (2020). Genome-wide RNAi-screen for regulators of UPR^{mt} in *Caenorhabditis elegans* mutants with defects in mitochondrial fusion.

Declaration of contribution as a co-author

In this dissertation, I present the results of my doctoral research in four chapters, which I conducted in the laboratory of Prof. Dr. Barbara Conradt from August 2014 until March 2020. Chapter I is an unpublished manuscript, which is currently in revision in G3 – Genes, Genomes, Genetics. Chapter II has been published in Cell Reports, Chapter III has been published in PLOS Genetics and Chapter IV has been published in iScience. All of the work in these four chapters has been accomplished by collaborations with other scientists. My contributions to these publications are listed for each of the chapter separately below.

Declaration of contribution as a co-author

Chapter I:

Simon Haeussler, Assa Yeroslaviz, Stéphane G. Rolland, Sebastian Luehr, Eric Lambie and Barbara Conradt, Genome-wide RNAi screen for regulators of UPR^{mt} in *Caenorhabditis elegans* mutants with defects in mitochondrial fusion. Unpublished manuscript.

Stéphane, Barbara and I planned the experimental design of the genome-wide RNAi screen. I conducted the RNAi screen, sequenced and re-screened all candidates and conducted the secondary screens. Sebastian wrote scripts for sorting of the candidates, identified orthologs that are listed in the OMIM database, identified the GO-terms containing 'mitochond' and helped constructing the final candidate list. Assa, Stéphane, Barbara and I planned the bioinformatic analysis. Assa carried out most of the bioinformatic analysis including gene ontology enrichment analysis using DAVID, transcription factor enrichment analysis and gene network analysis, while I performed the mitochondrial targeting sequences prediction. Stéphane crossed the *fzo-1(tm1133)* mutant both in *bcIs78* and *zcIs13* alleles and I did the image acquisition, processing and analysis of the resulting strains. Eric conducted RNAi-experiments using ribosomal and *kgb-1(RNAi)* during revision experiments. Assa and I prepared all the figures and I wrote the manuscript, together with Stéphane and Barbara.

Chapter II:

Stéphane G. Rolland, Sandra Schneid, Melanie Schwarz, Elisabeth Rackles, Christian Fischer, **Simon Haeussler**, Saroj G. Regmi, Assa Yeroslaviz, Bianca Habermann, Dejana Mokranjac, Eric Lambie and Barbara Conradt, 2019, Compromised mitochondrial protein import acts as a signal for UPR^{mt}. Cell Reports 28(7). https://doi.org/10.1016/j.celrep.2019.07.049.

Of the 171 genes that are described in chapter II to induce UPR^{mt} when inactivated by RNAi, I identified 38 candidate genes. For this, I re-screened all enhancers of *fzo-1(tm1133)*-induced UPR^{mt} (identified in the RNAi screen from chapter I) in wild-type animals. The candidates that also induce UPR^{mt} in wild type and which have a mitochondrial function were included in the final list of inducers of UPR^{mt}.

Declaration of contribution as a co-author

Chapter III:

Simon Haeussler, Fabian Köhler, Michael Witting, Madeleine F. Premm, Stéphane G. Rolland Christian Fischer, Laetitia Chauve, Olivia Casanueva, Barbara Conradt, 2020, Autophagy compensates for defects in mitochondrial dynamics. PLOS Genetics 16(3): https://doi.org/10.1371/journal.pgen.1008638

Fabian, Michael, Stéphane, Olivia, Barbara and I designed the experiments of chapter III. Fabian, Michael, Madeleine, Laetitia and I performed the experiments. Fabian performed the autophagy screen and produced all data using the *gfp::lgg-1* and *sqst-1::gfp* transgenes. Michael performed the mass spectrometry experiments including data analysis. Madeleine performed the experiments using the *zcIs9* allele (P_{hsp-60}*::gfp*), which I crossed into the *fzo-1(tm1133)* mutant background. I cloned and integrated the single-copy P_{hsp-6}*::gfp* transgene resulting in isolation of the *bcSi9* allele and crossed it into the *fzo-1(tm1133)* background. Laetitia performed the single worm qPCR on the *bcSi9* and *zcIs13* transgenes and analyzed the resulting data. Christian wrote the scripts for image analysis and quantification of fluorescence intensity. I performed the RNAi screen and all subsequent secondary screens. I produced all data using the *bcSi9* transgene and prepared the samples for mass spectrometry. Fabian and I wrote the paper, together with Michael, Stéphane and Barbara.

Chapter IV:

Christian A. Fischer, Laura Besora-Casals, Stéphane G. Rolland, **Simon Haeussler**, Kritarth Singh, Michael Duchen, Barbara Conradt, Carsten Marr, 2020, MitoSegNet: easy to use deep learning segmentation for analysing mitochondrial morphology. iScience 23(10). https://doi.org/10.1016/j.isci.2020.101601

In chapter IV, I was involved in the initial design of the project and together with Stéphane, had a consultative role concerning mitochondrial biology. I provided all images for the manual segmentation to train the MitoSegNet algorithm, which was then performed by Christian and Laura.

Simon Häußler Fabian Köhler Barbara Conradt

Abbreviations

°C	Degree Celsius
AA	Amino acid
ATP	Adenosine triphosphate
CDP	Cytidine biphosphate
CO_2	Carbon dioxide
CoA	Acetyl-coenzyme A
COPI	Coat complex I
COPII	Coat complex II
DAG	Diacylglycerol
DNA	Deoxyribonucleic acid
ds	Double-stranded
ER	Endoplasmic reticulum
ETC	Electron transport chain
EthBr	Ethidium bromide
ESCRT	Endosomal sorting complex required for transport
$FADH_2$	Flavin adenine dinucleotide
FAO	β-oxidation of fatty acids
Gbp	Giga base pairs
GFP	Green fluorescent protein
GO	Gene ontology
GDP	Guanosine diphosphate
GPCR	G-protein-coupled receptor
GTP	Guanosine triphosphate

Abbreviations

IMM	Inner mitochondrial membrane
IMS	Intermembrane space
IP_3	Inositol triphosphate
IP_3R	Inositol triphosphate receptor
Mbp	Mega base pairs
MEFs	Mouse embryonic fibroblasts
MIA	Mitochondrial intermembrane space assembly
mitoCPR	Mitochondrial compromised protein import response
MPP	Mitochondrial processing peptidase
mtDNA	Mitochondrial deoxyribonucleic acid
mPOS	Mitochondrial precursor over-accumulation stress
MTS	Mitochondrial targeting sequence
MVB	Multivesicular bodies
NADH	Nicotinamide adenine dinucleotide
NLS	Nuclear localization sequence
OCR	Oxygen consumption rate
OMM	Outer mitochondrial membrane
OXPHOS	Oxidative phosphorylation
PAM	Presequence translocase-associated motor
PI	Phosphatidylinositol
PI4P	Phosphatidylinositol 4-phosphate
$PI(4,5)P_2$	Phosphatidylinositol 4,5-biphosphate
RNA	Ribonucleic acid
RNAi	Ribonucleic acid interference

Abbreviations

ROS	Reactive oxygen species
SAM	Sorting and assembly
SUMO	Small ubiquitin-like modifier
TCA	Tricarboxylic acid cycle
TF	Transcription factor
TG	Triacylglycerols
TOM	Translocase of the outer mitochondrial membrane
tRNA	Transfer ribonucleic acid
UPR^{am}	Unfolded protein response activated by mistargeting of proteins
UPR^{mt}	Mitochondrial unfolded protein response
$\Delta\psi$	Mitochondrial membrane potential
µm	Micro meter

1. Abstract

Mitochondria are central for cellular metabolism and therefore, mitochondrial homeostasis is tightly controlled. Mitochondrial dynamics, the mitochondrial unfolded protein response (UPR^{mt}) and autophagy (or mitophagy) are quality control mechanisms that ensure mitochondrial homeostasis and, hence, proper functionality. The interplay of these quality control mechanisms is subject of this dissertation. In a genome-wide RNAi screen for modulators of UPR^{mt} in *Caenorhabditis elegans* mutants with defects in mitochondrial fusion, we identified 299 suppressors and 86 enhancers of *fzo-1(tm1133)*-induced UPR^{mt}.

The complete list of candidates including a bioinformatic analysis of the dataset is presented in chapter I. We find that our dataset is highly conserved in humans and that a substantial part has implications in human disease. Furthermore, many of our candidates have roles in development, suggesting that mitochondrial function and homeostasis is adjusted during development and maintained throughout life. Moreover, we predominantly identified non-mitochondrial suppressors of UPR^{mt} in our dataset, which implies that mitochondrial fitness plays a vital role in cellular homeostasis since many pathways exist outside of mitochondria that compensate for defects in mitochondrial homeostasis. Conversely, we primarily identified mitochondrial enhancers in our dataset, suggesting that mitochondrial homeostasis can scarcely be affected by disruption of processes outside of mitochondria. However, we identified the maintenance of contact sites between mitochondria and the ER to be of importance for mitochondrial homeostasis. In addition, disruption of receptor-mediated endocytosis is another non-mitochondrial process that affects mitochondrial homeostasis and we speculate that disrupting endocytosis may affect cell non-autonomous UPR^{mt} signaling. Moreover, we found a potential link between pre-mRNA splicing and UPR^{mt} and identified several genes involved in IP_3 signaling in our dataset, suggesting that this pathway may regulate UPR^{mt} in *fzo-1(tm1133)* mutants. Finally, we identified a so far uncharacterized gene to induce UPR^{mt} and lead to altered mitochondrial morphology when knocked-down or mutated. We name this gene *miga-1*, according to its mammalian orthologs.

Chapter II describes the findings of another genome-wide RNAi screen for inducers of UPR^{mt} in wild-type animals, which was mainly conducted by Stéphane Rolland and Sandra Schneid. The enhancers of *fzo-1(tm1133)*-induced UPR^{mt} (chapter I), which are known or are predicted to have a mitochondrial function and induce UPR^{mt} upon depletion also in the absence of mitochondrial stress, were added to this dataset. Altogether, we identified all mitochondrial

processes, except mitochondrial calcium homeostasis and mitophagy, to induce UPR^{mt} when disrupted. Analysis of this dataset suggests that the current understanding of the UPR^{mt}, which is thought to counteract 'mito-nuclear' imbalance of mitochondrial multi-subunit protein complexes in situations of stress, cannot be applied to many of the identified candidate genes in our screen. Instead, we propose that a decrease in mitochondrial membrane potential, which has been shown to be accompanied by a decrease in mitochondrial import competence, is the common phenotype shared by all candidates in our dataset. Interestingly, we analyzed the mitochondrial targeting sequence (MTS) of ATFS-1^{ATF4,5}, the master regulator of the UPR^{mt} response, and found that due to its comparably weakness, ATFS-1^{ATF4,5} import into mitochondria is sensitive to subtle changes in mitochondrial membrane potential. Consequently, ATFS-1^{ATF4,5} cannot be imported into mitochondria in situations of mitochondrial stress but instead, translocates from the cytosol into the nucleus to activate its transcriptional program. In conclusion, we find that mitochondrial stress and the concomitant decrease in mitochondrial membrane potential is sensed by the MTS of ATFS-1^{ATF4,5}, which acts as a molecular switch to turn the UPR^{mt} on or off.

In chapter III, we describe another subset of candidates from the screen in chapter I, which induce autophagy and suppress UPR^{mt} in *fzo-1(tm1133)* upon knock-down. Initially, we identified three genes of the endosomal sorting complex required for transport (ESCRT) in our dataset and found evidence in the literature that these are negative regulators of autophagy in *C. elegans*. Subsequently, we tested all 299 suppressors of *fzo-1(tm1133)*-induced UPR^{mt} and strikingly, found that 143 induce autophagy when knocked-down. Moreover, we find that mitochondrial membrane potential, which is decreased in *fzo-1(tm1133)* mutants, is increased when ESCRT components or LET-363^{TOR} are depleted, thereby leading to suppression of UPR^{mt} in these animals. Furthermore, we find that autophagy and UPR^{mt} functionally interact, since blocking autophagy induces UPR^{mt} in the absence of mitochondrial stress. Finally, we analyzed the lipidome of *fzo-1(tm1133)*, *drp-1(tm1108)* and *spg-7(ad2249)* mutants and found that the levels of certain triacylglycerols (TGs) are altered in mutants with defects in mitochondrial dynamics (*fzo-1(tm1133)* and *drp-1(tm1108)*). Induction of autophagy partially reverts the levels of these TGs in *fzo-1(tm1133)*. This suggests that mitochondrial metabolism is fueled with lipids, which may be released from lipid droplets upon induction of autophagy. Furthermore, we speculate that this in turn leads to increased metabolic activity, an increase in mitochondrial membrane potential and consequently suppression of UPR^{mt} in *fzo-1(tm1133)* mutants.

Abstract

Chapter IV describes a new method for automated segmentation of mitochondrial morphology. Segmentation of mitochondrial morphology is crucial for subsequent statistical analysis and currently still a major issue in computational biology. Therefore, we established a new method for automated segmentation of mitochondrial morphology using a deep learning algorithm. Our U-net based algorithm 'MitoSegNet' was manually trained to segment mitochondrial morphology in microscopic images of *C. elegans* body wall muscle cells and we show that it can also segment images of tissue culture cells, which have previously not been shown to the algorithm. Furthermore, we find that MitoSegNet outperforms the currently available segmentation tools in single object comparison, as well as in five feature descriptors.

2. Introduction

2.1 *C. elegans* as a model in molecular biology

The nematode *C. elegans* has first been isolated, described and named (*Rhabditis elegans*) by the French librarian Émile Maupas in Algiers (Maupas, 1899, 1900). Victor M. Nigon and Ellsworth C. Doughtery developed more sophisticated culturing conditions for nematodes in the laboratory, studied their reproduction and conducted the first genetic experiments (Nigon, 1943; Nigon and Dougherty, 1949; Dougherty *et al.*, 1959; Fatt and Dougherty, 1963). Geneticist Sydney Brenner introduced *C. elegans* as a model for modern genetic studies in cell and developmental biology and published his results in 1974 (Brenner, 1974; Sulston and Brenner, 1974). In 1998, the *C. elegans* genome was the first genome of a multi-cellular organism to be completely sequenced (Consortium, 1998).

C. elegans is a transparent, free-living nematode that is around one millimeter in length as an adult. The majority of animals in a *C. elegans* population are self-fertilizing hermaphrodites, which lay around 300 eggs during their reproductive phase. Males exist in *C. elegans* populations under laboratory conditions, but do not appear very frequently (0.1-0.2%). Embryos are laid early during their development and therefore are covered by a strong protective shell. After the embryo hatches, larvae are molting four times to reach adulthood and these timepoints mark the four larval stages of larval development (Wood *et al.*, 1988). The fourth and last larval stage in development is easily detectable in brightfield microscopy and therefore is often used in experimental setups in the laboratory (Figure 1).

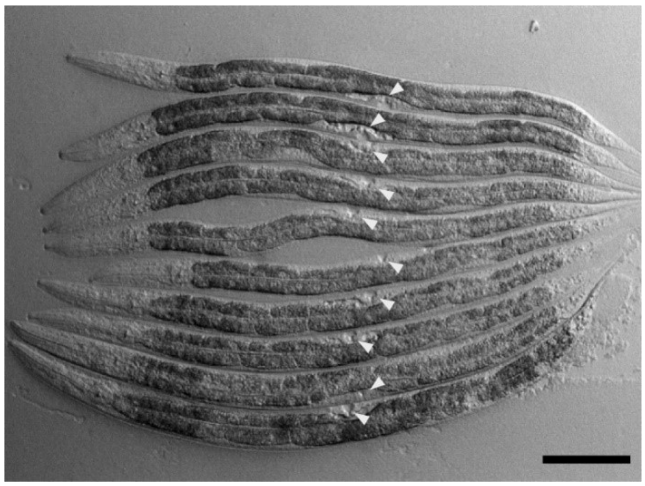

Figure 1: Microscopic image of *C. elegans* larvae in the fourth larval stage (L4). Animals are easily detectable at this stage since the developing vulva appears as a white dot in brightfield microscopy, indicated by white arrowheads. Scale bar: 100 µm.

The generation time under controlled laboratory conditions is approximately 3.5 days at 20 °C. *C. elegans* is fed with different *Escherichia coli* strains (e.g. OP50, HT115, HB101), depending on the laboratory or experimental setup, which also has an influence on its metabolism. The *C. elegans* genome is around 100 Mbp long and codes for approximately 20,000 protein coding genes and 28,000 non-coding RNAs and pseudogenes (Consortium, 1998; Hillier *et al.*, 2005) and approximately 41% of the genes are conserved in humans (Shaye and Greenwald, 2011; Kim *et al.*, 2018). The genome consists of five autosomal chromosomes and one sex chromosome, the latter of which is present only once in males. For comparison, the human genome consists of 22 autosomal chromosomes and two sex chromosomes (XY) and according to the 'Genome Reference Consortium Human Build 38 patch release 13 (GRCh38.p13, December 2013)', it encompasses around 3.1 Gbp. The human genome encodes for approximately 21,000 protein coding genes and around 39,000 non-coding RNAs and pseudogenes (International Human Genome Sequencing, 2004).

C. elegans was the first multi-cellular organism that has been fully sequenced (Consortium, 1998; Hillier *et al.*, 2005). This allowed the development of reverse genetic tools like the knock-down of genes by RNA-interference (RNAi). Fire and colleagues found that production of 'antisense RNA' leads to specific knock-down of a gene of interest (Fire *et al.*, 1991). Initial studies utilized 'antisense (single-stranded) RNA' that was either expressed from a plasmid or directly injected into the gonads (Fire *et al.*, 1991; Guo and Kemphues, 1995). Subsequently, this method has been optimized in *C. elegans* and led to the discovery that knock-down efficiency of genes can be drastically increased by using double-stranded (ds) RNA (Fire *et al.*, 1998). Different methods for dsRNA delivery have been developed over time, including dsRNA injection and soaking (Tabara *et al.*, 1998). Finally, the idea to express dsRNA in bacteria on which the worms feed further simplified knock-down by RNAi in *C. elegans* (Timmons and Fire, 1998; Kamath *et al.*, 2000). Finally, this led to construction of RNAi-libraries that cover large parts of the *C. elegans* genome (Kamath and Ahringer, 2003; Rual *et al.*, 2004), which enables *C. elegans* researchers to conduct genome-wide screens using reverse genetics.

2.2 Mitochondria – general overview

Mitochondria are eukaryotic organelles that are 0.5-1 µm in diameter and classically referred to as the 'powerhouse of the cell' due to their function in energy conversion. According to the endosymbiotic theory, mitochondria are the remnants of previously free-living aerobic proteobacteria that were taken up by heterotrophic anaerobe eubacteria around 2 billion years ago (Gabaldón and Huynen, 2004; Timmis *et al.*, 2004). Therefore, mitochondria have their own genome and are encompassed by two membranes that facilitate compartmentalization required for versatile metabolic pathways taking place in mitochondria (Figure 2).

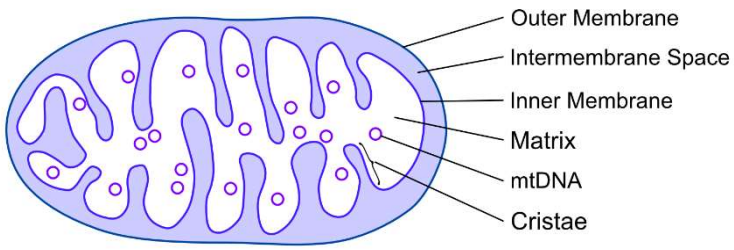

Figure 2: Schematic overview of a mitochondrion and its compartments and structures. mtDNA – mitochondrial DNA. Schematic adapted from (McBride et al., 2006).

The outer mitochondrial membrane (OMM) has a relatively low protein content and contains porins through which ions and small molecules can diffuse freely, as well as the translocase of the outer mitochondrial membrane (TOM), an active transporter for high-molecular weight proteins. Furthermore, several other proteins are associated with the OMM or reside in it, which play roles in apoptosis, innate immunity and mitochondrial dynamics (Walther and Rapaport, 2009). The aqueous space between the OMM and the inner mitochondrial membrane (IMM) is called the intermembrane space (IMS) where some of the proteins required for protein translocation to the mitochondrial matrix are located, as well as cytochrome c, which is associated with the IMM. The IMM is highly impermeable and contains the redox carriers (complex I-IV) required for oxidative phosphorylation (OXPHOS) and the adenosine triphosphate (ATP) synthase for generation of ATP in the matrix. It also contains the translocase of the inner mitochondrial membrane (TIM) for active transport of proteins across the membrane. Furthermore, the IMM is invaginated into numerous cristae to enlarge the surface area and therefore the ability to produce ATP (Neupert and Herrmann, 2007; Chacinska *et al.*, 2009). The mitochondrial matrix is the aqueous space enclosed by the inner membrane, which contains many enzymes of the tricarboxylic acid cycle (TCA) and the oxidation of pyruvate and fatty acids. Additionally, it contains mitochondrial ribosomes, tRNA and the mitochondrial genome which codes for 37

genes (van der Bliek *et al.*, 2017). Apart from the mitochondrial functions in bioenergetics, many other processes are regulated by or at mitochondria. For example, apoptosis can be initiated through the release of cytochrome c from the IMS, which acts as a signal to induce cell death. Furthermore, cellular calcium levels are to some extent regulated by the voltage-dependent anion channel (VDAC) at the OMM of mitochondria.

2.3 Mitochondrial import

The mitochondrial proteome in higher eukaryotes consists, depending on the organism, of 1200-1800 proteins, the bulk (99%) of which is encoded in the nuclear genome (Smith and Robinson, 2015; Muthye and Lavrov, 2020). The gene transfer from the mitochondrial to the nuclear genome in the course of evolution required the formation of a complex machinery for protein import into mitochondria. Most of the mitochondrial proteins are imported by active transport through TOM, the multi-subunit main entry gate. Depending on a proteins function and localization, five different sorting pathways are currently distinguished (Neupert and Herrmann, 2007; Chacinska *et al.*, 2009; Becker *et al.*, 2012; Harbauer *et al.*, 2014; Wiedemann and Pfanner, 2017).

The classical import pathway into the mitochondrial matrix is referred to as the presequence pathway, which translocates more than half of mitochondrial proteins (Vögtle *et al.*, 2009). It translocates mitochondrial precursor proteins that contain a cleavable mitochondrial targeting sequence (MTS or 'presequence') at the N-terminus (Fölsch *et al.*, 1998). Presequences typically vary between 10-50 amino acids (AA) in length and form amphipathic α-helices with a hydrophobic side and a positively charged side (Roise *et al.*, 1986). The primary structure differs greatly among presequences but certain properties of the amphipathic α-helices are well conserved, which facilitate prediction of the MTS (Claros and Vincens, 1996; Neupert and Herrmann, 2007). Three different receptors (TOM20, TOM22, TOM70) of the TOM complex recognize the presequence of the mitochondrial precursor, which, upon translocation through the TOM40 channel, is transferred to the TIM complex (Mokranjac and Neupert, 2015). The efficiency of translocation across the IMM is determined by the electrophoretic effect of the mitochondrial membrane potential ($\Delta\psi$) on the positive net charge of the presequence (Martin *et al.*, 1991). TIM23 facilitates translocation in cooperation with the presequence translocase-associated motor (PAM) (Truscott *et al.*, 2001). PAM contains the ATP-dependent

mitochondrial heat-shock protein 70 (mtHSP70) (Kang *et al.*, 1990) and the mitochondrial processing peptidase (MPP), which cleaves the presequence off in the mitochondrial matrix (Hawlitschek *et al.*, 1988). Mitochondrial inner membrane proteins are either imported into the mitochondrial matrix and then exported and inserted into the IMM by OXA1 (Hell *et al.*, 2001) or contain a non-cleavable hydrophobic stretch after the aminoterminal presequence and are laterally inserted into the mitochondrial inner membrane via TIM23 (van der Laan *et al.*, 2007).

The carrier pathway imports hydrophobic proteins of the mitochondrial metabolite carrier family and proteins containing multiple transmembrane domains into the IMS from where they are inserted into the IMM. These proteins contain internal targeting signals that are recognized by the import receptor TOM70 and TOM22 and pass through the TOM40 channel across the OMM. They are then transferred through the IMS by small TIM chaperones and inserted into the IMM via the TIM22 complex in a mitochondrial membrane potential ($\Delta\psi$) dependent manner (Endres *et al.*, 1999; Curran *et al.*, 2002; Rehling *et al.*, 2003).

The majority of mitochondrial IMS proteins contains specific cysteine motifs and is imported via the mitochondrial intermembrane space assembly (MIA) pathway. The precursor enters the IMS via the TOM complex and is recognized by MIA40 (Chacinska *et al.*, 2004). Subsequently, MIA40 introduces disulfide bonds into the precursor protein with the help of ERV1 in order to oxidize and thereby fold the precursor protein into its mature form (Mesecke *et al.*, 2005; Rissler *et al.*, 2005).

Additionally, at least two alternative import routes exist for lateral insertion of proteins containing α-helical and β-barrel transmembrane segments into the OMM. Multi-spanning, tail-anchored and signal-anchored OMM proteins as well as most subunits of the TOM-complex contain α-helical transmembrane domains and are inserted by the mitochondrial import (MIM) complex (Becker *et al.*, 2008; Hulett *et al.*, 2008; Popov-Čeleketić *et al.*, 2008). This insertion route does not require the TOM40 channel but uses a transient interaction with the TOM70 receptor instead. β-barrel proteins of the OMM contain β-hairpin recognition motifs (Jores *et al.*, 2016) and are inserted via the sorting and assembly (SAM) complex. Precursors of these proteins translocate through the TOM40 channel and are transferred to the SAM complex via small TIM chaperones of the IMS (Paschen *et al.*, 2003; Wiedemann *et al.*, 2003; Klein *et al.*, 2012).

2.4 Mitochondrial metabolism

Mitochondria are referred to as 'the powerhouses of the cell' due to their primary function in the generation of ATP. Overall, mitochondrial oxidative metabolism accounts for approximately 95% of the cellular ATP production. For this, three different enzymatic pathways exist in mitochondria that utilize different substrates; the electron transport chain (ETC), the tricarboxylic acid (TCA) cycle and the β-oxidation of fatty acids (FAO). Furthermore, these pathways are interconnected and share some of their metabolites. For example, both FAO and the TCA cycle provide reduced nicotinamide adenine dinucleotide (NADH) and flavin adenine dinucleotide ($FADH_2$) that function as electron carriers for the ETC (Nsiah-Sefaa and McKenzie, 2016).

The FAO pathway in mitochondria breaks down fatty acids, thereby supplying acetyl-coenzyme A (CoA) for fatty acid synthesis, the TCA cycle or the generation of ketone bodies, depending on the tissue and/or environmental conditions. Fatty acids derived from the diet, adipose tissue, intracellular storage sites like lipid droplets, peroxisomes or lysosomes first need to be converted to fatty acyl-CoA ester in the cytosol and then to fatty acylcarnitine at the OMM before being imported into mitochondria by the carnitine system (McGarry and Brown, 1997; Wanders *et al.*, 2010). Upon import into the mitochondrial matrix, fatty acylcarnitine is converted back to fatty acyl-CoA ester. The breakdown of fatty acyl-CoA ester in the mitochondrial matrix requires four enzymatic reactions: dehydrogenation, hydration, another dehydrogenation, followed by thiolytic cleavage. These reactions result in one molecule of two-carbon acetyl-CoA, two electrons, which supply the ETC in form of NADH and $FADH_2$, and a fatty acyl-CoA ester molecule that has been shortened by two carbon atoms. Subsequently, the fatty acyl-CoA ester can undergo as many cycles of oxidation in the so-called FAO spiral until only acetyl-CoA remains (Bartlett and Eaton, 2004; Wanders *et al.*, 2010; Nsiah-Sefaa and McKenzie, 2016; Spinelli and Haigis, 2018).

The TCA- or citric acid cycle is an amphibolic pathway in eukaryotes that is central for the production of ATP and provides intermediates, which are crucial for the biosynthesis of lipids and nucleotides. Furthermore, TCA cycle metabolites have been shown to be required for post translational modifications of chromatin and thereby influence cellular signaling and gene expression (Martínez-Reyes and Chandel, 2020). The TCA cycle indirectly accounts for the majority of oxygen consumption and ATP production and therefore is central for aerobic metabolism, even though its reactions do not require oxygen (Akram, 2014). Moreover, several

allosteric regulators exist within the cycle, which enables for an appropriate regulation of metabolic flux. For example, reduced NADH accumulates when the ETC is dysfunctional and inhibits all enzymes of the TCA cycle (Martínez-Reyes and Chandel, 2020). The TCA cycle starts with acetyl-CoA, derived from oxidation of fatty acids, carbohydrates or amino acids, and consists of a series of eight subsequent reactions, with some intermediates directly feeding into the ETC (Figure 3).

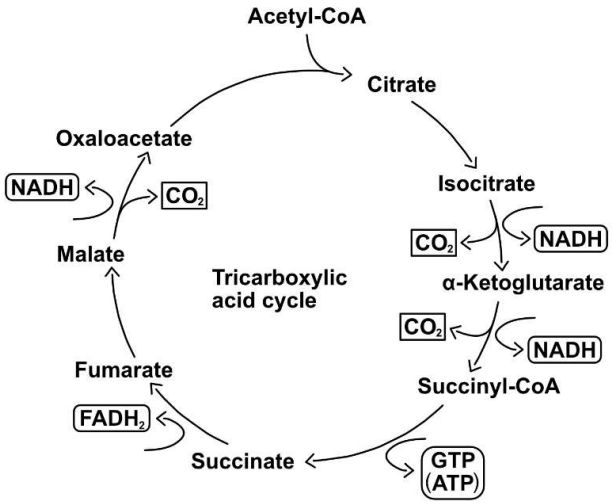

Figure 3: Schematic overview of the citric acid cycle (TCA) which consists of eight subsequent reactions and supplies the ETC with NADH and $FADH_2$. Many intermediates of the TCA cycle are crucial for lipid and nucleotide biosynthesis. Schematic adapted from (Martínez-Reyes and Chandel, 2020).

Acetyl-CoA and oxaloacetate are initially converted to citrate, which, in the next step is isomerized to isocitrate. Isocitrate is dehydrogenated to oxalosuccinate and then decarboxylated to α-ketoglutarate. This step also produces reduced NADH and CO_2. α-ketoglutarate is dehydrogenated to succinyl-CoA, again producing NADH and CO_2. When CoA is removed from succinyl-CoA to produce succinate, guanosine diphosphate (GDP) is simultaneously phosphorylated to form GTP, which later is converted to ATP. Next, succinate is dehydrogenated to fumarate generating reduced $FADH_2$. Hydration of fumarate produces malate, which is dehydrogenated to regenerate oxaloacetate. This final step again produces NADH and CO_2. The NADH and $FADH_2$ molecules produced by the TCA cycle directly feed into the ETC (Akram, 2014; Anderson *et al.*, 2018).

The ETC generates an electrochemical gradient across the IMM that is used by the ATP synthase for the generation of ATP, a process called oxidative phosphorylation (OXPHOS) (Figure 4). The multimeric OXPHOS complexes are conserved from yeast to humans, as well as the ATP synthase, which is conserved from bacteria to plants and across the animal kingdom.

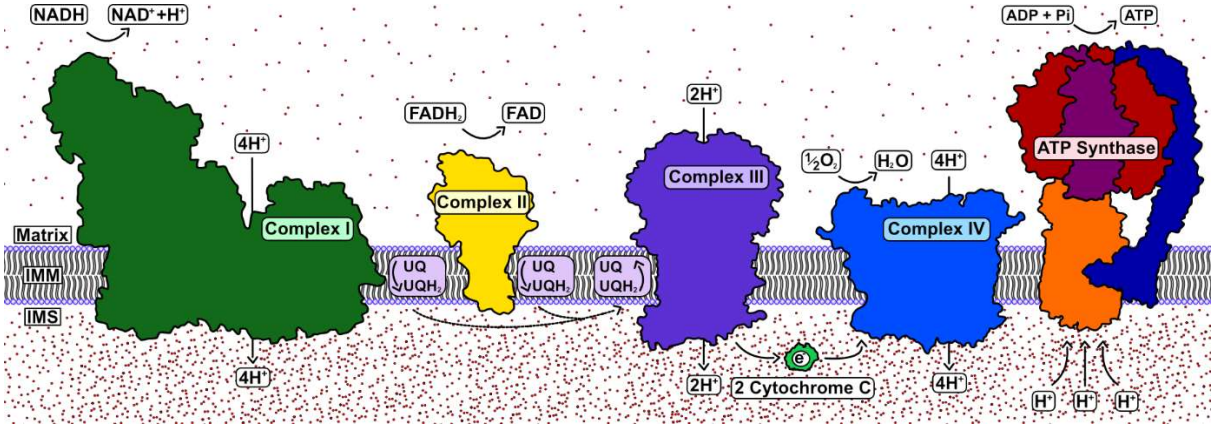

Figure 4: Schematic overview of the ETC and the ATP synthase. Complexes I-IV of the electron transport chain pump protons into the intermembrane space (IMS), thereby producing an electrochemical gradient across the inner mitochondrial membrane (IMM). This electrochemical gradient is used to set the ATP synthase in motion, which facilitates the phosphorylation of ADP to form ATP. UQ: Ubiquinone. Schematic adapted from (Letts and Sazanov, 2017).

All enzymes of the ETC (Complexes I-IV) and the ATP synthase are located in cristae of the IMM and form higher order structures in different stoichiometries called supercomplexes. The exact mechanism leading to their formation, as well as their function is currently highly debated (Chaban *et al.*, 2014). OXPHOS complexes I, III and IV are encoded by both nuclear and mitochondrial genomes and the assembly of these multi-subunit complexes requires high coordination of many assembly factors. Reduced NADH and $FADH_2$ molecules from glycolysis in the cytosol, FAO or the TCA cycle fuel the ETC and thereby indirectly the ATP synthase. Complex I (NADH dehydrogenase) and complex II (succinate dehydrogenase) bind and oxidize NADH and $FADH_2$ via their iron-sulfur clusters, respectively, thereby reducing ubiquinone (Figure 4). The accompanied conformational change of complex I during this process allows for the translocation of four protons into the IMS. Next, reduced ubiquinone diffuses to complex III (cytochrome c oxidoreductase) and is re-oxidized while the electrons are passed to cytochrome c. Again, two protons can pass the IMM via complex III into the IMS during this process. Complex IV (cytochrome c oxidase) then oxidizes cytochrome c and reduces molecular oxygen to form water while four protons are pumped into the IMS. The pumping of protons into the IMS creates an electrochemical potential that drives phosphorylation of ADP by complex V (ATP synthase) (Chaban *et al.*, 2014; Nsiah-Sefaa and McKenzie, 2016; Signes and Fernandez-Vizarra, 2018; Sousa *et al.*, 2018). The c-ring of the IMM-embedded F_0 part of the ATP synthase (indicated in orange in Figure 4) is rotating upon binding and transport of protons from the IMS into the matrix, thereby setting the central stalk of the F_1 part in motion. This stepwise rotation allows for conformational changes in the non-moving α and ß subunits of the F_1 head (indicated in red and purple in Figure 4) that enables

ADP and phosphate binding, phosphorylation of ADP in the active site and the release of ATP. This mechanism requires 3 protons from the IMS per molecule of ATP (Sousa *et al.*, 2018).

2.5 Mitochondrial dynamics

Mitochondria are central hubs for many metabolic and biosynthetic pathways and play an important role in other processes like cellular calcium homeostasis and apoptosis. Thus, mitochondrial homeostasis is tightly regulated by various mechanisms to ensure an intact and healthy population of mitochondria. Furthermore, the mitochondrial network is required to respond to certain environmental stimuli, which are often accompanied by changing energy demands. Mitochondrial plasticity is crucial for both the response to changing energy demands as well as mitochondrial quality control and is regulated by fission and fusion of mitochondrial membranes (Youle and van der Bliek, 2012). Mitochondrial dynamics is controlled by guanosine triphosphatases (GTPases) of the dynamin family, which are conserved from yeast to humans (Hales and Fuller, 1997; Otsuga *et al.*, 1998; Smirnova *et al.*, 1998; Bleazard *et al.*, 1999; Labrousse *et al.*, 1999; Shepard and Yaffe, 1999; Santel and Fuller, 2001; Chen *et al.*, 2003; Santel *et al.*, 2003; Ichishita *et al.*, 2008; Kanazawa *et al.*, 2008).

Mitochondrial fission in mammals has been shown to primarily occur at contact sites between the endoplasmic reticulum (ER) and mitochondria (Friedman *et al.*, 2011). Specifically, future fission events are initiated at sites where the ER is wrapped around mitochondria (Friedman *et al.*, 2011), which enables polymerization of actin filaments (Korobova *et al.*, 2013; Li *et al.*, 2014; Manor *et al.*, 2015). Subsequently, the myosin motor protein is recruited, which pulls on these actin filaments leading to a pre-constriction of mitochondria (Korobova *et al.*, 2013; Korobova *et al.*, 2014). Finally, the cytosolic protein DRP1 (Dnm1p in *Saccharomyces cerevisiae*, DRP-1 in *Caenorhabditis elegans*) is recruited to fission sites where it matures to form constricting spirals around mitochondria and drives mitochondrial fission by GTP hydrolysis (Figure 5) (Ingerman *et al.*, 2005; Ji *et al.*, 2015; Ji *et al.*, 2017). In *C. elegans*, DRP-1^{DRP1} has been shown to control mitochondrial morphology in body wall muscle cells of *C. elegans* since mitochondria appear blebby and elongated upon *drp-1(RNAi)* and in *drp-*1^{DRP1} mutants (Labrousse *et al.*, 1999). Moreover, *drp-1(RNAi)* has been shown to result in high embryonic lethality due to a mitochondrial segregation defect during cell division.

Furthermore, basal oxygen consumption rate (OCR) in *drp-1*^{DRP1} mutants has been shown to be elevated, while maximal OCR is decreased (Luz *et al.*, 2015).

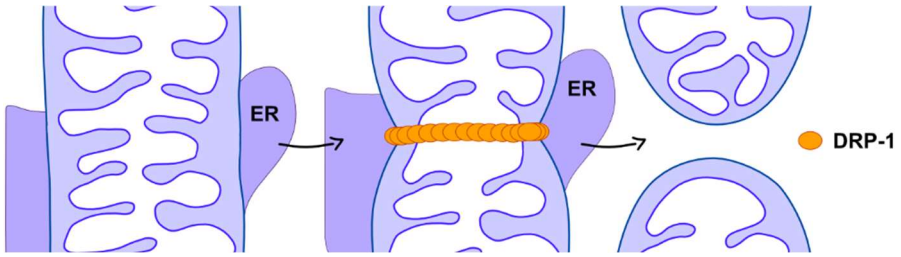

Figure 5: Simplified overview of mitochondrial fission by DRP-1. The endoplasmic reticulum wraps around mitochondria to mark future fission sites where DRP-1 assembles and drives mitochondrial fission by GTP hydrolysis. ER: Endoplasmic reticulum. Schematic adapted from (Zhu *et al.*, 2018).

Mitochondrial fusion of the OMM and IMM are each mediated by different GTPases. Defects in mitochondrial fusion have first been observed in *Drosophila melanogaster* (*D. melanogaster*) mutants during spermatogenesis, which lead to the identification of the first GTPase controlling mitochondrial dynamics (Hales and Fuller, 1997). The altered mitochondrial morphology in spermatids was described as '*fuzzy onions*' and the gene therefore was named *fzo*. Two orthologs of *fzo* exist in mammalian systems (Mitofusin1/2(MFN1/2)) (Santel and Fuller, 2001; Chen *et al.*, 2003), while there is one in each *S. cerevisiae* (Fzo1p (Rapaport *et al.*, 1998)) and *C. elegans* (FZO-1 (Ichishita *et al.*, 2008)). Biochemical analyses of Fzo1p localization and topology in yeast have shown that this protein is located on the OMM and that the coiled coil domain at its C-terminus, consisting of two hydrophobic heptad repeats, as well as the GTPase domain at its N-terminus are exposed to the cytosol, thereby facilitating OMM tethering and fusion, respectively (Hermann *et al.*, 1998; Rapaport *et al.*, 1998). Moreover, it has been shown that this topology is conserved from yeast to humans (Rojo *et al.*, 2002). The model for fusion of two adjacent mitochondrial membranes has been described to be dependent on the dimerization of antiparallel coiled-coil domains of Mitofusins resulting in tethering prior to fusion (Figure 6) (Koshiba *et al.*, 2004).

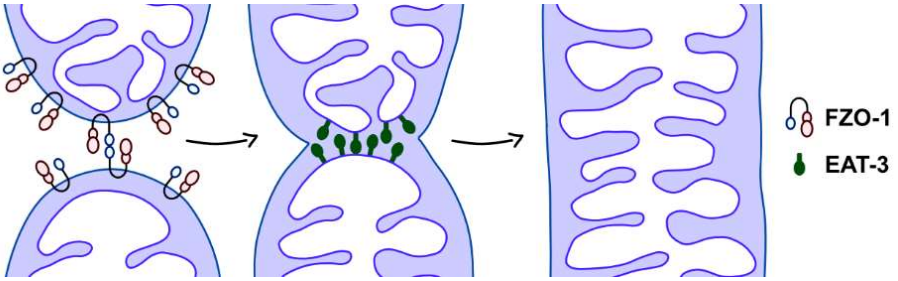

Figure 6: Simplified overview of mitochondrial fusion. FZO-1 drives fusion of the OMM, while EAT-3 drives fusion of the IMM. Both these processes require GTP. Schematic adapted from (Zhu *et al.*, 2018).

Furthermore, OMM fusion *in vitro* is dependent on the proton gradient (Meeusen *et al.*, 2004). More recently, the topology and the associated model of tethering via the coiled coil domain has been challenged since partial MFN1 proteins, only containing the GTPase domains, have been shown to dimerize (Qi *et al.*, 2016; Cao *et al.*, 2017). Moreover, the carboxy termini of Mitofusins have been shown to be located in the IMS or embedded in the OMM (Mattie *et al.*, 2017). Therefore, membrane tethering and -fusion may also occur only via the GTPase domains of adjacent Mitofusins. This illustrates that OMM fusion is still poorly understood and, therefore, is currently still under investigation. Moreover, it has recently been shown that mitochondrial fusion events are also linked to contact sites between the ER and mitochondria, both in human tissue culture and yeast (Abrisch *et al.*, 2020), as it was shown for mitochondrial fission before (Friedman *et al.*, 2011). The understanding of the exact molecular processes of mitochondrial fusion in *C. elegans* so far is limited. *fzo-1*^{MFN1,2} mutants show fragmented and swollen mitochondrial morphology (Ichishita *et al.*, 2008), reduced brood size and increased embryonic lethality (Machiela *et al.*, 2020). Moreover, these mutants have reduced pharyngeal pumping and thrashing rates (Johnson and Nehrke, 2010), as well as reduced maximal respiratory capacity (Luz *et al.*, 2015), all of which is indicative for reduced metabolic flux. Furthermore, *fzo-1*^{MFN1,2} mutants may have defects in FAO since acylcarnitine has been shown to accumulate in these mutants (Weir *et al.*, 2017).

The GTPase required for fusion of the IMM has first been identified in *S. cerevisiae* (Mgm1p (Wong *et al.*, 2000; Sesaki *et al.*, 2003; Wong *et al.*, 2003; Meeusen *et al.*, 2006)) and its orthologs in other systems have subsequently been described (OPA1 (Olichon *et al.*, 2002), EAT-3 (Figure 6) (Kanazawa *et al.*, 2008)). Mgm1p is located in the IMM facing the IMS and can be laterally inserted into the IMM in its large isoform or is processed proteolytically in an ATP-dependent manner into its short isoform, which localizes to the IMS (Herlan *et al.*, 2003; McQuibban *et al.*, 2003; Herlan *et al.*, 2004; Zick *et al.*, 2009). Both large and short isoforms are required for IMM fusion in yeast (Herlan *et al.*, 2004). Furthermore, it has been shown that IMM fusion is $\Delta\psi$ dependent *in vitro* (Meeusen *et al.*, 2004). The first studies in mammalian systems indicated that only the long isoforms of the various splice variants of OPA1 are required for mitochondrial fusion, which are processed upon dissipation of $\Delta\psi$ (Duvezin-Caubet *et al.*, 2006; Ishihara *et al.*, 2006). This $\Delta\psi$-dependent processing was proposed to serve as a mitochondrial quality control mechanism and led to the discovery of stress-induced OPA1 processing by OMA1 (Ehses *et al.*, 2009; Head *et al.*, 2009). Subsequent publications revealed that OPA1 can be processed at two cleavage sites by several different proteases, including

YME1L and OMA1, and that both short and long isoforms are required for IMM fusion even though this seems to be context or tissue- and cell type specific, respectively (Griparic *et al.*, 2007; Song *et al.*, 2007; Ehses *et al.*, 2009; Head *et al.*, 2009). More recently, this model has again been challenged by the finding that mouse embryonic fibroblasts (MEFs) lacking both OMA1 and YME1L show tubular mitochondria, although to a much lesser extent than in wild type (Anand *et al.*, 2014). In *C. elegans*, *eat-3*^{OPA1} mutants have initially been identified to be eating defective and later, EAT-3^{OPA1} has been shown to be required for IMM fusion of mitochondria (Avery, 1993; Kanazawa *et al.*, 2008). Furthermore, mitochondria of *eat-3*^{OPA1} mutants are fragmented and have reduced numbers of cristae and are instead further divided by septae, which only very rarely appear in mitochondria of wild-type animals (Kanazawa *et al.*, 2008; Byrne *et al.*, 2019). Moreover, *eat-3*^{OPA1} mutant animals show severe developmental defects, reduced brood size and are sensitive to oxidative stress. Additionally, *eat-3*^{OPA1} mutants have been shown to have reduced total fat mass, as well as pharyngeal pumping and thrashing rates (Johnson and Nehrke, 2010; Byrne *et al.*, 2019; Machiela *et al.*, 2020).

In summary, mitochondrial membrane fusion is facilitated by GTPases located on the OMM, which initially tether two adjacent mitochondria and, upon GTP hydrolysis, bring the two OMM in close proximity in order to fuse. In the following step, the GTPase located on the IMMs of the previously separate mitochondria facilitate fusion through oligomerization in an ATP- and $\Delta\psi$-dependent manner (Figure 6). Even though there has been extensive research in the field of mitochondrial dynamics, its bioenergetic control still remains largely unclear. As described above, both fission and fusion are GTP dependent processes and mitochondrial fusion is to some extent also $\Delta\psi$-dependent. However, the exact mechanisms how the cellular energy state and metabolic flux control mitochondrial dynamics is poorly understood. Conversely, the consequences of perturbed mitochondrial dynamics on metabolism remain elusive.

Mitochondrial dynamics additionally plays an important role in cellular homeostasis. Short term stress or reduced ETC activity has been shown to result in mitochondrial hyper fusion in order to maintain ATP levels (Tondera *et al.*, 2009; Rolland *et al.*, 2013). Persistent mitochondrial stress on the other hand, leads to fragmentation of the mitochondrial network, a process that also occurs during ageing (Regmi *et al.*, 2014; Jiang *et al.*, 2015). In addition to situations of stress, mitochondrial dynamics is also crucial to maintain an intact population of mitochondria under non-stressed physiological conditions. Mitochondria have been shown to

fuse in order to exchange and thereby complement their content (Yoneda *et al.*, 1994; Nakada *et al.*, 2001; Ono *et al.*, 2001; Chen *et al.*, 2005; Eisner *et al.*, 2014). Moreover, mitochondrial fission is required for the selective removal of depolarized mitochondria via mitophagy (Twig *et al.*, 2008), another cellular quality control mechanism, which is later described in more detail.

2.6 Mitochondrial unfolded protein response (UPR^{mt})

The mitochondrial unfolded protein response (UPR^{mt}) is a conserved retrograde signaling pathway that restores homeostasis in dysfunctional mitochondria. The transcriptional upregulation of mitochondrial chaperones upon mitochondrial stress, induced by ethidium bromide (EthBr) treatment, has first been described in mammalian cell culture (Martinus *et al.*, 1996; Zhao *et al.*, 2002). The construction of transcriptional green fluorescent protein (GFP) reporters of the mitochondrial chaperones *hsp-6*^{mtHSP70} and *hsp-60*^{HSPA1} in the laboratory of David Ron allowed detailed studies in *C. elegans* (Yoneda *et al.*, 2004). Yoneda and colleagues found increased expression of these reporters upon ethidium bromide (EthBr) (reduces mitochondrial DNA (mtDNA) content by inhibition of mtDNA replication) or paraquat treatment (inhibits complex I and induces accumulation of reactive oxygen species (ROS)). Furthermore, screening of chromosome I for inducers of mitochondrial chaperone expression by RNAi identified 32 mitochondrial proteins, most of which have roles in the ETC, mitochondrial metabolism, mitochondrial protein synthesis or -import. Additionally, the mitochondrial matrix AAA-protease *spg-7*^{AFG3L2} was identified. Remarkably, the authors concluded from this data that knock-down of most genes in their dataset (as well as the EthBr and paraquat treatments) lead to perturbations of the mitochondrial folding environment and therefore named this pathway the mitochondrial unfolded protein response. They reasoned that many of the identified proteins are part of hetero-oligomeric complexes, which are encoded in the mitochondrial and the nuclear genome, leading to a ‘mito-nuclear imbalance’ and consequently the accumulation of these subunits upon mitochondrial stress. This in turn was proposed to require the expression of mitochondrial chaperones (Yoneda *et al.*, 2004). Subsequently, a genome-wide RNAi screen for suppressors of UPR^{mt}, induced by an unidentified mutation (*zc32*), was conducted leading to the following model.

The master regulator 'Activating Transcription Factor associated with Stress-1 (ATFS-1^{ATF4,5})' harbors an N-terminal MTS and, in the absence of mitochondrial stress, is imported into mitochondria where it is degraded by the mitochondrial LONP-1^{LONP1} protease (Haynes *et al.*, 2010; Nargund *et al.*, 2012). In certain situations of mitochondrial stress, unfolded or misfolded proteins accumulate in the mitochondrial matrix (Figure 7). This accumulation can be caused by excessive production of ROS or mutations in the mitochondrial genome, which was proposed to lead to an imbalance of mitochondrial and nuclear encoded subunits of mitochondrial proteins (Houtkooper *et al.*, 2013). This in turn leads to an overload of protease and chaperone capacity in mitochondria. UPR^{mt} was proposed to be activated when the accumulating proteins are degraded into small peptide fragments by the matrix protease CLPP-1^{CLPP} (Haynes *et al.*, 2007). Subsequently, these peptides are exported from the matrix by HAF-1^{ABCB10} and diffuse freely into the cytosol (Haynes *et al.*, 2010). This efflux of peptide fragments then somehow leads to inhibition of mitochondrial import and consequently to decreased import efficiency of ATFS-1^{ATF4,5} into mitochondria (Nargund *et al.*, 2012). As a result, cytosolic ATFS-1^{ATF4,5} is imported into the nucleus due to its C-terminal nuclear localization sequence (NLS) and activates the transcriptional program of UPR^{mt}, together with UBL-5^{UBL5} and DVE-1^{SATB1} (Benedetti *et al.*, 2006; Haynes *et al.*, 2007; Haynes *et al.*, 2010; Nargund *et al.*, 2012).

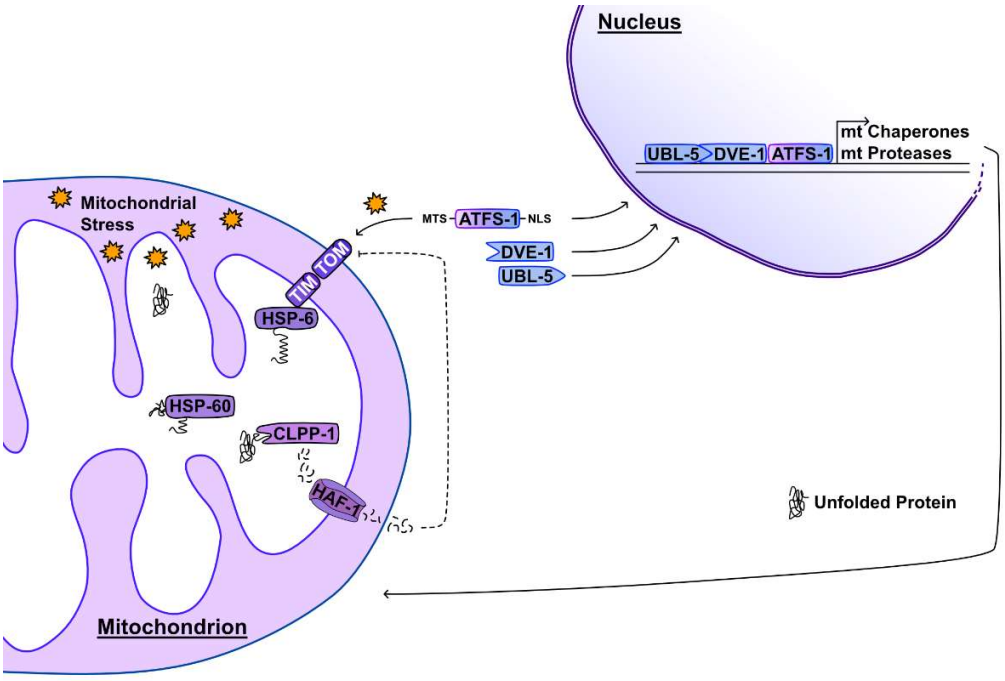

Figure 7: Proposed UPR^{mt} model according to Haynes and colleagues (~2010). Unfolded proteins accumulate in the mitochondrial matrix, which are cleaved into small peptides by CLPP-1. These peptides are transported into the cytosol by HAF-1 and somehow inhibit mitochondrial import, leading to ATFS-1^{ATF4,5} translocation from the cytosol into the nucleus and the concomitant induction of UPR^{mt}. Schematic adapted from (Jovaisaite *et al.*, 2014).

Furthermore, the kinase GCN-2^{EIF2AK4} was proposed to act in a complementary pathway to that of ATFS-1^{ATF4,5} (Baker *et al.*, 2012). Baker and colleagues speculated that ROS coming from mitochondria somehow activate GCN-2^{EIF2AK4}, which they showed to phosphorylate translation initiation factor 2 alpha (EIF-2A^{EIF2A}) upon mitochondrial stress. Phosphorylation of EIF-2A^{EIF2A} has previously been shown to lead to attenuation of cytosolic translation and has been implicated in other stress responses before (Boye and Grallert, 2020). Reducing the amount of nuclear encoded subunits of mitochondrial proteins would equilibrate the mito-nuclear imbalance and therefore re-establish mitochondrial homeostasis (Baker *et al.*, 2012). Consequently, activation of the UPR^{mt} has in the beginning been mostly perceived as a response that restores homeostasis by expression of chaperones and proteases, thereby re-establishing the 'protein folding environment' in mitochondria.

A broader understanding of the UPR^{mt} as a transcriptional program that also has an impact on cellular metabolism emerged only later. Upon UPR^{mt} activation, genes required for oxidative phosphorylation and the TCA cycle have been shown to be repressed while expression of glycolysis related genes are induced (Nargund *et al.*, 2012; Nargund *et al.*, 2015). Additionally, ETC assembly factors, iron-sulfur biogenesis components as well as mitochondrial chaperones are induced upon mitochondrial stress in an ATFS-1^{ATF4,5}-dependent manner (Nargund *et al.*, 2015). Therefore, activation of UPR^{mt} allows for metabolic adaptation when mitochondria are dysfunctional. Furthermore, inhibition of the mevalonate pathway has been shown to suppress UPR^{mt} but the mechanisms behind the requirement of mevalonate pathway metabolites, which control many aspects of cellular metabolism, for activation of UPR^{mt} remain unknown (Liu *et al.*, 2014; Ranji *et al.*, 2014). Several enzymes of the mevalonate pathway have been shown to be upregulated via ATFS-1^{ATF4,5}, which has been proposed to act as a compensatory mechanism in order to supply enough metabolites in situations of mitochondrial dysfunction (Nargund *et al.*, 2012; Ranji *et al.*, 2014; Nargund *et al.*, 2015; Oks *et al.*, 2018). Moreover, the ceramide and sphingolipid biosynthetic pathways have been shown to be involved in UPR^{mt} signaling (Liu *et al.*, 2014). These findings highlight the importance of UPR^{mt} activation and its role in metabolic adaptation in situations of mitochondrial dysfunction and -stress.

In the meantime, signaling of the UPR^{mt} pathway itself has been further characterized and several other players have been identified. The nuclear co-factor LIN-65 and the histone methyltransferase MET-2 have been shown to be required for nuclear translocation of DVE-1^{SATB-1} and facilitate epigenetic modifications and chromatin reorganization (Tian *et al.*, 2016).

In addition, activation of UPR^{mt} has been shown to be dependent on the histone demethylases JMJD-1.2^{PHF8} and JMJD-3.1^{JMJD3} (Merkwirth *et al.*, 2016). Post-translational modifications also have been shown to affect UPR^{mt} activation. ULP-4^{SENP6,7} deSUMOylates DVE-1^{SATB-1} and ATFS-1^{ATF4,5}, is required for nuclear translocation of DVE-1^{SATB-1} and stabilizes cytosolic ATFS-1^{ATF4,5} upon mitochondrial stress (Gao *et al.*, 2019). UPR^{mt} activation has also been shown to be propagated in a cell non-autonomous fashion. Specifically, mitochondrial stress occurring in neurons results in a systemic induction of UPR^{mt} (Durieux *et al.*, 2011; Berendzen *et al.*, 2016; Shao *et al.*, 2016; Kim and Sieburth, 2018; Zhang *et al.*, 2018; Kim and Sieburth, 2020). Serotonin and the neuropeptide FLP-2 have been shown to propagate the mitochondrial stress signal from neurons to peripheral tissues (Berendzen *et al.*, 2016; Shao *et al.*, 2016). Furthermore, the cell non-autonomous propagation of UPR^{mt} requires components of the retromer complex and the Wnt signaling pathway (Zhang *et al.*, 2018), as well as the G-protein-coupled receptor (GPCR) FSHR-1 and the sphingosine kinase SPHK-1 (Kim and Sieburth, 2018, 2020).

2.7 Autophagy and Mitophagy

The autophagic pathway is a cellular recycling system that targets cytosolic constituents, long lived proteins and defective organelles to the lysosome for degradation. Furthermore, autophagy is induced upon starvation to degrade cellular components as a compensatory mechanism for the lack of nutrient supply (Mizushima, 2007). Autophagy is an evolutionary conserved quality control mechanism, which leads to disease when deregulated. The machinery initiating and controlling the autophagic pathway has to a great extent been discovered in *S. cerevisiae* and orthologs for most of these genes have later been identified in mammalian systems, *C. elegans* and *D. melanogaster* (Levine and Klionsky, 2004). Depending on the material or organelle that is being recycled, it is referred to as autophagy, mitophagy, ER-phagy, pexophagy, nucleophagy or lysophagy (Anding and Baehrecke, 2017).

The induction of autophagy is suppressed by the target of rapamycin (TOR) kinase (ortholog of LET-363 in *C. elegans*) and its downstream effectors. Upon induction of autophagy, the initiator complex, including ATG1 (ortholog of UNC-51 in *C. elegans*), is assembled at the pre-autophagosomal structure, leading to formation of the phagophore (Feng *et al.*, 2014; Palmisano and Meléndez, 2019). The cargo that is being recycled is subsequently engulfed by

the expanding phagophore, thereby forming the autophagosome (Figure 8). This elongation and expansion step during autophagosome formation requires assembly of additional ATG complexes, which include ATG8 (ortholog of LGG-1 in *C. elegans*), a protein that is lipidated and incorporated into the autophagosomal membranes. Subsequently, the autophagosome fuses with a lysosome and becomes an autolysosome, where hydrolases degrade the cargo and recycle its components (Levine and Klionsky, 2004; Mizushima, 2007; Feng *et al.*, 2014).

In *C. elegans*, autophagosomes can be visualized using a GFP::LGG-1^{GABARAP} fusion protein (Figure 8) (Jenzer *et al.*, 2015; Zhang *et al.*, 2015; Palmisano and Meléndez, 2016; Chen *et al.*, 2017). Its fluorescent emission is quenched in autolysosomes due to the low pH in the lysosomal compartment. Furthermore, degradation of GFP::LGG-1^{GAPARAP} in autolysosomes can be detected using western blot analysis. The appearance of 'cleaved GFP' on the blot membrane is indicative for the lysosomal turnover of GFP::LGG-1^{GAPARAP} (Mizushima *et al.*, 2010; Chapin *et al.*, 2015; Klionsky *et al.*, 2016). SQST-1^{p62}::GFP is often used in parallel to validate the induction of autophagy using fluorescence microscopy, since this fusion protein accumulates when autophagy is blocked in a later stage (e.g. when fusion of autophagosomes with lysosomes is blocked) (Tian *et al.*, 2010).

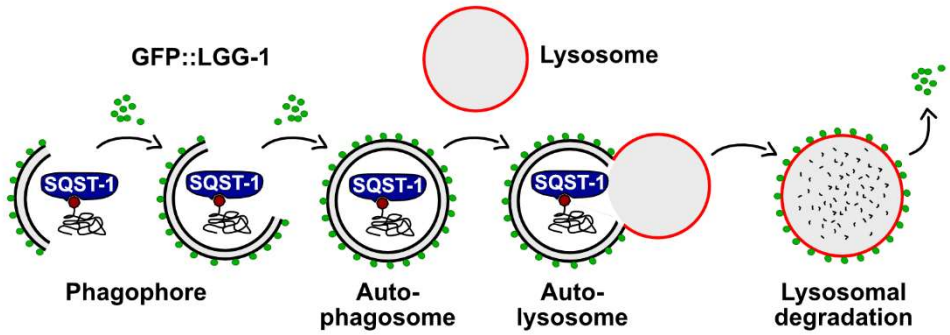

Figure 8: Schematic of the autophagic pathway. Upon induction of autophagy, a phagophore forms around the cargo. The phagophore elongates to build an autophagosome, which fuses with the lysosome in order to degrade its cargo. Lysosomal enzymes degrade the cargo and LGG-1 is recycled. Schematic modified from (Jing and Lim, 2012).

Mitophagy targets defective mitochondria to the lysosome for recycling and has been shown to be regulated via several different pathways. Initial studies have shown that PINK (ortholog of PINK-1 in *C. elegans*), an OMM kinase, accumulates on depolarized mitochondria and phosphorylates other OMM proteins. Subsequently, the E3 ligase Parkin (ortholog of PDR-1 in *C. elegans*) is recruited and ubiquitinates OMM proteins, which serves as a so called 'eat me' signal for the autophagic machinery (Narendra *et al.*, 2008; Matsuda *et al.*, 2010; Narendra

et al., 2010; Vives-Bauza *et al.*, 2010; Koyano *et al.*, 2014; Lazarou *et al.*, 2015). The available data for the *C. elegans* orthologs PINK-1 and PDR-1 so far is limited since reliable assays to specifically monitor mitophagy do not exist (Springer *et al.*, 2005; Palikaras *et al.*, 2015; Cooper *et al.*, 2017). Additionally, PINK- and Parkin- independent mitophagy pathways have been discovered that also lead to degradation of mitochondria via the autophagic machinery (Allen *et al.*, 2013; Bhujabal *et al.*, 2017; Villa *et al.*, 2017; Di Rita *et al.*, 2018). Various mitophagy receptors have been identified in mammalian systems, including NIX (Zhang and Ney, 2008; Zhang and Ney, 2009; Novak *et al.*, 2010), BNIP3 (Zhang and Ney, 2009; Hanna *et al.*, 2012) and FUNDC1 (Liu *et al.*, 2012), the latter two of which have orthologs in *C. elegans* (Palikaras *et al.*, 2015; Lim *et al.*, 2019).

2.8 The endosomal sorting complexes required for transport (ESCRT)

Receptor-mediated endocytosis is a cellular transport mechanism targeting cargo to the lysosome for degradation. Thereby, the ESCRT plays a central role in the maturation of endosomes. Amino acids and lipids are transported into the cell from the extracellular space towards the lysosomal compartment in this manner. Upon arrival, the cargo binds to a receptor at the plasma membrane, leading to invagination of the membrane and ubiquitination of the receptor (Michelet *et al.*, 2010; Christ *et al.*, 2017) (Figure 9).

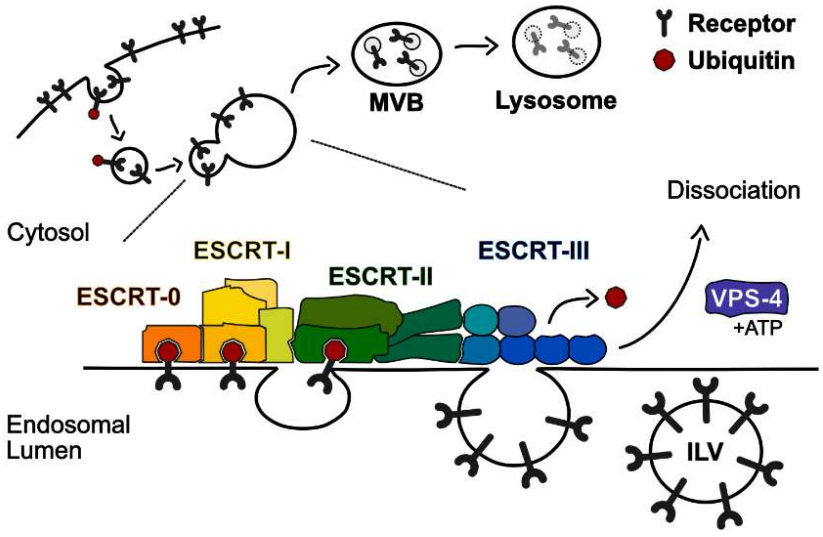

Figure 9: Schematic overview of the assembly and disassembly of the endosomal sorting complexes required for transport (ESCRT). ESCRT-I, -II, -III are multimeric complexes each consisting of 4 or more proteins. MVB: Multivesicular body, ILV: Intraluminal vesicle. Schematic adapted from (Michelet and Legouis, 2012).

The ubiquitylated receptor acts as a signal to recruit the ESCRT. Subsequently, the four hetero-multimeric ESCRT subcomplexes (ESCRT-0 – ESCRT-III) are assembling at the invaginated membrane in order to sort and pack the cargo into intraluminal vesicles, thereby forming multivesicular bodies (MVBs). Finally, the receptor is de-ubiquitylated and the ATPase VPS-4^{VPS4} dissociates the whole complex. Subsequently, the generated MVBs are targeted for lysosomal degradation. Recently, apart from the canonical role in endocytosis, other functions of ESCRT in development and cellular signaling have been shown (Michelet *et al.*, 2010; Christ *et al.*, 2017). Moreover, depletion of either of the ESCRT subunits causes different defects and responses in mammals, flies, yeast and nematodes. While depletion of ESCRT components leads to a block in autophagy in mammals, flies and yeast due to its role in lysosomal fusion and closure of autophagosomes, respectively, it has been shown to induce autophagy in *C. elegans* (Filimonenko *et al.*, 2007; Lee *et al.*, 2007; Rusten *et al.*, 2007; Tamai *et al.*, 2007; Djeddi *et al.*, 2012; Michelet and Legouis, 2012; Guo *et al.*, 2014; Lefebvre *et al.*, 2018; Takahashi *et al.*, 2018; Zhou *et al.*, 2019).

2.9 Inositol triphosphate (IP_3) signaling

The IP_3 pathway processes signals from the extracellular space through an intracellular signaling cascade. Upon binding of certain substrates, such as hormones, growth factors or neurotransmitters to their receptors in the plasma membrane, phospholipase C (PLC) gets activated by GPCRs and hydrolyzes phosphatidylinositol 4,5-biphosphate (PIP_2), thereby generating IP_3 and diacylglycerol (DAG) (Berridge, 2009). Subsequently, these two second messengers mediate several cellular responses. Specifically, IP_3 binds to the IP_3 receptor (IP_3R) at the ER, leading to the release of calcium from the ER into the cytosol, mitochondria and lysosomes (Kania *et al.*, 2017). Interestingly, in mammals, calcium transfer into mitochondria has been shown to occur at ER-mitochondria contact sites (ERMCs) that harbor IP_3R, as well as the voltage-dependent anion channel (VDAC) and the Mitofusins MFN1&2 (Raturi and Simmen, 2013; Marchi *et al.*, 2014; Burgoyne *et al.*, 2015). Moreover, spatial and temporal calcium oscillations have been shown to regulate many diverse processes, such as secretion, proliferation, fertility, metabolism and cell death (Decrock *et al.*, 2013). Therefore, IP_3 signaling is versatile and controls many different aspects of cellular physiology.

3. Objectives

Mitochondrial membrane dynamics has been studied extensively over the past 20 years, but its role in the physiological context still remains largely unknown. How the bioenergetic state influences mitochondrial morphology, as well as the consequences of disrupted mitochondrial dynamics on development and mitochondrial homeostasis are currently poorly understood. Thus, we use *Caenorhabditis elegans* as a model to study the mitochondrial unfolded protein response (UPR^{mt}) in animals with a block in mitochondrial fusion. Identification of modulators of this stress response, which acts to restore mitochondrial homeostasis and to adjust mitochondrial metabolism, may help to better understand the defects observed in mutants in which mitochondrial dynamics is blocked and to learn more about the UPR^{mt} pathway itself. Therefore, we performed a genome-wide screen for modulators of the UPR^{mt} response in mitochondrial fusion deficient mutants.

Chapter I

Genome-wide RNAi screen for regulators of UPR^{mt} in *Caenorhabditis elegans* mutants with defects in mitochondrial fusion

Simon Haeussler, Assa Yeroslaviz, Stéphane G. Rolland, Sebastian Luehr, Eric Lambie and Barbara Conradt

Unpublished manuscript

Chapter I

Genome-wide RNAi screen for regulators of UPR^{mt} in *Caenorhabditis elegans* mutants with defects in mitochondrial fusion

Simon Haeussler[*], Assa Yeroslaviz[†], Stéphane G. Rolland[*,‡,1], Sebastian Luehr[*], Eric Lambie[*,**] and Barbara Conradt[*,§,**,1]

Author Affiliation:

[*] Faculty of Biology, Ludwig-Maximilians-University Munich, 82152 Planegg-Martinsried, Germany

[†] Computational Biology Group, Max Planck Institute of Biochemistry, 82152 Planegg-Martinsried, Germany

[‡] Present address: Center for Genomic Integrity, Institute for Basic Science (IBS), Ulsan 44919, South Korea

[§] Center for Integrated Protein Science, Ludwig-Maximilians-University Munich, 82152 Planegg-Martinsried, Germany

[**] Department of Cell and Developmental Biology, Division of Biosciences, University College London, London WC1E 6AP, United Kingdom

Author List Footnotes:

[1] Lead Contacts

UPR^{mt} screen in *fzo-1(tm1133)* mutants (37 characters)

Keywords: mitochondrial unfolded protein response, mitochondrial dynamics, fzo-1, IP_3 signaling, Mitoguardin

Correspondence:

Barbara Conradt, Department of Cell and Developmental Biology, Division of Biosciences, University College London, Gower Street, London WC1E 6AP, United Kingdom; Email: b.conradt@ucl.ac.uk

Stéphane Rolland, Center for Genomic Integrity, Institute for Basic Science (IBS), Ulsan 44919, South Korea; Email: srolland@ibs.re.kr

Chapter I

ABSTRACT

Mitochondrial dynamics plays an important role in mitochondrial quality control and the adaptation of metabolic activity in response to environmental changes. The disruption of mitochondrial dynamics has detrimental consequences for mitochondrial and cellular homeostasis and leads to the activation of the mitochondrial unfolded protein response (UPR^{mt}), a quality control mechanism that adjusts cellular metabolism and restores homeostasis. To identify genes involved in the induction of UPR^{mt} in response to a block in mitochondrial fusion, we performed a genome-wide RNAi screen in *Caenorhabditis elegans* mutants lacking the gene *fzo-1*, which encodes the ortholog of mammalian Mitofusin, and identified 299 suppressors and 86 enhancers. Approximately 90% of these 385 genes are conserved in humans, and one third of the conserved genes have been implicated in human disease. Many genes in our dataset have roles in developmental processes, which implies that mitochondrial function and the response to stress are defined during development and maintained throughout life. Our dataset primarily contains mitochondrial enhancers and non-mitochondrial suppressors of UPR^{mt}, suggesting that the maintenance of mitochondrial homeostasis has evolved as a critical cellular function, which, when disrupted, can be compensated for by many different cellular processes. Analysis of the subsets of 'non-mitochondrial' enhancers and 'mitochondrial' suppressors suggests that organellar contact sites, especially between the ER and mitochondria, are of importance for mitochondrial homeostasis. In addition, we identified several genes involved in IP_3 signaling that modulate UPR^{mt} in *fzo-1* mutants and found a potential link between pre-mRNA splicing and UPR^{mt} activation.

(244/250 words)

Chapter I

INTRODUCTION

Mitochondria are important for cellular adenosine triphosphate (ATP) production, iron-sulfur-cluster biogenesis, lipid metabolism and apoptosis, and therefore, mitochondrial homeostasis is tightly regulated by several quality control mechanisms (Tatsuta and Langer, 2008; Kornmann, 2014). Moreover, mitochondria are required to respond to environmental challenges, which are often accompanied by alterations in energy demand (Youle and van der Bliek, 2012). Mitochondrial dynamics controls mitochondrial shape and -distribution, thus playing a central role in both mitochondrial homeostasis and the adjustment to changing energy demands (Yaffe, 1999; van der Bliek *et al.*, 2013). Dynamics of mitochondrial membranes is controlled by large guanosine triphosphate-binding proteins (GTPases) of the dynamin-like family, which are conserved from yeast to humans (Hales and Fuller, 1997; Otsuga *et al.*, 1998; Smirnova *et al.*, 1998; Bleazard *et al.*, 1999; Labrousse *et al.*, 1999; Shepard and Yaffe, 1999; Chen *et al.*, 2003; Santel *et al.*, 2003; Ichishita *et al.*, 2008; Kanazawa *et al.*, 2008). In the nematode *Caenorhabditis elegans*, fusion of the outer and inner mitochondrial membrane (OMM and IMM) is facilitated by FZO-1^{MFN1,2} (Ichishita *et al.*, 2008) and EAT-3^{OPA1} (Kanazawa *et al.*, 2008), respectively. Conversely, fission of the OMM and IMM is carried out by DRP-1^{DRP1} (Labrousse *et al.*, 1999), whose ortholog in *Saccharomyces cerevisiae* (Dnm1p) has been shown to form constricting spirals around mitochondria (Ingerman *et al.*, 2005). The disruption of mitochondrial dynamics has detrimental consequences for mitochondrial and ultimately cellular homeostasis and is associated with several human diseases. Thus, mitochondrial homeostasis is controlled by several additional protective quality control mechanisms, including the mitochondrial unfolded protein response (UPR^{mt}) and mitophagy (Chen and Chan, 2004; Youle and van der Bliek, 2012; van der Bliek *et al.*, 2013; Kornmann, 2014). How these quality control mechanisms are coordinated with mitochondrial dynamics is not fully understood. Recently, disruption of mitochondrial dynamics has been shown to induce UPR^{mt} (Kim and Sieburth, 2018; Zhang *et al.*, 2018; Rolland *et al.*, 2019; Haeussler *et al.*, 2020). UPR^{mt} has been studied extensively in the past decade using genome-wide RNAi screens in *C. elegans* (Haynes *et al.*, 2007; Runkel *et al.*, 2013; Bennett *et al.*, 2014; Liu *et al.*, 2014; Rolland *et al.*, 2019). Upon mitochondrial stress and the concomitant decrease in mitochondrial membrane potential, the master regulator of UPR^{mt}, ‘activating transcription factor associated with stress 1’ (ATFS-1^{ATF4,5}), instead of being imported into mitochondria, translocates to the nucleus, where it activates a broad transcriptional program (Haynes *et al.*, 2010; Nargund *et al.*, 2012; Rolland *et al.*, 2019). UPR^{mt} activation leads to the expression of a large set of cytoprotective genes including genes encoding chaperones (*e.g. hsp-6*^{mtHSP70} and *hsp-60*^{HSDP1}, whose transcription is

commonly used to monitor UPR^{mt} activation (Yoneda *et al.*, 2004)) or proteases, and has been shown to promote mitochondrial biogenesis and coordinate cellular metabolism (Nargund *et al.*, 2012; Nargund *et al.*, 2015). (All genes that are specifically up- or downregulated upon induction of UPR^{mt} are referred to as UPR^{mt} effectors.) Moreover, UPR^{mt} has been shown to act in a cell non-autonomous way, and once activated in a certain tissue can result in a systemic response (Durieux *et al.*, 2011; Shao *et al.*, 2016; Kim and Sieburth, 2018; Zhang *et al.*, 2018; Kim and Sieburth, 2020).

In this study, we performed a genome-wide RNAi screen to identify regulators of UPR^{mt} in *fzo-1(tm1133)* mutants and identified 299 suppressors and 86 enhancers. We analyzed this dataset using bioinformatic tools, such as GO enrichment analysis, gene network analysis and analysis of transcription factor binding sites in promotors of candidate genes. Furthermore, we determined the specificities of the candidates identified with respect to their ability to modulate UPR^{mt} using secondary screens. Finally, we identified the *C. elegans* ortholog of the mammalian genes *Miga1* and *Miga2*, which have been implicated in mitochondrial fusion, and demonstrate that the loss of the *C. elegans* ortholog leads to mitochondrial fragmentation and the induction of UPR^{mt}.

Chapter I

METHODS

General *C. elegans* methods and strains

C. elegans strains were cultured as previously described (Brenner, 1974). Bristol N2 was used as the wild-type strain. All experiments were carried out at 20°C and all strains were maintained at 20°C. The following alleles and transgenes were used: LGI: *spg-7(ad2249)* (Zubovych *et al.*, 2010); LGII: *fzo-1(tm1133)* (National BioResource Project); *eat-3(ad426)* (Kanazawa *et al.*, 2008); LGIV: *drp-1(tm1108)* (National BioResource Project); LGV: *miga-1(tm3621)* (National BioResource Project). Additionally, the following multi-copy integrated transgenes were used: *zcIs9* ($P_{hsp\text{-}60}$*::gfp::unc-54 3'UTR*), *zcIs13* ($P_{hsp\text{-}6}$*::gfp::unc-54 3'UTR*) (Yoneda *et al.*, 2004); *bcIs78* ($P_{myo\text{-}3}$*::gfp*^{mt}) (Rolland *et al.*, 2013).

RNA-mediated interference

RNAi by feeding was performed using the updated 'Ahringer' RNAi library (Kamath and Ahringer, 2003), which covers around ~87% of the currently annotated *C. elegans* protein coding genes. For the primary and secondary screens with the multi-copy *zcIs13* transgene in the *fzo-1(tm1133)*, *drp-1(tm1108), eat-3(ad426)* or *spg-7(ad2249)* background, RNAi clones were cultured overnight in 100 µL of LB containing carbenicillin (100 µg/mL) in a 96 well plate format at 37°C and 200 rpm. 10 µL of each RNAi culture was used to seed one well of a 24 well RNAi plate containing 0.25% Lactose (w/v) as described previously (Rolland *et al.*, 2019). The plates were incubated at 20°C in the dark. 24 hours later, 3 L4 larvae of all strains carrying the *fzo-1(tm1133)* and *spg-7(ad2249)* allele, and 2 L4 larvae of *drp-1(tm1108)* were transferred to each well of the RNAi plates. The F1 generation was scored by eye for fluorescence intensity of the $P_{hsp\text{-}6\ \mathrm{mtHSP70}}$*gfp* reporter after 4-12 days and compared to worms of the respective genotype on the negative control *sorb-1(RNAi)*.

Screening procedure and sequencing of RNAi-clones

For the primary screen, all RNAi clones of the library were tested once. Bacterial RNAi clones that enhanced or suppressed the $P_{hsp\text{-}6\ \mathrm{mtHSP70}}$*gfp* reporter were picked from the wells and inoculated in 100 µL of LB containing carbenicillin (100 µg/mL) in a 96 well plate format and cultured overnight at 37°C and 200 rpm. Glycerol stocks of these overnight cultures were prepared the following day by adding 100 µL of LB containing 30% glycerol and frozen at -80°C. After all RNAi clones of the library were tested, the 657 identified candidates were re-

tested at least three times in duplicates for verification of the observed phenotype. The RNAi clones that reproduced the suppression or enhancement phenotype at least three out of six times were considered as verified candidates.

The 385 verified RNAi clones were sequenced. For this, colony PCRs were performed directly from the glycerol stocks using the primers *L4440F* and *L4440R*. To remove excessive primers and nucleotides, PCR products were treated with ExoSAP-IT™ (Applied Biosystems, Cat.no. 78200.200.UL) according to manufacturer's protocol. After PCR clean-up, samples were sent for sequencing using *L4440F* primer.

L4440 F 5'-TGGATAACCGTATTACCGCC-3'

L4440 R 5'-GTTTTCCCAGTCACGACGTT-3'

According to our sequencing results, seven of the RNAi clones covered two genes. These are indicated in column B ('Sequence') in Table S1. These RNAi clones were assigned to the GO group of the gene, which was predominantly covered by our sequencing result and all subsequent analysis were carried out using this gene.

Subsequently, the verified and sequenced clones were rescreened in technical duplicates in three independent experiments in the secondary screens in *drp-1(tm1108)*, *eat-3(ad426)* and *spg-7(ad2249)* mutant backgrounds.

Identification of human orthologs

Human orthologs and OMIM data (Amberger *et al.*, 2018) were extracted from wormbase.org using https://intermine.wormbase.org (Harris *et al.*, 2019). Human orthologs were then manually verified using 'alliancegenome.org' (The Alliance of Genome Resources, 2019), 'orthodb.org' (Kriventseva *et al.*, 2018), 'ensembl.org' (Hunt *et al.*, 2018) and 'uniprot.org' (Consortium, 2018).

Prediction of mitochondrial localization and mitochondrial targeting sequences

First, https://intermine.wormbase.org (Harris *et al.*, 2019) was used to identify all candidate genes, which are related to any mitochondrial processes/pathways. To that end, we extracted all 698 genes currently associated with at least one of the 404 GO-terms containing 'mitochond' and checked how many of our 385 candidate genes are among them. Additionally, we used the online platform 'MitoProt' (https://ihg.gsf.de/ihg/mitoprot.html) (Claros and Vincens, 1996) for computational prediction of mitochondrial targeting sequences. Proteins for which the prediction of a mitochondrial targeting sequence was ≥0.5 were considered to be mitochondrial.

Gene ontology enrichment analysis using DAVID

In search of enriched gene ontology terms, we used the DAVID tool (version 6.8 (Huang *et al.*, 2008, 2009)) and ran the list of candidates against all genes of the *C. elegans* genome as a background list. Using an EASE score from the modified fisher-exact test, the clustering algorithm groups genes based on their association in GO categories and assigns a significance value to the group (Huang *et al.*, 2007). The clustered groups were then plotted using modified functions from the GO plot package (R version 1.0.2 (Walter *et al.*, 2015)).

Transcription factor enrichment analysis

We searched for enriched transcription factors using the tool g:Profiler (a tool for functional enrichment analysis using over-representation (Raudvere *et al.*, 2019)). The two input lists (suppressors and enhancers of *fzo-1(tm1133)*-induced UPR^{mt}) with WBGene-IDs of the identified candidate genes were used to search in the Transfac database (annotations: TRANSFAC Release 2019.1 classes: v2 (Knüppel *et al.*, 1994; Matys *et al.*, 2006)).

Construction of gene networks of FZO-1 and MFN1/2, and the UPR^{mt}

The *C. elegans* interactomes were compiled for FZO-1 or all 16 genes that are currently associated with the GO-term 'mitochondrial unfolded protein response' (GO:0034514) from scientific literature (Durinck *et al.*, 2009; Simonis *et al.*, 2009) and databases such as mentha (Calderone *et al.*, 2013), BioGRID3.5 (Oughtred *et al.*, 2018), IntAct (Orchard *et al.*, 2014) and STRING (Szklarczyk *et al.*, 2018) (STRING was only used to build the FZOome). The human orthologs of those genes were identified and were searched as well. Whenever possible, the interaction partners were converted back to *C. elegans* genes using biomaRt (Durinck *et al.*, 2009) and available scientific literature (Shaye and Greenwald, 2011; Kim *et al.*, 2018). The complete list of interactions was uploaded to cytoscape (v.3.7.2 (Shannon *et al.*, 2003)) and a network was calculated, highlighting both enhancers and suppressors from the screening results.

Image acquisition, processing and analysis

For each mutant (Figure S1), 10-20 animals were immobilized with M9 buffer containing 150 mM sodium azide on 2% agarose pads and imaged using a Leica GFP dissecting microscope (M205 FA) and Leica Application Suite software (3.2.0.9652).

Mitochondrial morphology was assessed in a strain carrying *bcIs78* ($P_{myo\text{-}3}$::gfp^{mt}) using a Zeiss Axioskop 2 with a 63x objective and MetaMorph software (Molecular Devices).

Chapter I

RESULTS & DISCUSSION

Genome-wide RNAi screen for suppressors and enhancers of *fzo-1(tm1133)*-induced UPR^{mt} identifies highly conserved set of genes with relevance to human health

The disruption of mitochondrial dynamics in *C. elegans* induces the mitochondrial unfolded protein response (UPR^{mt}) (Kim and Sieburth, 2018; Zhang *et al.*, 2018; Rolland *et al.*, 2019; Haeussler *et al.*, 2020). To identify genes affecting mitochondrial homeostasis in animals with defects in mitochondrial dynamics, we used a loss-of-function mutation of *fzo-1*^{MFN1,2}*, tm1133*, (National BioResource Project) to induce the UPR^{mt} reporter P*hsp-6* mtHSP70*gfp (zcIs13)* and screened the *C. elegans* genome for modifiers. To that end, we used RNA-mediated interference (RNAi) and targeted ~87% of the currently annotated protein coding genes (Kamath and Ahringer, 2003) (Figure 1A). The moderate induction of the P*hsp-6* mtHSP70*gfp* reporter in the *fzo-1(tm1133)* background allowed the identification of both suppressors and enhancers of the response. Using a protocol in which the F1 generation is scored for P*hsp-6* mtHSP70*gfp* expression levels in the fourth larval stage of development (L4), we initially identified 657 candidate genes of which 385 reproduced. Of the 385 candidates identified, 299 act as suppressors and 86 as enhancers (Figure 1B and Table S1). In order to assess whether the 86 identified enhancers are specific to the *fzo-1(tm1133)* background or if their depletion induces UPR^{mt} also in the absence of mitochondrial stress, we knocked them down in a wild-type background and tested for induction of the P*hsp-6* mtHSP70*gfp* reporter. All except three genes (*copd-1*^{ARCN1}, *F25H9.6*^{PPCDC}, *F32A7.4*^{METTL17}) induce P*hsp-6* mtHSP70*gfp* expression when knocked-down in wild-type animals, suggesting that the induction of UPR^{mt} by depletion of these candidates is independent of the loss of *fzo-1*. (Candidates that encode mitochondrial proteins and that induce UPR^{mt} in a wild-type background upon knock-down were included in a recent publication, which reported the systematic identification of mitochondrial inducers of UPR^{mt} (Rolland *et al.*, 2019)).

Among the 299 suppressors, only 25 (8%) have previously been found to suppress UPR^{mt} induced by other means upon knock-down (Haynes *et al.*, 2007; Runkel *et al.*, 2013; Liu *et al.*, 2014). Similarly, among the 86 enhancers, only 15 (17%) have previously been shown to induce UPR^{mt} upon knock-down (indicated 'previously identified' in the 'overview' sheet of Table S1). This may be due to different genetic backgrounds and to differences in RNAi-protocols. Moreover, false negatives in RNAi screens have been estimated to vary between 10% and 30%, even if the same protocol is used by the same laboratory (Simmer *et al.*, 2003).

Using 'alliancegenome.org' (The Alliance of Genome Resources, 2019), 'orthodb.org' (Kriventseva *et al.*, 2018), 'ensembl.org' (Hunt *et al.*, 2018), 'uniprot.org' (Consortium, 2018)

and 'wormbase.org' (Harris *et al.*, 2019) databases, we found that approximately 90% of the suppressors and enhancers (348) have at least one ortholog in humans (indicated 'Human ortholog' in the 'overview' sheet of Table S1). For comparison, the overall conservation of genes from *C. elegans* to humans is only about 41% (Shaye and Greenwald, 2011; Kim *et al.*, 2018). Moreover, we found that the orthologs of 36% (126) of the conserved candidates have previously been associated with human disease and are listed in the 'Online Mendelian Inheritance in Man' database (Amberger *et al.*, 2018) (indicated 'OMIM' in the 'overview' and 'OMIM' sheet of Table S1). In summary, we identified a set of predominantly conserved genes, many of them relevant to human health, which when knocked-down affect mitochondrial homeostasis in mutants with defects in mitochondrial fusion.

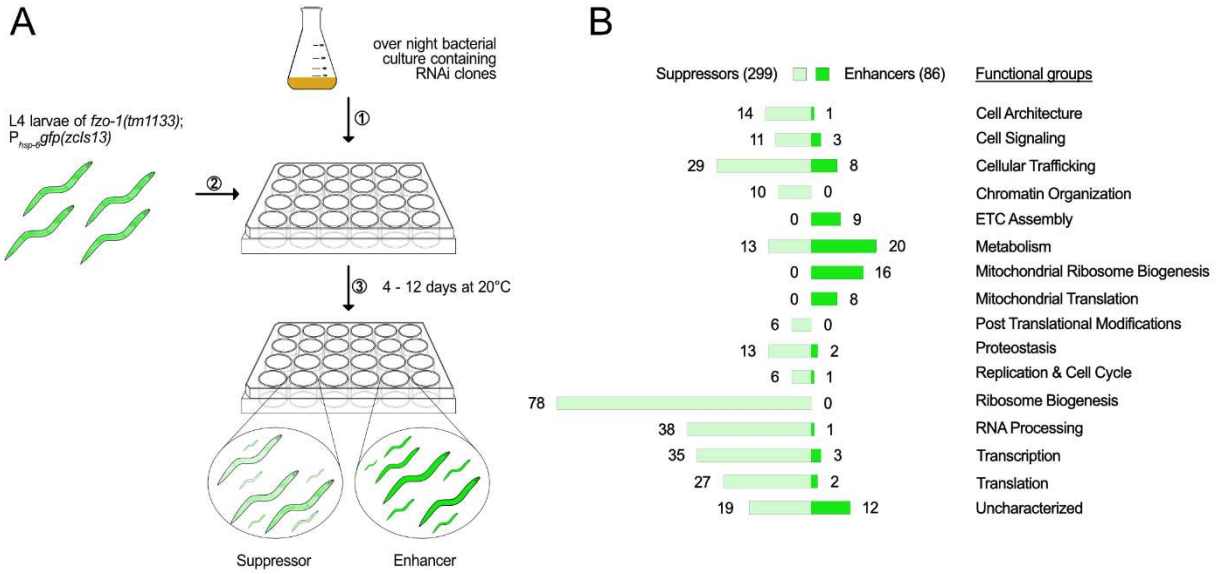

Figure 1: Overview of genome-wide RNAi screen for suppressors and enhancers of *fzo-1(tm1133)*-induced UPR^{mt}. (A) Schematic overview of the RNAi screening procedure using the RNAi feeding library (Kamath and Ahringer, 2003) in *fzo-1(tm1133)* mutants that express the UPR^{mt} reporter P*hsp-6* mtHSP70*gfp (zcIs13)* . The moderate induction of the reporter in the *fzo-1(tm1133)* background allowed screening for both suppressors and enhancers of the response. **(B)** The screen resulted in identification of 299 suppressors and 86 enhancers of *fzo-1(tm1133)*-induced UPR^{mt}, which were sorted into categories that we defined according to their function. ETC: electron transport chain.

Genes with functions in development, receptor-mediated endocytosis and metabolism modulate UPR^{mt} signaling

In order to obtain an overview of the type of processes that affect *fzo-1(tm1133)*-induced UPR^{mt}, we analyzed the gene ontology (GO) terms of all 385 candidates, sorted them into 'functional groups' (Figure 1B) and performed a clustered gene enrichment analysis using DAVID (Huang *et al.*, 2008, 2009) (Table S2 and Figure 2). (Thirty-one suppressors and enhancers could not be assigned to functional groups since these genes are uncharacterized in *C. elegans* and/or lack orthologs in humans. For this reason, they were assigned to the functional group 'uncharacterized' (Figure 1B)).

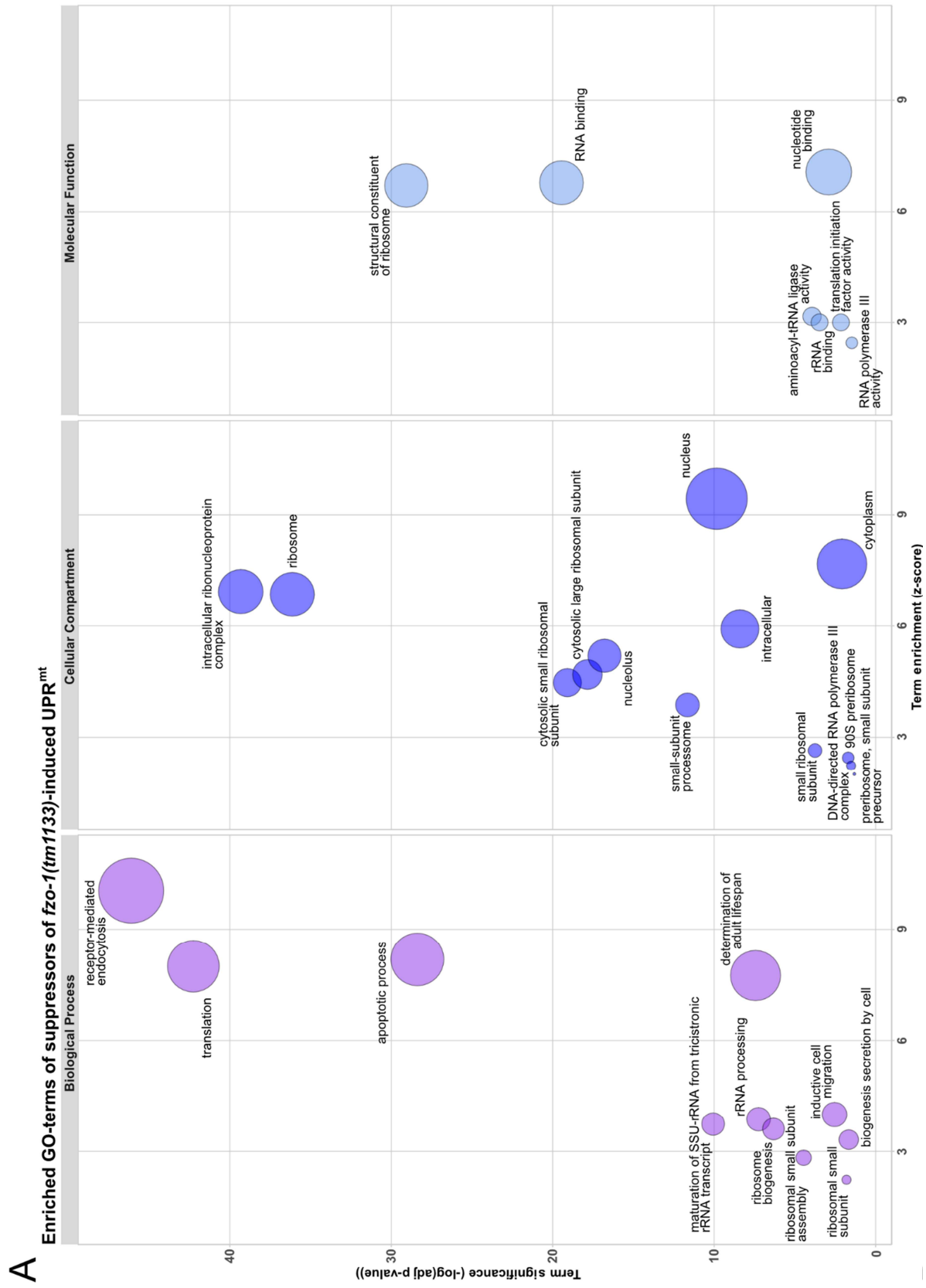
A
Enriched GO-terms of suppressors of fzo-1(tm1133)-induced UPRmt
Biological Process
Cellular Compartment
Molecular Function
receptor-mediated endocytosis
translation
apoptotic process
maturation of SSU-rRNA from tricistronic rRNA transcript
rRNA processing
ribosome biogenesis
ribosomal small subunit assembly
inductive cell migration
ribosomal small subunit
biogenesis
determination of adult lifespan
secretion by cell
intracellular ribonucleoprotein complex
ribosome
cytosolic small ribosomal subunit
cytosolic large ribosomal subunit
nucleolus
small-subunit processome
nucleus
intracellular
small ribosomal subunit
DNA-directed RNA polymerase III complex
90S preribosome
preribosome, small subunit precursor
cytoplasm
structural constituent of ribosome
RNA binding
aminoacyl-tRNA ligase activity
rRNA binding
translation initiation factor activity
RNA polymerase III activity
nucleotide binding
Term significance (-log(adj p-value))
Term enrichment (z-score)
0
10
20
30
40
3
6
9

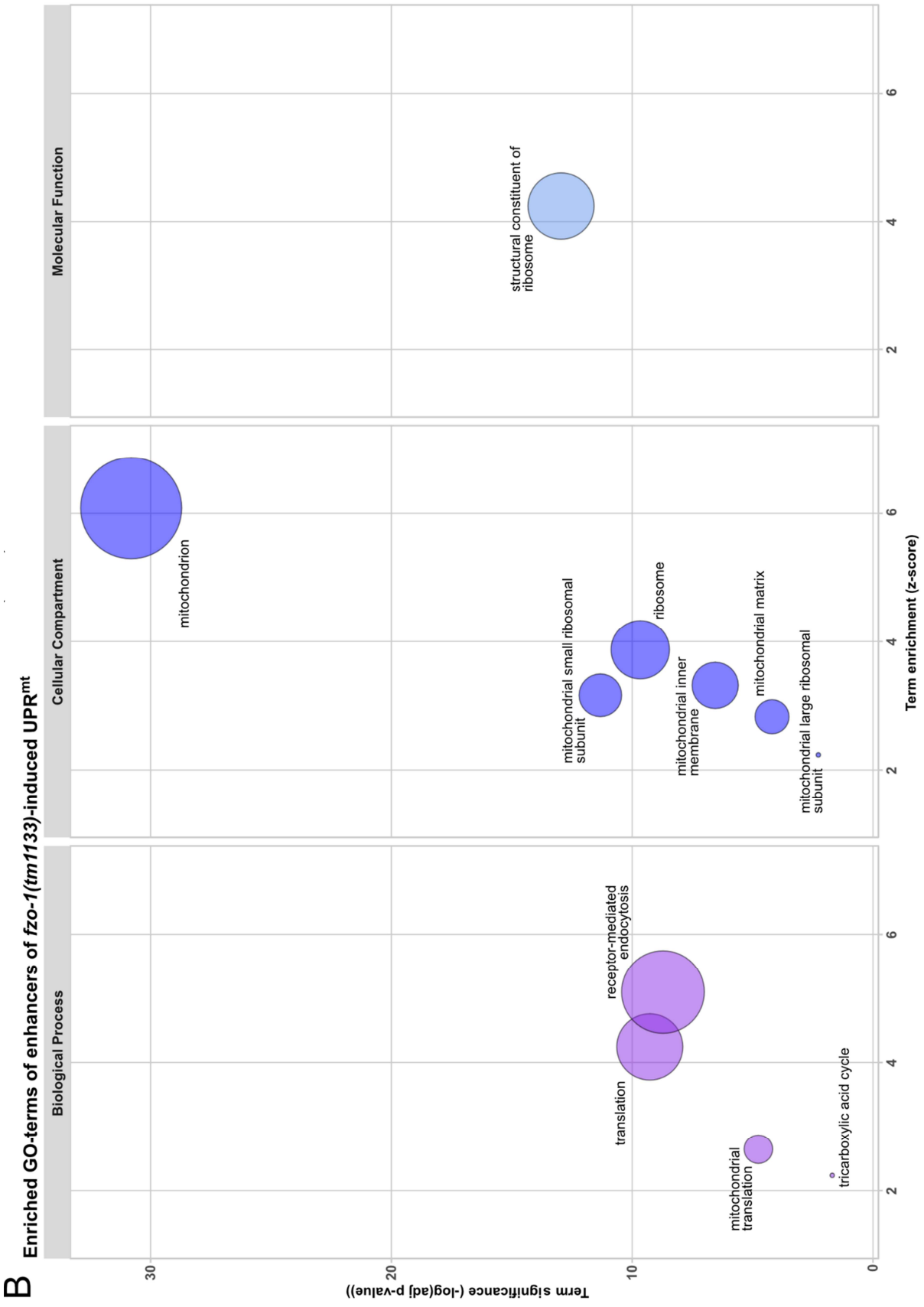
B
Enriched GO-terms of enhancers of fzo-1(tm1133)-induced UPRmt
Biological Process
Cellular Compartment
Molecular Function
Term significance (-log(adj p-value))
Term enrichment (z-score)
mitochondrion
mitochondrial small ribosomal subunit
ribosome
mitochondrial inner membrane
mitochondrial matrix
mitochondrial large ribosomal subunit
structural constituent of ribosome
receptor-mediated endocytosis
translation
mitochondrial translation
tricarboxylic acid cycle

Figure 2: Gene ontology enrichment analysis of suppressors and enhancers of *fzo-1(tm1133)*-induced UPR^{mt} using DAVID. (A) Results of the clustered gene ontology enrichment analysis of suppressors of *fzo-1(tm1133)*-induced UPR^{mt} using DAVID (Huang *et al.*, 2008, 2009). **(B)** Results of the clustered gene ontology enrichment analysis of enhancers of *fzo-1(tm1133)*-induced UPR^{mt} using DAVID. **(A) & (B)** Statistically significant (P >0.05) enriched GO-terms, except the nematode specific GO-terms, of *fzo-1(tm1133)*-induced UPR^{mt} are depicted. Circle size correlates with the number of genes associated with a specific GO-term.

In the clustered gene enrichment analysis, we found that the majority of both suppressors and enhancers are associated with at least one of the following GO-terms: 'nematode larval development', 'embryo development ending in birth or egg hatching' or 'reproduction' (Table S2). It has been shown that reducing the functions of some genes encoding components of the ETC (e.g. *cox-5B(RNAi)*) in specific tissues and at specific times during development can lead to both systemic activation of UPR^{mt} and longevity (Dillin *et al.*, 2002; Rea *et al.*, 2007; Durieux *et al.*, 2011). This indicates that the activity levels of mitochondria in an individual animal are 'set' at a specific developmental stage and, once set, are maintained throughout development and adult life. Our results demonstrate that disrupting development compromises this process, thereby affecting an animal's ability to cope with mitochondrial stress and to respond to UPR^{mt} activation, which is expected to indirectly affect processes such as its lifespan. In support of this notion, we found that approximately 20% of the suppressors carry the GO-term 'determination of adult lifespan'.

Among the suppressors, the GO-term 'receptor-mediated endocytosis' is enriched (Figure 2A and Table S2). It contains many genes with roles in vesicular trafficking and vesicle budding. Genes required for vesicular trafficking have been shown to affect mitochondrial morphology and homeostasis when inactivated, and it has been proposed that this is the result of altered contact sites between organelles and altered lipid transfer into mitochondria (Altmann and Westermann, 2005). Furthermore, we recently demonstrated that approximately half of the candidates in this GO-category are negative regulators of autophagy. Upon knock-down, these genes suppress *fzo-1(tm1133)*-induced UPR^{mt} most probably by inducing autophagy thereby causing changes in lipid metabolism (Haeussler *et al.*, 2020). Moreover, many cellular signaling pathways originate at the plasma membrane and, thus, are dependent on endocytosis (Sorkin and von Zastrow, 2009; Di Fiore and von Zastrow, 2014). Therefore, we speculate that depletion of the genes associated with the GO-term 'receptor mediated endocytosis' may either

cause changes in lipid metabolism thereby suppressing UPR^{mt} or disrupt cell non-autonomous UPR^{mt} signaling.

The functional group 'ribosome biogenesis' contains 78 (26%) of the suppressors (Figure 1B) and includes both small- and large ribosomal subunits, as well as proteins with roles in the maturation or transport of ribosomal subunits and rRNAs. Accordingly, in all three GO-domains (Biological Process, Cellular Compartment, Molecular Function), we found that several GO-terms related to the ribosome were significantly enriched (Figure 2A and Table S2). (The GO-term 'apoptotic process' also contains many ribosomal subunits leading to its enrichment in our analysis.)

Moreover, we assigned a substantial part of the suppressors to the groups 'RNA processing' (38), 'transcription' (35) and 'translation' (27) (Figure 1B). Hence, we found five GO-terms related to translation-, two to transcription- and one to RNA-related processes to be enriched in a statistically significant manner in the GO enrichment analysis (Figure 2A and Table S2). These results raise the question whether knock-down of the candidates involved in cytosolic translation specifically suppresses UPR^{mt} or simply reduces the expression of the P*hsp-6* mtHSP70*gfp* reporter. We recently showed that knock-down of the cytosolic tRNA synthetase *hars-1*^{HARS1}, which we found to suppress P*hsp-6* mtHSP70*gfp* expression in *fzo-1(tm1133)* and which presumably also compromises cytosolic translation, results in reduced expression of a control reporter, P*ges-1* GES2*gfp* (Haeussler *et al.*, 2020). Therefore, we cannot exclude the possibility that the knock-down of candidates related to the functional groups of transcription, RNA processing, ribosome biogenesis and translation may, at least to some extent, interfere with reporter expression *per se*.

Among the enhancers, we assigned most candidates to the functional groups 'metabolism' and 'mitochondrial ribosome biogenesis' as well as 'cellular trafficking', 'mitochondrial translation' and 'ETC assembly' (Figure 1B). Accordingly, GO analysis of the enhancers shows that the cellular compartments 'mitochondrion', 'mitochondrial small ribosomal subunit', 'mitochondrial large ribosomal subunit', 'mitochondrial inner membrane', 'mitochondrial matrix' and 'ribosome' are enriched (Figure 2B and Table S2). In addition, the biological processes 'translation' (which also includes 'mitochondrial translation'), 'tricarboxylic acid cycle' and 'receptor-mediated endocytosis' are enriched as is the molecular function 'structural constituent of ribosome' (Figure 2B and Table S2). Among the enhancers carrying the GO-term 'receptor-mediated endocytosis', we identified many subunits of the mitochondrial ribosome and genes required for mitochondrial translation, which are most likely misannotated and

therefore led to enrichment of this GO-term. In summary, we showed that disrupting mitochondrial translation and metabolism induces UPR^{mt} in *fzo-1(tm1133)*. Disruption of these processes has also previously been shown to induce UPR^{mt} in wild type (Durieux *et al.*, 2011; Houtkooper *et al.*, 2013). Therefore, we conclude that reducing mitochondrial function induces UPR^{mt} independently of the genetic background.

In summary, the GO enrichment analysis revealed that depletion of the majority of candidates in our dataset may modulate UPR^{mt} due to their role in development. Furthermore, we propose that the suppressors with roles in endocytosis modulate UPR^{mt} signaling indirectly and speculate that cellular signaling and/or alterations in organellar contact sites may influence mitochondrial metabolism and hence, UPR^{mt} signaling. Finally, we find disruption of mitochondrial metabolism and translation to robustly enhance UPR^{mt} signaling in *fzo-1(tm1133)*.

Mitochondrial fitness balances cellular homeostasis

Next, we determined which fraction of the identified enhancers and suppressors encode proteins that have a mitochondrial function or localize to mitochondria. We extracted all 698 genes that are associated with at least one of the 404 GO-terms containing ‘mitochond’ using the ‘WormMine’ database (https://intermine.wormbase.org) (Harris *et al.*, 2019), and then determined how many of our candidate genes are associated with any of these GO-terms. Using this approach, we identified 11 suppressors and 59 enhancers that encode proteins that localize to mitochondria or play a role in mitochondrial metabolism and dynamics, respectively (indicated ‘GO mitochond’ in ‘Overview’ and ‘Mitochondrial’ sheet of Table S1). Next, we used the online platform ‘MitoProt’ (https://ihg.gsf.de/ihg/mitoprot.html) (Claros and Vincens, 1996) for computational prediction of mitochondrial targeting sequences and identified an additional 5 suppressors and 14 enhancers that are predicted to localize to mitochondria (cut-off value ≥ 0.5) (indicated ‘MitoProt prediction’ in ‘Mitochondrial’ sheet of Table S1). Third, by literature searches, we found that the orthologs of 3 enhancers localize to mitochondria (Shafqat *et al.*, 2003; Spaan *et al.*, 2005; Cambier *et al.*, 2012). In summary, 76 out of 86 (88%) enhancers and 16 out of 299 (5%) suppressors encode proteins that have a mitochondrial function. This suggests that only few processes exist outside of mitochondria that can perturb mitochondrial homeostasis when disrupted. Conversely, many processes and mechanisms exist outside of mitochondria that can compensate for mitochondrial dysfunction, thereby ensuring mitochondrial and consequently cellular homeostasis.

Among the 10 'non-mitochondrial' enhancers of UPR^{mt} are three genes (*F29B9.8*, *Y61A9LA.11*, *C25H3.10*) with yet unknown function, which lack orthologs in other systems. ORC-1^{ORC1} is a component of the origin recognition complex and plays a role in DNA replication (Gavin *et al.*, 1995; Ohta *et al.*, 2003; Tatsumi *et al.*, 2003). The disruption of DNA replication or cell cycle progression has previously not been reported to lead to UPR^{mt} induction. We speculate that disruption of DNA replication leads to developmental defects and therefore induces UPR^{mt}. *F25H9.6*^{PPCDC} is the *C. elegans* ortholog of phosphopantothenoylcysteine decarboxylase, an enzyme required for biosynthesis of coenzyme A (CoA) (Daugherty *et al.*, 2002). Thus, knock-down of *F25H9.6*^{PPCDC} may interfere with critical biosynthetic and metabolic pathways (including the TCA cycle) and therefore enhance UPR^{mt}. NHR-209^{HNF4A,G} is orthologous to Hepatocyte Nuclear Factor 4α (HNF4A) and belongs to the family of nuclear hormone receptors, a class of cofactor and ligand-inducible transcription factors (TFs) that regulate various cellular processes, including metabolism, development and homeostasis (Aranda and Pascual, 2001; Bolotin *et al.*, 2010). Interestingly, long-chain fatty acids are ligands of HNF4A and, depending on their chain length and degree of saturation, activate or repress the transcriptional activity of HNF4A (Hertz *et al.*, 1998; Dhe-Paganon *et al.*, 2002; Wisely *et al.*, 2002; Duda *et al.*, 2004). Furthermore, HNF4α activity has been shown to be required for ß-oxidation of fatty acids both in mice and *Drosophila melanogaster* (Palanker *et al.*, 2009; Chen *et al.*, 2020). Thus, NHR-209^{HNF4A,G} may have a similar role in *C. elegans* and act as a metabolic sensor, which when deactivated, enhances UPR^{mt} in *fzo-1(tm1133)*. Moreover, we identified *cpna-3*^{CPNE5,8,9}, an ortholog of mammalian copine family members, a class of calcium dependent phospholipid binding proteins with roles in intracellular signaling and membrane trafficking (Creutz *et al.*, 1998; Tomsig *et al.*, 2003; Tomsig *et al.*, 2004; Ramsey *et al.*, 2008). Previously, another gene of the copine family, *gem-4*^{CPNE8}, has been shown to be upregulated upon UPR^{mt} activation (Nargund *et al.*, 2012). Therefore, we speculate that signaling via copine family members may be important for UPR^{mt} regulation. Another non-mitochondrial enhancer, *copd-1*^{ARCN1}, encodes a protein orthologous to the delta subunit of coatomer in *S. cerevisiae* and humans (RET2 and ARCN1, respectively), which is involved in the formation of coat protein complex I (COPI) vesicles. COPI vesicles play a central role in the secretory pathway and are required for the retrieval of lipids and proteins from the Golgi apparatus and the subsequent retrograde transport of these lipids and proteins to the ER (Lee *et al.*, 2004; Beck *et al.*, 2009). Furthermore, the trafficking to their final destination of most non-mitochondrial and non-peroxisomal transmembrane proteins, as well as proteins required for the release of neurotransmitters, such as SNARE proteins, is dependent on COPI-mediated transport (Beck *et*

al., 2009). Thus, disruption of the secretory pathway affects many intra- and intercellular signaling pathways, including the Ras and TOR signaling pathways, as well as signaling via G-protein-coupled receptors (GPCRs) and receptor tyrosine kinases (Farhan and Rabouille, 2011). Moreover, disruption of the retrograde transport system has been shown to lead to erroneous secretion of ER resident proteins (e.g. ER chaperones) and, consequently, to the activation of UPR in the ER (UPR^{ER}) (Aguilera-Romero *et al.*, 2008; Izumi *et al.*, 2016). Therefore, we speculate that the enhancement of UPR^{mt} induction in *fzo-1(tm1133)* animals upon *copd-1(RNAi)* may be due to alterations in one of the above-mentioned signaling pathways. This notion is supported by the finding that phospholipase C ($PLC\text{-}1^{PLCE1}$), a GPCR associated enzyme, is among the non-mitochondrial enhancers, as well as *srh-40* (serpentine receptor class H), which is predicted to encode a GPCR. Taken together, we identified many genes among the 'non-mitochondrial' enhancers, which regulate intra- and intercellular signaling cascades, and we speculate that these may play a role in signaling of UPR^{mt}, both in a cell autonomous and cell non-autonomous fashion. In addition, we identified 'non-mitochondrial' enhancers that directly regulate metabolic homeostasis and, thus, enhance UPR^{mt} in *fzo-1(tm1133)* mutants.

Among the 16 identified 'mitochondrial suppressors' of UPR^{mt} are candidates, such as $TFG\text{-}1^{TFG}$ and $GBF\text{-}1^{GBF1}$, that encode proteins that have been shown to associate with mitochondria but also other organelles. $GBF\text{-}1^{GBF1}$ is a guanine nucleotide exchange factor (GEF) for the small GTPase $ARF\text{-}1.2^{ARF1}$, which in yeast recruits $ARF\text{-}1.2^{ARF1,3}$ to ER-mitochondria contact sites (Ackema *et al.*, 2014). Depletion of $GBF\text{-}1^{GBF1}$ leads to altered $ARF\text{-}1.2^{ARF1,3}$ localization and changes in mitochondrial morphology both in yeast and *C. elegans* and this appears to be independent of their roles in endosomal transport (Ackema *et al.*, 2014). Ackema and colleagues observed an increase in mitochondrial connectivity upon $GBF\text{-}1^{GBF1}$ depletion, similar to that observed upon knock-down of $miro\text{-}1^{MIRO1}$ and $vdac\text{-}1^{VDAC}$, both of which encode proteins that also localize to ER-mitochondria contact sites. However, the alterations in mitochondrial morphology of $FZO\text{-}1^{MFN1,2}$ depleted animals were shown to be epistatic to the changes in mitochondrial morphology observed upon *gbf-1(RNAi)* and *arf-1.2(RNAi)*. Therefore, the suppression of UPR^{mt} observed in *fzo-1(tm1133)* animals upon *gbf-1(RNAi)* may not be due to a rescue of the mitochondrial morphology defect but rather be the consequence of changes in ER-mitochondria contact sites. This highlights the importance of organellar contact sites for the maintenance of mitochondrial and consequently cellular homeostasis. Furthermore, we identified $TFG\text{-}1^{TFG}$, a component of the secretory pathway via COPII vesicles (Witte *et al.*, 2011), as a suppressor of *fzo-1(tm1133)*-induced UPR^{mt}. COPII vesicles transport newly synthesized proteins and lipids from specialized ER zones, so called ER exit sites (ERES), to

the Golgi apparatus (Budnik and Stephens, 2009; Kurokawa and Nakano, 2018). Similar to what we propose for *copd-1(RNAi)* (see above), we speculate that disruption of the secretory pathway may lead to alterations in cellular signaling, ER-mitochondria contact sites and, depending on the context, either to suppression or enhancement of UPR^{mt}. Taken together, we demonstrate that the perturbation of primarily mitochondrial processes leads to the enhancement of UPR^{mt}. However, the identification of non-mitochondrial enhancers demonstrates that disruption of processes taking place outside of mitochondria can also compromise mitochondrial function and activate or enhance UPR^{mt}. Alterations in cellular signaling pathways and/or organellar contact sites may play a role in this respect. Moreover, we find that the majority of suppressors of *fzo-1(tm1133)*-induced UPR^{mt} are non-mitochondrial, suggesting that many cellular pathways outside of mitochondria exist that can compensate for mitochondrial stress and, hence, ensure mitochondrial homeostasis. In line with this notion, we identified a few 'mitochondrial suppressors', most of which are involved in the maintenance of contacts to other organelles, especially the ER.

Defects in mitochondrial fusion and fission are suppressed and enhanced by the same pathways

In order to define the specificity of the 299 suppressors and 86 enhancers, we carried out secondary screens. To identify general modifiers of UPR^{mt}, we rescreened the candidates in the background of *spg-7(ad2249),* which induces UPR^{mt} (Figure S1). *spg-7*^{AFG3L2} encodes a mitochondrial matrix AAA-protease, which induces UPR^{mt} when depleted and which is commonly used as a positive control for UPR^{mt} activation (Yoneda *et al.*, 2004; Haynes *et al.*, 2007; Haynes *et al.*, 2010). To identify genes in our dataset that specifically modify UPR^{mt} induced by defects in mitochondrial membrane fusion, we rescreened all candidates in the *eat-3(ad426)* background, in which IMM fusion is blocked. Finally, to identify genes that may modulate UPR^{mt} induced by defects in mitochondrial dynamics, we rescreened all candidates in the *drp-1(tm1108)* background, in which mitochondrial fission is blocked. In the *drp-1(tm1108)* background, of the 385 candidates, 291 suppress and 59 enhance. In the *eat-3(ad426)* background, 242 suppress and, 49 enhance. Finally, in the *spg-7(ad2249)* background, 181 suppress and 54 enhance (Table S1). (Of note, there is an inverse correlation between the level of P$_{hsp-6}$ $_{mtHSP70}$*gfp* expression in the above-mentioned mutant background and the number of candidates that reproduce. Hence, the level of reporter expression may correlate with the number of false negatives in a given dataset of the secondary screens, for both suppressors and

enhancers.) Since more suppressors reproduced in *drp-1(tm1108)* and *eat-3(ad426)* compared to *spg-7(ad2249)*, we conclude that defects in mitochondrial dynamics, to some extent, are suppressed or enhanced by the same pathways. Moreover, the suppressors of *fzo-1(tm1133)*-induced UPR^{mt} that were sorted into the functional groups 'ribosome biogenesis', 'RNA processing' and 'translation', reproduced comparably well in all secondary screens. Thus, attenuation of cytosolic translation may either be a general mechanism to suppress UPR^{mt} or, as discussed above, interfere with reporter expression. Among the enhancers, genes that sorted into the functional groups 'ETC assembly factors', 'mitochondrial ribosome biogenesis' and 'mitochondrial translation' showed the highest overlap among the secondary screens (Table S1), which demonstrates that disruption of mitochondrial translation robustly enhances UPR^{mt}, independent of genetic background.

Twelve candidates that suppressed UPR^{mt} in the primary screen using *fzo-1(tm1133)*, enhanced UPR^{mt} in one or more of the secondary screens. Conversely, ten enhancers of *fzo-1(tm1133)*-induced UPR^{mt} suppress UPR^{mt} in at least one of the mutants in the secondary screens (listed in 'opposing UPR^{mt} phenotypes' sheet in Table S1). For example, knock-down of *icd-1*$^{\beta NAC}$ suppresses P$_{hsp\text{-}6\ mtHSP70}$*gfp* in all mitochondrial dynamics-related backgrounds, but enhances *spg-7(ad22449)*-induced UPR^{mt}. Knock-down of *icd-1*$^{\beta NAC}$ in *C. elegans* has been reported to induce UPR^{ER} in wild-type embryos (Arsenovic *et al.*, 2012). Furthermore, *icd-1*$^{\beta NAC}$ has been described as a cytosolic stress sensor, which in the absence of stress associates with ribosomes to promote cytosolic translation, and which acts as a chaperone in the cytosol upon heat stress (Kirstein-Miles *et al.*, 2013). We recently showed that *icd-1*$^{\beta NAC}$ is a negative regulator of autophagy and that increased autophagic flux fuels mitochondria with certain triacylglycerols, thereby suppressing UPR^{mt} in *fzo-1(tm1133)* and *drp-1(tm1108)* mutants (Haeussler *et al.*, 2020). Thus, blocking mitochondrial dynamics may reduce the flux of lipids into mitochondria, which can be compensated for by the induction of autophagy and we speculate that this mechanism may also apply to *eat-3(ad426)* mutants. Conversely, we speculate that defects in mitochondrial homeostasis induced by a point mutation in *spg-7*, may exert stress to the cytosol and that this is normally compensated for by factors, such as *icd-1*$^{\beta NAC}$. Knocking-down *icd-1*$^{\beta NAC}$ may therefore increase cytosolic stress, which in turn enhances UPR^{mt} in *spg-7(ad2249)* mutants. Taking the candidates into account that have opposing UPR^{mt} phenotypes in the secondary screens, 95% of the suppressors and 66% of the enhancers reproduce in *drp-1(tm1108)*, while 79% of the suppressors and 57% of the enhancers reproduce in *eat-3(ad426)*. We found the lowest overlap of candidate genes in *spg-7(ad2249)* mutants, with 59% of the suppressors and 60% of the enhancers reproducing in this background. Taken together, the

results of the secondary screens show that there are candidates that, when depleted, act to influence UPR^{mt} signaling in general whereas others are specific to a certain type of UPR^{mt} induction, such as the disruption of mitochondrial dynamics.

Transcription factor enrichment analysis identifies factors with roles in development, metabolism and oxidative stress response

Next, we identified TF binding sites in the promoters of our candidates using ChIP-seq datasets from the modENCODE project (Celniker *et al.*, 2009) in order to test for enrichment of TFs that bind to these sites. To that end, we used g:Profiler, a tool for functional enrichment analysis using over-representation (Raudvere *et al.*, 2019), which utilizes TRANSFAC resources (Knüppel *et al.*, 1994; Matys *et al.*, 2006). Using this approach, we found 15 TFs to be enriched in a statistically significant manner. Ten of these TFs only bind promotor regions of suppressors (7) or enhancers (3) ('suppressor- or enhancer specific'). The remaining five TFs bind to promotor regions of both suppressors and enhancers ('shared') (Figure 3 and Table S3). The 'shared' TFs have previously been implicated in cell fate determination or developmental timing (Figure 3 and Table S3). Five out of seven 'suppressor specific' TFs have been shown to exclusively control developmental processes. The remaining two 'suppressor-specific' TFs are ELT-3^{GATA3,4} and HLH-11^{TFAP4}, which have been shown to play a role in development, ageing and the response to oxidative stress (Gilleard *et al.*, 1999; Budovskaya *et al.*, 2008; Hu *et al.*, 2017) and to act as a dietary sensor that regulates metabolic gene expression, respectively (Soo-Ung *et al.*, 2009; Watson *et al.*, 2013).

A

	Gene name	Human Ortholog	Sequence Logo	*P*-value	Reference
Suppressor specific	*hlh-2::cnd-1*	*NEUROD1,4,6*		3.36E-13	[1],[2]
	blmp-1	*PRDM1*		4.52E-05	[3],[4],[5]
	efl-1	*E2F4, E2F5*		4.54E-05	[6],[7],[8],[9]
	pal-1	*CDX1*		0.000402	[10],[11],[12]
	hlh-2::hlh-19	*TCF12::ASCL4*		0.001199	[1],[13]
	elt-3	*GATA3,4*		0.020084	[14],[15],[16]
	hlh-11	*TFAP4*		0.032103	[1],[17],[18]
Enhancer specific	*skn-1*	*NF2, NFE2L1,2,3*		0.049665	[19],[20],[21],[22],[23],[24],[25]
	hlh-29	*n.a.*		0.049665	[1],[26],[27],[28]
	vab-7	*EVX2*		0.049665	[29],[30],[31]
Shared	*ceh-48*	*ONECUT1,2,3*	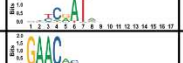	Table S3	[32],[33],[34]
	lin-14	*n.a.*	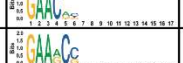	Table S3	[35]
	che-1	*ZNF500, ZSCAN4*		Table S3	[36],[37],[38],[39]
	grh-1	*GRHL1*	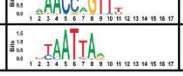	Table S3	[40],[41],[42]
	lim-4	*LHX6,8*		Table S3	[43],[44]

B

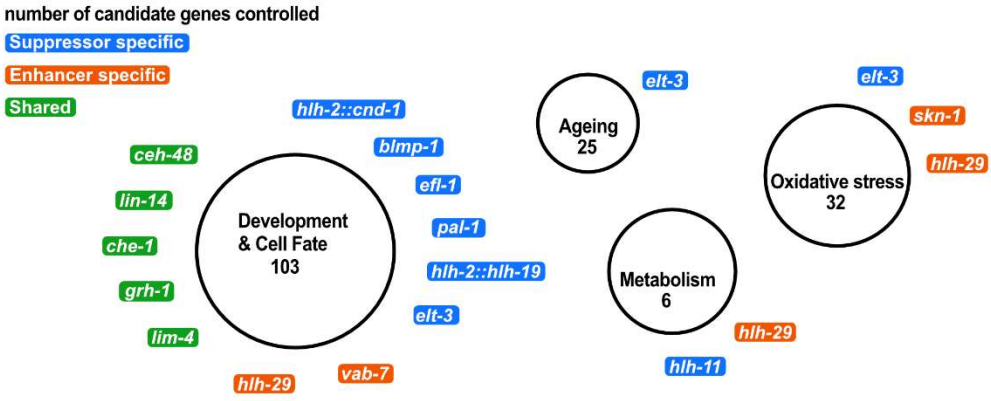

Figure 3: Enrichment analysis of transcription factors binding to promotors of candidate genes that suppress or enhance *fzo-1(tm1133)*-induced UPR^{mt}. (A) Transcription factor (TF) binding sites were identified using the modENCODE database (Celniker *et al.*, 2009) and enrichment analysis was performed separately for suppressors and enhancers of *fzo-1(tm1133)*-induced UPR^{mt} using g:profiler (Knüppel *et al.*, 1994; Raudvere *et al.*, 2019). TFs that are statistically enriched among the candidate genes are shown. References: [1] (Grove *et al.*, 2009), [2] (Hallam *et al.*, 2000), [3] (Horn *et al.*, 2014), [4] (Huang *et al.*, 2014), [5] (Armakola and Ruvkun, 2019), [6] (Ceol and Horvitz, 2001), [7] (Garbe *et al.*, 2004), [8] (Chi and Reinke, 2006), [9] (Miller *et al.*, 2016), [10] (Baugh *et al.*, 2005), [11] (Maduro *et al.*, 2005), [12] (Lei *et al.*, 2009), [13] (Schwarz *et al.*, 2012), [14] (Gilleard *et al.*, 1999), [15] (Budovskaya *et al.*, 2008), [16] (Hu *et al.*, 2017), [17] (Soo-Ung *et al.*, 2009), [18] (Watson *et al.*, 2013), [19] (An and Blackwell, 2003), [20] (An *et al.*, 2005), [21] (Inoue *et al.*, 2005), [22] (Nargund *et al.*,

2012), [23] (Nargund *et al.*, 2015), [24] (Kim and Sieburth, 2018), [25] (Wu *et al.*, 2018) [26] (Neves and Priess, 2005), [27] (McMiller *et al.*, 2007), [28] (Quach *et al.*, 2013), [29] (Ahringer, 1996), [30] (Esmaeili *et al.*, 2002), [31] (Pocock *et al.*, 2004), [32] (Jacquemin *et al.*, 2003), [33] (Furuno *et al.*, 2008), [34] (Klimova *et al.*, 2015), [35] (Ambros and Horvitz, 1984), [36] (Chang *et al.*, 2003), [37] (Uchida *et al.*, 2003), [38] (Etchberger *et al.*, 2007), [39] (Rahe and Hobert, 2019), [40] (Huang *et al.*, 1995), [41] (Wilanowski *et al.*, 2002), [42] (Venkatesan *et al.*, 2003), [43] (Pradel *et al.*, 2007), [44] (Kim *et al.*, 2015). **(B)** Graphical representation of enriched TFs and the cellular processes they control. 'Suppressor specific' TFs are indicated in blue, 'enhancer specific' TFs in orange and 'shared' TFs in green. The number of candidate genes controlled by a certain group of TFs is indicated in each circle below the functional group name.

Three TFs (SKN-1^{NFE2,NFE2L1,2,3}, HLH-29 and VAB-7^{EVX2}) were identified to be 'enhancer-specific' (Figure 3 and Table S3). VAB-7^{EVX2} and HLH-29 are both required for certain aspects of development (Ahringer, 1996; Esmaeili *et al.*, 2002; Pocock *et al.*, 2004; Neves and Priess, 2005; McMiller *et al.*, 2007; Grove *et al.*, 2009) and HLH-29 has additional roles in fatty acid metabolism and energy homeostasis (McMiller *et al.*, 2007; Quach *et al.*, 2013). Furthermore, HLH-29 and SKN-1^{NFE2,NFE2L1,2,3} are regulators of the oxidative stress response (An and Blackwell, 2003; An *et al.*, 2005; Inoue *et al.*, 2005; Quach *et al.*, 2013) and SKN-1^{NFE2,NFE2L1,2,3} has previously been implicated in the UPR^{mt} pathway in *C. elegans* (Nargund *et al.*, 2012; Nargund *et al.*, 2015; Wu *et al.*, 2018). In summary, we identified several TFs that bind to promotors of our candidate genes, which have previously been implicated in oxidative stress response, cellular metabolism and development in *C. elegans*. Interestingly, *fzo-1(tm1133)* mutants have previously been shown to be slightly sensitive to oxidative stress and have increased levels of carbonylated proteins, a measure for oxidative damage (Yasuda *et al.*, 2011). Moreover, in *isp-1(qm150)* and *clk-1(qm30)* mutants, both of which have increased levels of reactive oxygen species (ROS) (Van Raamsdonk *et al.*, 2010; Yang and Hekimi, 2010; Dues *et al.*, 2017), UPR^{mt} activation has been shown to lead to ATFS-1^{ATF4,5}-dependent expression of genes required for detoxification of reactive oxygen species (Wu *et al.*, 2018). This induction is orchestrated by ATFS-1^{ATF4,5} but may, to some extent, additionally be facilitated through activation of ELT-3^{GATA3,4} and HLH-29, as it has previously been shown for SKN-1^{NFE2,NFE2L1,2,3} (Nargund *et al.*, 2012; Nargund *et al.*, 2015; Wu *et al.*, 2018). The identification of many TFs controlling developmental processes is in agreement with our finding that GO-terms related to developmental processes are enriched among our dataset. This again highlights that the activity levels of critical cellular processes and responses in somatic tissues appear to

be set during development. Finally, we previously found that the induction of autophagy suppresses UPR^{mt} in *fzo-1(tm1133)* mutants most likely through increased metabolic activity (Haeussler *et al.*, 2020). In our analysis, we identified two TFs, which regulate energy homeostasis and metabolic gene expression. This supports the notion that UPR^{mt} in *fzo-1(tm1133)* mutants acts to compensate for metabolic defects. In summary, we identified several TFs with roles in development, oxidative stress response and metabolism that previously have not been connected to UPR^{mt} signaling. These TFs may be specific to UPR^{mt} in *fzo-1(tm1133)* but some may generally be involved in UPR^{mt} signaling.

Interactome of UPR^{mt} reveals potential new regulators

In order to determine whether any of the suppressors or enhancers that we identified have previously been shown to interact with *fzo-1*^{MFN1,2} or its mammalian orthologs *MFN1* or *MFN2*, we built a gene network containing all known interactions of *fzo-1*^{MFN1,2} and its mammalian orthologs *MFN1* and *MFN2*. Using the interaction databases 'string-db.org', 'IntAct', 'BioGRID3.5', 'Genemania', 'CCSB' and 'mentha' (Warde-Farley *et al.*, 2010; Calderone *et al.*, 2013; Orchard *et al.*, 2014; Rolland *et al.*, 2014; Oughtred *et al.*, 2018; Szklarczyk *et al.*, 2018), we included genetic and physical interactions (but not predicted interactions or co-expression data) and uploaded them to the cytoscape software (Shannon *et al.*, 2003) to calculate a complete interaction network. The resulting network contains 38 genes and 67 interactions (Figure S2). None of the 10 interactors of *fzo-1*^{MFN1,2} in *C. elegans* was identified in our screen (turquois dots in Figure S2). Next, we manually annotated the *C. elegans* orthologs of 24 interactors of *Mfn1* or *Mfn2* in mammals (except FAF2, MAVS, TCHP, SLC25A38 for which we did not find any orthologs in *C. elegans*, indicated in dark blue in Figure S2) but again did not find any overlap between the gene network and our screen dataset (orange dots in Figure S2). In summary, in our screen for modifiers of *fzo-1(tm1133)*-induced UPR^{mt}, we did not find any previously known interactors of *fzo-1*^{MFN1,2}. These could either have been missed in the RNAi screen, be essential in the *fzo-1(tm1133)* background or not have a function in mitochondrial homeostasis and, hence, UPR^{mt} signaling.

Similar to the approach described above, we used the 16 *C. elegans* genes currently associated with the GO-term 'mitochondrial unfolded protein response' (GO:0034514) (referred to as 'input genes'), identified their human orthologs and included known physical and genetic interactors from the interaction databases 'BioGRID3.5', 'IntAct' and 'mentha' (Calderone *et al.*, 2013; Orchard *et al.*, 2014; Oughtred *et al.*, 2018) to calculate an interaction network

containing 2603 genes and 4655 interactions (Figures S3, Figure S4, Figure S5). In this 'UPR^{mt}ome', we identified 129 genes (including the 16 'input genes'), 36 of which are enhancers and 77 of which are suppressors of *fzo-1(tm1133)*-induced UPR^{mt}, with a total of 213 interactions (Figure 4 and Table S4).

For the 'input gene' *atfs-1*^{ATF4,5} , we found five interactors (*gtf-2F2*^{GTF2F2}, *lin-54*^{LIN54}, *rps-6*^{RPS6}, *spr-2*^{SET}, *tbp-1*^{TBP}) that suppress *fzo-1(tm1133)*-induced UPR^{mt} and the gene products of four of these localize to the nucleus (Sopta *et al.*, 1989; Lichtsteiner and Tjian, 1993; Wen *et al.*, 2000; Thomas *et al.*, 2003; Harrison *et al.*, 2006; Tabuchi *et al.*, 2011). These could potentially facilitate or directly be involved in the transcription of UPR^{mt} effectors upon activation of the UPR^{mt} response. Moreover, for the 'input gene' *ubl-5*^{UBL5}, we found four interactors that overlap with our dataset of suppressors, three of which are splicing factors (*pqbp-1.2*^{PQBP1}*, sfa-1*^{SF1}*, snr-3*^{SNRPD1}) (Thomas *et al.*, 1988; Krämer, 1992; Arning *et al.*, 1996; Imafuku *et al.*, 1998; Kambach *et al.*, 1999; Mazroui *et al.*, 1999; Waragai *et al.*, 1999). Of note, HUB1, the ortholog of UBL-5^{UBL5} in *Saccharomyces pombe*, has been shown to interact with components of the spliceosome. Furthermore, the loss of *HUB1* results in reduced splicing efficiency of a variety of mRNAs (Wilkinson *et al.*, 2004). Thus, the identification of the splicing factor genes *pqbp-1.2*^{PQBP1}*, sfa-1*^{SF1}*, snr-3*^{SNRPD1} in our dataset presents an interesting potential link between UPR^{mt} activation and pre-mRNA splicing via UBL-5^{UBL5}. In addition, we identified *taf-4*^{TAF4}, which encodes an associated factor of transcription factor TFIID, to interact with the 'input gene' *sphk-1*^{SPHK1,2} and to suppress *fzo-1(tm1133)*-induced UPR^{mt} upon knock-down. *taf-4*^{TAF4} has previously been shown to be required for life span extension in *isp-1(qm150)*, *clk-1(qm30)* and *tpk-1(qm162)* mutants, (Walker *et al.*, 2001; Walker *et al.*, 2004; Khan *et al.*, 2013). Finally, we identified many genes interacting with the 'input gene' *bar-1*^{JUP,CTNNB1}, which has previously been shown to be involved in cell non-autonomous propagation of UPR^{mt} signaling (Zhang *et al.*, 2018). Among these interactors is phospholipase C (*plc-1*^{PLCE}), which enhances *fzo-1(tm1133)*-induced UPR^{mt} and plays a central role in the inositol triphosphate (IP_3) signaling pathway (Clandinin *et al.*, 1998; Kariya *et al.*, 2004). In summary, we identified several genes in our dataset using gene network analysis that have previously not been identified to play a role in UPR^{mt} signaling in *C. elegans*. The genes with roles in pre-mRNA splicing and IP_3 signaling may be particularly interesting in this respect. Furthermore, we propose that these genes may directly influence UPR^{mt} signaling through interactions with known players of the UPR^{mt} pathway.

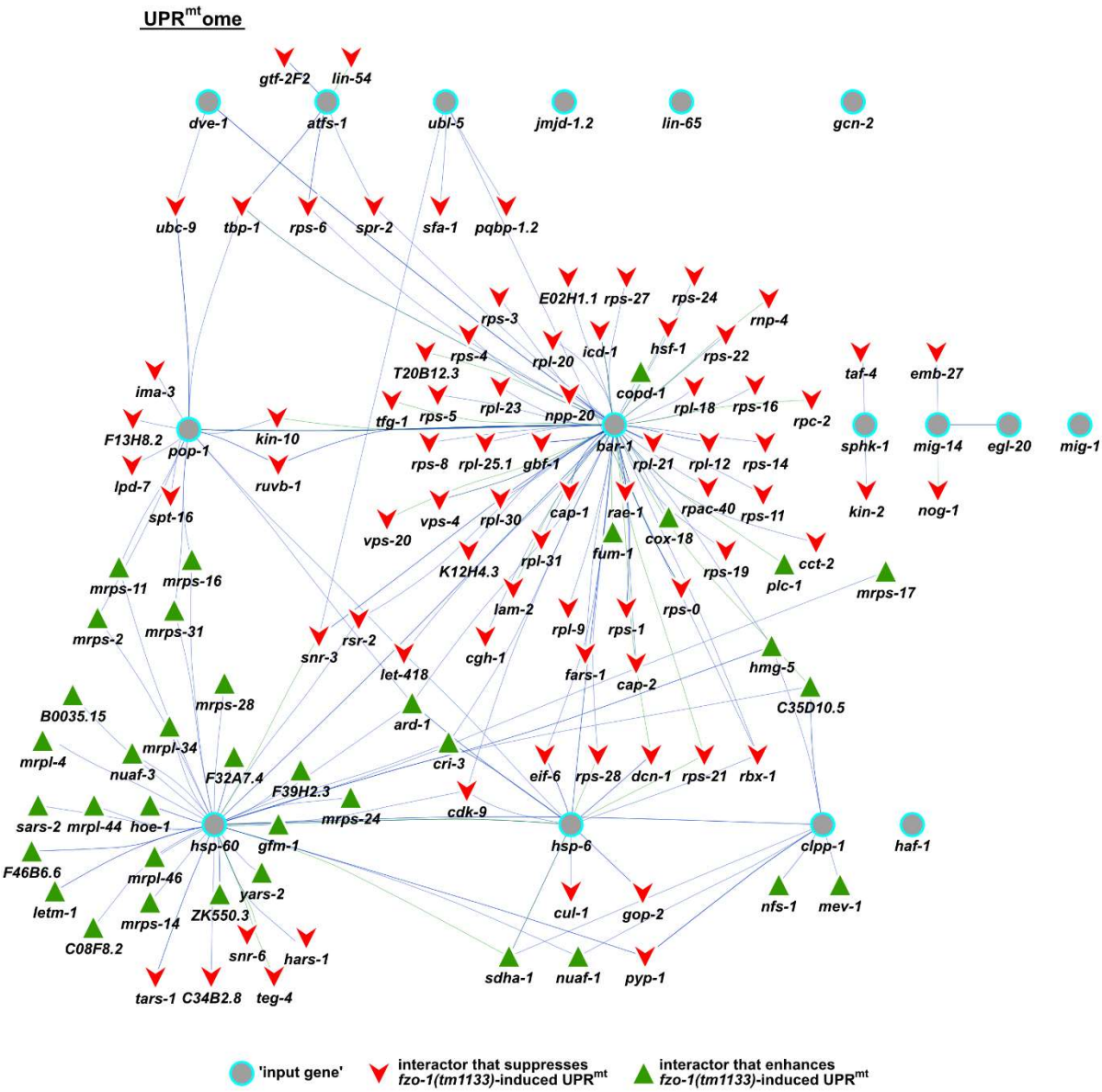

Figure 4: Analysis of a gene network – the UPR^{mt}ome. Interactors of all genes that are currently associated with the GO-term 'mitochondrial unfolded protein response' and of their human orthologs were identified to build the complete UPR^{mt}ome using 'IntAct', 'BioGRID3.5' and 'mentha' databases (Calderone *et al.*, 2013; Orchard *et al.*, 2014; Oughtred *et al.*, 2018). 129 genes are depicted, which overlapped between the complete UPR^{mt}ome and the candidate list of our screen in *fzo-1(tm1133)* mutants. Turquois circles: 'input genes' currently associated with GO-term 'mitochondrial unfolded protein response', red arrowheads: suppressors of *fzo-1(tm1133)*-induced UPR^{mt} that overlap with the complete UPR^{mt}ome, green triangles: enhancers of *fzo-1(tm1133)*-induced UPR^{mt} that overlap with the complete UPR^{mt}ome. Interactions of two genes that were identified for *C. elegans* genes are indicated with green lines, interactions that were identified in human orthologs are indicated with blue lines.

Interactome analysis reveals involvement of IP_3 signaling pathway in UPR^{mt} regulation in *fzo-1(tm1133)*

In our gene network analysis, we identified *plc-1*^{PLCE}, which encodes phospholipase C, as an interactor of *bar-1*$^{\beta\text{-catenin}}$ (Byrne *et al.*, 2007). Interestingly, we and others found several genes that play a role in inositol triphosphate (IP_3) signaling (Figure 5) (Liu *et al.*, 2014). The IP_3 pathway is well known for its role in the regulation of intracellular calcium levels and transmits signals from the extracellular space via GPCRs and second messengers to the ER (Berridge, 2009). Thus, this signaling pathway may have a role in cell non-autonomous propagation of UPR^{mt}.

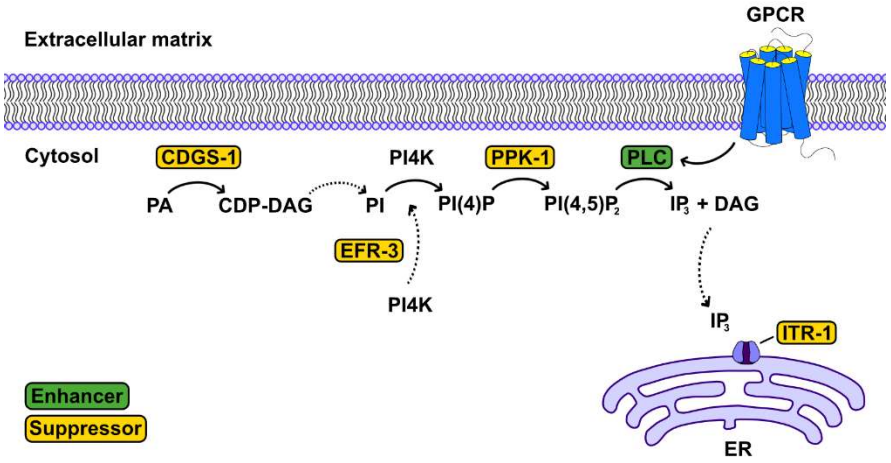

Figure 5: Candidate genes with roles in IP_3 signaling. We identified four genes in our dataset that either play a direct role in the IP_3 signaling pathway or are crucial for the synthesis of phosphatidylinositol-4,5-biphosphate ($PI(4,5)P_2$). The IP_3 receptor has previously been identified (Liu *et al.*, 2014). Suppressors are shown in yellow boxes, enhancers in green boxes. PA phosphatidic acid, CDP-DAG cytidine biphosphate-diacylglycerol, PI phosphatidylinositol, PI(4)P phosphatidylinositol-4-phosphate, IP_3 inositol triphosphate, ER endoplasmic reticulum, GPCR G-protein coupled receptor.

We identified the enzyme CDGS-1^{CDS1}, which is essential for the production of phosphatidylinositol (PI) (Wu *et al.*, 1995; Vance, 1998), and EFR-3^{EFR3B}, which targets PI-4-kinase (PI4K) to the plasma membrane (Nakatsu *et al.*, 2012). Furthermore, we identified the sole type I PIP kinase in *C. elegans,* PPK-1^{PIP5K1A} (Weinkove *et al.*, 2008), which phosphorylates PI4P to form $PI(4,5)P_2$ (Ishihara *et al.*, 1996; Loijens and Anderson, 1996). PLC-1^{PLCE} is activated via GPCR and hydrolyzes $PI(4,5)P_2$ to generate the second messengers DAG and IP_3, known regulators of several signal transduction pathways (Clandinin *et al.*, 1998; Kariya *et al.*, 2004). One mechanism that is dependent on IP_3-signaling is the release of calcium

from the ER (Clandinin *et al.*, 1998; Kariya *et al.*, 2004; Kovacevic *et al.*, 2013). Interestingly, the IP_3 receptor at the ER, ITR-1^{ITPR1}, has previously also been identified as a suppressor of antimycin-induced UPR^{mt} (Liu *et al.*, 2014). Thus, it is tempting to speculate that altering IP_3 signaling influences cellular calcium signaling in *fzo-1(tm1133)*, thereby affecting mitochondrial homeostasis and consequently UPR^{mt} signaling. Moreover, we propose that the effect on UPR^{mt} signaling may be indirect since we previously showed that knock-down of mitochondrial genes controlling calcium homeostasis does not induce UPR^{mt} in wild type (Rolland *et al.*, 2019). Furthermore, we propose that *fzo-(tm1133)* mutants may be more prone to changes in IP_3 signaling and, consequently, calcium signaling since these mutants may have altered ER-mitochondria contact sites, as shown in tissue culture cells lacking the mammalian ortholog MFN2 (de Brito and Scorrano, 2008; Cosson *et al.*, 2012; Filadi *et al.*, 2015, 2016; Leal *et al.*, 2016; Naon *et al.*, 2016; Basso *et al.*, 2018).

miga-1(tm3621) mutants show mitochondrial fragmentation and induce UPR^{mt}

One of the enhancers we identified is *K01D12.6*, which is conserved from *C. elegans* to humans. The *D. melanogaster* ortholog of this gene has previously been identified in a screen for genes, which when knocked-down induce photoreceptor cell neurodegeneration. Furthermore, it was shown to be required for the maintenance of mitochondrial morphology and hence, named '*Mitoguardin*' (Zhang *et al.*, 2016). Moreover, the two orthologs of this gene in mammals (*MIGA1*, *MIGA2*) were found to regulate mitochondrial fusion and to be critical for mitochondrial function in human tissue culture cells and in mice (Liu *et al.*, 2016; Zhang *et al.*, 2016; Liu *et al.*, 2017). Therefore, we named *K01D12.6* '*mitoguardin homolog-1* (*miga-1*)'. We verified UPR^{mt} induction using the P$_{hsp\text{-}60\ \mathrm{HSPD1}}$*gfp (zcIs9)* reporter in the *miga-1(tm3621)* mutant background (Figure 6A). On average, the induction of P$_{hsp\text{-}60\ \mathrm{HSPD1}}$*gfp* is higher in *miga-1(tm3621)* animals compared to *fzo-1(tm1133)* animals. Moreover, we tested the effects of *miga-1(tm3621)* on steady-state mitochondrial morphology, which, in *C. elegans*, is carried out using a mitochondrial matrix-targeted GFP under a promoter that expresses the transgene in body wall muscle cells (P$_{myo\text{-}3\ \mathrm{MYH}}$*gfp*^{mt}) (Labrousse *et al.*, 1999; Ichishita *et al.*, 2008; Rolland *et al.*, 2013). While wild-type worms show a tubular network of mitochondria, *miga-1(tm3621)* mutants have a 'fragmented mitochondria' phenotype, which is less severe than that caused by the loss of *fzo-1* (Figure 6B). In summary and in line with previous observations in other organisms, we see drastic changes in mitochondrial morphology in *miga-1(tm3621)* mutants, which are accompanied by the induction of UPR^{mt}.

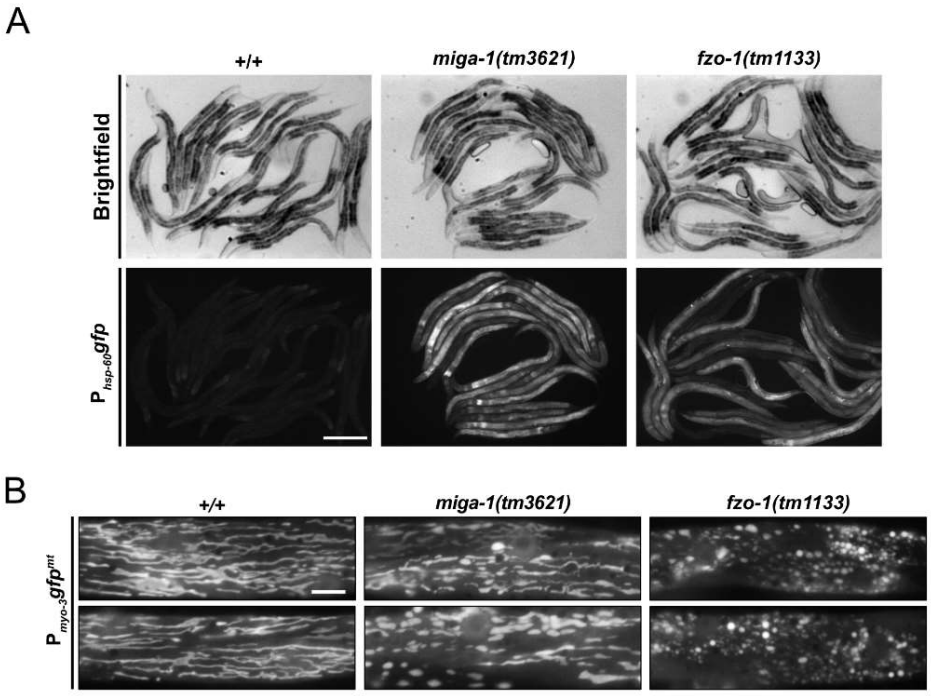

Figure 6: *miga-1(tm3621)* mutants induce UPR^{mt} and have altered mitochondrial morphology. (A) Fluorescence images of L4 larvae expressing P*hsp-60* mtHSPD1*gfp (zcIs9)* in wild type (+/+), *miga-1(tm3621)* or *fzo-1(tm1133)* mutants. Scale bar: 200 µm **(B)** Fluorescence images of L4 larvae expressing mitochondrial targeted *gfp* (P*myo-3*gfp^{mt}) in wild type (+/+), *miga-1(tm3621)* or *fzo-1(tm1133)* mutants. Representative images are shown. Scale bar: 10 µm.

ACKNOWLEDGEMENT

We thank members of the Conradt lab and the ‘Mito Club’ for lively discussions. We thank M. Bauer, L. Jocham, N. Lebedeva and M. Schwarz for excellent technical support and S. Mitani (National BioResource Project, Tokyo, Japan) for *fzo-1*(*tm1133*), *drp-1(tm1108)* and *miga-1(tm3621)*. Some strains were provided by the CGC, which is funded by NIH Office of Research Infrastructure Programs (P40 OD010440). DFG funding (CO204/6-1 and CO204/9-1).

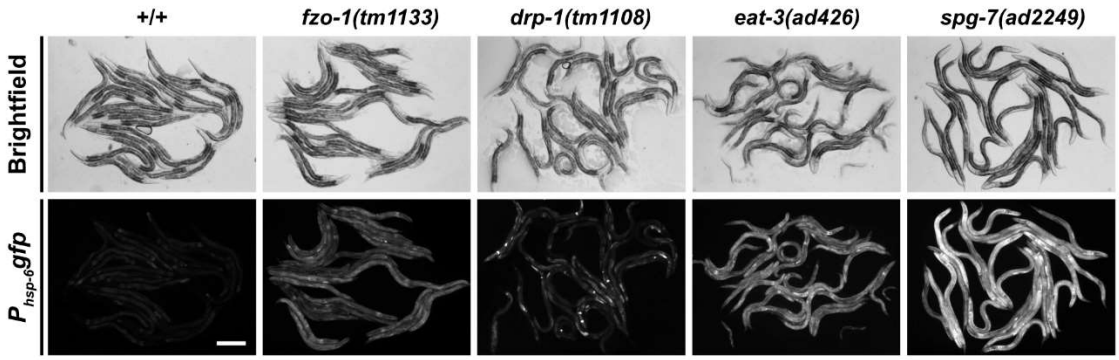

Figure S1: Mutations in GTPases of the dynamin family induce the UPR^{mt}. *fzo-1(tm1133), drp-1(tm1108)* and *eat-3(ad426)* mutants differ in the level of induction of the P$_{hsp\text{-}6}$ mtHSP70*gfp (zcIs13)* reporter, as compared to wild type (+/+). *spg-7(ad2249)* is used as a positive control. Scale bar: 200 µm.

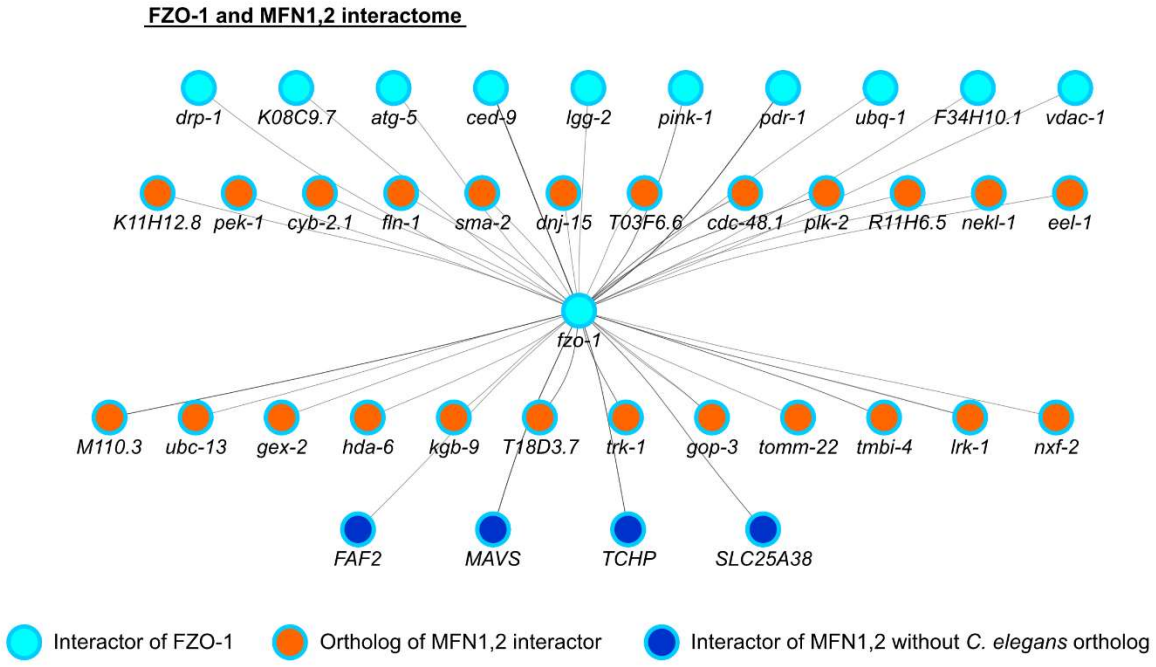

Figure S2: Analysis of a gene network – the FZOome. Interactors of *C. elegans* FZO-1 and of its human orthologs MFN1 and MFN2 were identified using 'string-db.org', 'IntAct', 'BioGRID3.5', 'Genemania', 'CCSB' and 'mentha' databases (Warde-Farley *et al.*, 2010; Calderone *et al.*, 2013; Orchard *et al.*, 2014; Rolland *et al.*, 2014; Oughtred *et al.*, 2018; Szklarczyk *et al.*, 2018). The identified candidates that suppressed or enhanced *fzo-1(tm1133)*-induced UPR^{mt} do not overlap with the FZOome. Turquois dots: interactors of FZO-1 in *C. elegans*; Orange dots: interactors of MFN1 or MFN2 which have orthologs in *C. elegans*; Blue dots: interactors of MFN1 or MFN2 in humans without any known orthologs in *C. elegans*.

REFERENCES

Ackema, K.B., Hench, J., Böckler, S., Wang, S.C., Sauder, U.*, et al.* (2014). The small GTPase Arf1 modulates mitochondrial morphology and function. The EMBO journal *33*, 2659-2675.

Aguilera-Romero , A., Kaminska , J., Spang , A., Riezman , H., and Muñiz , M. (2008). The yeast p24 complex is required for the formation of COPI retrograde transport vesicles from the Golgi apparatus. Journal of Cell Biology *180*, 713-720.

Ahringer, J. (1996). Posterior patterning by the Caenorhabditis elegans even-skipped homolog vab-7. Genes & Development *10*, 1120-1130.

Altmann, K., and Westermann, B. (2005). Role of Essential Genes in Mitochondrial Morphogenesis in Saccharomyces cerevisiae. Molecular Biology of the Cell *16*, 5410-5417.

Amberger, J.S., Bocchini, C.A., Scott, A.F., and Hamosh, A. (2018). OMIM.org: leveraging knowledge across phenotype–gene relationships. Nucleic Acids Research *47*, D1038-D1043.

Ambros, V., and Horvitz, H.R. (1984). Heterochronic mutants of the nematode Caenorhabditis elegans. Science (New York, NY) *226*, 409.

An, J.H., and Blackwell, T.K. (2003). SKN-1 links C. elegans mesendodermal specification to a conserved oxidative stress response. Genes & Development *17*, 1882-1893.

An, J.H., Vranas, K., Lucke, M., Inoue, H., Hisamoto, N.*, et al.* (2005). Regulation of the *Caenorhabditis elegans* oxidative stress defense protein SKN-1 by glycogen synthase kinase-3. Proceedings of the National Academy of Sciences of the United States of America *102*, 16275.

Aranda, A., and Pascual, A. (2001). Nuclear Hormone Receptors and Gene Expression. Physiological Reviews *81*, 1269-1304.

Armakola, M., and Ruvkun, G. (2019). Regulation of Caenorhabditis elegans neuronal polarity by heterochronic genes. Proceedings of the National Academy of Sciences *116*, 12327.

Arning, S., Grüter, P., Bilbe, G., and Krämer, A. (1996). Mammalian splicing factor SF1 is encoded by variant cDNAs and binds to RNA. RNA *2*, 794-810.

Arsenovic, P.T., Maldonado, A.T., Colleluori, V.D., and Bloss, T.A. (2012). Depletion of the C. elegans NAC Engages the Unfolded Protein Response, Resulting in Increased Chaperone Expression and Apoptosis. PloS one *7*, e44038.

Basso, V., Marchesan, E., Peggion, C., Chakraborty, J., von Stockum, S.*, et al.* (2018). Regulation of ER-mitochondria contacts by Parkin via Mfn2. Pharmacological Research *138*, 43-56.

Baugh, L.R., Hill, A.A., Claggett, J.M., Hill-Harfe, K., Wen, J.C., *et al.* (2005). The homeodomain protein PAL-1 specifies a lineage-specific regulatory network in the C. elegans embryo. Development *132*, 1843.

Beck, R., Ravet, M., Wieland, F.T., and Cassel, D. (2009). The COPI system: Molecular mechanisms and function. FEBS Letters *583*, 2701-2709.

Bennett, C.F., Vander Wende, H., Simko, M., Klum, S., Barfield, S., *et al.* (2014). Activation of the mitochondrial unfolded protein response does not predict longevity in *Caenorhabditis elegans*. Nature communications *5*, 3483.

Berridge, M.J. (2009). Inositol trisphosphate and calcium signalling mechanisms. Biochimica et Biophysica Acta (BBA) - Molecular Cell Research *1793*, 933-940.

Bleazard, W., McCaffery, J.M., King, E.J., Bale, S., Mozdy, A., *et al.* (1999). The dynamin-related GTPase Dnm1 regulates mitochondrial fission in yeast. Nature cell biology *1*, 298-304.

Bolotin, E., Liao, H., Ta, T.C., Yang, C., Hwang-Verslues, W., *et al.* (2010). Integrated approach for the identification of human hepatocyte nuclear factor 4α target genes using protein binding microarrays. Hepatology *51*, 642-653.

Brenner, S. (1974). The Genetics of *Caenorhabditis Elegans*. Genetics *77*, 71-94.

Budnik, A., and Stephens, D.J. (2009). ER exit sites – Localization and control of COPII vesicle formation. FEBS Letters *583*, 3796-3803.

Budovskaya, Y.V., Wu, K., Southworth, L.K., Jiang, M., Tedesco, P., *et al.* (2008). An elt-3/elt-5/elt-6 GATA Transcription Circuit Guides Aging in C. elegans. Cell *134*, 291-303.

Byrne, A.B., Weirauch, M.T., Wong, V., Koeva, M., Dixon, S.J., *et al.* (2007). A global analysis of genetic interactions in Caenorhabditis elegans. Journal of Biology *6*, 8.

Calderone, A., Castagnoli, L., and Cesareni, G. (2013). mentha: a resource for browsing integrated protein-interaction networks. Nature Methods *10*, 690-691.

Cambier, L., Rassam, P., Chabi, B., Mezghenna, K., Gross, R., *et al.* (2012). M19 modulates skeletal muscle differentiation and insulin secretion in pancreatic β-cells through modulation of respiratory chain activity. PloS one *7*, e31815.

Celniker, S.E., Dillon, L.A.L., Gerstein, M.B., Gunsalus, K.C., Henikoff, S., *et al.* (2009). Unlocking the secrets of the genome. Nature *459*, 927-930.

Ceol, C.J., and Horvitz, H.R. (2001). dpl-1 DP and efl-1 E2F Act with lin-35 Rb to Antagonize Ras Signaling in C. elegans Vulval Development. Molecular cell *7*, 461-473.

Chang, S., Johnston, R.J., and Hobert, O. (2003). A transcriptional regulatory cascade that controls left/right asymmetry in chemosensory neurons of C. elegans. Genes & Development *17*, 2123-2137.

Chen, H., and Chan, D.C. (2004). Mitochondrial dynamics in mammals. Current topics in developmental biology *59*, 119-144.

Chen, H., Detmer, S.A., Ewald, A.J., Griffin, E.E., Fraser, S.E.*, et al.* (2003). Mitofusins Mfn1 and Mfn2 coordinately regulate mitochondrial fusion and are essential for embryonic development. The Journal of cell biology *160*, 189-200.

Chen, L., Vasoya, R.P., Toke, N.H., Parthasarathy, A., Luo, S.*, et al.* (2020). HNF4 Regulates Fatty Acid Oxidation and Is Required for Renewal of Intestinal Stem Cells in Mice. Gastroenterology *158*, 985-999.e989.

Chi, W., and Reinke, V. (2006). Promotion of oogenesis and embryogenesis in the C. elegans gonad by EFL-1/DPL-1 (E2F) does not require LIN-35 (pRB). Development *133*, 3147.

Clandinin, T.R., DeModena, J.A., and Sternberg, P.W. (1998). Inositol Trisphosphate Mediates a RAS-Independent Response to LET-23 Receptor Tyrosine Kinase Activation in C. elegans. Cell *92*, 523-

Claros, M.G., and Vincens, P. (1996). Computational Method to Predict Mitochondrially Imported Proteins and their Targeting Sequences. European Journal of Biochemistry *241*, 779-786.

Consortium, T.U. (2018). UniProt: a worldwide hub of protein knowledge. Nucleic Acids Research *47*, D506-D515.

Cosson, P., Marchetti, A., Ravazzola, M., and Orci, L. (2012). Mitofusin-2 Independent Juxtaposition of Endoplasmic Reticulum and Mitochondria: An Ultrastructural Study. PloS one *7*, e46293.

Creutz, C.E., Tomsig, J.L., Snyder, S.L., Gautier, M.C., Skouri, F.*, et al.* (1998). The copines, a novel class of C2 domain-containing, calcium-dependent, phospholipid-binding proteins conserved from Paramecium to humans. The Journal of biological chemistry *273*, 1393-1402.

Daugherty, M., Polanuyer, B., Farrell, M., Scholle, M., Lykidis, A.*, et al.* (2002). Complete Reconstitution of the Human Coenzyme A Biosynthetic Pathway via Comparative Genomics. Journal of Biological Chemistry *277*, 21431-21439.

de Brito, O.M., and Scorrano, L. (2008). Mitofusin 2 tethers endoplasmic reticulum to mitochondria. Nature *456*, 605.

Dhe-Paganon, S., Duda, K., Iwamoto, M., Chi, Y.-I., and Shoelson, S.E. (2002). Crystal Structure of the HNF4α Ligand Binding Domain in Complex with Endogenous Fatty Acid Ligand. Journal of Biological Chemistry *277*, 37973-37976.

Di Fiore, P.P., and von Zastrow, M. (2014). Endocytosis, signaling, and beyond. Cold Spring Harbor perspectives in biology *6*, a016865.

Dillin, A., Hsu, A.-L., Arantes-Oliveira, N., Lehrer-Graiwer, J., Hsin, H.*, et al.* (2002). Rates of Behavior and Aging Specified by Mitochondrial Function During Development. Science (New York, NY) *298*, 2398-2401.

Duda, K., Chi, Y.-I., and Shoelson, S.E. (2004). Structural Basis for HNF-4α Activation by Ligand and Coactivator Binding. Journal of Biological Chemistry *279*, 23311-23316.

Dues, D.J., Schaar, C.E., Johnson, B.K., Bowman, M.J., Winn, M.E.*, et al.* (2017). Uncoupling of oxidative stress resistance and lifespan in long-lived isp-1 mitochondrial mutants in Caenorhabditis elegans. Free Radical Biology and Medicine *108*, 362-373.

Durieux, J., Wolff, S., and Dillin, A. (2011). The cell-non-autonomous nature of electron transport chain-mediated longevity. Cell *144*, 79-91.

Durinck, S., Spellman, P.T., Birney, E., and Huber, W. (2009). Mapping identifiers for the integration of genomic datasets with the R/Bioconductor package biomaRt. Nature protocols *4*, 1184-1191.

Esmaeili, B., Ross, J.M., Neades, C., Miller, D.M., and Ahringer, J. (2002). The C. elegans even-skipped homologue vab-7 specifies DB motoneurone identity and axon trajectory. Development *129*, 853.

Etchberger, J.F., Lorch, A., Sleumer, M.C., Zapf, R., Jones, S.J.*, et al.* (2007). The molecular signature and cis-regulatory architecture of a C. elegans gustatory neuron. Genes & Development *21*, 1653-1674.

Farhan, H., and Rabouille, C. (2011). Signalling to and from the secretory pathway. Journal of cell science *124*, 171-180.

Filadi, R., Greotti, E., Turacchio, G., Luini, A., Pozzan, T.*, et al.* (2015). Mitofusin 2 ablation increases endoplasmic reticulum–mitochondria coupling. Proceedings of the National Academy of Sciences *112*, E2174-E2181.

Filadi, R., Greotti, E., Turacchio, G., Luini, A., Pozzan, T.*, et al.* (2016). Presenilin 2 Modulates Endoplasmic Reticulum-Mitochondria Coupling by Tuning the Antagonistic Effect of Mitofusin 2. Cell reports *15*, 2226-2238.

Furuno, K., Ikeda, K., Hamano, S., Fukuyama, K., Sonoda, M.*, et al.* (2008). Onecut transcription factor OC2 is a direct target of T-bet in type-1 T-helper cells. Genes & Immunity *9*, 302-308.

Garbe, D., Doto, J.B., and Sundaram, M.V. (2004). Caenorhabditis elegans lin-35/Rb, efl-1/E2F and Other Synthetic Multivulva Genes Negatively Regulate the Anaphase-Promoting Complex Gene mat-3/APC8. Genetics *167*, 663.

Gavin, K.A., Hidaka, M., and Stillman, B. (1995). Conserved initiator proteins in eukaryotes. Science (New York, NY) *270*, 1667-1671.

Gilleard, J.S., Shafi, Y., Barry, J.D., and McGhee, J.D. (1999). ELT-3: ACaenorhabditis elegansGATA Factor Expressed in the Embryonic Epidermis during Morphogenesis. Developmental Biology *208*, 265-280.

Grove, C.A., De Masi, F., Barrasa, M.I., Newburger, D.E., Alkema, M.J.*, et al.* (2009). A Multiparameter Network Reveals Extensive Divergence between C. elegans bHLH Transcription Factors. Cell *138*, 314-327.

Haeussler, S., Köhler, F., Witting, M., Premm, M.F., Rolland, S.G.*, et al.* (2020). Autophagy compensates for defects in mitochondrial dynamics. PLoS genetics *16*, e1008638.

Hales, K.G., and Fuller, M.T. (1997). Developmentally regulated mitochondrial fusion mediated by a conserved, novel, predicted GTPase. Cell *90*, 121-129.

Hallam, S., Singer, E., Waring, D., and Jin, Y. (2000). The C. elegans NeuroD homolog cnd-1 functions in multiple aspects of motor neuron fate specification. Development *127*, 4239.

Harris, T.W., Arnaboldi, V., Cain, S., Chan, J., Chen, W.J.*, et al.* (2019). WormBase: a modern Model Organism Information Resource. Nucleic Acids Research *48*, D762-D767.

Harrison, M.M., Ceol, C.J., Lu, X., and Horvitz, H.R. (2006). Some *C. elegans* class B synthetic multivulva proteins encode a conserved LIN-35 Rb-containing complex distinct from a NuRD-like complex. Proceedings of the National Academy of Sciences *103*, 16782-16787.

Haynes, C.M., Petrova, K., Benedetti, C., Yang, Y., and Ron, D. (2007). ClpP mediates activation of a mitochondrial unfolded protein response in *C. elegans*. Developmental cell *13*, 467-480.

Haynes, C.M., Yang, Y., Blais, S.P., Neubert, T.A., and Ron, D. (2010). The matrix peptide exporter HAF-1 signals a mitochondrial UPR by activating the transcription factor ZC376.7 in *C. elegans*. Molecular cell *37*, 529-540.

Hertz, R., Magenheim, J., Berman, I., and Bar-Tana, J. (1998). Fatty acyl-CoA thioesters are ligands of hepatic nuclear factor-4α. Nature *392*, 512-516.

Horn, M., Geisen, C., Cermak, L., Becker, B., Nakamura, S.*, et al.* (2014). DRE-1/FBXO11-Dependent Degradation of BLMP-1/BLIMP-1 Governs C. elegans Developmental Timing and Maturation. Developmental cell *28*, 697-710.

Houtkooper, R.H., Mouchiroud, L., Ryu, D., Moullan, N., Katsyuba, E.*, et al.* (2013). Mitonuclear protein imbalance as a conserved longevity mechanism. Nature *497*, 451-457.

Hu, Q., D'Amora, D.R., MacNeil, L.T., Walhout, A.J.M., and Kubiseski, T.J. (2017). The Oxidative Stress Response in *Caenorhabditis elegans* Requires the GATA Transcription Factor ELT-3 and SKN-1/Nrf2. Genetics *206*, 1909.

Huang, D.W., Sherman, B.T., and Lempicki, R.A. (2008). Bioinformatics enrichment tools: paths toward the comprehensive functional analysis of large gene lists. Nucleic Acids Research *37*, 1-13.

Huang, D.W., Sherman, B.T., and Lempicki, R.A. (2009). Systematic and integrative analysis of large gene lists using DAVID bioinformatics resources. Nature Protocols *4*, 44-57.

Huang, D.W., Sherman, B.T., Tan, Q., Collins, J.R., Alvord, W.G.*, et al.* (2007). The DAVID Gene Functional Classification Tool: a novel biological module-centric algorithm to functionally analyze large gene lists. Genome Biol *8*, R183.

Huang, J.D., Dubnicoff, T., Liaw, G.J., Bai, Y., Valentine, S.A.*, et al.* (1995). Binding sites for transcription factor NTF-1/Elf-1 contribute to the ventral repression of decapentaplegic. Genes & Development *9*, 3177-3189.

Huang, T.-F., Cho, C.-Y., Cheng, Y.-T., Huang, J.-W., Wu, Y.-Z.*, et al.* (2014). BLMP-1/Blimp-1 Regulates the Spatiotemporal Cell Migration Pattern in C. elegans. PLoS genetics *10*, e1004428.

Hunt, S.E., McLaren, W., Gil, L., Thormann, A., Schuilenburg, H.*, et al.* (2018). Ensembl variation resources. Database *2018*.

Ichishita, R., Tanaka, K., Sugiura, Y., Sayano, T., Mihara, K.*, et al.* (2008). An RNAi Screen for Mitochondrial Proteins Required to Maintain the Morphology of the Organelle in Caenorhabditis elegans. The Journal of Biochemistry *143*, 449-454.

Imafuku, I., Waragai, M., Takeuchi, S., Kanazawa, I., Kawabata, M.*, et al.* (1998). Polar Amino Acid-Rich Sequences Bind to Polyglutamine Tracts. Biochemical and Biophysical Research Communications *253*, 16-20.

Ingerman, E., Perkins, E.M., Marino, M., Mears, J.A., McCaffery, J.M.*, et al.* (2005). Dnm1 forms spirals that are structurally tailored to fit mitochondria. The Journal of cell biology *170*, 1021-1027.

Inoue, H., Hisamoto, N., An, J.H., Oliveira, R.P., Nishida, E.*, et al.* (2005). The C. elegans p38 MAPK pathway regulates nuclear localization of the transcription factor SKN-1 in oxidative stress response. Genes & Development *19*, 2278-2283.

Ishihara, H., Shibasaki, Y., Kizuki, N., Katagiri, H., Yazaki, Y.*, et al.* (1996). Cloning of cDNAs Encoding Two Isoforms of 68-kDa Type I Phosphatidylinositol4-phosphate 5-Kinase. Journal of Biological Chemistry *271*, 23611-23614.

Izumi, K., Brett, M., Nishi, E., Drunat, S., Tan, E.-S., *et al.* (2016). ARCN1 Mutations Cause a Recognizable Craniofacial Syndrome Due to COPI-Mediated Transport Defects. Am J Hum Genet *99*, 451-459.

Jacquemin, P., Lemaigre, F.P., and Rousseau, G.G. (2003). The Onecut transcription factor HNF-6 (OC-1) is required for timely specification of the pancreas and acts upstream of Pdx-1 in the specification cascade. Developmental Biology *258*, 105-116.

Kamath, R.S., and Ahringer, J. (2003). Genome-wide RNAi screening in *Caenorhabditis elegans*. Methods (San Diego, Calif) *30*, 313-321.

Kambach, C., Walket, S., and Nagai, K. (1999). Structure and assembly of the spliceosomal small nuclear ribonucleoprotein particles. Current Opinion in Structural Biology *9*, 222-230.

Kanazawa, T., Zappaterra, M.D., Hasegawa, A., Wright, A.P., Newman-Smith, E.D., *et al.* (2008). The *C. elega* Opa1 Homologue EAT-3 Is Essential for Resistance to Free Radicals. PLoS genetics *4*, e1000022.

Kariya, K.-i., Kim Bui, Y., Gao, X., Sternberg, P.W., and Kataoka, T. (2004). Phospholipase Cε regulates ovulation in Caenorhabditis elegans. Developmental Biology *274*, 201-210.

Khan, M.H., Ligon, M., Hussey, L.R., Hufnal, B., Farber, R., *et al.* (2013). TAF-4 is required for the life extension of isp-1, clk-1 and tpk-1 Mit mutants. Aging *5*, 741-758.

Kim, J., Yeon, J., Choi, S.-K., Huh, Y.H., Fang, Z., *et al.* (2015). The Evolutionarily Conserved LIM Homeodomain Protein LIM-4/LHX6 Specifies the Terminal Identity of a Cholinergic and Peptidergic C. elegans Sensory/Inter/Mot Neuron-Type. PLoS genetics *11*, e1005480.

Kim, S., and Sieburth, D. (2018). Sphingosine Kinase Activates the Mitochondrial Unfolded Protein Response and Is Targeted to Mitochondria by Stress. Cell reports *24*, 2932-2945.e2934.

Kim, S., and Sieburth, D. (2020). FSHR-1/GPCR Regulates the Mitochondrial Unfolded Protein Response in *Caenorhabditis elegans*. Genetics *214*, 409-418.

Kim, W., Underwood, R.S., Greenwald, I., and Shaye, D.D. (2018). OrthoList 2: A New Comparative Genomic Analysis of Human and *Caenorhabditis elegans* Genes. Genetics *210*, 445-461.

Kirstein-Miles, J., Scior, A., Deuerling, E., and Morimoto, R.I. (2013). The nascent polypeptide-associated complex is a key regulator of proteostasis. The EMBO journal *32*, 1451-1468.

Klimova, L., Antosova, B., Kuzelova, A., Strnad, H., and Kozmik, Z. (2015). Onecut1 and Onecut2 transcription factors operate downstream of Pax6 to regulate horizontal cell development. Developmental Biology *402*, 48-60.

Knüppel, R., Dietze, P., Lehnberg, W., Frech, K., and Wingender, E. (1994). TRANSFAC Retrieval Program: A Network Model Database of Eukaryotic Transcription Regulating Sequences and Proteins. Journal of Computational Biology *1*, 191-198.

Kornmann, B. (2014). Quality control in mitochondria: use it, break it, fix it, trash it. F1000Prime Rep *6*, 15-15.

Kovacevic, I., Orozco, J.M., and Cram, E.J. (2013). Filamin and Phospholipase C-ε Are Required for Calcium Signaling in the Caenorhabditis elegans Spermatheca. PLoS genetics *9*, e1003510.

Krämer, A. (1992). Purification of splicing factor SF1, a heat-stable protein that functions in the assembly of a presplicing complex. Molecular and Cellular Biology *12*, 4545-4552.

Kriventseva, E.V., Kuznetsov, D., Tegenfeldt, F., Manni, M., Dias, R.*, et al.* (2018). OrthoDB v10: sampling the diversity of animal, plant, fungal, protist, bacterial and viral genomes for evolutionary and functional annotations of orthologs. Nucleic Acids Research *47*, D807-D811.

Kurokawa, K., and Nakano, A. (2018). The ER exit sites are specialized ER zones for the transport of cargo proteins from the ER to the Golgi apparatus. The Journal of Biochemistry *165*, 109-114.

Labrousse, A.M., Zappaterra, M.D., Rube, D.A., and van der Bliek, A.M. (1999). *C. elegans* Dynamin-Related Protein DRP-1 Controls Severing of the Mitochondrial Outer Membrane. Molecular cell *4*, 815-826.

Leal, N.S., Schreiner, B., Pinho, C.M., Filadi, R., Wiehager, B.*, et al.* (2016). Mitofusin-2 knockdown increases ER–mitochondria contact and decreases amyloid β-peptide production. Journal of Cellular and Molecular Medicine *20*, 1686-1695.

Lee, M.C.S., Miller, E.A., Goldberg, J., Orci, L., and Schekman, R. (2004). Bi-directional protein transport between the ER and Golgi. Annual Review of Cell and Developmental Biology *20*, 87-123.

Lei, H., Liu, J., Fukushige, T., Fire, A., and Krause, M. (2009). Caudal-like PAL-1 directly activates the bodywall muscle module regulator hlh-1 in C. elegans to initiate the embryonic muscle gene regulatory network. Development *136*, 1241.

Lichtsteiner, S., and Tjian, R. (1993). Cloning and properties of the Caenorhabditis elegans TATA-box-binding protein. Proceedings of the National Academy of Sciences *90*, 9673-9677.

Liu, X.-M., Zhang, Y.-L., Ji, S.-Y., Zhao, L.-W., Shang, W.-N.*, et al.* (2017). Mitochondrial Function Regulated by Mitoguardin-1/2 Is Crucial for Ovarian Endocrine Functions and Ovulation. Endocrinology *158*, 3988-3999.

Liu, X.-M., Zhang, Y.-P., Ji, S.-Y., Li, B.-T., Tian, X.*, et al.* (2016). Mitoguardin-1 and -2 promote maturation and the developmental potential of mouse oocytes by maintaining mitochondrial dynamics and functions. Oncotarget *7*.

Liu, Y., Samuel, B.S., Breen, P.C., and Ruvkun, G. (2014). *Caenorhabditis elegans* pathways that surveil and defend mitochondria. Nature *508*, 406-410.

Loijens, J.C., and Anderson, R.A. (1996). Type I Phosphatidylinositol-4-phosphate 5-Kinases Are Distinct Members of This Novel Lipid Kinase Family. Journal of Biological Chemistry *271*, 32937-32943.

Maduro, M.F., Kasmir, J.J., Zhu, J., and Rothman, J.H. (2005). The Wnt effector POP-1 and the PAL-1/Caudal homeoprotein collaborate with SKN-1 to activate C. elegans endoderm development. Developmental Biology *285*, 510-523.

Matys, V., Kel-Margoulis, O.V., Fricke, E., Liebich, I., Land, S.*, et al.* (2006). TRANSFAC and its module TRANSCompel: transcriptional gene regulation in eukaryotes. Nucleic acids research *34*, D108-110.

Mazroui, R., Puoti, A., and KrÄMer, A. (1999). Splicing factor SF1 from Drosophila and Caenorhabditis: Presence of an N-terminal RS domain and requirement for viability. RNA *5*, 1615-1631.

McMiller, T.L., Sims, D., Lee, T., Williams, T., and Johnson, C.M. (2007). Molecular characterization of the Caenorhabditis elegans REF-1 family member, hlh-29/hlh-28. Biochimica et Biophysica Acta (BBA) - Gene Structure and Expression *1769*, 5-19.

Miller, J.G., Liu, Y., Williams, C.W., Smith, H.E., and O'Connell, K.F. (2016). The E2F-DP1 Transcription Factor Complex Regulates Centriole Duplication in Caenorhabditis elegans. G3: Genes|Genomes|Genetics *6*, 709.

Nakatsu, F., Baskin, J.M., Chung, J., Tanner, L.B., Shui, G.*, et al.* (2012). PtdIns4P synthesis by PI4KIIIα at the plasma membrane and its impact on plasma membrane identity. The Journal of cell biology *199*, 1003-1016.

Naon, D., Zaninello, M., Giacomello, M., Varanita, T., Grespi, F.*, et al.* (2016). Critical reappraisal confirms that Mitofusin 2 is an endoplasmic reticulum–mitochondria tether. Proceedings of the National Academy of Sciences *113*, 11249-11254.

Nargund, Amrita M., Fiorese, Christopher J., Pellegrino, Mark W., Deng, P., and Haynes, Cole M. (2015). Mitochondrial and Nuclear Accumulation of the Transcription Factor ATFS-1 Promotes OXPHOS Recovery during the UPRmt. Molecular cell *58*, 123-133.

Nargund, A.M., Pellegrino, M.W., Fiorese, C.J., Baker, B.M., and Haynes, C.M. (2012). Mitochondrial Import Efficiency of ATFS-1 Regulates Mitochondrial UPR Activation. Science (New York, NY) *337*, 587-590.

Neves, A., and Priess, J.R. (2005). The REF-1 Family of bHLH Transcription Factors Pattern C. elegans Embryos through Notch-Dependent and Notch-Independent Pathways. Developmental cell *8*,

Ohta, S., Tatsumi, Y., Fujita, M., Tsurimoto, T., and Obuse, C. (2003). The ORC1 cycle in human cells: II. Dynamic changes in the human ORC complex during the cell cycle. The Journal of biological chemistry *278*, 41535-41540.

Orchard, S., Ammari, M., Aranda, B., Breuza, L., Briganti, L.*, et al.* (2014). The MIntAct project--IntAct as a common curation platform for 11 molecular interaction databases. Nucleic acids research *42*, D358-363.

Otsuga, D., Keegan, B.R., Brisch, E., Thatcher, J.W., Hermann, G.J.*, et al.* (1998). The Dynamin-related GTPase, Dnm1p, Controls Mitochondrial Morphology in Yeast. Journal of Cell Biology *143*, 333-

Oughtred, R., Stark, C., Breitkreutz, B.-J., Rust, J., Boucher, L.*, et al.* (2018). The BioGRID interaction database: 2019 update. Nucleic Acids Research *47*, D529-D541.

Palanker, L., Tennessen, J.M., Lam, G., and Thummel, C.S. (2009). Drosophila HNF4 Regulates Lipid Mobilization and β-Oxidation. Cell metabolism *9*, 228-239.

Pocock, R., Ahringer, J., Mitsch, M., Maxwell, S., and Woollard, A. (2004). A regulatory network of T-box genes and the even-skipped homologue vab-7 controls patterning and morphogenesis in C. elegans. Development *131*, 2373.

Pradel, E., Zhang, Y., Pujol, N., Matsuyama, T., Bargmann, C.I.*, et al.* (2007). Detection and avoidance of a natural product from the pathogenic bacterium Serratia marcescens by Caenorhabditis elegans. Proceedings of the National Academy of Sciences *104*, 2295.

Quach, T.K., Chou, H.T., Wang, K., Milledge, G.Z., and Johnson, C.M. (2013). Genome-Wide Microarrray Analysis Reveals Roles for the REF-1 Family Member HLH-29 in Ferritin Synthesis and Peroxide Stress Response. PloS one *8*, e59719.

Rahe, D.P., and Hobert, O. (2019). Restriction of Cellular Plasticity of Differentiated Cells Mediated by Chromatin Modifiers, Transcription Factors and Protein Kinases. G3: Genes|Genomes|Genetics *9*, 2287.

Ramsey, C.S., Yeung, F., Stoddard, P.B., Li, D., Creutz, C.E.*, et al.* (2008). Copine-I represses NF-kappaB transcription by endoproteolysis of p65. Oncogene *27*, 3516-3526.

Raudvere, U., Kolberg, L., Kuzmin, I., Arak, T., Adler, P.*, et al.* (2019). g:Profiler: a web server for functional enrichment analysis and conversions of gene lists (2019 update). Nucleic Acids Research *47*, W191-W198.

Rea, S.L., Ventura, N., and Johnson, T.E. (2007). Relationship Between Mitochondrial Electron Transport Chain Dysfunction, Development, and Life Extension in Caenorhabditis elegans. PLOS Biology *5*, e259.

Rolland, S.G., Motori, E., Memar, N., Hench, J., Frank, S.*, et al.* (2013). Impaired complex IV activity in response to loss of LRPPRC function can be compensated by mitochondrial hyperfusion. Proceedings of the National Academy of Sciences of the United States of America *110*, E2967-2976.

Rolland, S.G., Schneid, S., Schwarz, M., Rackles, E., Fischer, C.*, et al.* (2019). Compromised Mitochondrial Protein Import Acts as a Signal for UPR^{mt}. Cell reports *28*, 1659-1669.e1655.

Rolland, T., Taşan, M., Charloteaux, B., Pevzner, Samuel J., Zhong, Q.*, et al.* (2014). A Proteome-Scale Map of the Human Interactome Network. Cell *159*, 1212-1226.

Runkel, E.D., Liu, S., Baumeister, R., and Schulze, E. (2013). Surveillance-activated defenses block the ROS-induced mitochondrial unfolded protein response. PLoS genetics *9*, e1003346.

Santel, A., Frank, S., Gaume, B., Herrler, M., Youle, R.J.*, et al.* (2003). Mitofusin-1 protein is a generally expressed mediator of mitochondrial fusion in mammalian cells. Journal of cell science *116*, 2763-2774.

Schwarz, E.M., Kato, M., and Sternberg, P.W. (2012). Functional transcriptomics of a migrating cell in Caenorhabditis elegans. Proceedings of the National Academy of Sciences *109*, 16246.

Shafqat, N., Marschall, H.-U., Filling, C., Nordling, E., Wu, X.-Q.*, et al.* (2003). Expanded substrate screenings of human and Drosophila type 10 17β-hydroxysteroid dehydrogenases (HSDs) reveal multiple specificities in bile acid and steroid hormone metabolism: characterization of multifunctional 3α/7α/7β/17β/20β/21-HSD. Biochemical Journal *376*, 49-60.

Shannon, P., Markiel, A., Ozier, O., Baliga, N.S., Wang, J.T.*, et al.* (2003). Cytoscape: A Software Environment for Integrated Models of Biomolecular Interaction Networks. Genome Research *13*, 2498-2504.

Shao, L.-W., Niu, R., and Liu, Y. (2016). Neuropeptide signals cell non-autonomous mitochondrial unfolded protein response. Cell Research *26*, 1182-1196.

Shaye, D.D., and Greenwald, I. (2011). OrthoList: A Compendium of C. elegans Genes with Human Orthologs. PloS one *6*, e20085.

Shepard, K.A., and Yaffe, M.P. (1999). The Yeast Dynamin-like Protein, Mgm1p, Functions on the Mitochondrial Outer Membrane to Mediate Mitochondrial Inheritance. Journal of Cell Biology *144*, 711-720.

Simmer, F., Moorman, C., van der Linden, A.M., Kuijk, E., van den Berghe, P.V.E.*, et al.* (2003). Genome-Wide RNAi of C. elegans Using the Hypersensitive rrf-3 Strain Reveals Novel Gene Functions. PLOS Biology *1*, e12.

Simonis, N., Rual, J.-F., Carvunis, A.-R., Tasan, M., Lemmens, I.*, et al.* (2009). Empirically controlled mapping of the Caenorhabditis elegans protein-protein interactome network. Nature Methods *6*, 47-54.

Smirnova, E., Shurland, D.-L., Ryazantsev, S.N., and van der Bliek, A.M. (1998). A Human Dynamin-related Protein Controls the Distribution of Mitochondria. Journal of Cell Biology *143*, 351-

Soo-Ung, L., Hyun-Ok, S., Wonhae, L., Gunasekaran, S., Jae-Ran, Y.*, et al.* (2009). Identification and Characterization of a Putative Basic Helix-Loop-Helix (bHLH) Transcription Factor Interacting with Calcineurin in C. elegans. Molecules and cells *28*, 455-461.

Sopta, M., Burton, Z.F., and Greenblatt, J. (1989). Structure and associated DNA-helicase activity of a general transcription initiation factor that binds to RNA polymerase II. Nature *341*, 410-414.

Sorkin, A., and von Zastrow, M. (2009). Endocytosis and signalling: intertwining molecular networks. Nature reviews Molecular cell biology *10*, 609-622.

Spaan, A.N., Ijlst, L., van Roermund, C.W.T., Wijburg, F.A., Wanders, R.J.A.*, et al.* (2005). Identification of the human mitochondrial FAD transporter and its potential role in multiple acyl-CoA dehydrogenase deficiency. Molecular Genetics and Metabolism *86*, 441-447.

Szklarczyk, D., Gable, A.L., Lyon, D., Junge, A., Wyder, S.*, et al.* (2018). STRING v11: protein–protein association networks with increased coverage, supporting functional discovery in genome-wide experimental datasets. Nucleic Acids Research *47*, D607-D613.

Tabuchi, T.M., Deplancke, B., Osato, N., Zhu, L.J., Barrasa, M.I.*, et al.* (2011). Chromosome-Biased Binding and Gene Regulation by the Caenorhabditis elegans DRM Complex. PLoS genetics *7*, e1002074.

Tatsumi, Y., Ohta, S., Kimura, H., Tsurimoto, T., and Obuse, C. (2003). The ORC1 cycle in human cells: I. cell cycle-regulated oscillation of human ORC1. The Journal of biological chemistry *278*, 41528-41534.

Tatsuta, T., and Langer, T. (2008). Quality control of mitochondria: protection against neurodegeneration and ageing. The EMBO journal *27*, 306-314.

The Alliance of Genome Resources, C. (2019). Alliance of Genome Resources Portal: unified model organism research platform. Nucleic Acids Research *48*, D650-D658.

Thomas, J.D., Conrad, R.C., and Blumenthal, T. (1988). The C. elegans Trans-spliced leader RNA is bound to Sm and has a trimethylguanosine cap. Cell *54*, 533-539.

Thomas, J.H., Ceol, C.J., Schwartz, H.T., and Horvitz, H.R. (2003). New Genes That Interact With *lin-35* Rb to Negatively Regulate the *let-60 ras* Pathway in *Caenorhabditis elegans*. Genetics *164*, 135-151.

Tomsig, J.L., Snyder, S.L., and Creutz, C.E. (2003). Identification of targets for calcium signaling through the copine family of proteins. Characterization of a coiled-coil copine-binding motif. The Journal of biological chemistry *278*, 10048-10054.

Tomsig, J.L., Sohma, H., and Creutz, C.E. (2004). Calcium-dependent regulation of tumour necrosis factor-alpha receptor signalling by copine. Biochem J *378*, 1089-1094.

Uchida, O., Nakano, H., Koga, M., and Ohshima, Y. (2003). The C. elegans che-1 gene encodes a zinc finger transcription factor required for specification of the ASE chemosensory neurons. Development *130*, 1215.

van der Bliek, A.M., Shen, Q., and Kawajiri, S. (2013). Mechanisms of Mitochondrial Fission and Fusion. Cold Spring Harbor Perspectives in Biology *5*.

Van Raamsdonk, J.M., Meng, Y., Camp, D., Yang, W., Jia, X.*, et al.* (2010). Decreased Energy Metabolism Extends Life Span in Caenorhabditis elegans Without Reducing Oxidative Damage. Genetics *185*, 559-571.

Vance, J.E. (1998). Eukaryotic lipid-biosynthetic enzymes: the same but not the same. Trends in biochemical sciences *23*, 423-428.

Venkatesan, K., McManus, H.R., Mello, C.C., Smith, T.F., and Hansen, U. (2003). Functional conservation between members of an ancient duplicated transcription factor family, LSF/Grainyhead. Nucleic Acids Research *31*, 4304-4316.

Walker, A.K., Rothman, J.H., Shi, Y., and Blackwell, T.K. (2001). Distinct requirements for C.elegans TAFII in early embryonic transcription. The EMBO journal *20*, 5269-5279.

Walker, A.K., Shi, Y., and Blackwell, T.K. (2004). An Extensive Requirement for Transcription Factor IID-specific TAF-1 in Caenorhabditis elegans Embryonic Transcription. Journal of Biological Chemistry *279*, 15339-15347.

Walter, W., Sánchez-Cabo, F., and Ricote, M. (2015). GOplot: an R package for visually combining expression data with functional analysis. Bioinformatics (Oxford, England) *31*, 2912-2914.

Waragai, M., Lammers, C.H., Takeuchi, S., Imafuku, I., Udagawa, Y.*, et al.* (1999). PQBP-1, a novel polyglutamine tract-binding protein, inhibits transcription activation by Brn-2 and affects cell survival. Human molecular genetics *8*, 977-987.

Warde-Farley, D., Donaldson, S.L., Comes, O., Zuberi, K., Badrawi, R.*, et al.* (2010). The GeneMANIA prediction server: biological network integration for gene prioritization and predicting gene function. Nucleic Acids Research *38*, W214-W220.

Tomsig, J.L., Snyder, S.L., and Creutz, C.E. (2003). Identification of targets for calcium signaling through the copine family of proteins. Characterization of a coiled-coil copine-binding motif. The Journal of biological chemistry *278*, 10048-10054.

Tomsig, J.L., Sohma, H., and Creutz, C.E. (2004). Calcium-dependent regulation of tumour necrosis factor-alpha receptor signalling by copine. Biochem J *378*, 1089-1094.

Uchida, O., Nakano, H., Koga, M., and Ohshima, Y. (2003). The C. elegans che-1 gene encodes a zinc finger transcription factor required for specification of the ASE chemosensory neurons. Development *130*, 1215.

van der Bliek, A.M., Shen, Q., and Kawajiri, S. (2013). Mechanisms of Mitochondrial Fission and Fusion. Cold Spring Harbor Perspectives in Biology *5*.

Van Raamsdonk, J.M., Meng, Y., Camp, D., Yang, W., Jia, X.*, et al.* (2010). Decreased Energy Metabolism Extends Life Span in Caenorhabditis elegans Without Reducing Oxidative Damage. Genetics *185*, 559-571.

Vance, J.E. (1998). Eukaryotic lipid-biosynthetic enzymes: the same but not the same. Trends in biochemical sciences *23*, 423-428.

Venkatesan, K., McManus, H.R., Mello, C.C., Smith, T.F., and Hansen, U. (2003). Functional conservation between members of an ancient duplicated transcription factor family, LSF/Grainyhead. Nucleic Acids Research *31*, 4304-4316.

Walker, A.K., Rothman, J.H., Shi, Y., and Blackwell, T.K. (2001). Distinct requirements for C.elegans TAFII in early embryonic transcription. The EMBO journal *20*, 5269-5279.

Walker, A.K., Shi, Y., and Blackwell, T.K. (2004). An Extensive Requirement for Transcription Factor IID-specific TAF-1 in Caenorhabditis elegans Embryonic Transcription. Journal of Biological Chemistry *279*, 15339-15347.

Walter, W., Sánchez-Cabo, F., and Ricote, M. (2015). GOplot: an R package for visually combining expression data with functional analysis. Bioinformatics (Oxford, England) *31*, 2912-2914.

Waragai, M., Lammers, C.H., Takeuchi, S., Imafuku, I., Udagawa, Y.*, et al.* (1999). PQBP-1, a novel polyglutamine tract-binding protein, inhibits transcription activation by Brn-2 and affects cell survival. Human molecular genetics *8*, 977-987.

Warde-Farley, D., Donaldson, S.L., Comes, O., Zuberi, K., Badrawi, R.*, et al.* (2010). The GeneMANIA prediction server: biological network integration for gene prioritization and predicting gene function. Nucleic Acids Research *38*, W214-W220.

Yoneda, T., Benedetti, C., Urano, F., Clark, S.G., Harding, H.P.*, et al.* (2004). Compartment-specific perturbation of protein handling activates genes encoding mitochondrial chaperones. Journal of cell science *117*, 4055-4066.

Youle, R.J., and van der Bliek, A.M. (2012). Mitochondrial fission, fusion, and stress. Science (New York, NY) *337*, 1062-1065.

Zhang, Q., Wu, X., Chen, P., Liu, L., Xin, N.*, et al.* (2018). The Mitochondrial Unfolded Protein Response Is Mediated Cell-Non-autonomously by Retromer-Dependent Wnt Signaling. Cell *174*, 870-883.e817.

Zhang, Y., Liu, X., Bai, J., Tian, X., Zhao, X.*, et al.* (2016). Mitoguardin Regulates Mitochondrial Fusion through MitoPLD and Is Required for Neuronal Homeostasis. Molecular cell *61*, 111-124.

Zubovych, I.O., Straud, S., Roth, M.G., and Newmeyer, D.D. (2010). Mitochondrial Dysfunction Confers Resistance to Multiple Drugs in *Caenorhabditis elegans*. Molecular Biology of the Cell *21*, 956-969.

Chapter II

Compromised mitochondrial protein import acts as a signal for UPR^{mt}

Stéphane G. Rolland, Sandra Schneid, Melanie Schwarz, Elisabeth Rackles, Christian Fischer, Simon Haeussler, Saroj G. Regmi, Assa Yeroslaviz, Bianca Habermann, Dejana Mokranjac, Eric Lambie and Barbara Conradt

Published: August 13, 2019. Cell Reports 28(7): https://doi.org/10.1016/j.celrep.2019.07.049

Cell Reports
Report

OPEN ACCESS
CellPress

Compromised Mitochondrial Protein Import Acts as a Signal for UPR^{mt}

Stéphane G. Rolland,[1,*] Sandra Schneid,[1] Melanie Schwarz,[1] Elisabeth Rackles,[1] Christian Fischer,[1,2] Simon Haeussler,[1] Saroj G. Regmi,[1,6] Assa Yeroslaviz,[3] Bianca Habermann,[3,5] Dejana Mokranjac,[4] Eric Lambie,[1,7] and Barbara Conradt[1,2,7,8,*]

[1]Faculty of Biology, LMU Munich, 82152 Planegg-Martinsried, Germany
[2]Center for Integrated Protein Science, LMU Munich, 82152 Planegg-Martinsried, Germany
[3]Max Planck Institute of Biochemistry, Computational Systems Biochemistry, Am Klopferspitz 18, 82152 Martinsried, Germany
[4]Biomedical Center Munich – Physiological Chemistry, LMU Munich, 82152 Planegg-Martinsried, Germany
[5]Present address: Aix-Marseille University, CNRS, IBDM UMR 7288, 13009 Marseille, France
[6]Present address: Division of Molecular and Cellular Biology, National Institute of Child Health and Human Development, NIH, Bethesda, MD 20892, USA
[7]Present address: Department of Cell and Developmental Biology, University College London, London, UK
[8]Lead Contact
*Correspondence: rolland@bio.lmu.de (S.G.R.), b.conradt@ucl.ac.uk (B.C.)
https://doi.org/10.1016/j.celrep.2019.07.049

SUMMARY

The induction of the mitochondrial unfolded protein response (UPR^{mt}) results in increased transcription of the gene encoding the mitochondrial chaperone HSP70. We systematically screened the *C. elegans* genome and identified 171 genes that, when knocked down, induce the expression of an *hsp-6* HSP70 reporter and encode mitochondrial proteins. These genes represent many, but not all, mitochondrial processes (e.g., mitochondrial calcium homeostasis and mitophagy are not represented). Knockdown of these genes leads to reduced mitochondrial membrane potential and, hence, decreased protein import into mitochondria. In addition, it induces UPR^{mt} in a manner that is dependent on ATFS-1 but that is not antagonized by the kinase GCN-2. We propose that compromised mitochondrial protein import signals the induction of UPR^{mt} and that the mitochondrial targeting sequence of ATFS-1 functions as a sensor for this signal.

INTRODUCTION

Ensuring that proteins acquire and maintain their proper conformation is essential, as unfolded or misfolded proteins are inactive and can form toxic aggregates that lead to disease (Macario et al., 2005). Protein quality control occurs at all times but can be upregulated via the "unfolded protein response" (UPR). UPR occurs in multiple cellular compartments, allowing localized responses to specific stresses (Gardner et al., 2013; Jovaisaite et al., 2014; Vabulas et al., 2010).

Mitochondrial UPR (UPR^{mt}) has been best characterized in the nematode *Caenorhabditis elegans*. The UPR^{mt} transcription factor ATFS-1 contains both mitochondrial and nuclear localization sequences (Nargund et al., 2012). In the absence of mitochondrial stress, ATFS-1 is imported into mitochondria and degraded by the mitochondrial protease LONP-1 (Nargund et al., 2012). Under stress conditions, unfolded proteins in the mitochondrial matrix have been proposed to be cleaved into peptides by the protease CLPP-1 (Haynes et al., 2007, 2010). Peptides generated are thought to be exported across the inner mitochondrial membrane (IMM) by the ABC transporter HAF-1 (Haynes et al., 2010). The release of peptides through HAF-1 has been proposed to block mitochondrial import by an unknown mechanism, resulting in the relocalization of ATFS-1 to the nucleus, where it activates the transcription of genes encoding mitochondrial chaperones and proteases (Haynes et al., 2010; Nargund et al., 2012). This pathway is at least partially conserved in mammals (Fiorese et al., 2016; Yano, 2017). An additional pathway has been described in *C. elegans*, which involves the cytoplasmic kinase GCN-2 (Baker et al., 2012). GCN-2 has been proposed to be activated by ROS generated by dysfunctional mitochondria. Once activated, GCN-2 phosphorylates the translation initiation factor eIF2α, thereby blocking general cytosolic translation, which has been proposed to help regain mitochondrial proteostasis by reducing the protein folding load of mitochondrial chaperones (Baker et al., 2012). Hence, the induction of UPR^{mt} is antagonized by the kinase GCN-2.

In *C. elegans*, UPR^{mt} can be induced by different types of stress, such as the knockdown of nuclear genes encoding subunits of the electron transport chain (ETC) (Durieux et al., 2011) or a block in mitochondrial translation (Houtkooper et al., 2013). These perturbations alter the stoichiometry between mitochondria- and nuclear-encoded ETC subunits ("mito-nuclear imbalance"), leading to the accumulation of unassembled subunits of ETC complexes and causing unfolded protein stress (Houtkooper et al., 2013). This stress has been proposed to trigger UPR^{mt} (Yoneda et al., 2004), but the mechanism through which this signal is transduced to the nucleus remains unclear.

To systematically identify genes and processes that trigger UPR^{mt} when compromised, we performed a genome-wide RNAi screen in *C. elegans*. We found that impairment of most,

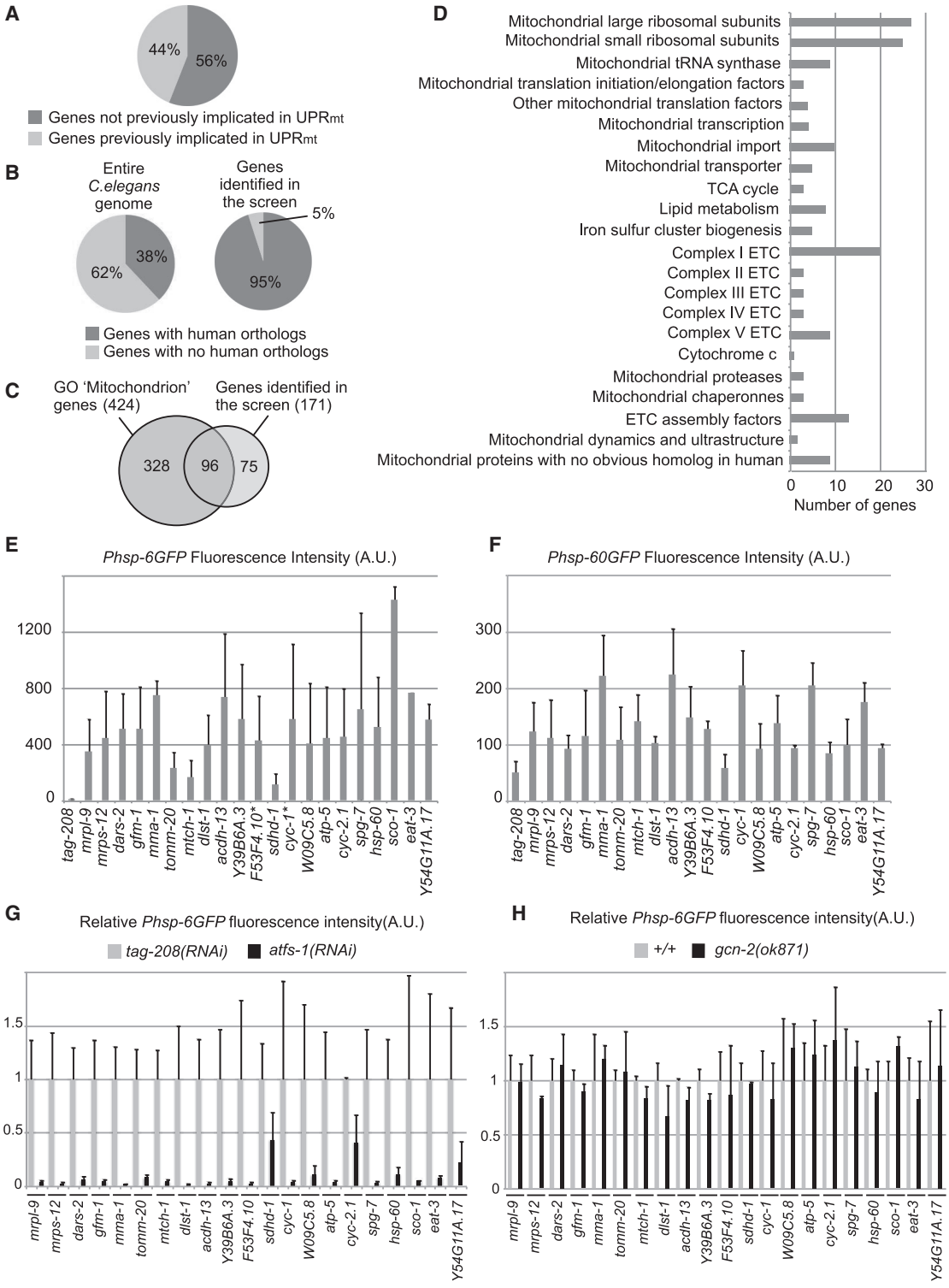

Figure 1. Genome-wide RNAi Screen Identifies Genes Required for the Maintenance of Mitochondrial Homeostasis

(A) Percentage of genes identified in our screen previously implicated or not in UPR^{mt}.

(B) Percentage of genes in the entire genome (Shaye and Greenwald, 2011) or among the genes identified in our screen with human orthologs.

(C) Overlap between genes of the GO "mitochondrion" and genes identified in our screen.

(D) The 171 candidates identified were grouped into 22 mitochondrial processes.

(legend continued on next page)

but not all, mitochondrial processes triggers UPR^{mt} that is dependent on ATFS-1 but not antagonized by GCN-2. Interestingly, some of these mitochondrial processes are not predicted to directly cause a mito-nuclear imbalance when blocked. Instead, they are predicted to cause a decrease in mitochondrial membrane potential. Therefore, we propose that a decrease in mitochondrial membrane potential acts as a signal that triggers UPR^{mt}. Furthermore, we propose that the mitochondrial targeting sequence (MTS) of ATFS-1 acts as a sensor for changes in mitochondrial membrane potential. Consistent with this model, we demonstrate that the "weak" MTS of ATFS-1 is essential for its ability to sense a decrease in mitochondrial membrane potential and to activate UPR^{mt}.

RESULTS

Genome-wide RNAi Screen for Genes that Induce UPR^{mt} When Knocked Down

To systematically identify *C. elegans* genes that induce UPR^{mt} when knocked down, we performed a genome-wide RNAi screen covering ≥90% of annotated *C. elegans* genes (Kamath and Ahringer, 2003). UPR^{mt} induction was monitored with a *hsp-6* HSP70 transcriptional reporter (P$_{hsp-6}$*GFP*) (Yoneda et al., 2004). We identified 198 "inducer" genes that reproducibly cause the upregulation of the P$_{hsp-6}$*GFP* reporter when knocked down. Among these, 171 encode proteins that have been shown to localize to mitochondria or are predicted to do so (Table S1A). We refer to this subset as the "mitochondrial inducers" and have focused our analyses on this group of genes.

The mitochondrial inducers encode proteins that represent each of the four major mitochondrial sub-compartments. Most of these genes have human orthologs (95%) and have not previously been identified as affecting UPR^{mt} (56%) (Bennett et al., 2014; Runkel et al., 2013) (Figures 1A and 1B). The inducers include 96 of the 424 genes in the Gene Ontology (GO) category "mitochondrion" (Figure 1C). Although the remaining 75 genes do not belong to this GO category, they encode proteins that have been shown, or are predicted, to localize to mitochondria. Concerning the remaining 328 genes that belong to the GO category "mitochondrion" and that we did not identify, we cannot exclude that we missed some because of RNAi efficiency. However, as shown below, compromising certain mitochondrial processes does not induce UPR^{mt}. In order to assess the specific nature and diversity of processes affected by the mitochondrial inducers, we analyzed all 57 sub-GO groups included in the GO category "mitochondrion." We found that the genes we identified are associated with 44 of these sub-GO groups and that 5 of these sub-GO groups were not previously identified as inducing UPR^{mt} when compromised (Table S1B).

Compromising Mitochondrial Ca^{2+} Homeostasis or Mitophagy Fails to Induce UPR^{mt}

The 13 sub-GO groups not represented by any of the 171 genes we identified include a total of 19 genes. We retested the 14 genes present in the RNAi library (Kamath and Ahringer, 2003) and identified two additional genes that induce P$_{hsp-6}$*GFP* expression when knocked down (Table S1C).

Mitochondrial Ca^{2+} homeostasis is one of the mitochondrial processes that did not induce UPR^{mt} when compromised. The sub-GO group "mitochondrial Ca^{2+} homeostasis" contains two genes: *mcu-1* and *emre-1*. In order to confirm our RNAi results, we analyzed animals carrying the *mcu-1* mutation *ju1154* (Xu and Chisholm, 2014) and showed that the loss of *mcu-1* does not induce the expression of the P$_{hsp-6}$*GFP* reporter, confirming that compromising mitochondrial Ca^{2+} homeostasis does not trigger UPR^{mt} (Figure S1A). Mitophagy (Pickrell and Youle, 2015) is another process that was not identified in our screen. Accumulation of misfolded proteins in the mitochondrial matrix of cultured mammalian cells has been shown to trigger PINK1- and Parkin-dependent mitophagy (Jin and Youle, 2013). We analyzed animals carrying a deletion in the *C. elegans* Parkin gene *pdr-1*, *lg103* (Springer et al., 2005) and animals carrying a deletion in the *C. elegans* PINK1 gene *pink-1*, *tm1779* (Sämann et al., 2009) and found that neither mutation induces the P$_{hsp-6}$*GFP* reporter (Figures S1B–S1E). In addition, the upregulation of the P$_{hsp-6}$*GFP* reporter by *spg-7(RNAi)* is not significantly affected by *pink-1(tm1779)* or *pdr-1(lg103)* (*spg-7* encodes the *C. elegans* homolog of the mitochondrial quality control protease AFG3L2). Finally, we did not observe any induction of the P$_{hsp-6}$*GFP* reporter upon the knockdown of the gene *dct-1*, which encodes the *C. elegans* BNIP3 homolog, thought to be required for mitophagy (Palikaras et al., 2015) (Table S1C). Thus, not all mitochondrial processes trigger UPR^{mt} activation when compromised.

UPR^{mt} Induced by Compromising Most Mitochondrial Processes Is Dependent on ATFS-1 but Is Not Antagonized by the Kinase GCN-2

We divided the 171 mitochondrial inducers into 22 groups on the basis of their roles in specific mitochondrial processes (Figure 1D). For most of the 22 groups, we selected one representative gene and quantified the induction of the P$_{hsp-6}$*GFP* reporter (Figure 1E). As a negative control, we knocked down *tag-208*, which encodes the *C. elegans* homolog of human Sorbin and does not induce UPR^{mt} when knocked down (Figures S1F and S1G). To confirm that the observed effects are not specific to *hsp-6* HSP70, we also quantified induction of a *hsp-60* HSP60 transcriptional reporter (P$_{hsp-60}$*GFP*) (Yoneda et al., 2004). With the exception of *sdhd-1*, knockdown of all genes caused P$_{hsp-60}$*GFP* upregulation (Figure 1F).

(E and F) Effect of the knockdown of one candidate for each mitochondrial process on the (E) P$_{hsp-6}$*GFP* and (F) P$_{hsp-60}$*GFP* reporters. Reporter expression was monitored by fluorescence microscopy and quantified (n = 2-3;mean and SD are shown; *RNAi was diluted with *tag-208(RNAi)*).

(G) Double RNAi with *tag-208(RNAi)* or *atfs-1(RNAi)*. Reporter expression was monitored by fluorescence microscopy and quantified (n = 2-3; mean and SD are shown).

(H) Knockdown was performed in wild-type (+/+) or a strain carrying *gcn-2(ok871)*. Reporter expression was monitored by fluorescence microscopy and quantified (n = 2–6; mean and SD are shown; *RNAi was diluted with *tag-208(RNAi)*).

In all panels, n is the number of biological replicates.

See also Table S1 and Figures S1 and S2.

Next, we tested whether UPR^{mt} induced by compromising the mitochondrial processes identified is dependent on the transcription factor ATFS-1 (Nargund et al., 2012). To that end, we performed double RNAi experiments with the representative genes and either *atfs-1*(*RNAi*) or, as a control, *tag-208*(*RNAi*). Double RNAi of any of the genes with *tag-208*(*RNAi*) induced the upregulation of the P$_{hsp-6}$*GFP* reporter (Figure 1G, gray bars). In contrast, double RNAi of any of the genes with *atfs-1*(*RNAi*) resulted in the complete suppression of the upregulation (black bars). We also tested whether the kinase GCN-2 plays a role in the induction of UPR^{mt} upon inactivation of the genes identified in our screen. To that end, we used a strain carrying the *gcn-2* loss-of-function mutation *ok871*. As shown in Figure 1H, for the genes tested, the upregulation of the P$_{hsp-6}$*GFP* reporter observed in wild-type animals (gray bars) was similar to that observed in *gcn-2(ok871)* mutant animals (black bars). We confirmed this result with an independent loss-of-function mutation *gcn-2*(*ok886)* (Figures S2A and S2B). In contrast, activation of the P$_{hsp-6}$*GFP* reporter by the loss-of-function mutation *clk-1(qm30)* (*clk-1* is required for ubiquinone synthesis) is enhanced by knockdown of *gcn-2* (Figure S2C), as published previously (Baker et al., 2012). Therefore, UPR^{mt} induced by compromising most mitochondrial processes is dependent on ATFS-1 but is not antagonized by the kinase GCN-2.

UPR^{mt} Is Triggered by Compromising Mitochondrial Processes that Are Required for the Maintenance of the Mito-nuclear Balance

The GO category ''mitochondrial translation'' is significantly enriched in our dataset (Table S1D). Among genes present in the RNAi library (Kamath and Ahringer, 2003), we identified 75% of the large subunits of the mitochondrial ribosome (*mrpl* genes) and ~96% of the small subunits of the mitochondrial ribosome (*mrps* genes). Furthermore, we also found nine genes encoding mitochondrial aminoacyl tRNA synthetases, and genes encoding mitochondrial translation initiation and elongation factors.

The GO category ''protein import into mitochondrial matrix'' is also significantly enriched in our dataset (Table S1D). We identified components of the TOM and TIM complexes (Figures 2A and 2B). (Some were previously identified as inducers of UPR^{mt}; Bennett et al., 2014; Runkel et al., 2014). We also confirmed that the knockdown of *timm-23*, which encodes the major subunit of the TIM23 complex, induces UPR^{mt}. We also identified *gop-3* and *tin-9.1*, which encode the homolog of the human SAMM50 protein, and the homolog of the small Tim protein Tim9, respectively (Figures 2A and 2B). Tim9 functions as a chaperone in the intermembrane space and assists beta-barrel proteins in reaching the SAM complex to be inserted into the outer mitochondrial membrane (OMM) (Wiedemann and Pfanner, 2017; Wiedemann et al., 2004). Tim9 also assists carrier proteins in reaching the TIM22 complex to be inserted into the IMM (Adam et al., 1999; Wiedemann and Pfanner, 2017). These two aspects of mitochondrial protein import were not previously identified as inducing UPR^{mt} when compromised.

Finally, we found that the knockdown of the nuclear-encoded subunits of complex I, III, IV, or V of the ETC also triggers UPR^{mt} and that several GO categories associated with ETC complexes are significantly enriched in our dataset. (Table S1D). Furthermore, we found that compromising assembly of complex I, III, or IV also leads to UPR^{mt} activation (e.g., by knockdown of *nuaf-1*, which encodes the homolog of the human complex I assembly factor NDUFAF1; *bcs-1*, which encodes the homolog of the human complex III assembly factor BCS1L; or *cox-14*, which encodes the homolog of the human complex IV assembly factor COX14; see Table S1).

The identification of mitochondrial translation, import and ETC as mitochondrial processes that when compromised induce UPR^{mt} is consistent with mito-nuclear imbalance and the resulting accumulation of unassembled subunits of ETC complexes being the signal that triggers UPR^{mt} (Houtkooper et al., 2013).

Mitochondrial Processes that Are Not Required for the Maintenance of the Mito-nuclear Balance Also Trigger UPR^{mt} When Compromised

We found that the knockdown of the cytochrome *c* gene *cyc-2.1* induces UPR^{mt}. The knockdown of *cyc-2.1* presumably causes a defect in the activity of the ETC; however, it is not predicted to directly cause mito-nuclear imbalance. In addition, we identified genes encoding subunits of complex II (*sdha-1*, *sdhd-1*, and *sdhc-1*). Although knockdown of these genes may cause an accumulation of other complex II subunits, it does not cause mito-nuclear imbalance, because all subunits of complex II are encoded in the nuclear genome. To test whether knockdown of any subunit of complex II induces UPR^{mt}, we individually knocked down the genes encoding all four subunits. As shown in Figures 2C and 2D, knockdown of any of these genes induces upregulation of the P$_{hsp-6}$*GFP* reporter. We also found that the level of endogenous HSP-6 protein but not HSP-60 protein significantly increases upon *sdhc-1(RNAi)* (Figure S3). Hence, compromising the ETC is sufficient to trigger UPR^{mt}.

The GO category ''tricarboxylic acid cycle'' is significantly enriched in our dataset (Table S1D). We identified several genes encoding subunits of enzymes of the tricarboxylic acid (TCA) cycle (Table S1A). Reduced levels of these proteins may lead to the disruption of the stoichiometry of their respective TCA complexes, thereby leading to the accumulation of unassembled proteins in the mitochondrial matrix. Alternatively, UPR^{mt} might also be triggered by the dysfunction of the TCA cycle itself. To test this hypothesis, we knocked down genes encoding the remaining enzymes of the TCA cycle. Knockdown of *aco-2*, *idha-1*, *cts-1*, *mdh-2*, and *fum-1* induce the P$_{hsp-6}$*GFP* reporter (Figure 3). We also found that the level of endogenous HSP-6 protein but not HSP-60 protein tends to slightly increase albeit not significantly upon *fum-1(RNAi)* (Figure S3) (It should be noted that because HSP-6 and HSP-60 are highly abundant proteins (Bensaddek et al., 2016), even small changes represent substantial changes in protein amounts. Furthermore, the basal expression level of P$_{hsp-6}$*GFP* is low in contrast to the high basal level of endogenous HSP-6 protein. Hence, the fold change of P$_{hsp-6}$*GFP* is likely an overestimation of the fold change of HSP-6. Finally, although tubulin is ubiquitously expressed, the UPR^{mt} transcriptional reporters are expressed mostly in intestinal cells. Hence, it is possible that UPR^{mt} is restricted to certain tissues. The HSP-6/tubulin or HSP-60/tubulin ratio might therefore underestimate the upregulation of HSP-6 or HSP-60 in the cells in which UPR^{mt} occurs. Such

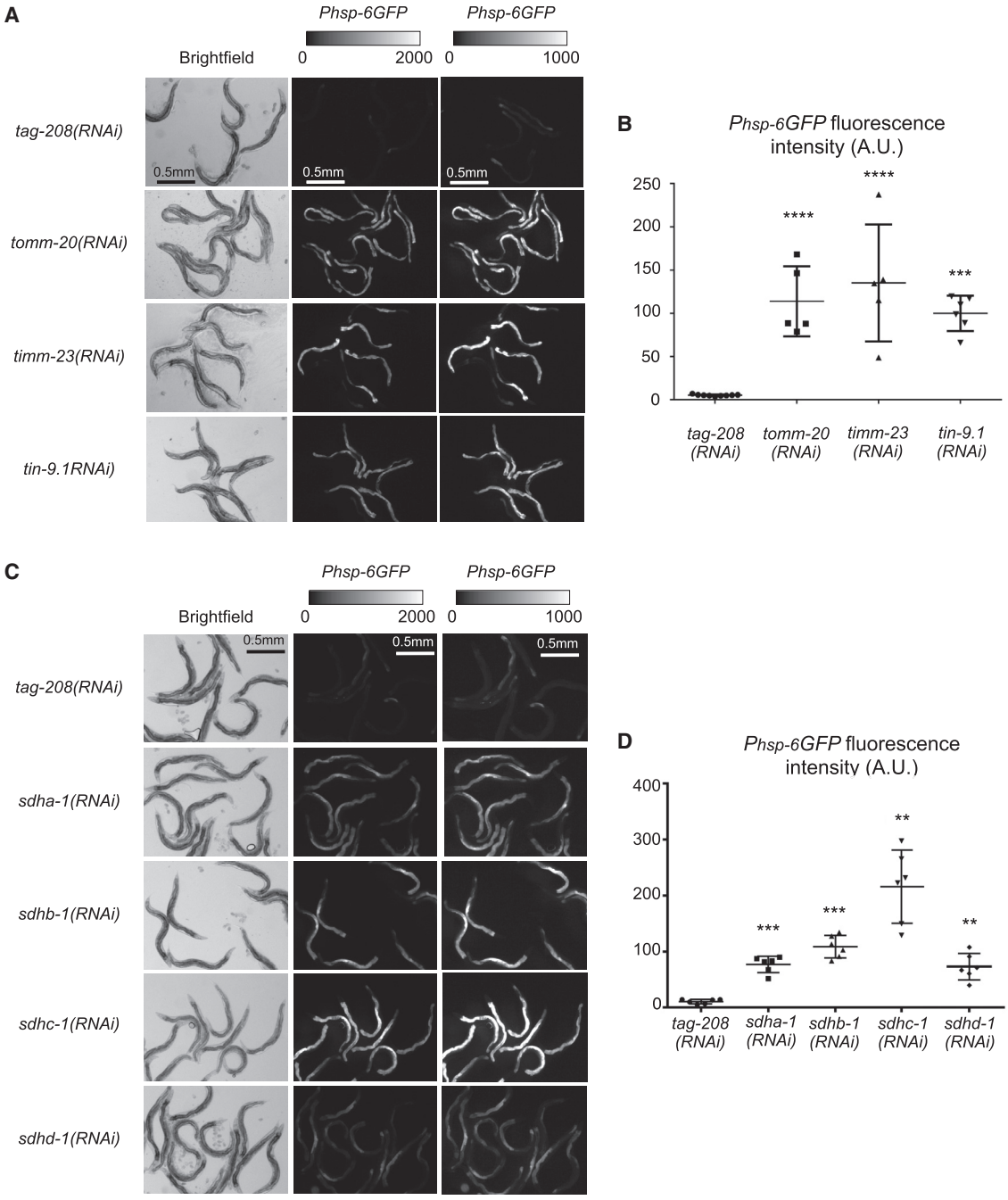

Figure 2. Knockdown of Mitochondrial Import Machinery or Complex II Induces UPR^{mt}

(A and C) Bright-field and fluorescence images of the P$_{hsp\text{-}6}$*GFP* reporter strain after different RNAi treatment to knock down the mitochondrial import machinery (A) or complex II subunits (C). Two intensity scales are shown.

(B and D) Quantification of P$_{hsp\text{-}6}$*GFP* fluorescence intensity (n ≥ 5; n is the number of biological replicates; mean and SD are shown; for B, ***p < 0.001 and ****p < 0.0001 by one-way ANOVA with Bonferroni's multiple-comparison test to *tag-208(RNAi)*; for D, **p < 0.01 and ***p < 0.001 by Welch's ANOVA with Games-Howell post hoc test to *tag-208(RNAi)*).

See also Figure S3.

an underestimation might affect HSP-60 more strongly than HSP-6, as *hsp-60* is less strongly transcriptionally upregulated upon mitochondrial stress than *hsp-6* (Haynes et al., 2007). Because CTS-1, FUM-1, and MDH-2 are homo-oligomeric enzymes, reduction in their levels will not cause proteotoxic stress. It will, however, cause a decrease in the activity of the TCA cycle. Hence, compromising the TCA cycle is sufficient to trigger UPR^{mt}.

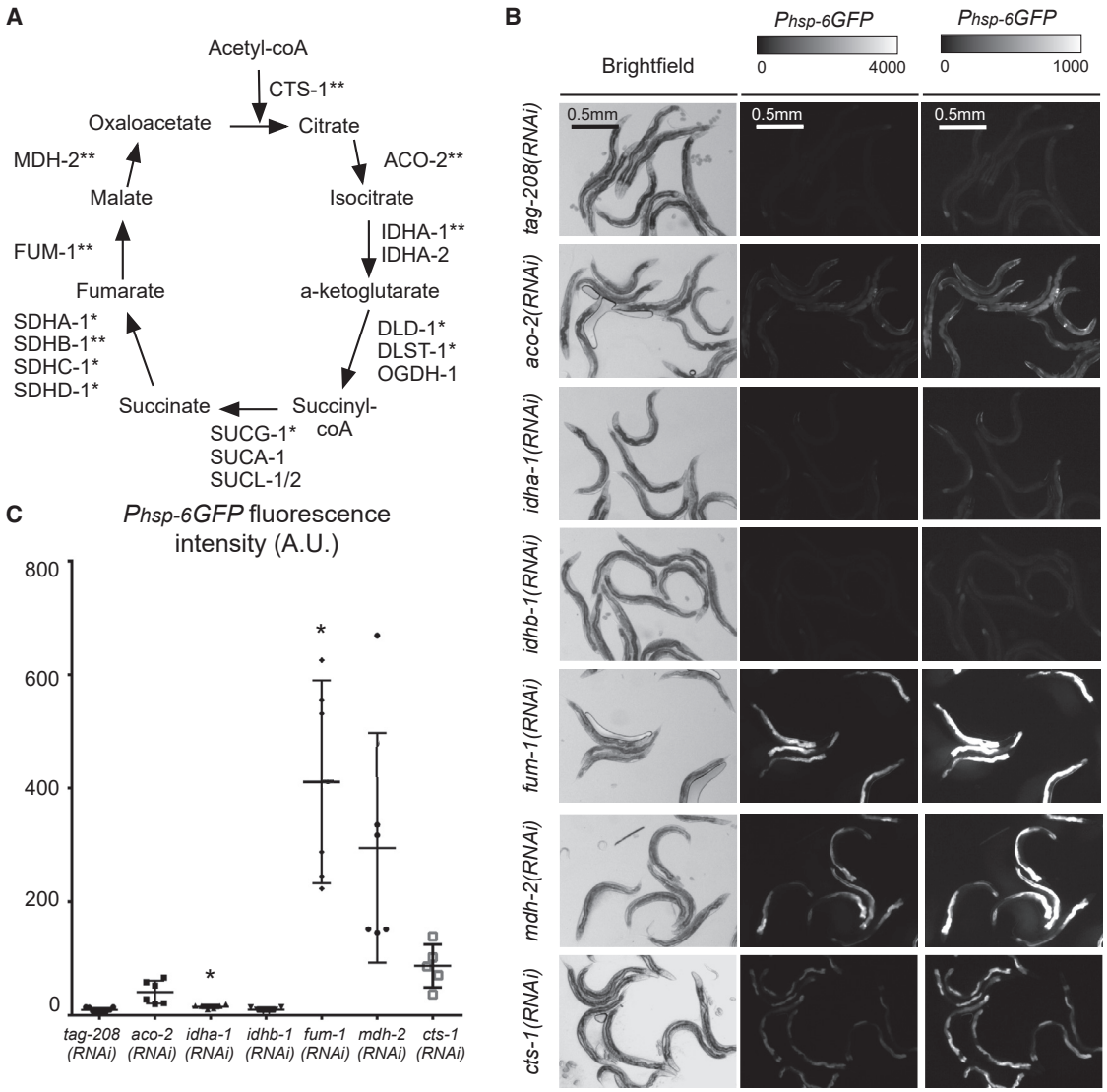

Figure 3. Knockdown of Any Enzyme of TCA Cycle Induces UPR^{mt}

(A) TCA cycle. Single and double asterisks indicate genes identified in our screen and subsequent experiments, respectively.

(B) Bright-field and fluorescence images of P$_{hsp-6}$*GFP* reporter strain after different RNAi treatment. Two intensity scales are shown.

(C) Quantification of P$_{hsp-6}$*GFP* fluorescence intensity (n ≥ 5; n is the number of biological replicates; mean and SD are shown; *p < 0.05 by Welch's ANOVA with Games-Howell post hoc test to *tag-208(RNAi)*).

See also Figures S3 and S4.

We also identified genes encoding proteins required for lipid catabolism (e.g., *ard-1*, *ech-6*, and *acdh-13* encode three mitochondrial beta-oxidation enzymes). The GO category "fatty acid biosynthetic process" is also enriched in our dataset (Table S1D). We identified two genes (*pgs-1* and *mdmh-35)* that encode proteins involved in cardiolipin (CL) biosynthesis, a lipid biosynthetic pathway that was not identified before as inducing UPR^{mt} when compromised. To confirm this result, we tested *crls-1*, which encodes CL synthase, and found that its knockdown induces the P$_{hsp-6}$*GFP* reporter expression (Figure S4). To test whether the biosynthesis of other lipids also induces UPR^{mt}, we tested *psd-1*, which encodes phosphatidylserine decarboxylase and plays a role in the biosynthesis of phosphatidylethanolamine (PE) (Osman et al., 2011). We found that knockdown of *psd-1* also induces P$_{hsp-6}$*GFP* reporter expression (Figure S4). Hence, compromising lipid metabolism triggers UPR^{mt}.

A Reduction in Mitochondrial Membrane Potential Correlates with the Induction of UPR^{mt}

Rather than directly causing mito-nuclear imbalance, the processes described above are predicted to cause a reduction in mitochondrial membrane potential. Although compromising the ETC directly causes a decrease in mitochondrial membrane potential, compromising the TCA cycle leads to a decrease in the

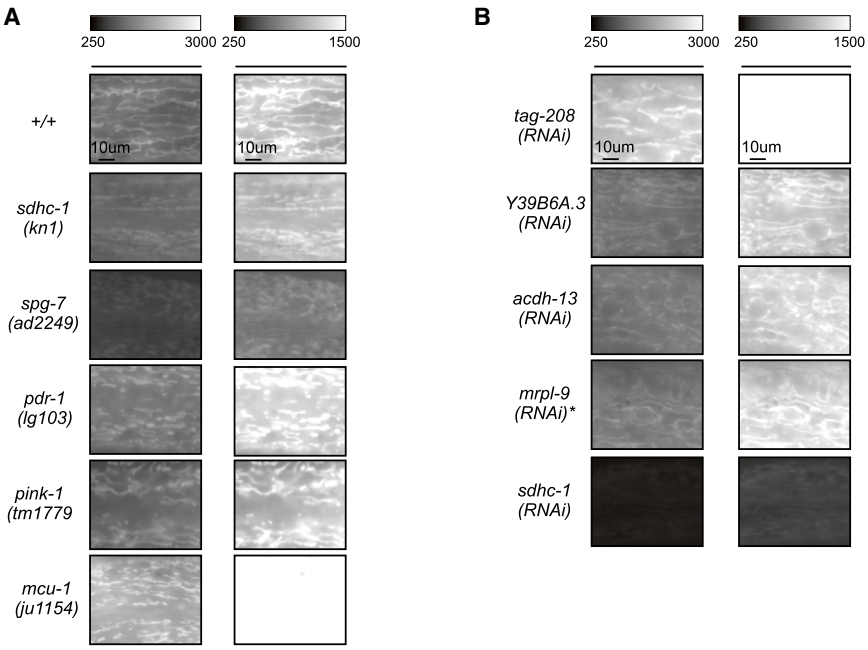

Figure 4. Genes that Induce UPR^{mt} When Knocked Down Are Required to Maintain Mitochondrial Membrane Potential

(A) Wild-type (+/+) or animals carrying different loss-of-function mutations were stained with TMRE. Representative images of mitochondria in hypodermal cells are shown with two intensity scales.

(B) Wild-type subjected to different RNAi (*mrpl-9(RNAi)* was diluted with *tag-208(RNAi)*) were stained with TMRE. Representative images of mitochondria in hypodermal cells are shown with two intensity scales.

(C and D) Quantification of TMRE fluorescence intensity per area (C, n ≥ 7; D, n ≥ 17; n is the number of animals analyzed; mean and SD are shown; *p < 0.05, ***p < 0.001, and ****p < 0.0001 by one-way ANOVA with Bonferroni's multiple-comparison test to *tag-208(RNAi)* or +/+; *sdhc-1(RNAi)* with data was not quantified, as the signal was too low to be detected by the segmentation macro; for *mcu-1(ju1154)* and *tag-208(RNAi)* the 250–1,500 intensity images are white because of saturation).

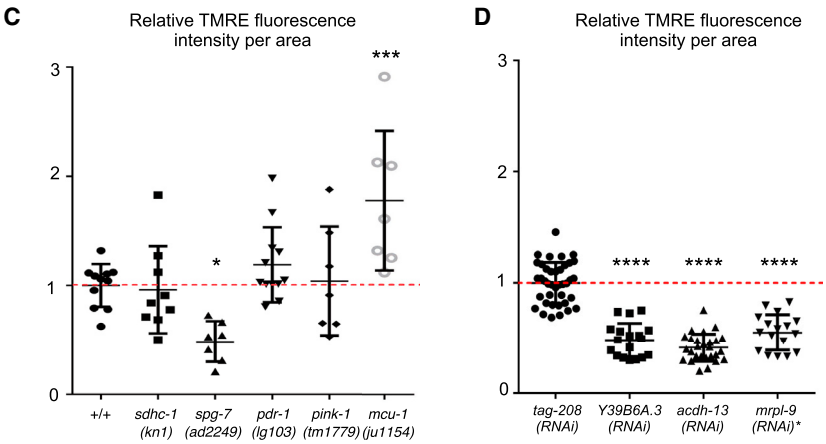

knocked down by mutation or RNAi and measured TMRE fluorescence intensity per area in mitochondria in hypodermal cells. We found that the knockdown of any of the genes tested results in a lower average mitochondrial TMRE fluorescence intensity. (Figure 4). The mitochondrial TMRE fluorescence intensity is proportional to mitochondrial membrane potential (Loew et al., 1993), indicating that the loss of genes that induce UPR^{mt} when knocked down results in a reduction in mitochondrial membrane potential. In contrast, animals carrying loss-of-function mutations in genes that do not induce UPR^{mt} when knocked down (such as *pdr-1(lg103)*, *pink-1(tm1779)*, or *mcu-1(ju1154)*), do not exhibit a lower average mitochondrial TMRE fluorescence intensity and therefore do not exhibit a reduction of mitochondrial membrane potential (Figure 4). Therefore, there is a correlation between a reduction in mitochondrial membrane potential and the induction of UPR^{mt}.

NADH level, resulting in a decrease in ETC function and, consequently, a reduction in mitochondrial membrane potential. Furthermore, compromising beta-oxidation causes a reduction in the level of acetyl-CoA entering the TCA cycle, indirectly causing a reduction in mitochondrial membrane potential. Finally, compromising CL biosynthesis has been shown to affect the formation of respiratory supercomplex in *S. cerevisiae* (Pfeiffer et al., 2003). Although this indirectly leads to proteotoxic stress, it also causes a reduction in mitochondrial membrane potential (Jiang et al., 2000). Finally, compromising PE biosynthesis in *S. cerevisiae* has been shown to cause a decrease in mitochondrial membrane potential (Böttinger et al., 2012).

To test whether genes that induce UPR^{mt} when knocked down are required to maintain mitochondrial membrane potential, using the mitochondrial potential-sensitive dye TMRE, we stained animals in which some of these genes had been

The MTS of ATFS-1 Acts as a Sensor for Mitochondrial Membrane Potential

Mitochondrial protein import is sensitive to mitochondrial membrane potential and depends on the net charge of the MTS (Martin et al., 1991). Mitochondrial proteins containing a MTS with a low net charge can only be imported into mitochondria with a high membrane potential. However, mitochondrial proteins containing a MTS with a high net charge can be imported even into mitochondria with a low membrane potential. The MTS of ATFS-1 has a lower net charge (+4) than that of

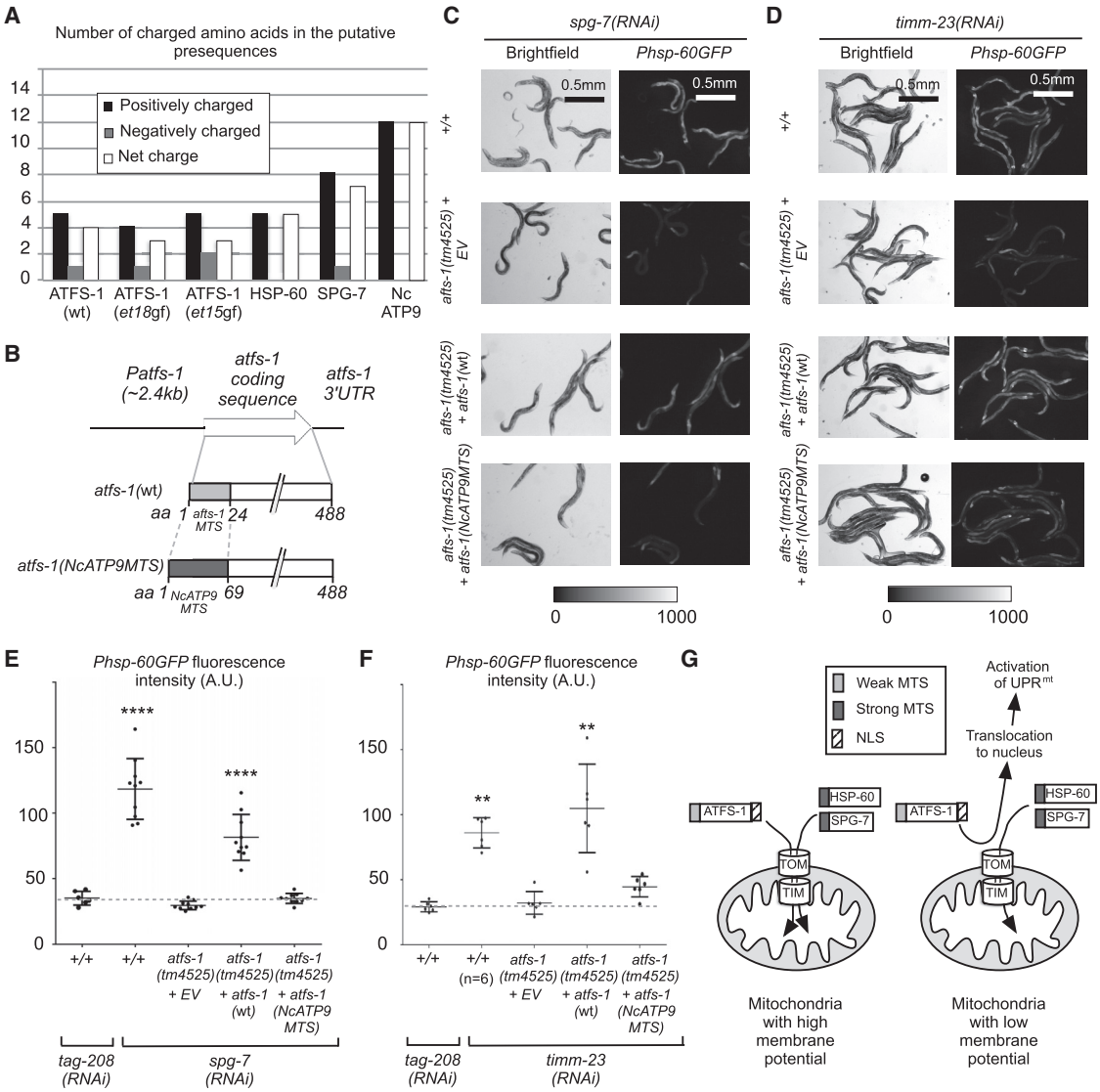

Figure 5. The Weak MTS of ATFS-1 Is Necessary for the Ability of ATFS-1 to Act as a Sensor of UPR^{mt}

(A) Analysis of the MTS of *C. elegans* ATFS-1(WT), ATFS-1(*et15*), ATFS-1(*et18*), HSP-60(WT), SPG-7(WT), and *N. crassa* ATP9.

(B) Schematic of the constructs. The MTS of ATFS-1 was replaced with the MTS of ATP synthase subunit 9 of *N. crassa* in the *atfs-1*(*NcATP9MTS*) construct.

(C) All strains carry the P$_{hsp-60}$*GFP* reporter. Wild-type (+/+) and *atfs-1*(*tm4525*) animals carrying the empty vector (EV), the *atfs-1*(WT) transgene, or the *atfs-1*(*NcATP9MTS*) transgene were treated with *spg-7*(*RNAi*) and analyzed by bright-field and fluorescence microscopy.

(D) Strains indicated in (C) were treated with *timm-23*(*RNAi*).

(E and F) Quantification of P$_{hsp-60}$*GFP* fluorescence intensity ($n \geq 6$; n = number of biological replicates; mean and SD are shown; for E, ****$p < 0.0001$ by Welch's ANOVA with Games-Howell post hoc test to +/+ with *tag-208(RNAi)*; for F, **$p < 0.01$ by Kruskal-Wallis with Dunn's multiple-comparisons test to +/+; *tag-208(RNAi)*).

(G) Model of activation of UPR^{mt}.

See also Figure S5.

HSP-60 (+5) or SPG-7 (+7) (Figure 5A). Animals carrying the *atfs-1* mutations *et15*gf or *et18*gf exhibit constitutive activation of UPR^{mt}. Interestingly, both mutations result in a reduction in the net charge of the MTS and presumably a reduction in mitochondrial import (Rauthan et al., 2013). Thus, we hypothesized that a decrease in mitochondrial membrane potential reduces the efficiency with which ATFS-1, but not HSP-60 or SPG-7, is imported into mitochondria.

To test this hypothesis we generated transgenic lines that express either a wild-type *atfs-1* rescuing construct (Figure 5B, *atfs-1*(WT) [wild-type]) or a rescuing construct encoding a modified ATFS-1 protein (ATFS-1(NcATP9MTS)), in which the N-terminal 24 amino acids have been replaced with the N-terminal 69 amino acids of the ATP synthase subunit 9 of *Neurospora crassa*, which is a strong MTS with a net charge of +12 (Figures 5A and 5B).

We found that the *atfs-1*(WT) transgene partially rescues the *atfs-1(tm4525)* phenotype, restoring induction of the P_{hsp-60}*GFP* reporter upon *spg-7*(*RNAi*) (Figures 5C and 5E). In contrast, we found that the *atfs-1(NcATP9MTS)* transgene fails to restore the induction of the P_{hsp-60}*GFP* reporter upon *spg-7(RNAi)*, although the levels of ATFS-1(NcATP9MTS) and ATFS-1(WT) proteins were similar (Figure S5). Hence, the ATFS-1(NcATP9MTS) protein is unable to activate UPR^{mt} in response to mitochondrial stress caused by *spg-7(RNAi).* We speculate that ATFS-1(NcATP9MTS) import is very efficient and not affected by a partial reduction in mitochondrial membrane potential caused by the loss of *spg-7* function. As a further test, we knocked down the gene *timm-23*, which compromises mitochondrial protein import directly. The strain carrying the *atfs-1*(WT) transgene fully restored the induction of the P_{hsp-60}*GFP* reporter upon *timm-23(RNAi)*. Furthermore, we observed a partial rescue of P_{hsp-60}*GFP* induction even in the strain carrying the *atfs-1*(*NcATP9MTS*) transgene (Figures 5D and 5F). Hence, in response to higher levels of mitochondrial stress (i.e., when mitochondrial import is directly compromised) ATFS-1(NcATP9MTS) is able to activate UPR^{mt}. Although this result supports our model, it also demonstrates that the ATFS-1(NcATP9MTS) protein is able to activate the transcriptional reporter and therefore is a functional transcription factor. On the basis of these findings, we propose that a reduction in mitochondrial membrane potential acts as a signal for the induction of UPR^{mt} and that the MTS of ATFS-1 acts as a sensor for this signal.

DISCUSSION

Similar to other UPRs, UPR^{mt} was proposed to be triggered by the accumulation of unfolded proteins (Yoneda et al., 2004). Although several lines of evidence are consistent with unfolded protein stress being the signal that triggers UPR^{mt} (Haynes et al., 2007, 2010; Houtkooper et al., 2013), it has so far only been shown in mammalian cells that a misfolded mitochondrial matrix protein can trigger it (Zhao et al., 2002). It has recently been noted that all perturbations known to induce UPR^{mt} are also likely to reduce mitochondrial import efficiency (Melber and Haynes, 2018). Therefore, it has been proposed that under these conditions, ATFS-1 relocalizes to the nucleus and activates UPR^{mt}. In order to better understand which signal triggers UPR^{mt}, we performed a genome-wide RNAi screen to systematically identify mitochondrial processes that induce UPR^{mt} when compromised.

Our results demonstrate that most mitochondrial processes trigger UPR^{mt} when compromised. Therefore, most mitochondrial processes are required for the maintenance of mitochondrial homeostasis. However, some processes, such as mitophagy, do not appear to be required. In addition, we found that a block in mitophagy has no effect on the induction of UPR^{mt}. Haynes and co-workers have proposed that UPR^{mt} is the first line of defense that can help mitochondria to regain homeostasis. If this line of defense fails, mitophagy is activated to eliminate irremediably damaged mitochondria (Pellegrino et al., 2013). Our data show that the converse is not the case (i.e., a block in mitophagy does not induce UPR^{mt}).

Our unbiased genome-wide approach confirms that blocking mitochondrial import leads to the activation of UPR^{mt}. Although the knockdown of components of the TOM or TIM23 complexes directly affects the import of ATFS-1, the effect of the knockdown of the small Tim protein Tim9 on ATFS-1 is likely indirect, because Tim9 is not involved in the import of mitochondrial matrix targeted protein. We also show that UPR^{mt} is induced in response to compromising mitochondrial processes (electron transport, TCA cycle, lipid catabolism, CL and PE biosynthesis) that are predicted to be required for the maintenance of mitochondrial membrane potential, but not for the maintenance of mito-nuclear balance. Furthermore, compromising any of the other mitochondrial processes that we identified in our screen is expected to at least indirectly reduce mitochondrial membrane potential. Although we cannot exclude that a decrease in mitochondrial ATP levels caused by a reduction in mitochondrial membrane potential participates in the activation of UPR^{mt} (because ATP is required for protein folding as well as mitochondrial import), we propose that a reduction in mitochondrial membrane potential is a general signal for the induction of UPR^{mt}. Consistent with this model, drugs known to cause a reduction in mitochondrial membrane potential (such as rotenone or antimycin) (Johnson et al., 1981) have been shown to induce UPR^{mt} (Liu et al., 2014; Runkel et al., 2013). Finally, it was shown that the induction of UPR^{mt} upon *spg-7(RNAi)* is partially dependent on the transporter HAF-1 (Haynes et al., 2010). Our model is still compatible with a role of HAF-1 in the UPR^{mt} pathway. We speculate that because peptides exported by HAF-1 are most likely charged, they may affect mitochondrial membrane potential when exported. Such peptides may also affect mitochondrial protein import as recently shown with isolated mammalian mitochondria *in vitro* (Oliveira and Hood, 2018).

Bioinformatic analysis revealed that the MTS of ATFS-1 is weaker than that of other mitochondrial proteins, such as HSP-60 or SPG-7. Furthermore, in contrast to HSP-60 and SPG-7, ATFS-1 additionally contains a C-terminal nuclear localization sequence (NLS). We propose that the combination of the NLS and the relative "weakness" of the MTS is essential for ATFS-1's function as a UPR^{mt} sensor. To test this, we generated a chimeric ATFS-1 protein containing a strong MTS and showed that this protein is unable to induce UPR^{mt} in response to lower levels of mitochondrial stress (i.e., *spg-7(RNAi)*) but is able to induce UPR^{mt} in response to higher levels of mitochondrial stress (i.e., *timm-23(RNAi)*). We speculate that this chimeric ATFS-1 protein is unable to act as a UPR^{mt} sensor in response to lower levels of mitochondrial stress because its import is very efficient and not affected by a decrease in mitochondrial membrane potential caused by *spg-7(RNAi)*. We propose a model in which defects in most mitochondrial processes lead to a decrease in mitochondrial membrane potential, which blocks the import of ATFS-1, thereby causing its relocalization to the nucleus. The effectors of UPR^{mt}, such as HSP-60 and SPG-7, can still be imported into these compromised mitochondria because their MTSs are stronger than that of ATFS-1 (Figure 5G). Consistent with this model, we demonstrated that UPR^{mt} induced by a defect in any of the mitochondrial processes identified in our screen is dependent on ATFS-1. In conclusion, we propose that

the predominant signal triggering UPR^{mt} is a decrease in mitochondrial membrane potential, which is sensed by the MTS of ATFS-1.

STAR★METHODS

Detailed methods are provided in the online version of this paper and include the following:

- KEY RESOURCES TABLE
- LEAD CONTACT AND MATERIALS AVAILABILITY
- EXPERIMENTAL MODEL AND SUBJECT DETAILS
  - *C. elegans* strains and culture conditions
  - Transgenic lines generation
- METHOD DETAILS
  - Genome wide RNA interference screen
  - Bioinformatic analysis
  - Further analysis of the candidates
  - Analysis of HSP-6 and HSP-60 protein levels
  - TMRE staining and quantification
- QUANTIFICATION AND STATISTICAL ANALYSIS
- DATA AND CODE AVAILABILITY

SUPPLEMENTAL INFORMATION

Supplemental Information can be found online at https://doi.org/10.1016/j.celrep.2019.07.049.

ACKNOWLEDGMENTS

We thank N. Memar, C. Osman, and members of the Conradt lab for comments on the manuscript. We thank N. Lebedeva and M. Bauer for excellent technical support; C. Haynes (UMass Medical School) for anti-ATFS-1 antibodies and the CMH5 strain; S. Mitani (National BioResource Project) for *atfs-1*(*tm4525*) and *pink-1*(*tm1779*); R. Baumeister (University of Freiburg) for *pdr-1*(*lg103*); and the Caenorhabditis Genetics Center (funded by NIH Office of Research Infrastructure Programs [P40 OD010440]) for strains. This work was supported by Deutsche Forschungsgemeinschaft (Center for Integrated Protein Science Munich [CIPSM; EXC 114]; CO204/6-1 and CO204/9-1 to B.C.; MO1944/1-2 and MO1944/2-1 to D.M.; LA3380/2-1 to E.L.; and RO5352/1-1 to S.G. Rolland).

AUTHOR CONTRIBUTIONS

S.G. Rolland designed and conducted the experiments and wrote the paper. B.C. and E.L. designed the experiments and wrote the paper. B.H. and D.M. designed the experiments. S.S., M.S., E.R., C.F., S.H., S.G. Regmi, and A.Y. conducted the experiments and generated reagents.

DECLARATION OF INTERESTS

The authors declare no competing interests.

Received: June 26, 2018
Revised: March 22, 2019
Accepted: July 16, 2019
Published: August 13, 2019

REFERENCES

Adam, A., Endres, M., Sirrenberg, C., Lottspeich, F., Neupert, W., and Brunner, M. (1999). Tim9, a new component of the TIM22.54 translocase in mitochondria. EMBO J. *18*, 313–319.

Baker, B.M., Nargund, A.M., Sun, T., and Haynes, C.M. (2012). Protective coupling of mitochondrial function and protein synthesis via the eIF2α kinase GCN-2. PLoS Genet. *8*, e1002760.

Bennett, C.F., Vander Wende, H., Simko, M., Klum, S., Barfield, S., Choi, H., Pineda, V.V., and Kaeberlein, M. (2014). Activation of the mitochondrial unfolded protein response does not predict longevity in *Caenorhabditis elegans*. Nat. Commun. *5*, 3483.

Bensaddek, D., Narayan, V., Nicolas, A., Murillo, A.B., Gartner, A., Kenyon, C.J., and Lamond, A.I. (2016). Micro-proteomics with iterative data analysis: proteome analysis in *C. elegans* at the single worm level. Proteomics *16*, 381–392.

Böttinger, L., Horvath, S.E., Kleinschroth, T., Hunte, C., Daum, G., Pfanner, N., and Becker, T. (2012). Phosphatidylethanolamine and cardiolipin differentially affect the stability of mitochondrial respiratory chain supercomplexes. J. Mol. Biol. *423*, 677–686.

Brenner, S. (1974). The genetics of *Caenorhabditis elegans*. Genetics *77*, 71–94.

Claros, M.G., and Vincens, P. (1996). Computational method to predict mitochondrially imported proteins and their targeting sequences. Eur. J. Biochem. *241*, 779–786.

Durieux, J., Wolff, S., and Dillin, A. (2011). The cell-non-autonomous nature of electron transport chain-mediated longevity. Cell *144*, 79–91.

Fiorese, C.J., Schulz, A.M., Lin, Y.F., Rosin, N., Pellegrino, M.W., and Haynes, C.M. (2016). The transcription factor ATF5 mediates a mammalian mitochondrial UPR. Curr. Biol. *26*, 2037–2043.

Gardner, B.M., Pincus, D., Gotthardt, K., Gallagher, C.M., and Walter, P. (2013). Endoplasmic reticulum stress sensing in the unfolded protein response. Cold Spring Harb. Perspect. Biol. *5*, a013169.

Hadwiger, G., Dour, S., Arur, S., Fox, P., and Nonet, M.L. (2010). A monoclonal antibody toolkit for *C. elegans*. PLoS ONE *5*, e10161.

Haynes, C.M., Petrova, K., Benedetti, C., Yang, Y., and Ron, D. (2007). ClpP mediates activation of a mitochondrial unfolded protein response in *C. elegans*. Dev. Cell *13*, 467–480.

Haynes, C.M., Yang, Y., Blais, S.P., Neubert, T.A., and Ron, D. (2010). The matrix peptide exporter HAF-1 signals a mitochondrial UPR by activating the transcription factor ZC376.7 in *C. elegans*. Mol. Cell *37*, 529–540.

Honda, S., Ishii, N., Suzuki, K., and Matsuo, M. (1993). Oxygen-dependent perturbation of life span and aging rate in the nematode. J. Gerontol. *48*, B57–B61.

Houtkooper, R.H., Mouchiroud, L., Ryu, D., Moullan, N., Katsyuba, E., Knott, G., Williams, R.W., and Auwerx, J. (2013). Mitonuclear protein imbalance as a conserved longevity mechanism. Nature *497*, 451–457.

Huang, W., Sherman, B.T., and Lempicki, R.A. (2009). Systematic and integrative analysis of large gene lists using DAVID bioinformatics resources. Nat. Protoc. *4*, 44–57.

Jiang, F., Ryan, M.T., Schlame, M., Zhao, M., Gu, Z., Klingenberg, M., Pfanner, N., and Greenberg, M.L. (2000). Absence of cardiolipin in the crd1 null mutant results in decreased mitochondrial membrane potential and reduced mitochondrial function. J. Biol. Chem. *275*, 22387–22394.

Jin, S.M., and Youle, R.J. (2013). The accumulation of misfolded proteins in the mitochondrial matrix is sensed by PINK1 to induce PARK2/Parkin-mediated mitophagy of polarized mitochondria. Autophagy *9*, 1750–1757.

Johnson, L.V., Walsh, M.L., Bockus, B.J., and Chen, L.B. (1981). Monitoring of relative mitochondrial membrane potential in living cells by fluorescence microscopy. J. Cell Biol. *88*, 526–535.

Jovaisaite, V., Mouchiroud, L., and Auwerx, J. (2014). The mitochondrial unfolded protein response, a conserved stress response pathway with implications in health and disease. J. Exp. Biol. *217*, 137–143.

Kamath, R.S., and Ahringer, J. (2003). Genome-wide RNAi screening in *Caenorhabditis elegans*. Methods *30*, 313–321.

Köhler, F., Müller-Rischart, A.K., Conradt, B., and Rolland, S.G. (2015). The loss of LRPPRC function induces the mitochondrial unfolded protein response. Aging (Albany N.Y.) *7*, 701–717.

Liu, Y., Samuel, B.S., Breen, P.C., and Ruvkun, G. (2014). *Caenorhabditis elegans* pathways that surveil and defend mitochondria. Nature *508*, 406–410.

Loew, L.M., Tuft, R.A., Carrington, W., and Fay, F.S. (1993). Imaging in five dimensions: time-dependent membrane potentials in individual mitochondria. Biophys. J. *65*, 2396–2407.

Macario, A.J., Grippo, T.M., and Conway de Macario, E. (2005). Genetic disorders involving molecular-chaperone genes: a perspective. Genet. Med. *7*, 3–12.

Martin, J., Mahlke, K., and Pfanner, N. (1991). Role of an energized inner membrane in mitochondrial protein import. Delta psi drives the movement of presequences. J. Biol. Chem. *266*, 18051–18057.

Melber, A., and Haynes, C.M. (2018). UPR^{mt} regulation and output: a stress response mediated by mitochondrial-nuclear communication. Cell Res. *28*, 281–295.

Nargund, A.M., Pellegrino, M.W., Fiorese, C.J., Baker, B.M., and Haynes, C.M. (2012). Mitochondrial import efficiency of ATFS-1 regulates mitochondrial UPR activation. Science *337*, 587–590.

Oliveira, A.N., and Hood, D.A. (2018). Effect of Tim23 knockdown in vivo on mitochondrial protein import and retrograde signaling to the UPR^{mt} in muscle. Am. J. Physiol. Cell Physiol. *315*, C516–C526.

Osman, C., Voelker, D.R., and Langer, T. (2011). Making heads or tails of phospholipids in mitochondria. J. Cell Biol. *192*, 7–16.

Palikaras, K., Lionaki, E., and Tavernarakis, N. (2015). Coordination of mitophagy and mitochondrial biogenesis during ageing in *C. elegans*. Nature *521*, 525–528.

Pellegrino, M.W., Nargund, A.M., and Haynes, C.M. (2013). Signaling the mitochondrial unfolded protein response. Biochim. Biophys. Acta *1833*, 410–416.

Peters, G.-J. (2018). userfriendlyscience: Quantitative analysis made accessible.https://cran.r-project.org/web/packages/userfriendlyscience/index.html.

Pfeiffer, K., Gohil, V., Stuart, R.A., Hunte, C., Brandt, U., Greenberg, M.L., and Schägger, H. (2003). Cardiolipin stabilizes respiratory chain supercomplexes. J. Biol. Chem. *278*, 52873–52880.

Pickrell, A.M., and Youle, R.J. (2015). The roles of PINK1, parkin, and mitochondrial fidelity in Parkinson's disease. Neuron *85*, 257–273.

Rauthan, M., Ranji, P., Aguilera Pradenas, N., Pitot, C., and Pilon, M. (2013). The mitochondrial unfolded protein response activator ATFS-1 protects cells from inhibition of the mevalonate pathway. Proc. Natl. Acad. Sci. U S A *110*, 5981–5986.

Riddle, D.L., Blumenthal, T., Meyer, B.J., and Priess, J.R. (1997). Introduction to *C. elegans*. In *C elegans* II, D.L. Riddle, T. Blumenthal, B.J. Meyer, and J.R. Priess, eds. (Cold Spring Harbor Laboratory Press).

RStudio Team (2015). RStudio: Integrated Development for R (RStudio).

Runkel, E.D., Liu, S., Baumeister, R., and Schulze, E. (2013). Surveillance-activated defenses block the ROS-induced mitochondrial unfolded protein response. PLoS Genet. *9*, e1003346.

Runkel, E.D., Baumeister, R., and Schulze, E. (2014). Mitochondrial stress: balancing friend and foe. Exp. Gerontol. *56*, 194–201.

Sämann, J., Hegermann, J., von Gromoff, E., Eimer, S., Baumeister, R., and Schmidt, E. (2009). *Caenorhabditits elegans* LRK-1 and PINK-1 act antagonistically in stress response and neurite outgrowth. J. Biol. Chem. *284*, 16482–16491.

Sato, Y., Nakajima, S., Shiraga, N., Atsumi, H., Yoshida, S., Koller, T., Gerig, G., and Kikinis, R. (1998). Three-dimensional multi-scale line filter for segmentation and visualization of curvilinear structures in medical images. Med. Image Anal. *2*, 143–168.

Schindelin, J. (2012). Fiji: an open-source platform for biological-image analysis. Nat. Methods *9*, 676–682.

Shaye, D.D., and Greenwald, I. (2011). OrthoList: a compendium of *C. elegans* genes with human orthologs. PLoS ONE *6*, e20085.

Springer, W., Hoppe, T., Schmidt, E., and Baumeister, R. (2005). A *Caenorhabditis elegans* Parkin mutant with altered solubility couples alpha-synuclein aggregation to proteotoxic stress. Hum. Mol. Genet. *14*, 3407–3423.

Sternberg, S.R. (1983). Biomedical image processing. Computer *16*, 22–34.

Stiernagle, T. (2006). Maintenance of C. elegans. In WormBook: The Online Review of C elegans Biology. http://www.wormbook.org/chapters/www_strainmaintain/strainmaintain.html.

Vabulas, R.M., Raychaudhuri, S., Hayer-Hartl, M., and Hartl, F.U. (2010). Protein folding in the cytoplasm and the heat shock response. Cold Spring Harb. Perspect. Biol. *2*, a004390.

Wiedemann, N., and Pfanner, N. (2017). Mitochondrial machineries for protein import and assembly. Annu. Rev. Biochem. *86*, 685–714.

Wiedemann, N., Truscott, K.N., Pfannschmidt, S., Guiard, B., Meisinger, C., and Pfanner, N. (2004). Biogenesis of the protein import channel Tom40 of the mitochondrial outer membrane: intermembrane space components are involved in an early stage of the assembly pathway. J. Biol. Chem. *279*, 18188–18194.

Xu, S., and Chisholm, A.D. (2014). *C. elegans* epidermal wounding induces a mitochondrial ROS burst that promotes wound repair. Dev. Cell *31*, 48–60.

Yano, M. (2017). ABCB10 depletion reduces unfolded protein response in mitochondria. Biochem. Biophys. Res. Commun. *486*, 465–469.

Yoneda, T., Benedetti, C., Urano, F., Clark, S.G., Harding, H.P., and Ron, D. (2004). Compartment-specific perturbation of protein handling activates genes encoding mitochondrial chaperones. J. Cell Sci. *117*, 4055–4066.

Zhao, Q., Wang, J., Levichkin, I.V., Stasinopoulos, S., Ryan, M.T., and Hoogenraad, N.J. (2002). A mitochondrial specific stress response in mammalian cells. EMBO J. *21*, 4411–4419.

Zubovych, I.O., Straud, S., and Roth, M.G. (2010). Mitochondrial dysfunction confers resistance to multiple drugs in *Caenorhabditis elegans*. Mol. Biol. Cell *21*, 956–969.

STAR★METHODS

KEY RESOURCES TABLE

REAGENT or RESOURCE	SOURCE	IDENTIFIER
Antibodies		
Rabbit anti-HSP-6	Köhler et al., 2015	N/A
Mouse anti-HSP-60	(Hadwiger et al., 2010) available at DHSB	HSP60 s
Rabbit anti-ATFS-1	Gift from C. Haynes (UMass Medical School)	N/A
Mouse anti-Tubulin DM1a	Sigma-Aldrich	Cat # T6199; RRID:AB_477583
Mouse anti-β-actin AC-15	Sigma-Aldrich	Cat # A-1978;RRID:AB_476692
Goat Anti-Mouse IgG (HL)-HRP Conjugate antibody	Biorad	Cat # 1706516;RRID:AB_11125547
Goat Anti-Rabbit IgG (HL)-HRP Conjugate antibody	Biorad	Cat # 1706515;RRID:AB_11125142
Bacterial and Virus Strains		
RNAi clones Ahringer library	Kamath and Ahringer, 2003	N/A
OP50	Caenorhabditis Genetics Center	OP50
HT115	Caenorhabditis Genetics Center	HT115
DH5α	ThermoFischer	Cat # 18265017
Chemicals, Peptides, and Recombinant Proteins		
IPTG	Carl-Roth	Cat # CN08.2
TMRE	ThermoFischer Scientific	Cat # T-669
Amersham ECL Western Blotting Detection Reagent	Sigma-Aldrich	Cat # GERPN2106
Amersham ECL prime Western Blotting Detection Reagent	Sigma-Aldrich	Cat # GERPN2236
Experimental Models: Organisms/Strains		
Wildtype C. elegans strain N2	Caenorhabditis Genetics Center	N2
TK22 (*sdhc-1(kn1) III*)	Caenorhabditis Genetics Center	TK22
DA2249 (*spg-7(ad2249) I*)	Caenorhabditis Genetics Center	DA2249
BR2430 (*pdr-1(lg103) III*)	Gift from R. Baumeister (University of Freiburg)	N/A
MD3399 (*pink-1(tm1779) II*)	This study	N/A
CZ19982 *(mcu-1(ju1154) IV)*	Caenorhabditis Genetics Center	CZ19982
SJ4100 (*zcIs13 V*)	Caenorhabditis Genetics Center	SJ4100
SJ4058 (*zcIs9*)	Caenorhabditis Genetics Center	SJ4058
MD3800 (*mcu-1(ju1154) IV; zcIs13 V*)	This study	N/A
MD4205 (*pink-1(tm1779) II; zcIs13 V*)	This study	N/A
MD4203 (*zcIs13 V*)	This study	N/A
MD4001 (*pdr-1(lg103) III; zcIs13 V*)	This study	N/A
MD4002 (*zcIs13 V*)	This study	N/A
MD4126 (*gcn-2(ok871) II; zcIs13 V*)	This study	N/A
MD4164 (*gcn-2(ok886) II; zcIs13 V*)	This study	N/A
MD4165 (*zcIs13* V)	This study	N/A
MD4284 (*oxTi179 II; unc-119(ed3) III; atfs-1(tm4525) V zcIs9 V*)	This study	N/A
MD4306 (*bcSi78* [*pCFJ350*] II; *unc-119*(*ed3*) III; *atfs-1* (*tm4525*) *zcIs9* V)	This study	N/A

(*Continued on next page*)

Continued

REAGENT or RESOURCE	SOURCE	IDENTIFIER
MD4314 (*bcSi80* [*pBC1753*] II; *unc-119*(*ed3*) III; *atfs-1* (*tm4525*) *zcIs9* V)	This study	N/A
MD4323 (*bcSi81* [*pBC1759*] II; *unc-119*(*ed3*) III; *atfs-1* (*tm4525*) *zcIs9* V)	This study	N/A
Oligonucleotides		
Forward primer to amplify *Patfs-1:atfs-1[CDS]:atfs-1 [3′UTR]* from gDNA *atfs-1FSpeI* 5′-ACTAGTTATCCC GATTCAAATCATTG-3′	This study	N/A
Reverse primer to amplify *Patfs-1:atfs-1[CDS]:atfs-1 [3′UTR]* from gDNA *atfs-1RAvrII* 5′-CCTAGGTTACAC AACTGCGTCACG-3′	This study	N/A
Primer for sequencing RNAi clones *L4440 F* 5′-TGGA TAACCGTATTACCGCC-3′	This study	N/A
Recombinant DNA		
pCFJ350 (empty MosSCI vector)	Addgene	Plasmid #34866
pBC1753 (*Patfs-1:atfs-1[CDS with afts-1MTS]: atfs-1[3′UTR])*	This study	N/A
pBC1759 (*Patfs-1:atfs-1[CDS with su9MTS]: atfs-1[3′UTR])*	This study	N/A
Software and Algorithms		
Fiji v. 2.0.0-rc-69/1.52i	Schindelin, 2012	https://imagej.net/Fiji/Downloads
Prism v. 6	GraphPad Software	https://www.graphpad.com/scientific-software/prism/
MitoProt	Claros and Vincens, 1996	https://ihg.gsf.de/ihg/mitoprot.html
Leica Application Suite v. 3.2.0.9652	Leica Microsystems	https://www.leica-microsystems.com/products/microscope-software/p/leica-application-suite/
Metamorph v. 7.1.0.0.	Molecular Device Corporation	https://www.moleculardevices.com/
David Database v. 6.8	Huang et al., 2009	https://david.ncifcrf.gov
Image Lab v. 5.2.1. build 11	Bio-Rad	http://www.bio-rad.com/de-de/product/image-lab-software
R Studio v. 1.1.423 with "userfriendlyscience" package	RStudio Team, 2015; Peters, 2018	https://www.rstudio.com

LEAD CONTACT AND MATERIALS AVAILABILITY

Further information and requests for resources and reagents should be directed to and will be fulfilled by the Lead Contact, Barbara Conradt (b.conradt@ucl.ac.uk).

All *C. elegans* strains and plasmids generated in this study are freely available upon request to the Lead Contact, Barbara Conradt (b.conradt@ucl.ac.uk).

EXPERIMENTAL MODEL AND SUBJECT DETAILS

C. elegans strains and culture conditions

C. elegans strains were cultured as previously described (Brenner, 1974). Bristol N2 was used as the wild-type strain. The screen was performed using the strain SJ4100, which carries the $P_{hsp\text{-}6}$*GFP* transcriptional reporter (Yoneda et al., 2004). Further experiments were performed using the strain SJ4058, which carries the mitochondrial chaperone *hsp-60* transcriptional reporter ($P_{hsp\text{-}60}$*GFP*) (Yoneda et al., 2004). Mutations used in this study were described by Riddle et al. (1997) except: (LG I) *spg-7*(*ad2249*) (Zubovych et al., 2010) (LG II) *gcn-2*(*ok871*) and *gcn-2*(*ok886)* (OMRF Knockout Group), *pink-1*(*tm1779*) (National BioResource Project), (LGIII) *pdr-1*(*lg103*) (Springer et al., 2005) and *mev-1*(*kn1*) (Honda et al., 1993), (LGIV) *mcu-1*(*ju1154*) (Xu and Chisholm, 2014) and (LGV) *atfs-1*(*tm4525*) (National BioResource Project).

Transgenic lines generation

To generate the *atfs-1* rescuing construct (*Patfs-1:atfs-1[CDS]:atfs-1[3′UTR]*), we used as a promoter the ~2.4kb DNA fragment between *ZC376.6*, the gene upstream of *atfs-1*, and the coding sequence of *atfs-1*. As a 3′UTR, we used the ~300bp DNA fragment downstream of the coding sequence of *atfs-1*, which is described in Wormbase as the 3′UTR of *atfs-1. Patfs-1:atfs-1[CDS]:atfs-1 [3′UTR]* was amplified from gDNA using the primer *atfs-1FSpeI* (5′-ACTAGTTATCCCGATTCAAATCATTG-3′) and *atfs-1RAvrII* (5′-CCTAGGTTACACAACTGCGTCACG-3′) and cloned into the MosSCI vector pCFJ350 to generate pBC1753. A second plasmid (pBC1759) was generated, in which the first 24 amino acids of ATFS-1 were replaced with the first 69 amino acids of the subunit 9 of ATP synthase of *Neurospora crassa*. In order to generate stably integrated, single-copy transgenes of these two constructs as well as the control vector, both plasmids as well as the empty pCFJ350 vector were used for MosSCI injection of the strain MD4284 (*oxTi179* II; *unc-119*(*ed3*) III; *atfs-1*(*tm4525*) *zcIs9* [P_{hsp-60}*GFP*] V). To generate the MD4284 strain, we crossed the strain CMH5 (*atfs-1*(*tm4525*) *zcIs9* [P_{hsp-60}*GFP*] V) (kind gift from C. Haynes) and EG8079 (*oxTi179* II *unc-119*(*ed3*) III). To determine the level of the ATFS-1 protein, the different transgenic lines were treated with *tag-208*(*RNAi*) or *lonp-1*(*RNAi*) and analyzed by Western using affinity purified rabbit anti-ATFS-1 antibodies (1:5000; generated by Nargund et al. [2012]) and anti-β-actin antibodies (1:2000, Sigma). We also generated a single copy *atfs-1(wt)::GFP* transgene. In contrast to the non-tagged *atfs-1(wt)* transgene, which restores the induction of the P_{hsp-60}*GFP* reporter upon *spg-7(RNAi)* to ~58% of wild-type level, the *afts-1(wt)::GFP* single copy transgene restores the induction of the P_{hsp-60}*GFP* reporter to only ~14% of wild-type level. Hence, the presence of GFP appears to negatively affect the ability of ATFS-1 to function as a transcription factor. The name and genotype of all the transgenic lines generated in this study are indicated in Table S2.

METHOD DETAILS

Genome wide RNA interference screen

The screen was performed using the technique of RNAi by feeding using the Ahringer RNAi library (Kamath and Ahringer, 2003).We specifically used the latest updated version of the library which covers more than 90% of the annotated genes of the *C. elegans* genome and is available from Source BioScience (www.lifesciences.sourcebioscience.com).

For the L4 screen, RNAi clones were cultured overnight in 100 μL of LB carbenicillin (100 μg/ml) in a 96 wells plate format on day 1. On day 2, 10 μL of the culture was used to inoculate 24 well lactose RNAi plates (similar to NGM medium (Stiernagle, 2006) with 4g/l bacto-tryptone instead of 2.5g/l of Bacto-Peptone and supplemented with 100 μg/ml Carbenicillin and 0.25% lactose (w/v)) and the plates were incubated at room temperature until the next day. On day 3, a synchronized population of L4 of the SJ4100 strain (P_{hsp-6}*GFP*) was resuspended in MPEG (M9 medium (Stiernagle, 2006) supplemented with 0.1% PEG (w/v)). Two L4 larvae were pipetted in each well of the 24 well plates. The plates were incubated at 20°C for four days and screened for GFP positive progeny. Positive candidates were re-screened in three independent experiments using 24 well 6mM IPTG RNAi plates (NGM medium (Stiernagle, 2006) supplemented with 25 μg/ml Carbenicillin and 6mM IPTG). As indicated in Table S1, the level of induction of UPR^{mt} was classified from 0 (basal expression of the P_{hsp-6}*GFP* reporter similar to the one observed in *tag-208(RNAi)* animals) to 3 (strong expression of the P_{hsp-6}*GFP* reporter).

For the L1 screen, a sub-library containing the 2000 genes described as essential for embryonic and larval development according to Ahringer and co-workers was generated (Kamath and Ahringer, 2003). RNAi clones were cultured overnight in 100 μL of LB carbenicillin (100 μg/ml) in a 96 well plate format on day 1. On day 2, 10 μL of the culture was used to inoculate 24 well lactose RNAi plates (see above) and the plates were incubated at room temperature until the next day. On day 2, gravid adults of the SJ4100 strain (P_{hsp-6}*GFP*) were bleached as previously described (Stiernagle, 2006). The embryos were incubated overnight in M9 medium in order to produce a synchronized population of L1 larvae the next morning. On day 3, 50 synchronized L1 larvae were inoculated onto each well of the 24 wells Lactose RNAi plates. The plates were incubated at 20°C for three days and screened for GFP positive animals. Positive candidates were re-screened in three independent experiments using 24 wells 6mM IPTG RNAi plates (see above).

Bioinformatic analysis

For prediction of the mitochondrial targeting sequence and its charge, we used the Mitoprot software ((Claros and Vincens, 1996); https://ihg.gsf.de/ihg/mitoprot.html). For the functional annotations and clustering we used the DAVID database v. 6.8 (Huang et al., 2009). The list of candidates was used as an input and was ran against the *C. elegans* background list for searching of enriched GO categories. The GO-term enrichment is calculated using a modified Fisher's exact test. The so-called EASE score provides a more conservative method to calculate the enrichment of a term, guaranteeing results consistency.

Further analysis of the candidates

RNAi clones were cultured overnight in 2ml of LB carbenicillin (100 μg/ml) at 37°C and 200rpm. The RNAi cultures were adjusted to 0.5OD and 50 μL was used to seed 30mm RNAi plates containing 6mM IPTG (see above). The plates were incubated at 20°C in the dark. [In the case of double RNAi, each RNAi culture was diluted 1:3 with *atfs-1*(*RNAi*) or *tag-208*(*RNAi*) bacteria.] 24 hours later, four L4 larvae of SJ4100 or SJ4058 were inoculated onto the RNAi plates and new RNAi plates were seeded. 24 hours later, the four adults of SJ4100 or SJ4058 were transferred onto new seeded RNAi plates and let to lay eggs for 4 hours at 20°C. The adults were then removed from the plates and the plates were further incubated for 4 days at 20°C (For the rescue experiments, the plates

were incubated for 5 days at 20°C). For each RNAi condition, ~10 animals were imaged using a Leica GFP dissecting microscope (M205 FA) and the software Leica Application Suite (3.2.0.9652). We used Fiji-implemented macro using the IJ1 Macro language to automate the intensity measurement within defined areas of 2-dimensional images using ImageJ. An automated threshold using the Triangle method was applied to the brightfield microscopy image, in order to generate a binary mask (The Triangle method was selected among the 16 available auto threshold methods of ImageJ as it provided the best results). The mask was then inverted and the Particle Analyzer of ImageJ was used to remove noise by setting a minimum size (10 pixels) for objects to be included in the mask. After removing manually any remaining unwanted objects, the mask was applied to the corresponding fluorescence microscopy image and mean fluorescence intensity was measured. The mean fluorescence intensity outside the mask was defined as the background. The script (''Worm_SignalQuantification.ijm'') used for the analysis can be found in Data S1.

Analysis of HSP-6 and HSP-60 protein levels

Two L4 larvae of N2 were inoculated on *tag-208(RNAi)*, *fum-1(RNAi)* or *sdhc-1(RNAi)* plates and the plates were incubated for 5 days at 20°C. Mixed-stage populations of worms were harvested in 1ml MPEG, washed 3 times with 1ml MPEG and resuspended in 1 volume of Laemmli buffer 2x. The samples were analyzed by SDS-PAGE and Western using a monoclonal anti-Tubulin (1:10000; Sigma), a polyclonal anti-HSP-6 (1:10000; (Köhler et al., 2015)) and a monoclonal anti-HSP-60 (1:2000; generated by Hadwiger et al. (2010) and available at DHSB). As secondary antibodies, we used horseradish peroxidase conjugated goat anti-mouse antibodies (BioRad #1706516) at 1:10000 for the anti-Tubulin and at 1:7500 for the anti-HSP-60. For the anti-HSP-6, we used a horseradish peroxidase conjugated goat anti-rabbit (BioRad #1706515) at 1:10000. Western was developed using ECL (Amersham #RPN2106) and images were quantified using the ChemiDoc XRS+ System (Bio-Rad).

TMRE staining and quantification

L2/L3 larvae were inoculated on NGM plates (Stiernagle, 2006) supplemented with 0.1 μM Tetramethylrhodamine, Ethyl Ester (TMRE) with a small inoculum of OP50 *E. coli* bacteria. After an incubation over-night at 20°C, L4 larvae were analyzed by fluorescence microscopy using a microscope equipped with a 63 × 1.4 NA oil lens (Axioskop 2; Carl Zeiss, Inc.) and a charge-coupled device camera (1300; Micromax). The acquisition was performed with 100ms exposure using the software Metamorph (Molecular Device Corporation; v. 7.1.0.0). For the RNAi experiments, L4 larvae were inoculated onto 6mM IPTG RNAi plates as indicated above. After 2 days, L2/L3 larvae of the F1 generation were inoculated on TMRE plates and analyzed the next day as indicated above. We used Fiji-implemented macro using the IJ1 Macro language to segment the images. Specifically, we used a background subtraction with the ''rolling ball'' algorithm with a ball radius of 15 pixels to remove continuous background signal from the image (Sternberg, 1983). This was followed by the application of the Tubeness plugin, which generates a score of how tube-like each point in the image is, by using the eigenvalues of the Hessian matrix to calculate the measure of ''tubeness'' (Sato et al., 1998). The resulting 32-bit image was converted to 8-bit and an automatic threshold (using the IsoData algorithm) was used to generate a binary mask. The final step involved the removal of any particles that are smaller than 10 pixels in size for they are assumed to be noise. After removing manually any remaining unwanted objects, another macro was used to measure mean fluorescence intensity. Specifically, all objects in the binary mask segmented with the first macro were selected and this selection was restored on the original image, allowing to measure the mean fluorescence intensity within regions that correspond to the binary mask. This binary mask corresponds to the TMRE labeled mitochondria in the image. The mean fluorescence intensity outside the mask was defined as the background and was subtracted from the signal. Since the mean fluorescence intensity corresponds to the sum of the gray values of all the pixels in the selection divided by the number of pixels in the selection, the values indicated in Figures 4C and 4D correspond to fluorescence intensities per area. The scripts (''TMRE Hessian_segmentation.ijm'' and ''TMRE mean_intensity_measurement.ijm'') used for the analysis can be found in Data S1.

QUANTIFICATION AND STATISTICAL ANALYSIS

For Figures 1, 2, 3, 5, S1, S2, and S4, n indicates the number of biological replicates analyzed for a given RNAi (One replicate corresponds to one individual RNAi plate. As indicated in METHOD DETAILS, for each replicate ~10 animals were imaged and the mean fluorescence intensity of these animals was measured). For Figure 4, n indicates the number of animals analyzed for a given genotype or RNAi. For Figure S3, n indicates the number of biological replicates analyzed by Western for a given RNAi. In the quantification of all the Figures, the mean values with the standard deviation are indicated. To perform the statistical analyses, we used the software Graphpad Prism 6 and R Studio Version 1.1.423 (RStudio Team, 2015) with the package ''userfriendlyscience'' (Peters, 2018).When comparing more than two independent groups, we tested the data for normality using the Kolmogorov-Smirnov test or Shapiro-Wilk test depending on sample size and for equal variance using the Brown-Forsythe test. When the data was normally distributed and showed equal variance, we used one-way ANOVA with Bonferroni's multiple comparison test. In the case of heteroscedasticity, we used a Welch's ANOVA with Games-Howell post hoc test. When the data was not normally distributed, we used a Kruskal-Wallis with Dunn's multiple comparisons test. When only comparing two independent groups, we tested for normality using

the Kolmogorov-Smirnov test or Shapiro-Wilk test depending on sample size and for equal variance using the F-test. We used unpaired two-sample t test when the data was normally distributed and Wilcoxon-Mann-Whitney-test when the data was not normally distributed. For the western-blot analysis (Figure S3), we used a one-sample t test when the data was normally distributed and a Wilcoxon signed rank test when the data was not normally distributed.

DATA AND CODE AVAILABILITY

The published article includes all datasets and code generated or analyzed during this study.

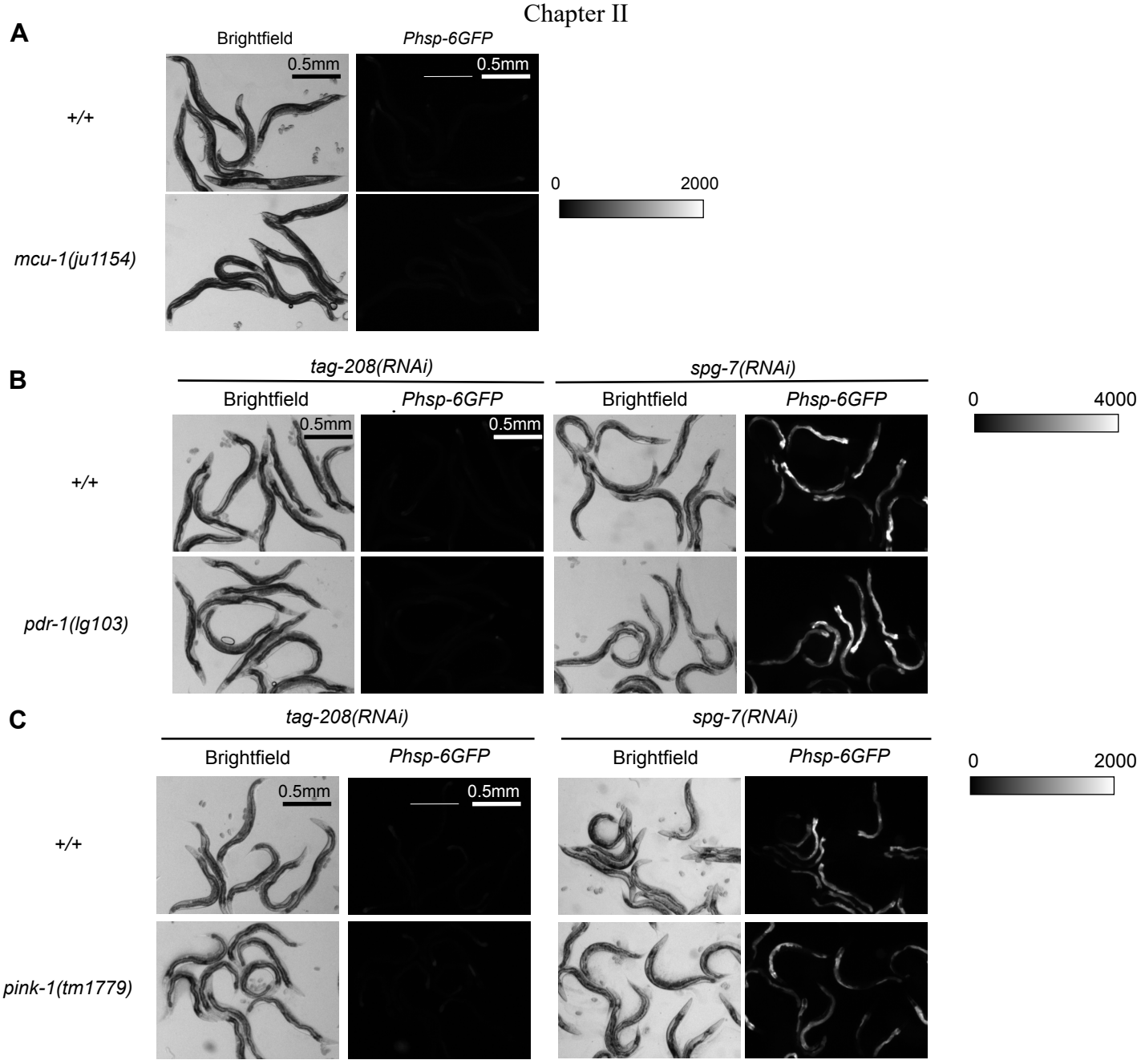
A
Brightfield
Phsp-6GFP
0.5mm
0.5mm
+/+
mcu-1(ju1154)
0
2000
B
tag-208(RNAi)
spg-7(RNAi)
Brightfield
Phsp-6GFP
Brightfield
Phsp-6GFP
0
4000
0.5mm
0.5mm
+/+
pdr-1(lg103)
C
tag-208(RNAi)
spg-7(RNAi)
Brightfield
Phsp-6GFP
Brightfield
Phsp-6GFP
0
2000
0.5mm
0.5mm
+/+
pink-1(tm1779)

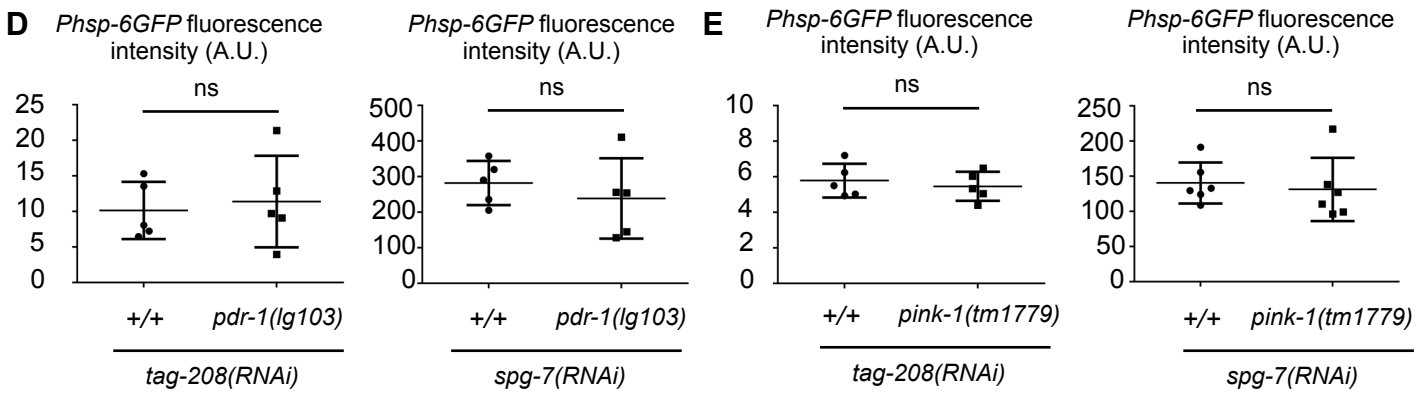
D
Phsp-6GFP fluorescence intensity (A.U.)
ns
25
20
15
10
5
0
+/+
pdr-1(lg103)
tag-208(RNAi)
Phsp-6GFP fluorescence intensity (A.U.)
ns
500
400
300
200
100
0
+/+
pdr-1(lg103)
spg-7(RNAi)
E
Phsp-6GFP fluorescence intensity (A.U.)
ns
10
8
6
4
2
0
+/+
pink-1(tm1779)
tag-208(RNAi)
Phsp-6GFP fluorescence intensity (A.U.)
ns
250
200
150
100
50
0
+/+
pink-1(tm1779)
spg-7(RNAi)

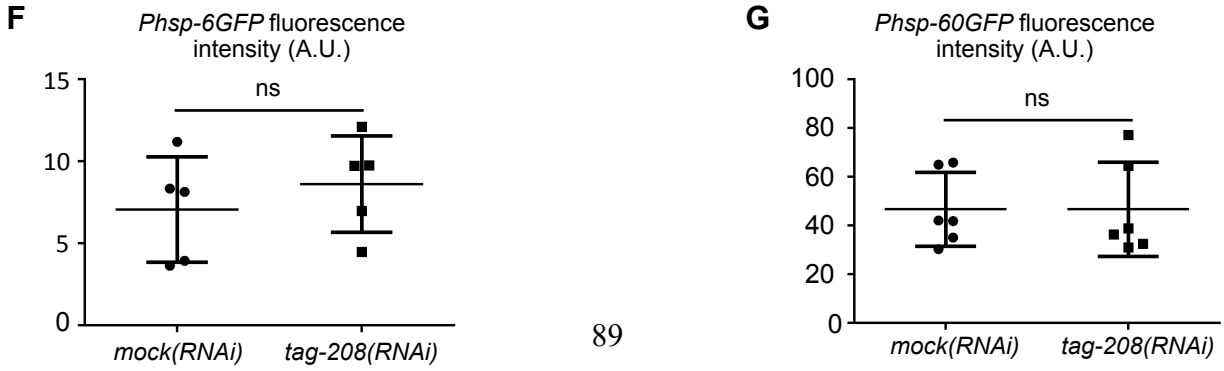
F
Phsp-6GFP fluorescence intensity (A.U.)
ns
15
10
5
0
mock(RNAi)
tag-208(RNAi)
G
Phsp-60GFP fluorescence intensity (A.U.)
ns
100
80
60
40
20
0
mock(RNAi)
tag-208(RNAi)

Figure S1: Compromising mitochondrial Ca^{2+} homeostasis and mitophagy fail to induce UPR^{mt} (Related to Figure 1). (A) Wild-type animals or *mcu-1(ju1154)* mutant animals carrying the mitochondrial chaperone *hsp-6* transcriptional reporter ($P_{hsp\text{-}6}GFP$) were analyzed by fluorescence microscopy. Brightfield and fluorescence microscopy analysis of the $P_{hsp\text{-}6}GFP$ transcriptional reporter strain (+/+) or the $P_{hsp\text{-}6}GFP$ transcriptional reporter strains carrying the *pdr-1(lg103)* mutation **(B)** or the *pink-1(tm1779)* mutation **(C)**. The wild-type strains (+/+) used as controls in each panel were isolated as F2 siblings of the homozygous mutants. **(D,E)** Quantification of the $P_{hsp\text{-}6}GFP$ fluorescence intensity is indicated. (n≥5 (n=number of biological replicates); mean and SD are shown; ns: the difference between wild-type (+/+) and *pdr-1(lg103)* or *pink-1(tm1779)* are not significant by unpaired t-test). Quantification of the $P_{hsp\text{-}6}GFP$ fluorescence intensity **(F)** or the $P_{hsp\text{-}60}GFP$ fluorescence intensity **(G)** upon treatment with *mock*(RNAi) (RNAi bacteria containing the empty L4440 vector) or *tag-208*(RNAi). (n=5 for panel F and n=6 for panel G (n=number of biological replicates); mean and SD are shown; ns: the differences are not significant by unpaired t-test for panel F and by Wilcoxon-Mann-Whitney-test test for panel G).

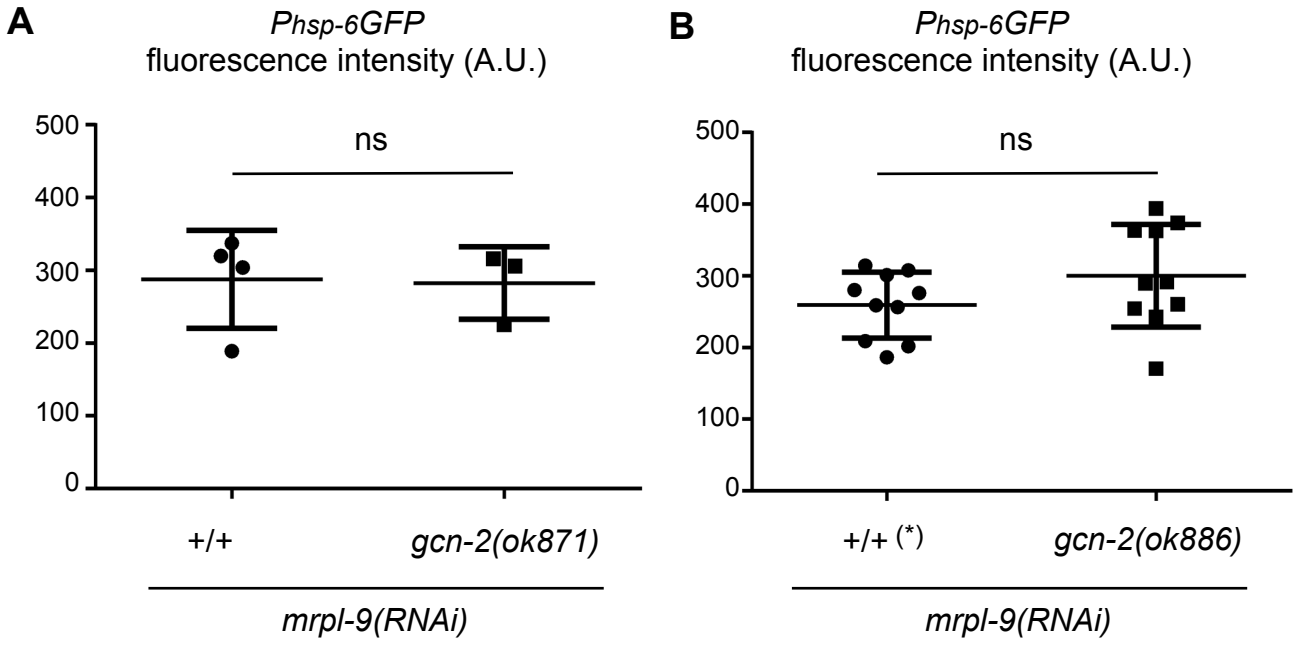
A
Phsp-6GFP
fluorescence intensity (A.U.)
500
400
300
200
100
0
ns
+/+
gcn-2(ok871)
mrpl-9(RNAi)
B
Phsp-6GFP
fluorescence intensity (A.U.)
500
400
300
200
100
0
ns
+/+ (*)
gcn-2(ok886)
mrpl-9(RNAi)

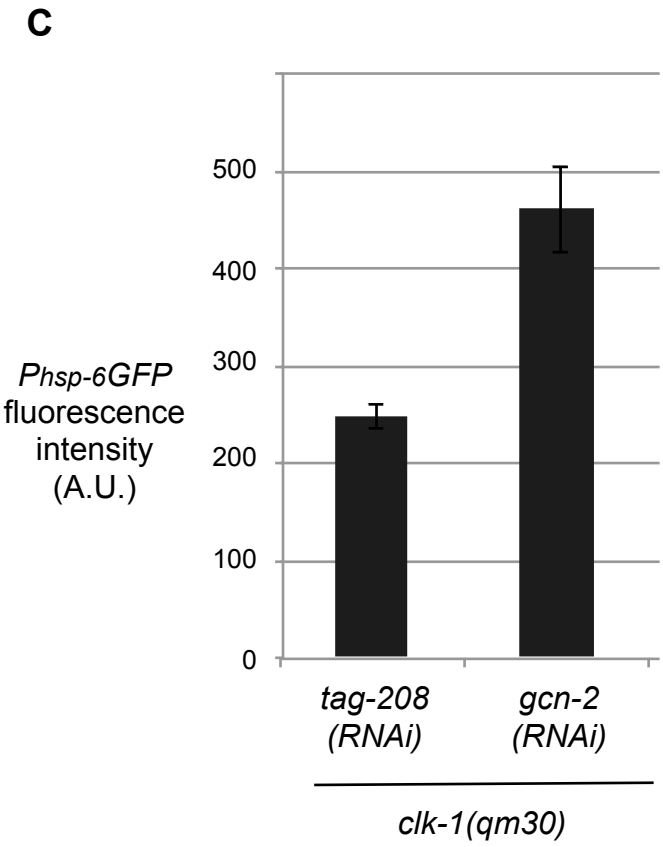
C
Phsp-6GFP
fluorescence
intensity
(A.U.)
500
400
300
200
100
0
tag-208
(RNAi)
gcn-2
(RNAi)
clk-1(qm30)

Figure S2: Effect of GCN-2 on UPR^{mt} induction (Related to Figure 1). (A) The strain carrying the P$_{hsp\text{-}6}$*GFP* transcriptional reporter strain in the wild-type background (+/+) and the *gcn-2(ok871)* mutant background were subjected to the knock-down of *mrpl-9*. Animals of the next generation were analyzed by fluorescence microscopy and the P$_{hsp\text{-}6}$*GFP* fluorescence intensity was quantified as described in methods. (n≥3 (n=number of biological replicates); mean and SD are shown; ns: the difference of UPR^{mt} induction between wild-type (+/+) and *gcn-2*(*ok871*) are not significant by Wilcoxon-Mann-Whitney-test) **(B)** The strain carrying the P$_{hsp\text{-}6}$*GFP* transcriptional reporter strain in the wild-type background (+/+) and the *gcn-2(ok886)* mutant background were subjected to the knock-down of *mrpl-9*. Animals of the next generation were analyzed by fluorescence microscopy and the P$_{hsp\text{-}6}$*GFP* fluorescence intensity was quantified as described in methods. (n=10 (n=number of biological replicates); mean and SD are shown; ns: the difference of UPR^{mt} induction between wild-type (+/+) and *gcn-2*(*ok886*) are not significant by unpaired t-test, * this wild-type strain was isolated as a F2 sibling of the homozygous *ok886* mutants) **(C)** The strain carrying the P$_{hsp\text{-}6}$*GFP* transcriptional reporter strain and the *clk-1(qm30)* mutation was subjected to *tag-208(RNAi)* and *gcn-2(RNAi)*. Animals of the next generation were analyzed by fluorescence microscopy and the P$_{hsp\text{-}6}$*GFP* fluorescence intensity was quantified as described in methods. (n=2 (n=number of biological replicates); mean and SD are shown).

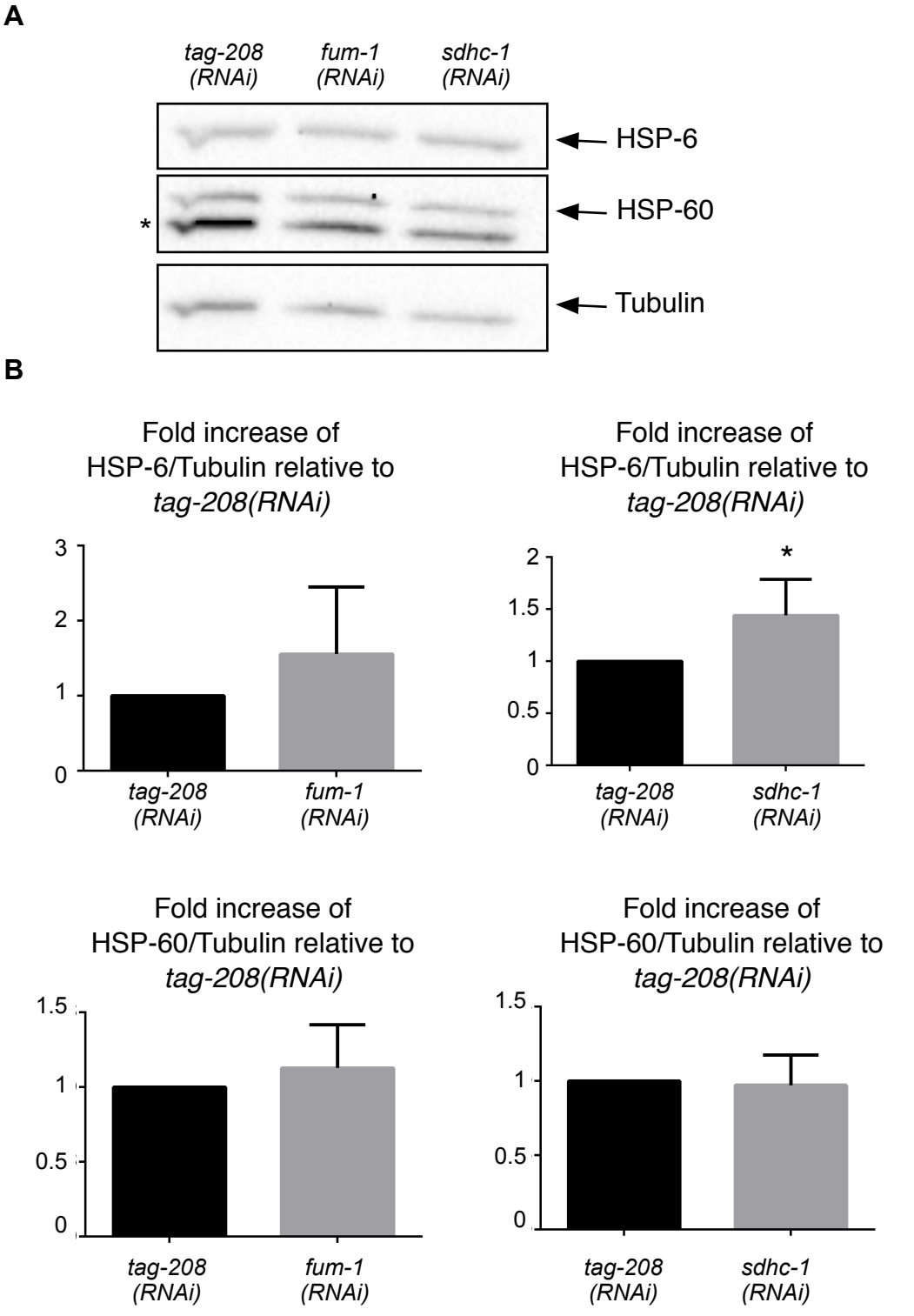
A
tag-208 (RNAi)
fum-1 (RNAi)
sdhc-1 (RNAi)
HSP-6
HSP-60
Tubulin
*
B
Fold increase of HSP-6/Tubulin relative to tag-208(RNAi)
3
2
1
0
tag-208 (RNAi)
fum-1 (RNAi)
Fold increase of HSP-6/Tubulin relative to tag-208(RNAi)
2
1.5
1
0.5
0
*
tag-208 (RNAi)
sdhc-1 (RNAi)
Fold increase of HSP-60/Tubulin relative to tag-208(RNAi)
1.5
1
0.5
0
tag-208 (RNAi)
fum-1 (RNAi)
Fold increase of HSP-60/Tubulin relative to tag-208(RNAi)
1.5
1
0.5
0
tag-208 (RNAi)
sdhc-1 (RNAi)

Figure S3: Knock-down of *fum-1* and *sdhc-1* induces the up-regulation of endogenous HSP-6 and HSP-60 proteins (Related to Figure 2 and 3). (A) Western analysis of animals treated with *tag-208(RNAi), fum-1(RNAi)* and *sdhc-1(RNAi)* using anti-HSP-6, anti-HSP-60 and anti-Tubulin antibodies. In the part of the blot showing the HSP-60 protein, * indicates the Tubulin protein. The membrane was probed with anti-Tubulin antibodies, then with anti-HSP-6 antibodies and then with anti-HSP-60 antibodies. The Tubulin band indicated by * is still visible after probing the membrane with anti-HSP-60 antibodies. **(B)** Quantification of the ratio of HSP-6/Tubulin and HSP-60/Tubulin relative to *tag-208(RNAi)* (n=5 (n=number of biological replicates); mean and SD are shown; * $p<0.05$ by one-sample t-test).

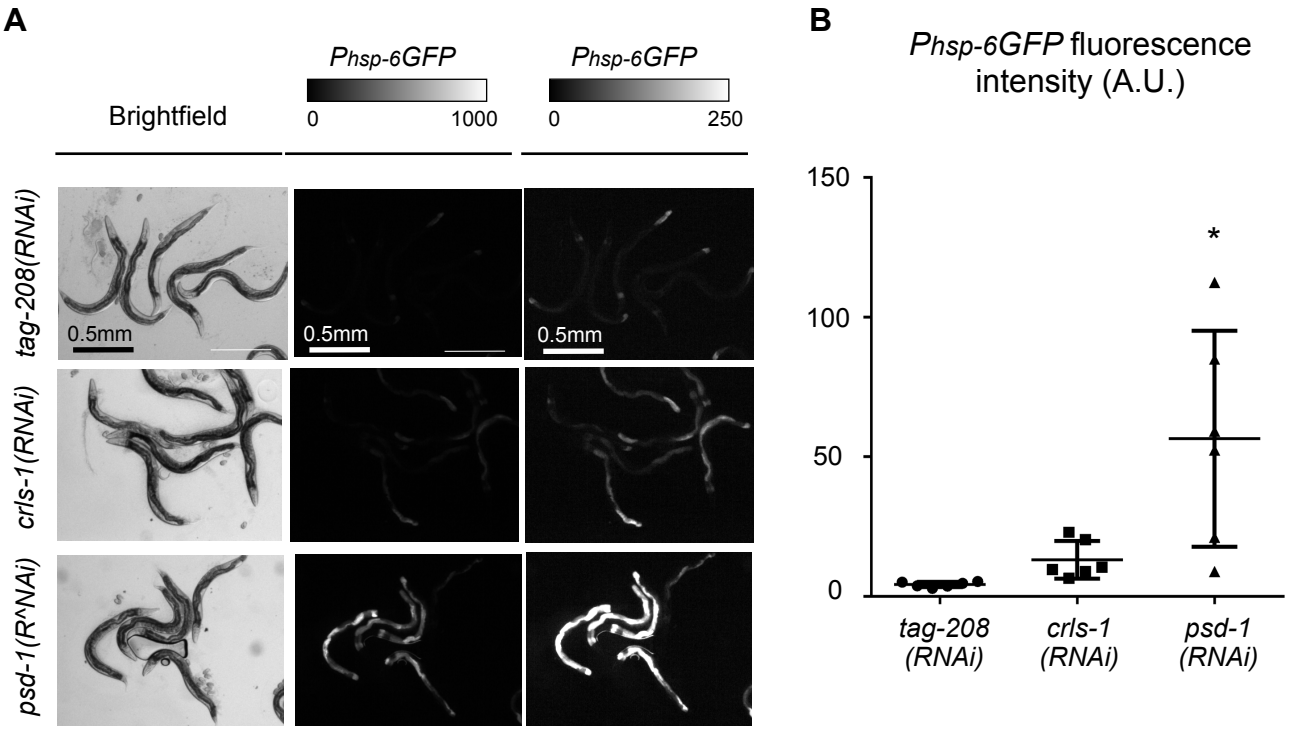

Figure S4: Knock-down of genes involved in lipid biosynthesis induces UPR^{mt} (Related to Figure 3). (A) Brightfield and fluorescence microscopy analysis of the P$_{hsp\text{-}6}$*GFP* transcriptional reporter treated with *tag-208(RNAi), psd-1(RNAi)* and *crls-1(RNAi).* Fluorescence images are shown with two different intensity scales. **(B)** Quantification of the P$_{hsp\text{-}6}$*GFP* fluorescence intensity. (n=6 (n=number of biological replicates); mean and SD are shown; * $p<0.05$ by Welch's ANOVA with Games-Howell post-hoc test to *tag-208(RNAi)*).

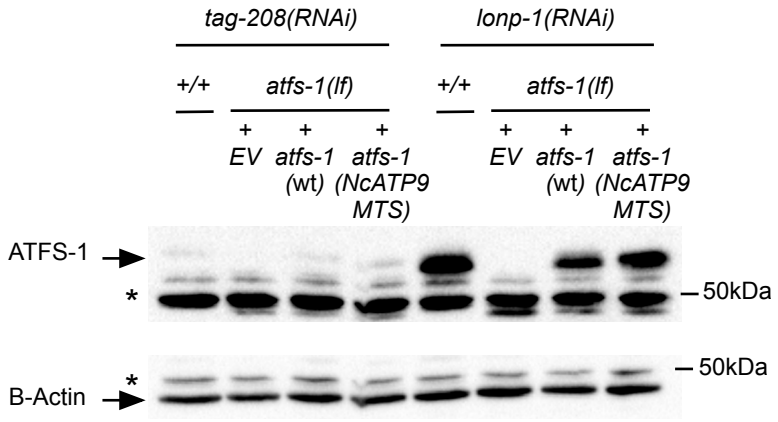

Figure S5: Analysis of the levels of ATFS-1 protein in the different transgenic lines (Related to Figure 5). To confirm that in the absence of UPR^{mt} induction, both ATFS-1(wt) and ATFS-1(NcATP9MTS) proteins are imported into mitochondria, the transgenic lines, indicated in Figure 5 panel C-F, were treated with either *tag-208(RNAi)* or *lonp-1(RNAi).* (*lonp-1* encodes the mitochondrial protease LONP-1, which is responsible for the degradation of ATFS-1 protein (Nargund et al., 2012)) and analyzed by Western using affinity purified rabbit anti-ATFS-1 antibodies (1:5000; generated by C. Haynes and co-workers (Nargund et al., 2012)) and anti-β-actin antibodies (1:2000, Sigma). Compared to *tag-208(RNAi), lonp-1(RNAi)* greatly increases the amount of both proteins demonstrating that both proteins are imported into mitochondria and degraded by LONP-1. * indicates nonspecific band detected with the anti-ATFS-1 antibodies. The membrane was probed with anti-ATFS-1 antibodies and then with anti-β-actin antibodies. The nonspecific band indicated by * is also visible after probing the membrane with anti-β-actin antibodies.

Table S2: Name and genotype of the transgenic strains used in this study (Related to STAR Methods).

Strain name	**Genotype**	**Notes**	**Reference**
SJ4100	*zcIs13 V*		(Yoneda et al., 2004)
SJ4058	*zcIs9*		(Yoneda et al., 2004)
MD3800	*mcu-1(ju1154) IV ; zcIs13 V*		This study
MD4205	*pink-1(tm1779) II ; zcIs13 V*	MD4205 and MD4203 are isogenic with the exception of *pink-1*(*tm1175*)	This study
MD4203	*zcIs13 V*		
MD4001	*pdr-1(lg103) III ; zcIs13 V*	MD4001 and MD4002 are isogenic with the exception of *pdr-1*(*lg103*)	This study
MD4002	*zcIs13 V*		This study
MD4126	*gcn-2(ok871) II ; zcIs13 V*		This study
MD4164	*gcn-2(ok886) II ; zcIs13 V*	MD4164 and MD4165 are isogenic with the exception of *gcn-2*(*ok886*)	This study
MD4165	*zcIs13* V		This study
MD4284	*oxTi179 II ; unc-119(ed3) III ; atfs-1(tm4525) V zcIs9 V*		This study
MD4306	*bcSi78* [*pCFJ350*] II ; *unc-119*(*ed3*) III ; *atfs-1*(*tm4525*) *zcIs9* V	Described in Figure 5 as *atfs-1*(*tm4525*) + EV (Empty Vector)	This study
MD4314	*bcSi80* [*pBC1753*] II ; *unc-119*(*ed3*) III ; *atfs-1*(*tm4525*) *zcIs9* V	Described in Figure 5 as *atfs-1*(*tm4525*) + *afts-1*(wt) rescue strain	This study
MD4323	*bcSi81* [*pBC1759*] II ; *unc-119*(*ed3*) III ; *atfs-1*(*tm4525*) *zcIs9* V	Described in Figure 5 as *atfs-1*(*tm4525*) + *afts-1*(*NcATP9MTS*) rescue strain	This study

Chapter III

Autophagy compensates for defects in mitochondrial dynamics

Simon Haeussler, Fabian Köhler, Michael Witting, Madeleine F. Premm, Stéphane G. Rolland, Christian Fischer, Laetitia Chauve, Olivia Casanueva, Barbara Conradt

Published: March 19, 2020. PLOS Genetics 16(3):
https://doi.org/10.1371/journal.pgen.1008638

RESEARCH ARTICLE

Autophagy compensates for defects in mitochondrial dynamics

Simon Haeussler[1☯], Fabian Köhler[1☯], Michael Witting[2,3], Madeleine F. Premm[1], Stéphane G. Rolland[1], Christian Fischer[1,4], Laetitia Chauve[5], Olivia Casanueva[5], Barbara Conradt[1,4,6]*

1 Faculty of Biology, Ludwig-Maximilians-University Munich, Munich, Germany, **2** Research Unit Analytical BioGeoChemistry, Helmholtz Zentrum München, Neuherberg, Germany, **3** Chair of Analytical Food Chemistry, Technische Universität München, Freising, Germany, **4** Center for Integrated Protein Science, Ludwig-Maximilians-University Munich, Planegg-Martinsried, Germany, **5** Epigenetics Programme, The Babraham Institute, Cambridge, United Kingdom, **6** Department of Cell and Developmental Biology, Division of Biosciences, University College London, London, United Kingdom

☯ These authors contributed equally to this work.
* b.conradt@ucl.ac.uk

OPEN ACCESS

Citation: Haeussler S, Köhler F, Witting M, Premm MF, Rolland SG, Fischer C, et al. (2020) Autophagy compensates for defects in mitochondrial dynamics. PLoS Genet 16(3): e1008638. https://doi.org/10.1371/journal.pgen.1008638

Editor: Gregory P. Copenhaver, The University of North Carolina at Chapel Hill, UNITED STATES

Received: June 18, 2019

Accepted: January 28, 2020

Published: March 19, 2020

Peer Review History: PLOS recognizes the benefits of transparency in the peer review process; therefore, we enable the publication of all of the content of peer review and author responses alongside final, published articles. The editorial history of this article is available here: https://doi.org/10.1371/journal.pgen.1008638

Data Availability Statement: All relevant data are within the manuscript and its Supporting Information files.

Funding: This work was supported by the Deutsche Forschungsgemeinschaft https://eur01.

Abstract

Compromising mitochondrial fusion or fission disrupts cellular homeostasis; however, the underlying mechanism(s) are not fully understood. The loss of *C. elegans fzo-1*^{MFN} results in mitochondrial fragmentation, decreased mitochondrial membrane potential and the induction of the mitochondrial unfolded protein response (UPR^{mt}). We performed a genome-wide RNAi screen for genes that when knocked-down suppress *fzo-1*^{MFN}(lf)-induced UPR^{mt}. Of the 299 genes identified, 143 encode negative regulators of autophagy, many of which have previously not been implicated in this cellular quality control mechanism. We present evidence that increased autophagic flux suppresses *fzo-1*^{MFN}(lf)-induced UPR^{mt} by increasing mitochondrial membrane potential rather than restoring mitochondrial morphology. Furthermore, we demonstrate that increased autophagic flux also suppresses UPR^{mt} induction in response to a block in mitochondrial fission, but not in response to the loss of *spg-7*^{AFG3L2}, which encodes a mitochondrial metalloprotease. Finally, we found that blocking mitochondrial fusion or fission leads to increased levels of certain types of triacylglycerols and that this is at least partially reverted by the induction of autophagy. We propose that the breakdown of these triacylglycerols through autophagy leads to elevated metabolic activity, thereby increasing mitochondrial membrane potential and restoring mitochondrial and cellular homeostasis.

Author summary

Various quality control mechanisms within the cell ensure mitochondrial homeostasis. Specifically, mitochondrial fission and fusion, the mitochondrial unfolded protein response (UPR^{mt}) and/or mitophagy are induced upon mitochondrial stress to maintain or restore mitochondrial homeostasis. How these different quality control mechanisms are coordinated and how they influence each other is currently not well understood.

safelinks.protection.outlook.com/?url=https%3A%2F%2Fwww.dfg.de%2Fen%2F&data=02%7C01%7C%7C381f38b59bcd4e9a567f08d7bba8aec2%7C1faf88fea9984c5b93c9210a11d9a5c2%7C0%7C0%7C637184205470464132&sdata=Eb4roXJqDx7UamjpWqYooqGw6RKzo5yD8jDFkLtapls%3D&reserved=0 (CO204/6-1, CO204/9-1 and EXC114 to BC). Some strains were provided by the CGC, which is funded by NIH Office of Research Infrastructure Programs https://eur01.safelinks.protection.outlook.com/?url=https%3A%2F%2Fwww.nih.gov%2F&data=02%7C01%7C%7C381f38b59bcd4e9a567f08d7bba8aec2%7C1faf88fea9984c5b93c9210a11d9a5c2%7C0%7C0%7C637184205470464132&sdata=LGLqn8cL5mhk9Xn6gWttZPV5hOmsiv%2Fi13%2BC6CDBYPU%3D&reserved=0 (P40 OD010440). The funders had no role in study design, data collection and analysis, decision to publish, or preparation of the manuscript.

Competing interests: The authors have declared that no competing interests exist.

Interestingly, the disruption of mitochondrial dynamics has recently been shown to induce UPR^{mt}. We performed a genome-wide RNAi screen for suppressors of UPR^{mt} induced by a block in mitochondrial fusion and found approximately half of the candidate genes identified to negatively regulate autophagy, a central quality control mechanism that adjusts cellular metabolism under conditions of stress. Furthermore, we found that induction of autophagy also suppresses UPR^{mt} induced by a block in mitochondrial fission. In addition, we demonstrate that defects in mitochondrial dynamics lead to changes in lipid metabolism, which can partially be reverted by the induction of autophagy. Taken together, our results suggest a so far unknown functional connection between UPR^{mt} and autophagy in animals with defects in mitochondrial dynamics.

Introduction

Mitochondrial dynamics plays an important role in the maintenance of mitochondrial function and, hence, cellular homeostasis [1]. Mitochondrial fission and fusion are both mediated by members of the family of dynamin-like guanosine triphosphatases (GTPases) [2]. In the nematode *Caenorhabditis elegans*, mitochondrial fission is facilitated by the cytosolic dynamin-like GTPase DRP-1^{DRP1}, which is recruited to mitochondria where it presumably forms constricting spirals as shown for its *Saccharomyces cerevisiae* counterpart Drp1 [3,4]. Conversely, fusion of the outer and inner mitochondrial membranes is carried out by the membrane-anchored dynamin-like GTPases FZO-1^{MFN} [5] and EAT-3^{OPA1} [6], respectively. The consequences with respect to mitochondrial function and cellular homeostasis of disrupting mitochondrial dynamics are not yet fully understood; however, it has recently been demonstrated that this activates a retrograde quality control signaling pathway referred to as the 'mitochondrial Unfolded Protein Response' (UPR^{mt}) [7,8]. In *C. elegans*, UPR^{mt} is activated upon mitochondrial stress, which leads to a decrease in mitochondrial membrane potential and the subsequent import into the nucleus of the 'Activating Transcription Factor associated with Stress 1' (ATFS-1^{ATF4,5}) [9,10]. ATFS-1^{ATF4,5} harbors both an N-terminal mitochondrial targeting sequence and a C-terminal nuclear localization sequence and is normally imported into mitochondria [11]. Upon mitochondrial stress, ATFS-1^{ATF4,5} is imported into the nucleus, where it cooperates with the proteins UBL-5^{UBL5} and DVE-1^{SATB1} to promote the transcription of genes that act to restore mitochondrial function and to adjust cellular metabolism [9,10,12,13]. Among these genes are the mitochondrial chaperone genes *hsp-6*^{mtHSP70} and *hsp-60*^{HSP60}, the transcriptional upregulation of which is commonly used to monitor UPR^{mt} activation [14].

Whereas UPR^{mt} is a quality control pathway that is activated upon mitochondrial stress, macro-autophagy (from now on referred to as 'autophagy') is a more general cellular quality control mechanism. Through autophagy, cytosolic constituents, long-lived proteins or dysfunctional organelles are degraded and recycled [15,16]. Upon the induction of autophagy, a double-membrane structure called 'phagophore' forms, which enlarges and eventually engulfs the cargo to form an 'autophagosome'. The autophagosome then fuses with a lysosome to form an 'autolysosome', in which the engulfed cargo is subsequently degraded by lysosomal hydrolases [16–18]. A key regulator of autophagy in *C. elegans* is the kinase LET-363^{mTOR} [19]. When cellular nutrients are abundant, LET-363^{mTOR} represses the 'induction complex', which includes UNC-51^{ULK}, a kinase that initiates autophagy [20–26].

Another vesicular process that targets cargo for degradation to the lysosome is endocytosis. The 'Endosomal Sorting Complex Required for Transport' (ESCRT) plays a critical role in

endocytosis [27,28]. The ESCRT is composed of five different subcomplexes (ESCRT-0, -I, -II, -III and the AAA-ATPase VPS4) and was originally identified because of its role in the formation of multivesicular bodies (MVBs), which enables ubiquitinated membrane proteins to be sorted into small intralumenal vesicles (ILVs) [29,30]. The ESCRT has since been shown to be required for a number of other cellular processes, such as cytokinesis and virus budding [27,31,32]. ESCRT activity has also been shown to affect autophagy. Studies in mammals and *Drosophila melanogaster* demonstrated that depleting ESCRT components results in a block in autophagy and that in these animals, the ESCRT is required for the fusion of endosomes with lysosomal compartments and also autophagosomes [33–36]. Moreover, ESCRT components have recently been shown to be involved in the closure of autophagosomes in mammals and yeast [37,38]. However, in *C. elegans*, the depletion of ESCRT components results in the induction of autophagy, which suggests that in this species, ESCRT function antagonizes or suppresses autophagy [39,40].

Whereas a functional connection between the ESCRT and autophagy has been established in yeast, nematodes, flies and mammals [33–40], functional connections between the ESCRT and UPR^{mt} or between autophagy and UPR^{mt} [40] have not been described or are poorly understood. In this study, we present evidence that in *C. elegans*, the ESCRT, autophagy and UPR^{mt} functionally interact. Specifically, we found that the induction of autophagy suppresses UPR^{mt} induced by a block in mitochondrial fusion or fission. Interestingly, lipid profiling revealed alterations in the lipidome of mutants defective in mitochondrial dynamics, and we present evidence that changes in the levels of certain types of triacylglycerols (TGs) in *fzo-1*^{MFN} mutants can be reverted by the induction of autophagy. We propose that through the breakdown of these triacylglycerols, the induction of autophagy leads to elevated metabolic activity, thereby increasing mitochondrial membrane potential and restoring mitochondrial and, hence, cellular homeostasis.

Results

In *C. elegans*, knock-down by RNA-mediated interference (RNAi) of genes encoding dynamin-like GTPases required for mitochondrial fusion (*fzo-1*^{MFN}, *eat-3*^{OPA1}) or mitochondrial fission (*drp-1*^{DRP1}) induces the 'mitochondrial Unfolded Protein Response' (UPR^{mt}) [7,8]. Using a multi-copy transgene of the transcriptional reporter P$_{hsp\text{-}6\ mtHSP70}$*gfp* (*zcIs13*) [14], we tested strong loss-of-function (lf) mutations of *fzo-1*^{MFN} and *drp-1*^{DRP1} (*fzo-1(tm1133)*, *drp-1 (tm1108)* (National BioResource Project)) and found that they induce UPR^{mt} to different degrees (S1A and S1C Fig). As a positive control, we used animals carrying a lf mutation of the gene *spg-7*^{AFG3L2} (*spg-7(ad2249)*), which encodes a mitochondrial metalloprotease required for mitochondrial function [41]. The *zcIs13* transgene shows very low baseline expression in wild-type animals and is widely used to monitor UPR^{mt} in *C. elegans* [7,9–14,42–44]. In the case of *fzo-1(tm1133)* animals, for example, its expression is induced more than 15-fold (S1C Fig). Furthermore, RNAi knock-down of *spg-7*^{AFG3L2} or genes encoding subunits of the electron transport chain (ETC), or treatments with drugs targeting the latter (e.g. antimycin) lead to strong induction of *zcIs13* expression [14,43]. This makes the *zcIs13* transgene suitable for high throughput, large-scale screens.

However, considering that *fzo-1(tm1133)* causes an increase in the amount of endogenous HSP-6^{mtHSP70} protein by only 1.44-fold (S1E Fig), the fold induction observed with the multi-copy *zcIs13* transgene may not reflect the physiological response with respect to UPR^{mt} induction by the loss of *fzo-1*^{MFN}. Furthermore, the *zcIs13* transgene exhibits large variability in expression between animals (inter-individual variability) (S1A Fig), which makes it difficult to obtain consistent results, especially when knocking-down genes using RNA-mediated

interference (RNAi). For this reason, we generated a single-copy transgene, *bcSi9* (integrated at a defined chromosomal location using MosSCI), of the transcriptional reporter $P_{hsp\text{-}6\ \mathrm{mtHSP70}}gfp$. As shown in S1B Fig, the *bcSi9* transgene shows low baseline expression and, in the case of *spg-7 (ad2249)* and *fzo-1(tm1133)*, an increase in expression of ~5-fold or ~4-fold, respectively (S1D Fig). Furthermore, compared to *fzo-1(tm1133)* animals carrying the multi-copy transgene *zcIs13*, *fzo-1(tm1133)* animals carrying the single-copy transgene *bcSi9* exhibit less inter-individual variability (S1A and S1B Fig). Similarly, *drp-1(tm1108)* animals carrying *bcSi9* show significantly less inter-individual variability compared to *drp-1(tm1108)* animals carrying the multi-copy transgene *zcIs13* (S1A and S1B Fig). Importantly, for all genotypes tested, we found that compared to the fold-induction observed with the multi-copy transgene *zcIs13*, the fold-induction observed with the single-copy transgene *bcSi9* correlated better with the fold-induction observed in the amount of endogenous HSP-6^{mtHSP70} protein (S1A–S1E Fig). Finally, to compare inter-individual variability of the expression of the two $P_{hsp\text{-}6\ \mathrm{mtHSP70}}gfp$ transgenes *zcIs13* and *bcSi9* as well as the endogenous *hsp-*6^{mtHSP70} locus in a quantitative manner, we performed single-worm RT-qPCR experiments in synchronized populations of 36 individual animals and compared inter-individual variability in expression of *zcIs13*, *bcSi9* or the endogenous *hsp-*6^{mtHSP70} locus to those of loci with low (*hsp-*1^{HSPA1L}), medium (*ttr-45*) or high (*nlp-29*) inter-individual variability in expression, respectively (S1F Fig). While the expression of the endogenous *hsp-*6^{mtHSP70} locus is not variable between individuals of a population, the expression of the multi-copy transgene *zcIs13* is highly variable in both a wild-type and *fzo-1(tm1133)* background (S1F Fig). Furthermore, the single-copy transgene *bcSi9* exhibits some inter-individual variability in expression, however, to a much lower degree than the transgene *zcIs13*. Therefore, based on these results, we decided to use the multi-copy transgene *zcIs13* for a genome-wide RNAi screen for suppressors of *fzo-1(tm1133)*-induced $\mathrm{UPR}^{\mathrm{mt}}$ and the single-copy transgene *bcSi9* for subsequent analyses of candidates identified (see below).

Depletion of ESCRT components suppresses *fzo-1(tm1133)*-induced $\mathrm{UPR}^{\mathrm{mt}}$

To identify genes that affect the induction of $\mathrm{UPR}^{\mathrm{mt}}$ in response to a block in mitochondrial fusion, we performed a genome-wide RNAi screen using *fzo-1(tm1133)* animals carrying the multi-copy $P_{hsp\text{-}6\ \mathrm{mtHSP70}}gfp$ transgene *zcIs13* (S1A Fig). To that end, we used an RNAi feeding library that covers approximately 87% of *C. elegans* protein coding genes [45] and analyzed animals of the F1 generation. Among the 299 suppressors identified, three genes, *vps-*4^{VPS4}, *vps-*20^{CHMP6} and *vps-*37^{VPS37}, encode components of the 'Endosomal Sorting Complex Required for Transport' (ESCRT) [27–30]. We analyzed the suppression of *fzo-1(tm1133)*-induced $\mathrm{UPR}^{\mathrm{mt}}$ using the single-copy $P_{hsp\text{-}6\ \mathrm{mtHSP70}}gfp$ transgene *bcSi9* and found that knockdown of *vps-*4^{VPS4} or *vps-*20^{CHMP6} by RNAi (referred to as '*vps-4(RNAi)*' or '*vps-20(RNAi)*') causes suppression by 39% or 23% on average, respectively (Fig 1A and 1C). *vps-37(RNAi)* does not result in a statistically significant suppression on average; however, some individual animals show strong suppression (see Fig 1A; *vps-37(RNAi)*; red arrowheads). As a positive control, we knocked-down the function of *atfs-*$1^{\mathrm{ATF4,5}}$ by RNAi, which results in suppression of *fzo-1(tm1133)*-induced $\mathrm{UPR}^{\mathrm{mt}}$ by 54% on average. (In a wild-type background, *atfs-1 (RNAi)*, *vps-4(RNAi)* or *vps-20(RNAi)* suppresses baseline expression of the *bcSi9* transgene by 8%, 14% or 14%, respectively (S2A Fig).) To confirm the suppression of *fzo-1(tm1133)*-induced $\mathrm{UPR}^{\mathrm{mt}}$ upon *ESCRT(RNAi)*, we used a multi-copy transgene *(zcIs9)* of a transcriptional reporter of the gene *hsp-*60^{HSP60} *(*$P_{hsp\text{-}60\ \mathrm{HSP60}}gfp$*)*, which is also transcriptionally upregulated in response to the induction of $\mathrm{UPR}^{\mathrm{mt}}$ [14]. Using the $P_{hsp\text{-}60\ \mathrm{HSP60}}gfp$ reporter, we found that *vps-37(RNAi)*, *vps-20(RNAi)* or *vps-4(RNAi)* suppresses by 34%, 41% or 33% on average, respectively (Fig 1B and 1D).

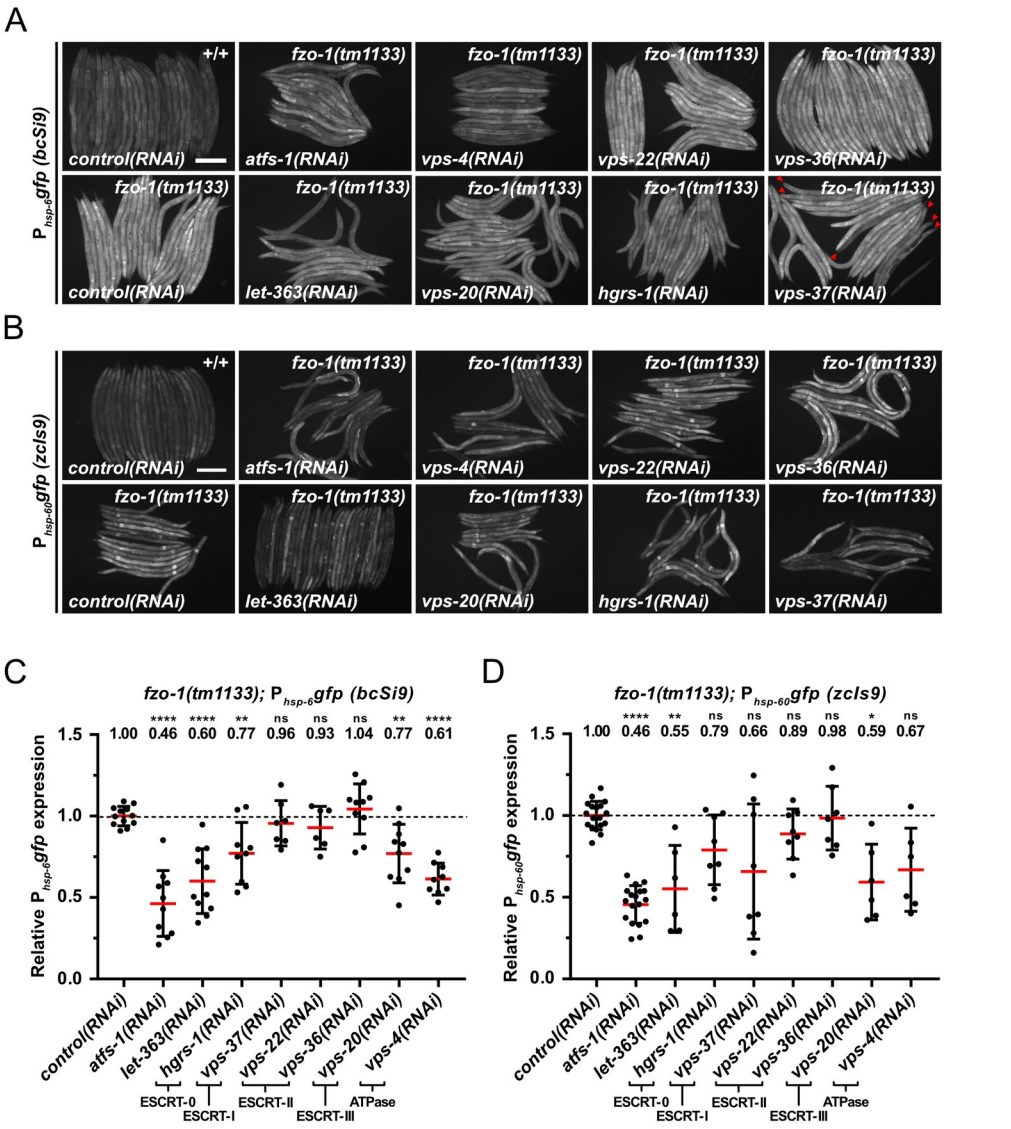

Fig 1. Depletion of ESCRT components and LET-363 suppresses *fzo-1(tm1133)*-induced UPR^{mt}. **(A)** Fluorescence images of L4 larvae expressing P$_{hsp-6}$*gfp (bcSi9)* in wild type (+/+) or *fzo-1(tm1133)*. L4 larvae were subjected to *control (RNAi)*, *atfs-1(RNAi)*, *vps-4(RNAi)*, *vps-20(RNAi)*, *vps-22(RNAi)*, *hgrs-1(RNAi)*, *vps-36(RNAi)*, *vps-37(RNAi)* or *let-363 (RNAi)* and the F1 generation was imaged. Red arrowheads indicate suppressed animals upon *vps-37(RNAi)*. Scale bar: 200 μm. **(B)** Fluorescence images of L4 larvae expressing P$_{hsp-60}$*gfp (zcIs9)* in wild type (+/+) or *fzo-1(tm1133)*. L4 larvae were subjected to *control(RNAi)*, *atfs-1(RNAi)*, *vps-4(RNAi)*, *vps-20(RNAi)*, *vps-22(RNAi)*, *hgrs-1(RNAi)*, *vps-36 (RNAi)*, *vps-37(RNAi)* or *let-363(RNAi)* and the F1 generation was imaged. Scale bar: 200 μm. **(C)** Quantifications of fluorescence images from panel A. After subtracting the mean fluorescence intensity of wild type (+/+) on *control (RNAi)*, the values were normalized to *fzo-1(tm1133)* on *control(RNAi)*. Each dot represents the quantification of fluorescence intensity of 15–20 L4 larvae. Values indicate means ± SD of at least 3 independent experiments in duplicates. $^{**}P<0.01$, $^{****}P<0.0001$ using one-way ANOVA with Dunnett's multiple comparison test to *control (RNAi)*. **(D)** Quantifications of fluorescence images from panel B. After subtracting the mean fluorescence intensity of wild type (+/+) on *control(RNAi)*, the values were normalized to *fzo-1(tm1133)* on *control(RNAi)*. Each dot represents the quantification of fluorescence intensity of 10–20 L4 larvae. Values indicate means ± SD of 3 independent experiments in duplicates. ns: not significant, $^{*}P<0.05$, $^{**}P<0.01$, $^{****}P<0.0001$ using Kruskal-Wallis test with Dunn's multiple comparison test to *control(RNAi)*.

https://doi.org/10.1371/journal.pgen.1008638.g001

To validate that the reduced P$_{hsp-6\ \mathrm{mtHSP70}}$*gfp (bcSi9)* and P$_{hsp-60\ \mathrm{HSP60}}$*gfp (zcIs9)* expression in *fzo-1(tm1133)* animals upon *ESCRT(RNAi)* is specific to the UPR^{mt} response, we tested a

transcriptional reporter, $P_{ges\text{-}1\ CES2}gfp$, that has a similar expression pattern as the two UPR^{mt} reporters. Depletion of ESCRT component VPS-4^{VPS4} or VPS-20^{CHMP6} does not result in suppression of the $P_{ges\text{-}1\ CES2}gfp$ reporter (Fig 2A and 2B), suggesting that ESCRT depletion does not cause degradation of cytosolic GFP *per se* but specifically suppresses the expression of the two UPR^{mt} reporters.

Since *vps-4*^{VPS4}, *vps-20*^{CHMP6} and *vps-37*^{VPS37} are part of different ESCRT subcomplexes (*vps-4*^{VPS4}—ATPase, *vps-20*^{CHMP6}—ESCRT-III, *vps-37*^{VPS37}—ESCRT-I) [27], we tested whether depletion of components of the two remaining ESCRT subcomplexes, ESCRT-0 and ESCRT-II, also suppresses *fzo-1(tm1133)*-induced UPR^{mt}. Using the $P_{hsp\text{-}6\ mtHSP70}gfp$ reporter *(bcSi9)*, we found that RNAi knock-down of *hgrs-1*^{HGS} (ESCRT-0) suppresses by 23% on average (Fig 1A and 1C). In contrast, RNAi knock-down of two genes encoding components of ESCRT-II, *vps-22*^{SNF8} and *vps-36*^{VPS36}, fails to suppress. Similarly, using the $P_{hsp\text{-}60\ HSP60}gfp$ reporter *(zcIs9)*, we found suppression by *hgrs-1(RNAi)* but not *vps-22(RNAi)* or *vps-36(RNAi)* (Fig 1B and 1D). Taken together, our results demonstrate that the depletion of components of ESCRT-0, -I, -III or VPS-4 ATPase can suppress *fzo-1(tm1133)*-induced UPR^{mt}.

Depletion of ESCRT components does not rescue the fragmented mitochondria phenotype in *fzo-1(tm1133)* animals but increases mitochondrial membrane potential

The loss of *fzo-1*^{MFN} function has a dramatic effect on steady-state mitochondrial morphology. This is easily detectable in *C. elegans* body wall muscles using a reporter that drives the expression of mitochondrial-matrix targeted GFP protein *(*$P_{myo\text{-}3\ MYH}gfp^{mt}$*)* [3,5,46]. In *control (RNAi)* animals, the mitochondria in body wall muscle cells are predominantly tubular (Fig 2C). In contrast, in *fzo-1(tm1133)* animals treated with *control(RNAi)*, the mitochondria are predominantly fragmented (referred to as 'fragmented mitochondria' phenotype). To determine whether the depletion of components of ESCRT-I or -III, or the depletion of the ATPase VPS-4^{VPS4} restores steady-state mitochondrial morphology, we analyzed mitochondrial morphology in *fzo-1(tm1133)* animals, in which *vps-4*^{VPS4}, *vps-20*^{CHMP6} or *vps-37*^{VPS37} had been knocked-down by RNAi. We found that knock-down of these genes has no effect on the fragmented mitochondria phenotype in body wall muscle cells of *fzo-1(tm1133)* animals (Fig 2C). Knock-down of *vps-4*^{VPS4}, *vps-20*^{CHMP6} or *vps-37*^{VPS37} in *fzo-1(tm1133)* animals also has no effect on mitochondrial morphology in hypodermal or intestinal cells (Fig 2E and S3B Fig). (ESCRT depletion has no effect on steady-state mitochondrial morphology in body wall muscle cells in a wild-type background (S3A Fig).)

Since we did not see a change in mitochondrial morphology in *fzo-1(tm1133)* animals upon *ESCRT(RNAi)*, we tested whether it affects mitochondrial membrane potential. Therefore, we stained larvae with TMRE (Tetramethylrhodamine ethyl ester), a membrane potential dependent dye that is commonly used in *C. elegans* to measure mitochondrial membrane potential in hypodermal cells [10,14]. To measure the intensity of TMRE signal, mitochondria in the fluorescent images were segmented using Fiji image software to generate a binary mask (S4 Fig). This mask, which includes all mitochondria of an image, was then used to measure TMRE fluorescence intensity per mitochondrial area in the raw image. Compared to wild type, TMRE fluorescence intensity per mitochondrial area was reduced by 63% in *fzo-1 (tm1133*) animals (Fig 2D). We found increased levels of TMRE fluorescence intensity per mitochondrial area in *fzo-1(tm1133*) animals upon *vps-4(RNAi)* (19%) or *vps-20(RNAi)* (33%), compared to *control(RNAi)* (Fig 2E and 2F). In contrast, ESCRT depletion in the wild-type background causes a reduction in TMRE fluorescence intensity per mitochondrial area by 24% upon *vps-4(RNAi)* or 18% upon *vps-20(RNAi)* (Fig 2G and 2H). Mitochondrial TMRE

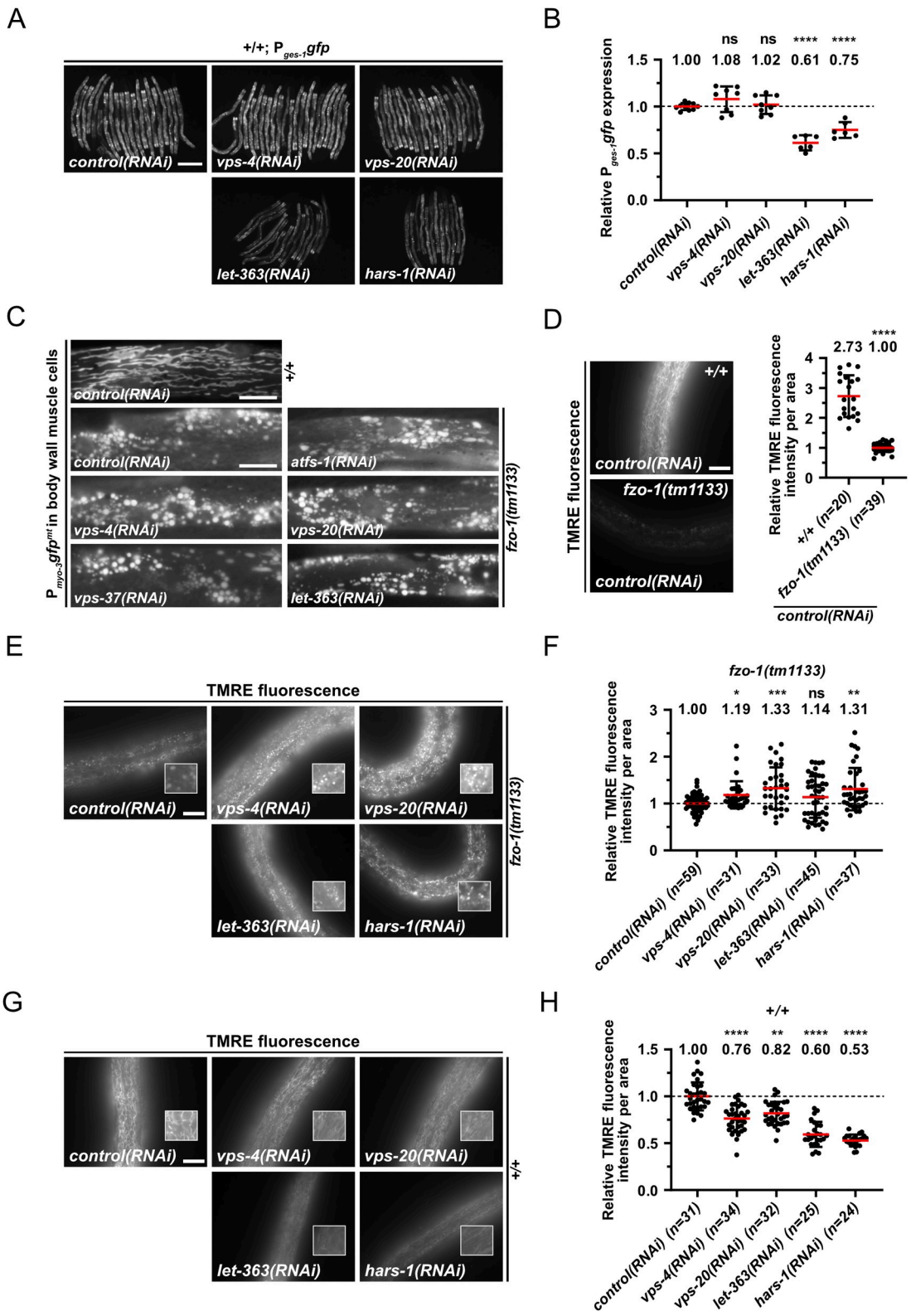

Fig 2. Induction of autophagy increases mitochondrial membrane potential and suppresses *fzo-1(tm1133)*-induced UPR^{mt}. **(A)** Fluorescence images of L4 larvae expressing P$_{ges-1}$*gfp* in wild type (+/+). L4 larvae were subjected to *control(RNAi)*, *vps-4 (RNAi)*, *vps-20(RNAi)*, *let-363(RNAi)* or *hars-1(RNAi)* and the F1 generation was imaged. Scale bar: 200 μm. **(B)** Quantifications of fluorescence images from panel A. The values were normalized to *control(RNAi)* and each dot represents the quantification of

fluorescence intensity of 15–20 L4 larvae. Values indicate means ± SD of 3 independent experiments in duplicates. ns: not significant, $^{****}P<0.0001$ using one-way ANOVA with Dunnett's multiple comparison test to *control(RNAi)*. **(C)** Fluorescence images of L4 larvae expressing $P_{myo\text{-}3}gfp^{mt}$ in wild type (+/+) or *fzo-1(tm1133)*. L4 larvae were subjected to *control(RNAi)*, *atfs-1 (RNAi)*, *vps-4(RNAi)*, *vps-20(RNAi)*, *vps-37(RNAi)* or *let-363(RNAi)* and the F1 generation was imaged. Scale bar: 10 μm. **(D)** Fluorescence images and quantifications of L4 larvae stained with TMRE in wild type (+/+) or *fzo-1(tm1133)*. L4 larvae were subjected to *control(RNAi)* and the F1 generation was stained with TMRE overnight and imaged. Scale bar: 10 μm. Values indicate means ± SD of 3 independent experiments in duplicates. $^{****}P<0.0001$ using unpaired two-tailed t-test with Welch's correction. **(E)** Fluorescence images of L4 larvae stained with TMRE in *fzo-1(tm1133)*. L4 larvae were subjected to *control(RNAi)*, *vps-4(RNAi)*, *vps-20(RNAi)*, *let-363(RNAi)* or *hars-1(RNAi)* and the F1 generation was stained with TMRE overnight and imaged. Scale bar: 10 μm. **(F)** Quantifications of fluorescence images from panel E. The values were normalized to *fzo-1(tm1133)* on *control(RNAi)* and each dot represents the quantification of fluorescence intensity per area from one L4 larvae. Values indicate means ± SD of 3 independent experiments in duplicates. ns: not significant, $^{*}P<0.05$, $^{**}P<0.01$, $^{***}P<0.001$ using Kruskal-Wallis test with Dunn's multiple comparison test to *control(RNAi)*. **(G)** Fluorescence images of wild-type L4 larvae stained with TMRE. L4 larvae were subjected to *control(RNAi)*, *vps-4(RNAi)*, *vps-20(RNAi)*, *let-363(RNAi)* or *hars-1(RNAi)* and the F1 generation was stained with TMRE overnight and imaged. Scale bar: 10 μm. **(H)** Quantifications of fluorescence images from panel G. The values were normalized to wild type on *control(RNAi)* and each dot represents the quantification of fluorescence intensity per area from one L4 larvae. Values indicate means ± SD of 3 independent experiments in duplicates. $^{**}P<0.01$, $^{****}P<0.0001$ using Kruskal-Wallis test with Dunn's multiple comparison test to *control(RNAi)*.

https://doi.org/10.1371/journal.pgen.1008638.g002

fluorescence intensity is proportional to mitochondrial membrane potential [47]. Therefore, *ESCRT(RNAi)* results in an increase in mitochondrial membrane potential in *fzo-1(tm1133)* mutants. Hence, our data suggests that the suppression of *fzo-1(tm1133)*-induced UPR^{mt} upon ESCRT depletion is due to rescue of the decreased mitochondrial membrane potential and not the fragmented mitochondria phenotype.

Depletion of ESCRT components increases autophagic flux in *fzo-1 (tm1133)* animals

Previous studies have shown that in *C. elegans*, the depletion of ESCRT components leads to the induction of autophagy [39,40]. We confirmed this in wild-type animals (S2B Fig) and tested whether ESCRT depletion also induces autophagy in *fzo-1(tm1133)* animals. First, we determined the basal level of autophagy in *fzo-1(tm1133)* animals using three different assays that utilize the reporters $P_{lgg\text{-}1\ \mathrm{GABARAP}}gfp::lgg\text{-}1$ and $P_{sqst\text{-}1\ \mathrm{p62}}sqst\text{-}1::gfp$, which are widely used to monitor autophagy in *C. elegans* [40,48–52]. Specifically, we determined the number of GFP::LGG-$1^{GABARAP}$ foci in hypodermal seam cells of animals of the fourth larval stage (L4 larvae) and found that the average number of GFP::LGG-$1^{GABARAP}$ foci increases from ~4 on average in wild-type animals (+/+) to ~23 on average in *fzo-1(tm1133)* animals (Fig 3A and 3B). As a positive control, we used RNAi against the gene *let-363*^{mTOR}, which induces autophagy when knocked-down [19]. As expected, *let-363(RNAi)* animals show an increase in the number of GFP::LGG-$1^{GABARAP}$ foci in hypodermal seam cells (~15 on average) (Fig 3A and 3B). To determine whether the increase in the number of GFP::LGG-$1^{GABARAP}$ foci is caused by a block in autophagy, we analyzed the expression of the reporter $P_{sqst\text{-}1\ \mathrm{p62}}sqst\text{-}1::gfp$. (The accumulation of SQST-1^{p62}::GFP is indicative of defective autophagic clearance [51].) Whereas embryos homozygous for a lf mutation of *unc-51*^{ULK}, *e369*, a gene required for autophagy [26], show strong accumulation of SQST-1^{p62}::GFP, we found that *fzo-1(tm1133)* embryos do not accumulate SQST-1^{p62}::GFP (Fig 3C). To further verify an increase in autophagic flux in *fzo-1 (tm1133)* animals, we used an immunoblotting assay based on the cleavage of the GFP::LGG-$1^{GABARAP}$ fusion protein (in autolysosomes) to generate a 'free GFP' fragment, referred to as 'cleaved GFP' [50,53,54]. As shown in Fig 3D, compared to wild type, *fzo-1(tm1133)* mutants exhibit a ~2.7-fold increase on average in the level of cleaved GFP. This confirms that autophagic flux is increased in animals lacking *fzo-1*^{MFN}.

To test whether depletion of ESCRT components can further increase autophagy in *fzo-1 (tm1133)* animals, we knocked-down *vps-4*^{VPS4}, *vps-20*^{CHMP6}, *hgrs-1*^{HGS} or *vps-37*^{VPS37} in *fzo-*

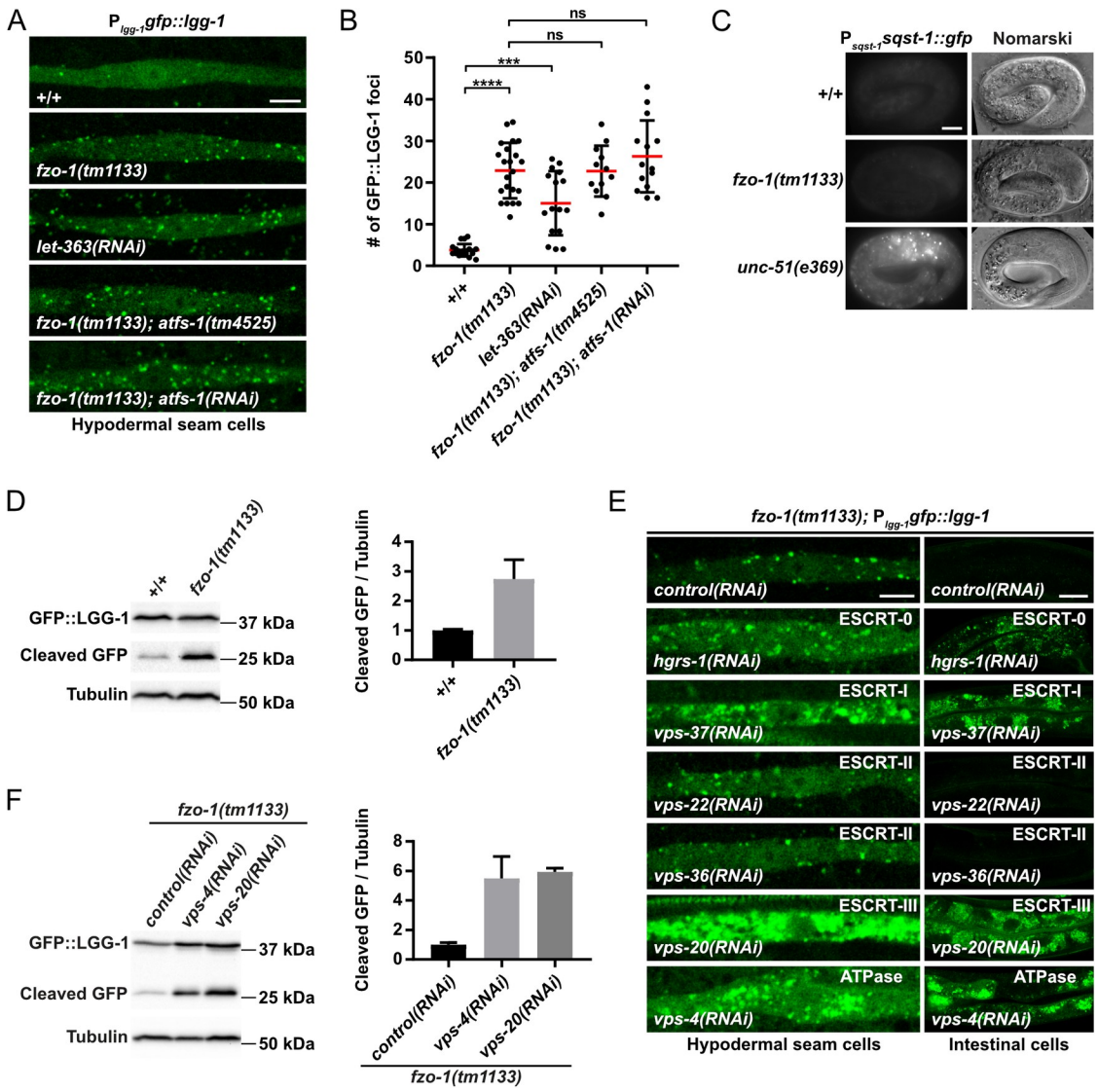

Fig 3. Autophagy is induced independently of ATFS-1^{ATF4,5} in *fzo-1(tm1133)* animals and further increased after ESCRT depletion. **(A)** P$_{lgg-1}$*gfp::lgg-1* expression in hypodermal seam cells of wild type (+/+), *fzo-1(tm1133)* or *fzo-1(tm1133); atfs-1 (tm4525)* L4 larvae. For RNAi against *let-363* and *atfs-1*, L4 larvae were subjected to the respective RNAi and the F1 generation was imaged. Scale bar: 5 μm. **(B)** Quantification of GFP::LGG-1 foci in hypodermal seam cells from panel A. Each dot represents the average amount of GFP::LGG-1 foci counted from 2–5 seam cells in one animal. n≥12 for each genotype; values indicate means ± SD; ns: not significant, $^{***}P<0.001$, $^{****}P<0.0001$ using Kruskal-Wallis test with Dunn's multiple comparison to wild type (+/+) or *fzo-1(tm1133)*, respectively. **(C)** Nomarski and fluorescent images of the P$_{sqst-1}$*sqst-1::gfp* translational reporter in embryos of wild type (+/+) or *fzo-1(tm1133)*. As a positive control for a block in autophagy, *unc-51(e369)* was used. Representative images of >60 embryos are shown. Scale bar: 10 μm. **(D)** Western blot analysis of cleaved GFP levels in wild type (+/+) or *fzo-1(tm1133)* using anti-GFP antibodies. Quantification of three independent experiments is shown. Values indicate means ± SD. **(E)** P$_{lgg-1}$*gfp::lgg-1* expression of *fzo-1(tm1133)* L4 larvae in hypodermal seam cells and intestinal cells upon *control(RNAi)*, *vps-4(RNAi)*, *vps-20(RNAi)*, *vps-22(RNAi)*, *hgrs-1(RNAi)*, *vps-36(RNAi)* or *vps-37(RNAi)*. Representative images of >80 animals from four independent biological replicates are shown. Scale bar hypodermal seam cells: 5 μm. Scale bar intestinal cells: 20 μm. **(F)** Western blot analysis of cleaved GFP levels in *fzo-1(tm1133)* upon *control(RNAi)*, *vps-4(RNAi)* or *vps-20(RNAi)* using anti-GFP antibodies. Quantification of four independent experiments is shown. Values indicate means ± SD.

https://doi.org/10.1371/journal.pgen.1008638.g003

1(tm1133) animals and analyzed GFP::LGG-1^{GABARAP} foci using the P$_{lgg-1\ GABARAP}$*gfp::lgg-1* reporter. We found that RNAi knock-down of each of these four genes in *fzo-1(tm1133)* animals causes a dramatic increase in the accumulation of GFP::LGG-1^{GABARAP} foci in

hypodermal seam cells as well as intestinal cells (Fig 3E). Furthermore, compared to *control (RNAi)*-treated animals, we found increased levels of cleaved GFP in *fzo-1(tm1133)* animals treated with *vps-4(RNAi)* (~5.5-fold) or *vps-20(RNAi)* (~5.9-fold) (Fig 3F). However, RNAi against the ESCRT-II components *vps-22*^{SNF8} or *vps-36*^{VPS36} (which fail to suppress *fzo-1 (tm1133)*-induced UPR^{mt} when knocked-down (Fig 1A–1D)) has no effect on the formation of GFP::LGG-1^{GABARAP} foci in hypodermal seam cells or intestinal cells (Fig 3E), probably due to an inefficient knock-down. In summary, our findings demonstrate that the depletion of components of ESCRT-0, -I, -III or the VPS-4 ATPase increases autophagic flux in *fzo-1 (tm1133)* animals.

Induction of autophagy suppresses *fzo-1(tm1133)*-induced UPR^{mt}

To determine whether increasing autophagy through means other than knock-down of ESCRT components also suppresses *fzo-1(tm1133)*-induced UPR^{mt}, we knocked-down *let-363*^{mTOR} by RNAi and examined the expression of P$_{hsp\text{-}6\ mtHSP70}$*gfp (bcSi9)* and P$_{hsp\text{-}60\ HSP60}$*gfp (zcIs9)* in *fzo-1(tm1133)* animals. We found that compared to controls, the expression of both reporters is significantly suppressed upon *let-363(RNAi)* in *fzo-1(tm1133)* animals (Fig 1A–1D). Specifically, on average, the expression of P$_{hsp\text{-}6\ mtHSP70}$*gfp* is suppressed by 40% and that of P$_{hsp\text{-}60\ HSP60}$*gfp* by 45%, which is comparable to the level of suppression observed upon RNAi knock-down of either *atfs-1*^{ATF4,5} or *vps-4*^{VPS4}. As shown for the depletion of ESCRT components, mitochondrial morphology upon *let-363(RNAi)* was found not to be altered in *fzo-1(tm1133)* or wild-type animals (Fig 2C, 2E and 2G and S3A and S3B Fig).

To obtain further evidence that induction of autophagy leads to suppression of *fzo-1 (tm1133)*-induced UPR^{mt}, we searched for additional genes with a regulatory role in autophagy in our dataset of 299 suppressors. We found 17 additional genes that were previously identified in a genome-wide RNAi screen for regulators of autophagy in *C. elegans* [40] (Fig 4A). Moreover, we used a database of autophagy-related genes and their orthologs (http://www.tanpaku.org/autophagy/index.html) [55], results from two screens for regulators of autophagy in mammals [56,57], three interaction databases (wormbase.org, genemania.org and string-db.org) followed by literature searches and identified 13 additional genes in our dataset that potentially induce autophagy upon knock-down (Fig 4A) [58–74]. Therefore, including the three genes encoding components of the ESCRT (*vps-4*^{VPS4}, *vps-20*^{CHMP6}, *vps-37*^{VPS37}), 33 of the 299 suppressors have previously been shown to induce autophagy when knocked-down.

Finally, we knocked-down all 299 suppressors in an otherwise wild-type background and tested for an increase in autophagy. Using this approach, we found that 126 genes encode negative regulators of autophagy (16 of which were among the 33 genes identified through our literature search; indicated by $^{\$}$ in Fig 4A), since they result in the accumulation of GFP::LGG-1^{GABARAP} foci in hypodermal seam cells and/or intestinal cells of larvae but not in the accumulation of SQST-1^{p62}::GFP in embryos when knocked-down (S1 Table). Adding the 17 genes that we identified through literature searches, which were not found in this 'autophagy' screen (Fig 4A), we, in total, found 143 out of 299 suppressors (~48%) of *fzo-1(tm1133)*-induced UPR^{mt} to negatively regulate autophagy.

To confirm that the additionally identified genes enhance autophagy also in the *fzo-1 (tm1133)* background, we knocked-down six of them (*cogc-2*^{COG2}, *cogc-4*^{COG4}, *hars-1*^{HARS}, *rpt-3*^{PSMC4}, *smgl-1*^{NBAS} and *ins-7*) and tested them for increased autophagic flux in *fzo-1 (tm1133)* animals. We found that the knock-down of each gene causes an increase in autophagic flux in *fzo-1(tm1133)* animals, most prominently in the intestine (Fig 4B). We also determined the level of cleaved GFP in these animals and found that, compared to *fzo-1(tm1133)*

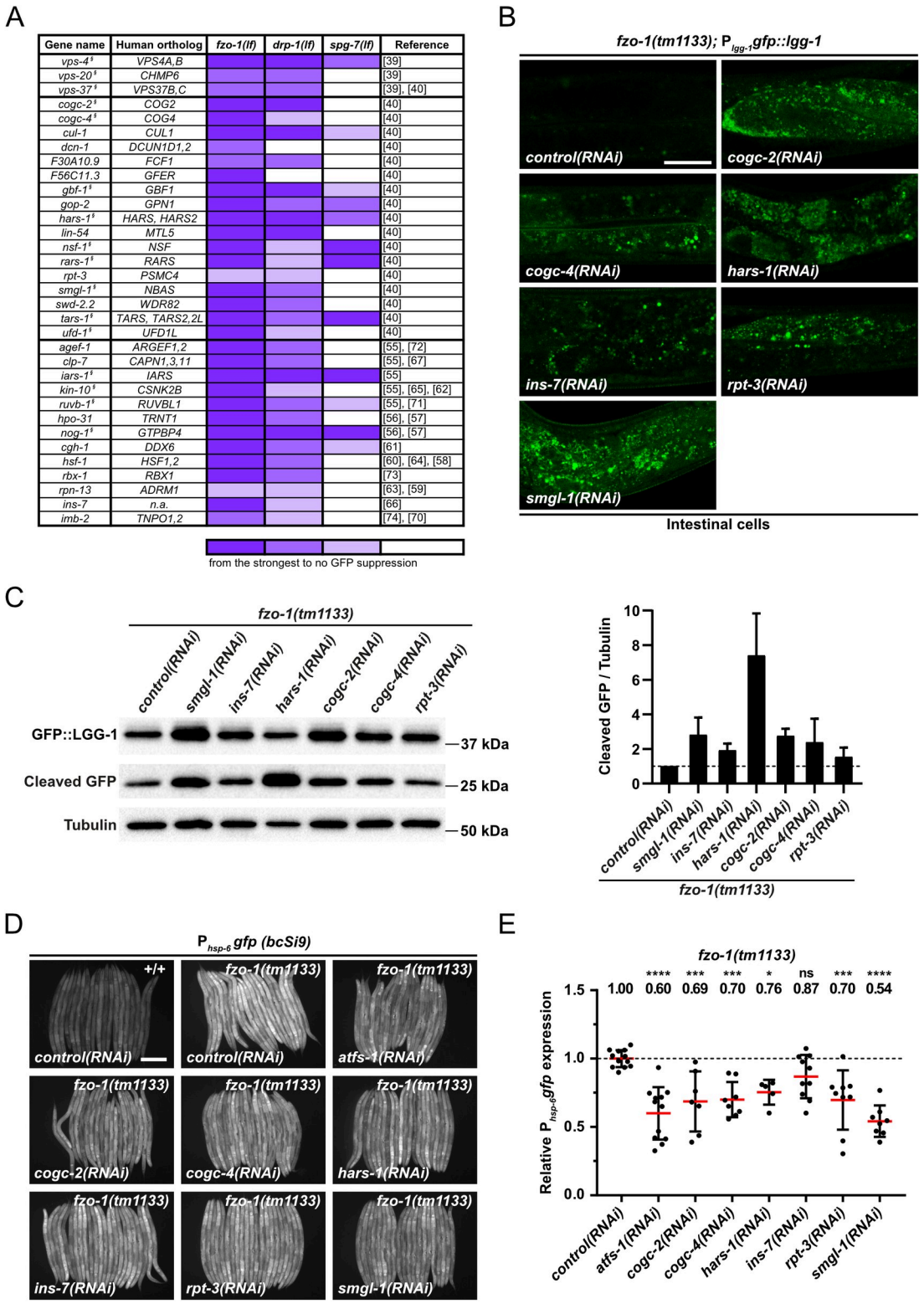

Fig 4. Additional candidates identified by RNAi screen that suppress *fzo-1(tm1133)*- and *drp-1(tm1108)*-induced UPR^{mt} through activation of autophagy. (A) List of candidate genes identified in the primary screen with *fzo-1(tm1133)*; P$_{hsp-6}$*gfp (zcIs13)* by RNAi. L4 larvae were subjected to the respective RNAi and the F1 generation was imaged. Candidate genes were screened three times in technical duplicates with the same reporter in two different mutant backgrounds: *drp-1(tm1108)* and *spg-7(ad2249)*. Fluorescence intensity was scored and classified from very strong suppression to weak suppression (gradual violet

coloring) or no suppression (white). § indicates genes that, upon knock-down in our experiments, showed accumulation of GFP::LGG-1 dots in hypodermal seam cells or intestinal cells. **(B)** P_{lgg-1}*gfp::lgg-1* expression of *fzo-1(tm1133)* L4 larvae in intestinal cells upon *control(RNAi)*, *cogc-2(RNAi)*, *cogc-4(RNAi)*, *hars-1(RNAi)*, *ins-7(RNAi)*, *rpt-3(RNAi)* or *smgl-1(RNAi)*. Representative images of >60 animals from four independent biological replicates are shown. Scale bar: 20 μm. **(C)** Western blot analysis of cleaved GFP levels in *fzo-1(tm1133)* upon *control(RNAi)*, *smgl-1(RNAi)*, *ins-7(RNAi)*, *hars-1(RNAi)*, *cogc-2(RNAi)*, *cogc-4(RNAi)* or *rpt-3(RNAi)* using anti-GFP antibodies. Quantification of three independent experiments is shown. Values indicate means ± SD. **(D)** Fluorescence images of L4 larvae expressing P_{hsp-6}*gfp (bcSi9)* in wild type (+/+) or *fzo-1(tm1133)*. L4 larvae were subjected to *control(RNAi)*, *atfs-1(RNAi)*, *cogc-2(RNAi)*, *cogc-4(RNAi)*, *hars-1(RNAi)*, *ins-7(RNAi)*, *rpt-3(RNAi)* or *smgl-1(RNAi)* and the F1 generation was imaged. Scale bar: 200 μm. **(E)** Quantifications of fluorescence images from panel D. After subtracting the mean fluorescence intensity of wild type (+/+) on *control(RNAi)*, the values were normalized to *fzo-1(tm1133)* on *control (RNAi)*. Each dot represents the quantification of fluorescence intensity of 15–20 L4 larvae. Values indicate means ± SD of at least 3 independent experiments in duplicates. ns: not significant, $^{*}P<0.05$, $^{***}P<0.001$, $^{****}P<0.0001$ using one-way ANOVA with Dunnett's multiple comparison test to *control(RNAi)*.

https://doi.org/10.1371/journal.pgen.1008638.g004

animals on *control(RNAi)*, the level is increased ranging from ~1.5-fold upon *rpt-3(RNAi)* to ~7.4-fold upon *hars-1(RNAi)* (Fig 4C). Using the single-copy $P_{hsp-6\ \mathrm{mtHSP70}}$*gfp* transgene *bcSi9*, we confirmed that the knock-down of *cogc-2*$^{\mathrm{COG2}}$, *cogc-4*$^{\mathrm{COG4}}$, *hars-1*$^{\mathrm{HARS}}$, *rpt-3*$^{\mathrm{PSMC4}}$, *smgl-1*$^{\mathrm{NBAS}}$ or *ins-7* suppresses *fzo-1(tm1133)*-induced UPR$^{\mathrm{mt}}$ (Fig 4D and 4E). Therefore, we propose that it is the increase in autophagic flux that suppresses *fzo-1(tm1133)*-induced UPR$^{\mathrm{mt}}$.

Since *let-363*$^{\mathrm{mTOR}}$ as well as some of the additionally identified candidates (such as *hars-1*$^{\mathrm{HARS}}$, *rars-1*$^{\mathrm{RARS}}$, *tars-1*$^{\mathrm{TARS}}$ or *iars-1*$^{\mathrm{IARS}}$) have roles in translation [19], we tested the effects of the depletion of *let-363*$^{\mathrm{mTOR}}$ or *hars-1*$^{\mathrm{HARS}}$ on $P_{ges-1\ \mathrm{GES2}}$*gfp* expression in order to exclude that their depletion simply attenuates synthesis of GFP protein. We found that *let-363(RNAi)* or *hars-1(RNAi)* leads to suppression of $P_{ges-1\ \mathrm{GES2}}$*gfp* expression by 39% or 25%, respectively (Fig 2A and 2B). However, we found that depletion of *let-363*$^{\mathrm{mTOR}}$ or *hars-1*$^{\mathrm{HARS}}$ also has a beneficial effect on mitochondrial membrane potential in *fzo-1(tm1133)* mutants since TMRE fluorescence intensity per mitochondrial area is increased by 14% or 31%, respectively while having the opposite effect in wild-type animals, in which it is decreased by 40% or 47%, respectively (Fig 2E–2H). This suggests that the suppression of *fzo-1(tm1133)*-induced UPR$^{\mathrm{mt}}$ upon depletion of *let-363*$^{\mathrm{mTOR}}$ or *hars-1*$^{\mathrm{HARS}}$ is the result of a combination of an increase in mitochondrial membrane potential and the attenuation of cytosolic translation.

The induction of autophagy is not *per se* beneficial for organismal fitness

Since mitochondrial membrane potential is increased in *fzo-1(tm1133)* animals upon induction of autophagy, we tested whether this has a beneficial effect at the organismal level. Using the 'thrashing' assay [75,76], we tested whether the motility of *fzo-1(tm1133)* animals is improved. As previously shown [77], thrashing rates are decreased in *fzo-1(tm1133)* mutants when compared to wild type (S5A Fig). We found that thrashing rates do not change upon *vps-4(RNAi)* or *vps-20(RNAi)* in either *fzo-1(tm1133)* or wild-type animals (S5B and S5C Fig). Therefore, increasing autophagic flux does not *per se* have beneficial effects on organismal fitness. In contrast, we found that thrashing rates are significantly increased upon *let-363(RNAi)* or *hars-1(RNAi)* in both *fzo-1(tm1133)* and wild-type animals (S5B and S5C Fig). Thus, the induction of autophagy can lead to increased motility under certain circumstances, but this effect may be covered upon depletion of ESCRT.

Depletion of ESCRT components in *fzo-1(tm1133)* animals with a block in autophagy results in embryonic lethality

To test the hypothesis that increased autophagic flux is necessary for the suppression of *fzo-1 (tm1133)*-induced UPR$^{\mathrm{mt}}$ in ESCRT-depleted animals, we generated a *fzo-1(tm1133); unc-51 (e369)* double mutant in the $P_{hsp-6\ \mathrm{mtHSP70}}$*gfp (bcSi9)* reporter background and subjected it to

RNAi against either *vps-4*^{VPS4} or *vps-20*^{CHMP6}. However, we found that either RNAi treatment results in progeny that undergoes embryonic arrest. To circumvent this problem, we subjected *fzo-1(tm1133)* mutants to double-RNAi against *unc-51*^{ULK} and *ESCRT* but failed to detect suppression of UPR^{mt} upon *ESCRT(RNAi)* diluted with *control(RNAi)* (S6A Fig). Next, we depleted ESCRT components by RNAi starting from the second larval stage (L2) (rather than in the parental generation and throughout development) and examined reporter expression once the animals had reached the fourth larval stage (L4). Interestingly, we found that subjecting *fzo-1 (tm1133)* L2 larvae to *vps-4(RNAi)* or *vps-20(RNAi)* does not increase autophagic flux and fails to suppress UPR^{mt}, while *atfs-1(RNAi)* is able to suppress UPR^{mt} under these conditions (S6B and S6C Fig). We repeated this experiment in the background of an RNAi-sensitizing mutation, *rrf-3(pk1426)*, but again were unable to detect suppression of the P$_{hsp\text{-}6\ \mathrm{mtHSP70}}$*gfp (bcSi9)* reporter upon *ESCRT(RNAi)* while *atfs-1(RNAi)* suppressed (S6D Fig). Based on these results, we conclude that *ESCRT(RNAi)* does not directly act on ATFS-1^{ATF4,5} to suppress UPR^{mt}. Instead, we propose that it affects UPR^{mt} indirectly through the induction of autophagy.

Blocking mitophagy does not prevent suppression in *fzo-1*(*tm1133*) animals of UPR^{mt} by ESCRT depletion

Since we were unable to test whether blocking autophagy blocks the suppression of *fzo-1 (tm1133)*-induced UPR^{mt} by depletion of ESCRT components, we tested the role of *pdr-1*^{Parkin}- and *fndc-1*^{FUNDC1,2}-dependent mitophagy in this context [78,79]. First, we used *fzo-1(tm1133); pdr-1(lg103)* double mutants, carrying the P$_{hsp\text{-}6\ \mathrm{mtHSP70}}$*gfp* (*bcSi9*) reporter, to test whether *pdr-1*^{Parkin}-dependent mitophagy is required for ESCRT-dependent suppression of *fzo-1(tm1133)*-induced UPR^{mt}. We found that knock-down of *vps-4*^{VPS4}, *vps-20*^{CHMP6} or *hgrs-1*^{HGS} still suppresses *fzo-1(tm1133)*-induced UPR^{mt} in the *pdr-1(lg103)* background (Fig 5A and 5B). Furthermore, compared to the level of suppression in *fzo-1(tm1133)* animals alone, the level of UPR^{mt} suppression in *fzo-1(tm1133); pdr-1(lg103)* animals is similar upon *vps-4(RNAi)* or *vps-20(RNAi)* and even higher upon *hgrs-1(RNAi)* (Figs 1A, 1C, 5A and 5B). Second, we tested whether depletion of ESCRT components suppresses UPR^{mt} in *fzo-1(tm1133) fndc-1(rny14)* double mutants and found that it does so to a similar extent (Fig 5C and 5D). Therefore, *pdr-1*^{Parkin}- and *fndc-1*^{FUNDC1,2}-dependent mitophagy are not required for the suppression of *fzo-1 (tm1133)*-induced UPR^{mt} upon ESCRT depletion.

Blocking autophagy in the absence of mitochondrial stress induces UPR^{mt}, but neither blocking nor inducing UPR^{mt} affects autophagy

Increasing autophagic flux suppresses *fzo-1(tm1133)*-induced UPR^{mt}. To test whether decreasing autophagic flux, conversely, induces UPR^{mt}, we analyzed *unc-51(e369)* animals (in which autophagy is blocked) and found that compared to wild-type animals, the P$_{hsp\text{-}6\ \mathrm{mtHSP70}}$*gfp* reporter is induced by 41% on average (Fig 5E and 5F). To determine whether the P$_{hsp\text{-}6\ \mathrm{mtHSP70}}$*gfp* reporter is also induced under conditions where UPR^{mt} is already activated, we analyzed *fzo-1(tm1133)*; *unc-51(e369)* double mutant animals. We found that, in the *fzo-1 (tm1133)* background, the loss of *unc-51*^{ULK} does not result in a significant increase in the expression of P$_{hsp\text{-}6\ \mathrm{mtHSP70}}$*gfp* (Fig 5E and 5F). Thus, blocking autophagy induces UPR^{mt} in the absence of mitochondrial stress but not under conditions where UPR^{mt} is already activated.

Next, we analyzed whether blocking or inducing UPR^{mt} affects autophagy. Therefore, we analyzed autophagy in animals homozygous for either the *atfs-1*^{ATF4,5} lf mutation *tm4525* or the *atfs-1*^{ATF4,5} gain-of-function (gf) mutation *et15*gf [11,80]. *atfs-1(tm4525)* has been shown to suppress the expression of the P$_{hsp\text{-}6\ \mathrm{mtHSP70}}$*gfp* and P$_{hsp\text{-}60\ \mathrm{HSP60}}$*gfp* reporters upon *spg-7*

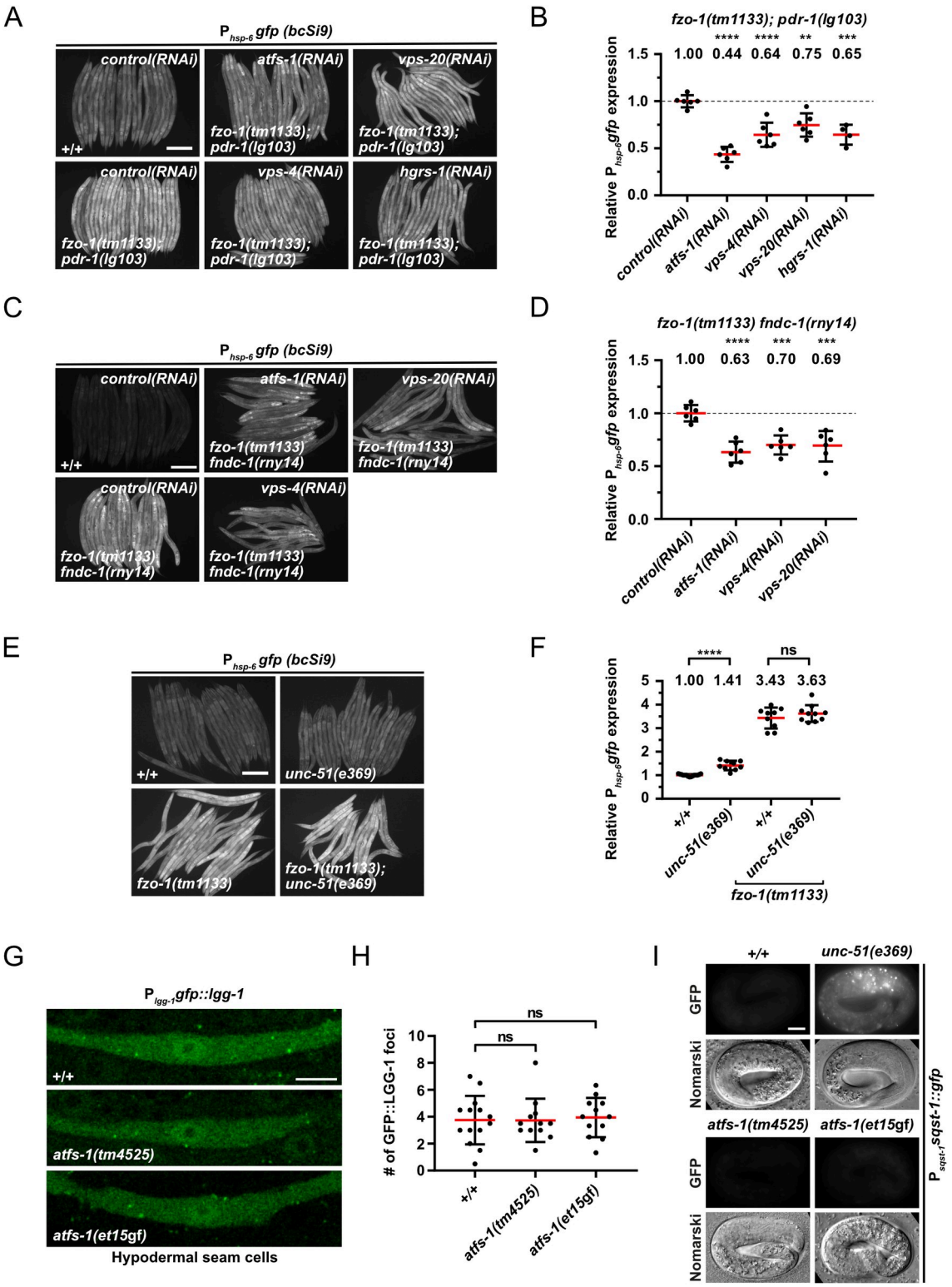

Fig 5. Functional interactions between mitophagy, autophagy and UPR^{mt}. (A) L4 larvae of *fzo-1(tm1133); pdr-1(lg103)* expressing P_{hsp-6}*gfp (bcSi9)* were subjected to *control(RNAi)*, *atfs-1(RNAi)*, *vps-4(RNAi)*, *vps-20(RNAi)* or *hgrs-1(RNAi)* and the F1 generation was imaged. Scale bar: 200 μm. **(B)** Quantifications of fluorescence images from panel A. After subtracting the mean fluorescence intensity of wild type (+/+) on *control(RNAi)*, the values were normalized to *fzo-1(tm1133); pdr-1(lg103)* on *control(RNAi)*. Each dot represents the quantification of fluorescence intensity of 15–20 L4 larvae. Values indicate means ± SD of 3 independent experiments in

duplicates. $^{**}P<0.01$, $^{***}P<0.001$, $^{****}P<0.0001$ using one-way ANOVA with Dunnett's multiple comparison test to *control(RNAi)*. **(C)** L4 larvae of *fzo-1(tm1133) fndc-1(rny14)* expressing P_{hsp-6}*gfp (bcSi9)* were subjected to *control(RNAi)*, *atfs-1(RNAi)*, *vps-4(RNAi)* or *vps-20(RNAi)* and the F1 generation was imaged. Scale bar: 200 μm. **(D)** Quantifications of fluorescence images from panel C. After subtracting the mean fluorescence intensity of wild type (+/+) on *control(RNAi)*, the values were normalized to *fzo-1(tm1133) fndc-1 (rny-14)* on *control(RNAi)*. Each dot represents the quantification of fluorescence intensity of 15–20 L4 larvae. Values indicate means ± SD of 3 independent experiments in duplicates. $^{***}P<0.001$, $^{****}P<0.0001$ using one-way ANOVA with Dunnett's multiple comparison test to *control(RNAi)*. **(E)** Fluorescence images of L4 larvae expressing P_{hsp-6}*gfp (bcSi9)* in wild type (+/+), *unc-51(e369)*, *fzo-1(tm1133)* or *fzo-1(tm1133); unc-51(e369)*. Scale bar: 200 μm. **(F)** Quantifications of fluorescence images from panel E. Each dot represents the quantification of fluorescence intensity of 15–20 L4 larvae. Values indicate means ± SD of at least 4 independent experiments in duplicates. ns: not significant, $^{****}P<0.0001$ using two-tailed t-test. **(G)** P_{lgg-1}*gfp::lgg-1* expression in hypodermal seam cells of wild type (+/+), *atfs-1(tm4525)* or *atfs-1(et15*gf*)* L4 larvae. Scale bar: 5 μm. **(H)** Quantification of GFP::LGG-1 foci in hypodermal seam cells from panel G. Each dot represents the average amount of GFP::LGG-1 foci counted from 2–5 seam cells in one animal. n≥12 for each genotype; values indicate means ± SD; ns: not significant using one-way ANOVA with Dunnett's multiple comparison test to wild type (+/+). **(I)** Nomarski and fluorescent images of the P_{sqst-1}*sqst-1::gfp* translational reporter in embryos of wild type (+/+), *atfs-1(tm4525)* or *atfs-1(et15*gf*)* animals. As a positive control for a block in autophagy, *unc-51(e369)* was used. Representative images of >60 embryos are shown. Scale bar: 10 μm.

https://doi.org/10.1371/journal.pgen.1008638.g005

(RNAi) and of the endogenous *hsp-6*$^{\text{mtHSP70}}$ and *hsp-60*$^{\text{HSP60}}$ loci upon *cco-1(RNAi)* [11,81]. Conversely, *atfs-1(et15*gf*)* has been shown to constitutively activate UPR$^{\text{mt}}$ [80]. We found that compared to wild-type animals, hypodermal seam cells of *atfs-1(tm4525)* or *atfs-1(et15*gf*)* animals show no significant changes in the number of GFP::LGG-1$^{\text{GABARAP}}$ foci (Fig 5G and 5H). In addition, *atfs-1(tm4525)* or *atfs-1(et15*gf*)* embryos do not accumulate SQST-1$^{\text{p62}}$::GFP foci (Fig 5I). Since it has previously been reported that mitochondrial stress induces autophagy in an *atfs-1*$^{\text{ATF4,5}}$-dependent manner [40], we also tested whether the loss of *atfs-1*$^{\text{ATF4,5}}$ suppresses autophagy in *fzo-1(tm1133)* animals. We found that the number of GFP::LGG-1$^{\text{GABARAP}}$ foci remains unchanged both in *fzo-1(tm1133)* animals upon *atfs-1(RNAi)* as well as *fzo-1(tm1133); atfs-1(tm4525)* double mutants (Fig 3A and 3B), demonstrating that the induction of autophagy in *fzo-1(tm1133)* mutants is ATFS-1$^{\text{ATF4,5}}$-independent. Finally, we tested whether increasing UPR$^{\text{mt}}$ in *fzo-1(tm1133)* mutants by introducing *atfs-1(et15*gf*)* affects autophagic flux. However, we found that *fzo-1(tm1133); atfs-1(et15*gf*)* double mutants are not viable. Therefore, blocking or inducing UPR$^{\text{mt}}$ by manipulating ATFS-1$^{\text{ATF4,5}}$ activity does not affect autophagic flux in wild type and blocking UPR$^{\text{mt}}$ does not affect autophagy in *fzo-1(tm1133)* animals.

The induction of autophagy suppresses UPR$^{\text{mt}}$ induced by a block in mitochondrial dynamics but not by the loss of *spg-7*$^{\text{AFG3L2}}$

To determine whether the suppression of UPR$^{\text{mt}}$ by increased autophagic flux is specific to *fzo-1(tm1133)*-induced UPR$^{\text{mt}}$, we tested all 143 suppressors of *fzo-1(tm1133)*-induced UPR$^{\text{mt}}$ with a role in autophagy for their ability to suppress *drp-1(tm1108)*- or *spg-7(ad2249)*-induced UPR$^{\text{mt}}$ using the multi-copy $P_{hsp-6\ \text{mtHSP70}}$*gfp* transgene *zcIs13*. As shown in Fig 4A and S1 Table, we found that the knock-down of 138 of the genes (~97%) also suppresses *drp-1 (tm1108)*-induced UPR$^{\text{mt}}$. In contrast, the knock-down of 90 of the genes (~63%) suppresses *spg-7(ad2249)*-induced UPR$^{\text{mt}}$. Among these 90 genes, 41 belong to the GO categories 'Translation' or 'Ribosome Biogenesis'. Hence, their depletion may interfere with synthesis of GFP.

Interestingly, we found that knock-down of *vps-4*$^{\text{VPS4}}$ but not *vps-20*$^{\text{CHMP6}}$ or *vps-37*$^{\text{VPS37}}$ also suppresses *spg-7(ad2249)*-induced UPR$^{\text{mt}}$ (Fig 4A). Therefore, we tested whether the knock-down of *vps-4*$^{\text{VPS4}}$ or *vps-20*$^{\text{CHMP6}}$ leads to increased autophagic flux in *spg-7(ad2249)* animals. We first analyzed the basal level of autophagy in *spg-7(ad2249)* animals using the $P_{lgg-1\ \text{GABARAP}}$*gfp::lgg-1* reporter and found that compared to wild type, the number of GFP::LGG-1$^{\text{GABARAP}}$ foci is increased 2-fold (from ~4 on average in wild-type animals to ~8 on average in *spg-7(ad2249)* animals) (S7A and S7B Fig). To determine whether this increase in autophagosomes is due to a block in autophagy, we analyzed the accumulation of SQST-1$^{\text{p62}}$::GFP using

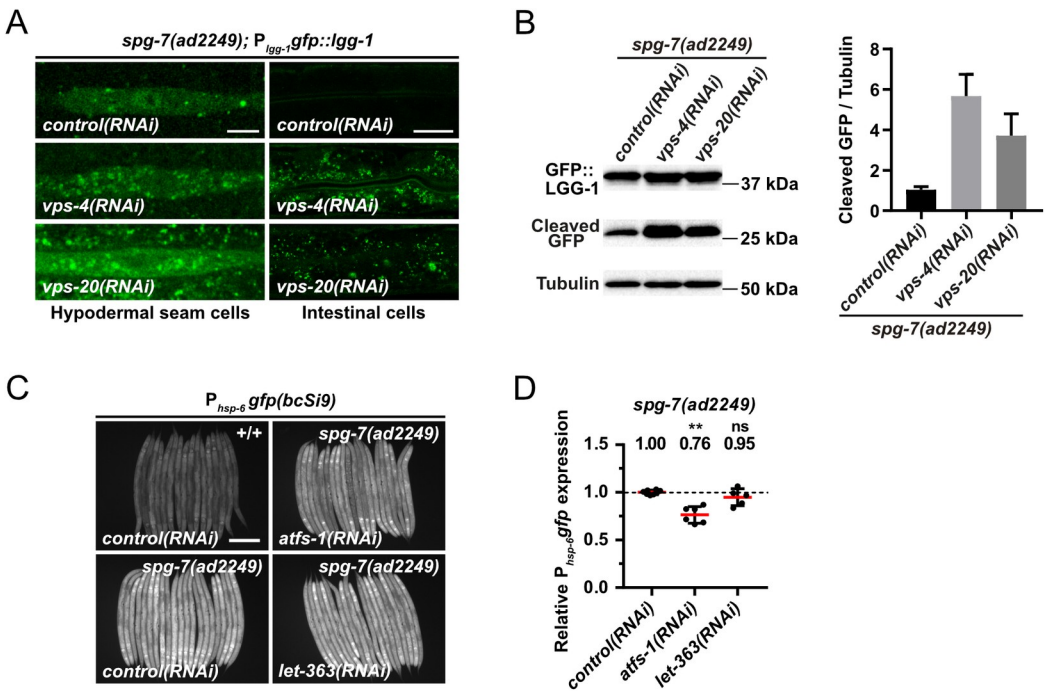

Fig 6. Induction of autophagy is not sufficient to suppress *spg-7(ad2249)*-induced UPR^{mt}. **(A)** P$_{lgg-1}$*gfp::lgg-1* expression of *spg-7(ad2249)* L4 larvae in hypodermal seam cells and intestinal cells upon *control(RNAi)*, *vps-4(RNAi)* or *vps-20(RNAi)*. Representative images of >80 animals from three independent biological replicates are shown. Scale bar hypodermal seam cells: 5 μm. Scale bar intestinal cells: 20 μm. **(B)** Western blot analysis of cleaved GFP levels in *spg-7(ad2249)* upon *control (RNAi)*, *vps-4(RNAi)* or *vps-20(RNAi)* using anti-GFP antibodies. Quantification of three independent experiments is shown. Values indicate means ± SD. **(C)** Fluorescence images of L4 larvae expressing P$_{hsp-6}$*gfp (bcSi9)* in wild type (+/+) or *spg-7(ad2249)*. L4 larvae were subjected to *control(RNAi)*, *atfs-1(RNAi)* or *let-363(RNAi)* and the F1 generation was imaged. Scale bar: 200 μm. **(D)** Quantifications of fluorescence images from panel C. After subtracting the mean fluorescence intensity of wild type (+/+) on *control(RNAi)*, the values were normalized to *spg-7(ad2249)* on *control(RNAi)*. Each dot represents the quantification of fluorescence intensity of 15–20 L4 larvae. Values indicate means ± SD of 3 independent experiments in duplicates. ns: not significant, $^{**}P<0.01$ using Kruskal-Wallis test with Dunn's multiple comparison test to *control(RNAi)*.

https://doi.org/10.1371/journal.pgen.1008638.g006

the P$_{sqst-1\ p62}$*sqst-1*::*gfp* reporter. We did not observe SQST-1^{p62}::GFP accumulation in *spg-7 (ad2249)* animals, thus indicating that autophagic flux is increased in *spg-7(ad2249)* mutants (S7C Fig). Next, we tested whether *vps-4(RNAi)* or *vps-20(RNAi)* further induces autophagy in the *spg-7(ad2249)* background and found that knock-down of *vps-4*^{VPS4} and also *vps-20*^{CHMP6} leads to an increase in the average number of GFP::LGG-1^{GABARAP} foci in hypodermal seam cells and intestinal cells (Fig 6A). Confirming an increase in autophagic flux, immunoblotting of GFP::LGG-1^{GABARAP} in *spg-7(ad2249)* animals revealed increased levels of cleaved GFP upon *vps-4(RNAi)* or *vps-20(RNAi)* (~5.7-fold and ~3.7-fold, respectively; Fig 6B). Finally, we tested whether the loss of *let-363*^{mTOR}, which induces autophagy and suppresses *fzo-1 (tm1133)*-induced UPR^{mt} (Fig 1A–1D), can suppress *spg-7(ad2249)*-induced UPR^{mt}. Using the single-copy P$_{hsp-6\ mtHSP70}$*gfp* transgene *bcSi9*, we found that RNAi knock-down of *let-363*^{mTOR} fails to suppress *spg-7(ad2249)*-induced UPR^{mt} (Fig 6C and 6D). In summary, these results indicate that UPR^{mt} induced by the loss of *spg-7*^{AFG3L2} is not suppressed by increasing autophagic flux. Based on these findings we propose that the induction of autophagy is sufficient to suppress UPR^{mt} induced by a block in mitochondrial dynamics but not by the loss of *spg-7*^{AFG3L2}.

Defects in mitochondrial dynamics lead to changes in the levels of certain types of triacylglyerols, which can partially be reverted by induction of autophagy

To elucidate how the induction of autophagy leads to suppression of UPR^{mt} in *fzo-1(tm1133)* and *drp-1(tm1108)* animals, we determined potential differences in metabolism in these genetic backgrounds. Since mitochondria and autophagy are known to regulate specific aspects of lipid metabolism, we performed non-targeted lipid profiling in *fzo-1(tm1133)*, *drp-1 (tm1108)* and *spg-7(ad2249)* mutant backgrounds and compared them to wild type.

Of the 5284 lipid 'features' detected, the levels of 3819 are changed in at least one of the three pairwise comparisons (*fzo-1(tm1133)* vs. wild type, *drp-1(tm1108)* vs. wild type, *spg-7 (ad2249)* vs. wild type) (S8A Fig). Among the 3819 lipid features that are changed, 1774 are currently annotated as lipids. Interestingly, a third of the annotated lipids, whose levels were changed, are triacylglycerols (TGs). TGs are storage lipids and make up a major part of lipid droplets, which are broken down into fatty acids and subsequently oxidized in mitochondria upon energy demand [82–84]. We initially determined the total amounts of TGs in the mutant backgrounds and compared them to that of wild type. Whereas *drp-1(tm1108)* mutants show an increase in the total amount of TGs, no changes are observed in *fzo-1(tm1133)* mutants and a decrease is detected in *spg-7(ad2249)* mutants (S8B Fig). To determine whether the amounts of TG species with a specific length of acyl chains and/or number of double bonds are altered, we plotted all 659 detected TGs and subsequently marked TGs that are specifically up- (red) or downregulated (blue) in *fzo-1(tm1133)*, *drp-1(tm1108)* or *spg-7(ad2249)* animals (S8C Fig and S2 Table). Consistent with the observed decrease in the total amount of TGs, most of the individual TG species are downregulated in *spg-7(ad2249)* mutants (S8B and S8C Fig). In the *drp-1(tm1108)* background, TG species with altered levels initially showed no distinct pattern regarding length of acyl chains or degree of desaturation (S8C Fig and S2 Table). However, in the *fzo-1(tm1133)* background, these TG species can be separated into two clusters. Whereas TGs with shorter acyl chains are downregulated in *fzo-1(tm1133)* mutants, 'longer' TGs with a higher degree of unsaturation are increased (S8C Fig and S2 Table). Interestingly, when looking at the overlap between *fzo-1(tm1133)* and *drp-1(tm1108)*, we observed a similar trend regarding changes in acyl length and desaturation for *drp-1(tm1108)* as well (S8D Fig and S2 Table).

Next, we tested whether the induction of autophagy can revert the specific changes in TG pattern observed in *fzo-1(tm1133)* mutants. Therefore, we knocked-down *vps-4*^{VPS4} or *cogc-2*^{COG2} to induce autophagy in *fzo-1(tm1133)* and wild-type animals and again, performed lipid profiling. We used principal component analysis (PCA) in order to show how distinct or similar the lipid profiles upon *vps-4(RNAi)* or *cogc-2(RNAi)* are. Interestingly, knock-down of *vps-4*^{VPS4} in either genotype was distinct from controls, which indicates major changes in the lipidome due to an efficient RNAi knock-down (Fig 7A). Moreover, we found that RNAi against *cogc-2*^{COG2} has only mild effects, since the samples cluster with controls in both genotypes. This might be attributed to a weak knock-down and most probably a weak induction of autophagy.

Subsequently, we specifically analyzed the TGs in *fzo-1(tm1133)* mutants on *control(RNAi)* and, consistent with our previous results (S8C Fig (left panel) and S2 Table), detected a decrease in the levels of TGs with shorter acyl chains while levels of TGs with longer chains increase, compared to wild type on *control(RNAi)* (Fig 7B (left panel) and S2 Table). The levels of TGs that are downregulated in the *fzo-1(tm1133)* background are either unchanged or further decreased upon depletion of *vps-4*^{VPS4} and the concomitant induction of autophagy (Fig 7B (middle panel) and S2 Table). In contrast, the levels of TGs that are upregulated in *fzo-1*

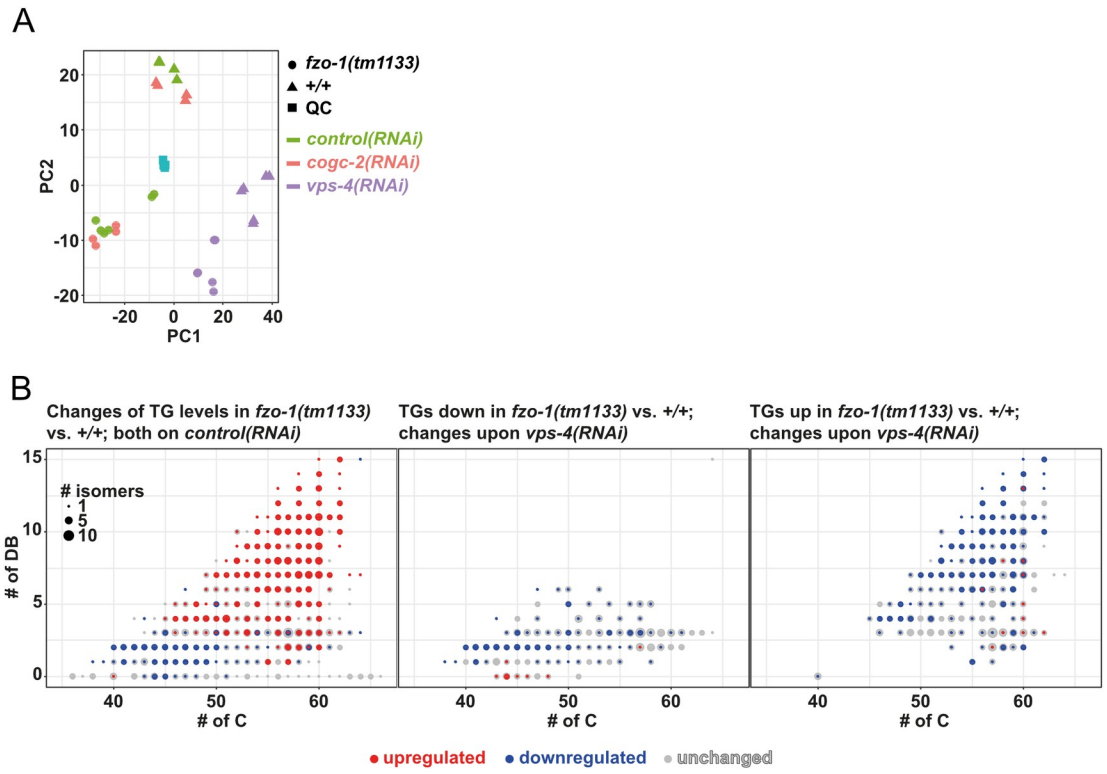

Fig 7. Induction of autophagy upon *vps-4(RNAi)* changes the levels of specific TGs in *fzo-1(tm1133)* mutants. (A) Principal component analysis (PCA) scores plot of wild-type (+/+) and *fzo-1(tm1133)* animals subjected to *control(RNAi)*, *cogc-2(RNAi)* or *vps-4(RNAi)*. Turquois squares indicate internal quality controls (QC). **(B)** Scatterplot indicating the distribution and changes in the levels of TG species in *fzo-1(tm1133)* mutants in comparison to wild type (+/+). The x-axis labels the number of carbons (# of C) and the y-axis the number of double bonds (DB) in the acyl sidechains. The size of a dot indicates the number of detected isomers for a specific sum composition. Grey dots represent all detected TGs species and blue and red dots indicate down- (blue) or upregulation (red).

https://doi.org/10.1371/journal.pgen.1008638.g007

(tm1133) animals are reduced upon induction of autophagy by knock-down of *vps-4*^{VPS4}, although not always to the levels of wild type (Fig 7B (right panel) and S2 Table). Upon *cogc-2 (RNAi)*, we detected only minor effects on the levels of TGs in *fzo-1(tm1133)* (S9A Fig and S2 Table), which is consistent with the relatively small changes in the lipid profile as assessed by PCA (Fig 7A). However, the levels of most TGs that are decreased upon *cogc-2(RNAi)* are also decreased upon depletion of *vps-4*^{VPS4} (S9B Fig), suggesting that the induction of autophagy caused by the two different knock-downs leads to partially overlapping changes in the levels of TGs. Taken together, we find that the levels of specific TGs are changed in a similar manner in mutants with defects in mitochondrial dynamics. Moreover, we show that some of these changes can be reverted by the induction of autophagy in *fzo-1(tm1133)* animals.

Discussion

Induction of autophagy increases mitochondrial membrane potential and suppresses UPR^{mt} in *fzo-1(tm1133)* mutants

We propose that the induction of autophagy partially restores membrane potential and thereby suppresses *fzo-1(tm1133)*-induced UPR^{mt}. Interestingly, a decrease in mitochondrial membrane potential has recently been shown to be the signal for UPR^{mt} induction [10]. Therefore, some aspect of mitochondrial stress that leads to both decreased membrane potential and the

induction of UPR^{mt} in *fzo-1(tm1133)* mutants can be rescued by the induction of autophagy in these animals. We were unable to verify our hypothesis since ESCRT-depleted *fzo-1(tm1133); unc-51(e369)* double mutants arrest during embryogenesis. This is in agreement with a study from Djeddi *et al*., which reported that induction of autophagy is a pro-survival mechanism in ESCRT-depleted animals [39]. Moreover, our data suggests that clearance of defective and depolarized mitochondria by *pdr-1*^{Parkin}- or *fndc-1*^{FUNDC1,2}-dependent mitophagy does not play a role in the suppression of *fzo-1(tm1133)*-induced UPR^{mt}. In addition, we propose that the induction of autophagy may lead to increased organismal fitness, but that this effect is masked by pleiotropic effects upon knock-down of certain genes such as the *ESCRT* genes.

Increased autophagic flux compensates for a block in mitochondrial dynamics

We provide evidence that the induction of autophagy can also compensate for a block in mitochondrial fission and, hence, for defects in mitochondrial dynamics. In contrast, induction of autophagy does not suppress *spg-7(ad2249)*-induced UPR^{mt}. Among the genes that suppress *spg-7(ad2249)*-induced UPR^{mt} almost half have roles in translation or ribosome biogenesis, the knock-down of which may impair GFP synthesis by compromising cytosolic translation. Furthermore, we speculate that the knock-down of the remaining genes suppresses *spg-7 (ad2249)*-induced UPR^{mt} through mechanisms other than the induction of autophagy. This supports the notion that UPR^{mt} induced by different types of mitochondrial stress are distinct in their mechanisms of induction and also in their mechanisms of suppression. In line with this, we found that different mitochondrial stresses have different impacts on the lipidome. Although FZO-1 and DRP-1 play different roles in mitochondrial dynamics, they have similar effects on the levels of many TGs when mutated. In contrast, the levels of these TGs are distinct in *spg-7(ad2249)* animals. The role of mitochondria in the metabolism of TGs is diverse. First, mitochondria are using fatty acids released from TGs upon lipolysis for energy production. Second, lipid droplet associated mitochondria deliver building blocks and energy for the synthesis of fatty acids and TGs. Fatty acids derived from this pathway typically show lower chain length and a higher degree of saturation [85]. Since we see a decrease in TGs with shorter chain length in *fzo-1(tm1133)* mutants, it is plausible that contact sites between lipid droplets and mitochondria are affected. Consistent with this, Benador *et al.* found high levels of MFN2 in lipid droplet associated mitochondria in brown adipose tissue of mice [85]. Furthermore, Rambold *et al.* reported that altered mitochondrial morphology in mouse embryonic fibroblasts lacking either *Opa1* or *Mfn1* affects fatty acid transfer from lipid droplets to mitochondria, thereby causing heterogeneous fatty acid distribution across the mitochondrial population [86]. Therefore, we speculate that the loss of *fzo-1*^{MFN} or *drp-1*^{DRP1} but not *spg-7*^{AFG3L2} leads to alterations in contact sites between lipid droplets and mitochondria and that these alterations lead to specific changes in metabolism.

Interestingly, we found that increasing autophagic flux in *fzo-1(tm1133)* animals reverts some of the changes in the levels of TGs. Consistent with these results, autophagy has been shown to have a role in the breakdown of TGs from lipid droplets, which ensures a constant fatty acid supply to mitochondria for β-oxidation [87], highlighting the importance of autophagy in fatty acid metabolism. More recently, autophagy has also been shown to directly affect the levels of enzymes involved in β-oxidation by causing the degradation of the co-repressor of PPARα, a master regulator of lipid metabolism [88]. Therefore, we propose that the induction of autophagy in mutants with defects in mitochondrial dynamics results in elevated breakdown of specific TGs that are used to fuel mitochondrial metabolism, thereby leading to increased mitochondrial membrane potential and suppression of UPR^{mt}.

Functional interactions between autophagy and UPR^{mt}

Protection of mitochondrial and ultimately cellular homeostasis was previously proposed to be dependent on the integration of different mitochondrial and cellular stress pathways but experimental data so far was limited [89]. The first evidence that autophagy can affect UPR^{mt} was the finding by Haynes *et al*. that knock-down of *rheb-1*^{RHEB}, a known positive regulator of TOR [90], suppresses the $P_{hsp\text{-}60\ HSP60}$*gfp* reporter [13]. Two more recent studies reported contradictory results with respect to the effect of blocking mitophagy on UPR^{mt} induction [7,91]. We demonstrate that a block in autophagy in the absence of mitochondrial stress induces UPR^{mt}. Blocking autophagy results in major changes in metabolism [92,93] which may, to some extent, be caused by decreased delivery of lipids into mitochondria. This could consequently lead to the activation of UPR^{mt} and thereby to a metabolic shift towards glycolysis [94]. Thus, *fzo-1(tm1133)* mutants, in which UPR^{mt} is already activated, are less dependent on their mitochondria with regard to energy production and this might explain why blocking autophagy in these animals does not further increase UPR^{mt}. Interestingly, based on our results, altering autophagy can influence UPR^{mt}, but changes in UPR^{mt} do not affect autophagy. In contrast, Guo *et al*. reported that upon mitochondrial stress, upregulation of both UPR^{mt} and autophagy is dependent on ATFS-1^{ATF4,5} [40] and Nargund *et al*. showed that a small subset of autophagy related genes are upregulated via ATFS-1^{ATF4,5} upon mitochondrial stress (induced by *spg-7(RNAi)*) [11]. However, we show that import of ATFS-1^{ATF4,5} into the nucleus under conditions where mitochondrial stress is absent, is not sufficient to induce autophagy. Taken together, we found a previously undescribed functional connection between autophagy and UPR^{mt}. We propose that the two pathways do not interact directly but that the induction of autophagy leads to improved mitochondrial function by affecting lipid metabolism and ameliorating cellular homeostasis, thereby suppressing UPR^{mt} in mutants with defects in mitochondrial dynamics (Fig 8).

Genome-wide RNAi screen identifies a new autophagy network

In our dataset of 299 suppressors of *fzo-1(tm1133)*-induced UPR^{mt} we found 143 genes that negatively regulate autophagy. Interestingly, 94% of these candidates (135/143) have orthologs in humans. We identified several components of the ubiquitin-proteasome system (UPS) (*rpt-3*^{PSMC4}, *rpn-13*^{ADRM1}, *ufd-1*^{UFD1}, *rbx-1*^{RBX1}, *cul-1*^{CUL1}) [73,95,96] and found evidence in the literature that activation of autophagy compensates for the loss of the UPS [59,63]. Additionally, we identified several genes that are involved in cell signaling, e.g. *ruvb-1*^{RUVBL1}, a

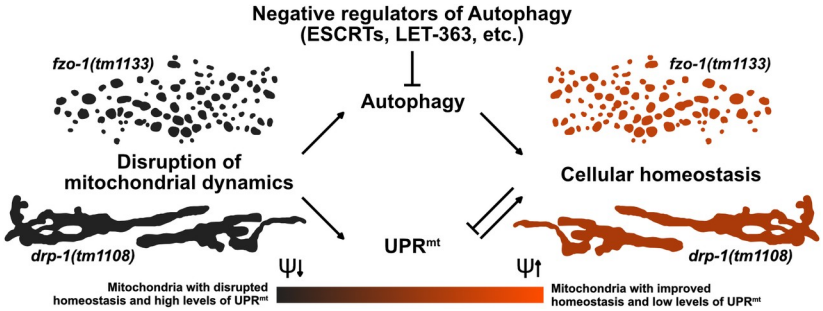

Fig 8. Autophagy compensates for defects in mitochondrial dynamics. The disruption of mitochondrial dynamics leads to altered mitochondrial morphology and to activation of UPR^{mt} and autophagy. We propose that in animals with compromised mitochondrial dynamics, the induction of autophagy fuels mitochondrial metabolism, thereby leading to increased mitochondrial membrane potential (ψ) and improved cellular homeostasis, which consequently results in suppression of UPR^{mt}.

https://doi.org/10.1371/journal.pgen.1008638.g008

component of the TOR pathway in *C. elegans* that induces autophagy when knocked-down [71]. Among the genes with roles in cellular trafficking, we found *imb-2*^{TNPO1,2}, a regulator of the nuclear transport of DAF-16^{FOXO} [70], which has been implicated in the regulation of autophagy [74]. Approximately one third of the candidates identified (44/143) are genes that regulate protein biosynthesis (S1 Table, GO categories 'Ribosome Biogenesis' and 'Translation'), which was shown to be protective against mitochondrial stress when impaired [97]. Baker and colleagues showed that knock-down of protein kinases involved in translation, such as *let-363*^{mTOR}, specifically suppress $P_{hsp-60\ HSP60}$*gfp (zcIs9)* expression. Based on our results, we propose that this effect could, to some extent, be due to the induction of autophagy. Taken together, we identified a broad range of cellular components and processes that all impact autophagy when deregulated, demonstrating the diverse and critical roles of autophagy in cellular homeostasis.

Conclusions

A block in mitochondrial dynamics leads to decreased mitochondrial membrane potential and the induction of UPR^{mt}. Lipid profiling indicates that a block in mitochondrial dynamics also causes an increase in the levels of certain types of TGs, which is reversed by induction of autophagy. We propose that the breakdown of these TGs through an autophagy-dependent process leads to elevated metabolic activity and that this causes an increase in mitochondrial membrane potential and the suppression of UPR^{mt}.

Methods

General *C. elegans* methods and strains

C. elegans strains were cultured as previously described [98]. Bristol N2 was used as the wild-type strain and the following alleles and transgenes were used: LGI: *spg-7(ad2249)* [41]; LGII: *fzo-1(tm1133)* (National BioResource Project), *rrf-3(pk1426)* [99], *fndc-1(rny14)* [78]; LGIII: *pdr-1(lg103)* [100]; LGIV: *drp-1(tm1108)* (National BioResource Project), *bcSi9* (P_{hsp-6}::*gfp*::*unc-54 3'UTR*) (this study), *frIs7 (nlp-29p*::*GFP + col-12p*::*DsRed)* [101]; LGV: *unc-51(e369)* [23], *atfs-1(tm4525)* (National BioResource Project), *atfs-1(et15*gf*)* [80]. Additionally, the following multi-copy integrated transgenes were used: *adIs2122(lgg-1p*::*GFP*::*lgg-1 + rol-6 (su1006))* [102], *bpIs151 (sqst-1p*::*sqst-1*::*GFP + unc-76(+))* [51], *zcIs9* (P_{hsp-60}::*gfp*::*unc-54 3'UTR)* [14], *zcIs13* (P_{hsp-6}::*gfp*::*unc-54 3'UTR)* [14], *zcIs18* (P_{ges-1}::*gfp(cyt))* [103], *bcIs79* ($P_{let-858}$::*gfp*^{mt}::*let-858 3'UTR + rol-6(su1006))*, *bcIs78* (P_{myo-3}::*gfp*^{mt}::*unc-54 3'UTR + rol-6(su1006)*) [46]. The strains MOC92 *bicIs10(hsp-1*::*tagRFP*::*unc-54 3'UTR)* and MOC119 *bicIs12(ttr-45p*::*tagRFP*::*ttr-45 3'UTR)* were generated in the Casanueva lab by gonadal microinjection of plasmids pMOC1 and pMOC2, respectively followed by genome integration via UV irradiation using a Stratagene UV Crosslinker (Stratalinker) [104]. The irradiation dose was 35mJ/cm^2 corresponding to Stratalinker power set up at 350. The single-copy integration allele *bcSi9* was generated using MosSCI [105] of the plasmid pBC1516. The strain EG8081 (*unc-119(ed3) III; oxTi177 IV*) was used for targeted insertion on LGIV [106]. The strain MD2988 ($P_{let-858}$*gfp*^{mt}) was generated by gonadal microinjection of the plasmid pBC938 followed by genome integration via EMS mutagenesis.

Plasmid construction

The plasmid pBC1516 was constructed using Gibson assembly [107]. The vector pCFJ350 (a gift from Erik Jorgensen; Addgene plasmid no. 34866) [108] was digested using AvrII. The putative *hsp-6* promoter (1695bp upstream of the start codon of *hsp-6*) + 30 bp of the *hsp-6*

gene were PCR amplified from gDNA using overhang primers to pCFJ350 5'- acgtcaccggttctagatacTCGAGTCCATACAAGCACTC -3' and *gfp*::*unc-54 3'UTR* 5'- ctttactcatGGAAGACAAGAATGATCGTG -3' (lower case letters indicating overhangs). *gfp*::*unc-54 3'UTR* was PCR amplified from pPD95.77 using overhang primers to P_{hsp-6} 5'- cttgtcttccATGAGTAAAGGAGAAGAACTTTTC -3' and pCFJ350 5'- tagagggtaccagagctcacAAACAGTTATGTTTGGTATATTGG -3' (lower case letters indicating overhangs).

The plasmid pBC938 was constructed using a classical cloning approach. Therefore, gfp^{mt} was amplified by PCR from pBC307 ($P_{hs}gfp^{mt}$) [109] using the following primers carrying a NheI or KpnI restriction site, respectively:

mitogfpFKpnI: 5'- GGTACCATGGCACTCCTGCAATCAC -3'

mitogfpRNheI: 5'- GCTAGCCTATTTGTATAGTTCATCCATGC -3'

The amplified fragment was then digested with KpnI and NheI and subsequently ligated into the NheI and KpnI digested backbone L3786 ($P_{let-858}$*NLS-GFP*) (L3786 was a gift from Andrew Fire (Addgene plasmid # 1593; http://n2t.net/addgene:1593; RRID:Addgene_1593)).

The plasmids pMOC1 and pMOC2 were generated by Gibson cloning, using Gibson Assembly Master Mix (New England Biolabs E2611) according to standard protocol using the vector pTagRFP-C as backbone (Evrogen). For the plasmid pMOC1 *(hsp-1p*::*tagRFP*::*unc-54 3'UTR))*, the 1.3 kb intergenic region upstream *hsp-1* was amplified and inserted at ScaI site, using the following primers:

hsp-1p fwd: 5'- GCCTCTAGAGTTACTTCGGCTCTATTACTG -3'

hsp-1p rev: 5'- tatcgcgagtTTTTACTGTAAAAAATAATTTAAAAATCAAGAAATAG -3'

The 3'UTR of *unc-54* was amplified and inserted at XhoI site using the primers:

unc54UTR RFP fwd: 5'- CTTAATTaaAGGACTCAGATCgtccaattactcttcaacatc -3'

unc54UTR RFP rev: 5'- CAGAATTCGAAGCTTGAGCttcaaaaaaatttatcagaag -3'

For the plasmid pMOC2 *(ttr-45p*::*tagRFP*::*ttr45 3'UTR)*, the 1.85 kb intergenic region upstream *ttr-45* was amplified and inserted at XbaI site, using the following primers:

ttr-45p fwd: 5'- GCCTGCAGGCGCGCCTctgaaaaaaaatcatattacaaatcag -3'

ttr-45p rev: 5'- AGATATCGCGAGTACTtgaaattttaaattttgaattttagtc -3'

The 3'UTR of *ttr-45*, contained in the following primer (lower case) was inserted at the XhoI site:

ttr-45UTR:

5'- TTaaAGGACTCAGATCaataattttgattttatgtataataaagactttatctcggGCTCAAGCTTCGAATT -3'

RNA-mediated interference

RNAi by feeding was performed using the Ahringer RNAi library [45]. *sorb-1(RNAi)* was used as a negative control (referred to as '*control(RNAi)*') in all RNAi experiments. For all experiments, except for the screens in *fzo-1(tm1133)*, *drp-1(tm1108)* and *spg-7(ad2249)*, RNAi clones were cultured overnight in 2 mL of LB carbenicillin (100 μg/mL) at 37˚C and 200 rpm. The RNAi cultures were adjusted to 0.5 OD and 50 μL were used to seed 30 mm RNAi plates containing 6 mM IPTG. The plates were incubated at 20˚C in the dark. 24 hours later, two L4 larvae of all wild-type strains or 16 L4 larvae of all strains carrying the *fzo-1(tm1133)* allele were inoculated onto the RNAi plates. L4 larvae of the F1 generation were collected after 4 days (wild-type strains) or 6–7 days (*fzo-1(tm1133)* mutants). *hars-1(RNAi)* was diluted 1:5 with *sorb-1(RNAi)* in all experiments. Larvae were imaged using M9 buffer with 150 mM sodium azide.

For the screens with the multi-copy *zcIs13* transgene in *fzo-1(tm1133)*, *drp-1(tm1108)* and *spg-7(ad2249)*, RNAi clones were cultured overnight in 100 μL of LB carbenicillin (100 μg/mL)

in a 96 well plate format at 37˚C and 200 rpm. 10 μL of the RNAi cultures was used to seed 24 well RNAi plates containing 0.25% Lactose (w/v). The plates were incubated at 20˚C in the dark. 24 hours later, 3 L4 larvae of all strains carrying the *fzo-1(tm1133)* and *spg-7(ad2249)* allele, and 2 L4 larvae of *drp-1(tm1108)* were inoculated onto the RNAi plates. The F1 generation was scored by eye for fluorescence intensity after 4–7 days.

Image acquisition, processing and analysis

For each RNAi condition, 10–20 animals were immobilized with M9 buffer containing 150 mM sodium azide on 2% agarose pads and imaged at 100x using a Leica GFP dissecting microscope (M205 FA) and the software Leica Application Suite (3.2.0.9652).

For image analysis, we used a Fiji-implemented macro using the IJ1 Macro language to automate the intensity measurement within defined areas of 2-dimensional images. An automated threshold using the Triangle method was applied to the fluorescence microscopy image, in order to generate a binary mask (The Triangle method was selected among the 16 available auto threshold methods of ImageJ as it provided the best results.). The mask was then inverted and the Particle Analyzer of ImageJ was used to remove noise by setting a minimum size (10 pixels) for objects to be included in the mask. After manually removing any remaining unwanted objects, the mask was applied to the corresponding fluorescent microscopy image and mean fluorescent intensity was measured. The mean fluorescent intensity outside the mask was defined as the background.

Mitochondrial morphology was assessed in a strain carrying *bcIs78* and *bcIs79* using a Zeiss Axioskop 2 and MetaMorph software (Molecular Devices).

TMRE staining and quantification

TMRE staining was performed with the F1 generation of respective RNAi treatments. L2 larvae were inoculated onto plates containing 0.1 μM TMRE (Thermo Life Sciences T669) and imaged in L4 stage using a 63x objective on Zeiss Axioskop 2 and MetaMorph software (Molecular Devices). Thereby TMRE is used in non-quenching mode and therefore suitable for quantifications and direct correlations to mitochondrial membrane potential.

The image is first converted to an 8-bit image, after which the continuous background signal is removed through background subtraction using the "rolling ball" algorithm with a ball radius of 15 pixels [110]. To remove remaining noise, two filters are applied. The first being a minimum filter with a value of 1, therefore replacing each pixel in the image with the smallest pixel value in a particular pixel's neighborhood. This is followed by a mean filter with a radius of 2, which replaces each pixel with the neighborhood mean. Next, the Tubeness plugin is run with a sigma value of 1.0, which generates a score of how tube-like each point in the image is by using the eigenvalues of the Hessian matrix to calculate the measure of "tubeness" [111]. The resulting 32-bit image is converted back to 8-bit and an automatic threshold (using the IsoData algorithm) generates a binary mask. The final step involves the removal of any particles that are smaller than 10 pixels in size for they are assumed to be noise.

Raw image files are opened in parallel to their appendant binary masks (generated by the segmentation macro) and a mask-based selection is created in the raw image. Within this selection measurements are obtained in the raw image and collected for subsequent analysis.

Western blot analysis

Mixed-stage populations of worms were harvested, washed three times in M9 buffer, and the pellets were lysed in 2x Laemmli buffer. For analysis of the additional candidates (Fig 4) 60–80 L4 stage animals were picked for western blotting. For analysis of endogenous HSP-6, 100 L4

larvae were harvested per genotype. The protein extracts were separated by 10% SDS-PAGE and transferred to a PVDF membrane (0.45 μm pore, Merck Millipore). To detect GFP and Tubulin, we used primary anti-GFP (1:1000, Roche 11814460001) and primary anti-α-Tubulin (1:5000, Abcam ab7291) antibodies and secondary horseradish peroxidase-conjugated goat anti-mouse antibodies (BioRad #1706516). To detect endogenous HSP-6, we used anti-HSP-6 (1:10,000) as described previously [42] and secondary horseradish peroxidase-conjugated goat anti-rabbit antibodies (BioRad #1706515). Blots were developed using ECL (Amersham) or ECL Prime (Amersham) according to manufacturer's protocol and images were quantified using the ChemiDoc XRS+ System (BioRad).

Analysis of autophagy and quantification of GFP::LGG-1 foci

L4 stage animals (except otherwise mentioned) were immobilized with M9 buffer containing 150 mM sodium azide on 2% agarose pads. Animals were imaged using a Leica TCS SP5 II confocal microscope (Leica Application Suite LAS software) with a 63x objective. GFP fluorescence was detected by excitation at 488 nm and emission at 507–518 nm. GFP::LGG-1 foci were counted in hypodermal seam cells on single images where the nucleus could clearly be seen. The amount of GFP::LGG-1 foci was counted in 2–5 seam cells per animal and the average number of GFP::LGG-1 foci per hypodermal seam cell was plotted for graphical representation and statistical analysis. SQST-1::GFP was imaged using Zeiss Axioskop 2 and MetaMorph software (Molecular Devices).

Analysis of thrashing rate

Body bends of L4 larvae were counted as previously described [75]. Briefly, the animals were transferred from the RNAi plates onto an empty NGM plate to get rid of all bacteria and then subsequently transferred into an empty petri dish filled with M9 buffer. After letting the L4 larvae adjust for one minute, they were recorded using a Samsung Galaxy S8 attached to a Leica MS5 stereomicroscope. The videos were played back at reduced speed using VLC media player (v3.0.8) and the number of body bends was counted manually for 1 minute.

Statistics

For experiments where two groups were compared, datasets were first tested for normality using Shapiro-Wilk normality test. If all samples of one dataset were found to be normally distributed, we conducted an unpaired two-tailed t-test. If samples were found to have non-equal variance, we conducted an unpaired tow-tailed t-test with Welch's correction. For experiments where more than two groups were compared, datasets were first tested for normal distribution using Shapiro-Wilk normality test and then tested for equal variance using Brown-Forsythe test. If samples of one dataset were found to be normally distributed and to have equal variance, one-way ANOVA with Dunnett's post hoc test was used to test for statistical significance with multiple comparisons to controls. If the dataset was not found to have normal distribution and/or have equal variance, Kruskal-Wallis test with Dunn's post hoc test for multiple comparisons to controls was used.

Lipid profiling using UPLC-UHR-ToF-MS

RNAi in lipidomic experiments was performed using *OP50(xu363)*, which is compatible for dsRNA production and delivery [112]. The L4440 plasmids containing the coding sequence of *sorb-1*, *cogc-2* or *vps-4* were purified from HT115 bacteria of the Ahringer library [45] using Qiagen Plasmid Mini Kit (Cat. No. 12125) and subsequently transformed into chemically

competent *OP50(xu363)*. Single clones were picked, sequenced and glycerol stocks were made for subsequent experiments. Bacterial clones were grown as described in section 'RNA-mediated interference' and 1 mL bacterial culture (OD_{600} = 0.5) was seeded onto 92 mm RNAi plates containing 1 mM IPTG. For *sorb-1(RNAi)* 120 L4 larvae, for *vps-4(RNAi)* 240 L4 larvae and for *cogc-2(RNAi)* 200 L4 larvae were transferred onto RNAi plates. Worms were collected in L4 stage after 6 days by washing the plates with MPEG. Worm pellets were subsequently washed using M9 and shock-frozen using liquid nitrogen and kept at -80˚C until extraction.

Lipids were extracted using the BUME method [113]. Briefly, worms were resuspended in 50 μL MeOH and transferred to custom made bead beating tubes. Samples were homogenized at 8000 rpm in a Precellys Bead Beater for 3 times 10 seconds with 20 seconds breaks in between. The additional Cryolys module was used with liquid nitrogen to prevent excessive heating of samples during disruption. 150 μL butanol and 200 μL heptane-ethyl acetate (3:1) was added to each sample sequentially which were then incubated for 1 h at 500 rpm / RT. 200 μL 1% acetic acid was added to each sample followed by centrifugation for 15 min at 13000 rpm / 4˚C. The upper organic phase was transferred to a fresh Eppendorf tube and the lower aqueous phase was re-extracted by the addition of 200 μL heptane-ethyl acetate followed by incubation and centrifugation as described above. The upper organic phase was transferred to the already obtained organic phase. The lower phase was transferred to a new Eppendorf tube and used for metabolomic analyses. Samples were evaporated to dryness and stored at -20˚C. For lipidomics, samples were re-dissolved in 50 μL 65% isopropanol / 35% acetonitrile / 5% H_2O, vortexed and 40 μL were transferred to an autosampler vial. The remaining 10 μL were pooled to form a QC sample for the entire study. The precipitated proteins in the aqueous phase were used for determination of protein content using a Bicinchoninic Acid Protein Assay Kit (Sigma-Aldrich, Taufkirchen, Germany).

Lipids were analyzed as previously described [114]. Briefly, lipids were separated on a Waters Acquity UPLC (Waters, Eschborn, Germany) using a Waters Cortecs C18 column (150 mm x 2.1 mm ID, 1.6 μm particle size, Waters, Eschborn Germany) and a linear gradient from 68% eluent A (40% H_2O / 60% acetonitrile, 10 mM ammonium formate and 0.1% formic acid) to 97% eluent B (10% acetonitrile / 90% isopropanol, 10 mM ammonium formate and 0.1% formic acid). Mass spectrometric detection was performed using a Bruker maXis UHR-ToF-MS (Bruker Daltonic, Bremen, Germany) in positive ionization mode using data dependent acquisition to obtain MS^1 and MS^2 information. Every ten samples, a pooled QC was injected to check performance of the UPLC-UHR-ToF-MS system and used for normalization.

Raw data was processed with Genedata Expressionist for MS 13.0 (Genedata AG, Basel, Switzerland). Preprocessing steps included noise subtraction, m/z recalibration, chromatographic alignment and peak detection and grouping. Data was exported for Genedata Expressionist for MS 13.0 Analyst statistical analysis software and as .xlxs for further investigation. Maximum peak intensities were used for statistical analysis and data was normalized on the protein content of the sample and an intensity drift normalization based on QC samples was used to normalize for the acquisition sequence.

Lipid features that were detected in all pooled QC samples and had a relative standard deviation (RSD) $< 30\%$ were further investigated by statistical analysis. 5284 features passed this filter and the different mutants were compared against the wild-type control using Welch test. Lipids with a p-value < 0.05 were considered to be significantly changed.

Lipids were putatively annotated on the MS^1 level using an in-house developed database for *C. elegans* lipids and bulk composition from LipidMaps [115], when available. Matching of MS^2 spectra against an in-silico database of *C. elegans* lipids and LipidBlast was performed using the masstrixR package [116] (https://github.com/michaelwitting/masstrixR) and only

hits with a forward and reverse matching score > 0.75 were considered. Annotations of interesting biological peaks were manually verified and corrected if necessary.

High throughput qRT-PCR on single worms using the Biomark system

cDNA from single worms was analyzed on the biomark system using Flex Six IFC. This nanofluidic chip allows the comparison of 12 target genes across 36 individual worms per genotype. We monitored biological variability in gene expression of targets: endogenous *hsp-6*, *hsp-60* and either *bcSi9* single-copy or *zcIs13* multi-copy transgenes. In addition, we monitored variability in gene expression of three "gold standard" control genes: either non-variable (*hsp-1*), medium variable (*ttr-45*) or highly variable (*nlp-29*). Ct values for all targets were normalized to the average of three housekeeping genes (*cdc-42*, *ire-1* and *pmp-3*).

Design of qRT-PCR primers. Primers sets were designed to quantify *C. elegans* post-spliced transcripts. Primer sets were designed to span exon-exon junctions using NCBI Primer Blast software and subsequently blasted against the *C. elegans* genome to test for off-target complementarity. The list of qRT-PCR primers used with their PCR efficiency and coefficient of determination (R^2) is shown in S3 Table.

Quantification of primer efficiency and specificity. Primers were selected for high PCR efficiency between 90 and 115%. To estimate primer efficiencies, a comprehensive titration of cDNA obtained from 500 ng of Trizol-extracted RNA was prepared within the range of linear amplification using a 1:2 series dilution. Each qRT-PCR reaction contained 1.5 μL of primer mix forward and reverse at 1.6 μM each, 3.5 μL of nuclease free water, 6 μL of 2X Platinum® SYBR® Green qPCR Supermix-UDG (Thermo Fisher Scientific PN 11744–500) and 1 μL of worm DNA lysate diluted or not. The qRT-PCR reactions were run on an iCycler system (Bio-Rad). PCR efficiencies were calculated by plotting the results of the titration of cDNA (Ct values versus log dilution) within the range of linear amplification. The efficiency was defined by the formula 100 x ($10^{(-1/slope)}$/2) with an optimal slope defined as -3.3 ($^{(1/3.3)}$) = 2.

Worm synchronization. Worms were grown at 20˚C and bleach synchronized. 36 worms per genotype were harvested at the L4.8/L4.9 stage based on vulval development [117], at about 48h post L1 plating for WT and about 65h post L1 plating for *fzo-1(tm1133)*.

Worm lysis for total RNA preparation of single worm RNA. During harvesting, synchronized worms were individually picked into 10 μL lysis buffer (Power SYBR® Green Cells-to-C_T™ kit, Thermo Fisher Scientific) in 8 strip PCR tubes. After harvesting the worms, the 8 strip PCR tubes were freeze-thawed 10 times by transferring tubes from a liquid nitrogen bath into a warm water bath (about 40ºC). Samples were vortexed during 20 minutes on a thermoblock set up at 4ºC. The samples were then quickly spun down and 1 μL of stop solution (Power SYBR Green Cells-to-C_T kit, Thermo Fisher scientific) was added in each tube. The samples were then stored at -80ºC before further processing. Storage time was no more than one week before proceeding to reverse transcription.

Reverse transcription. Reverse Transcription PCR (RT-PCR) was performed by adding 5 μL of lysis mix (lysis buffer and stop solution) to 1.25 μL of Reverse Transcription Master Mix (Fluidigm PN 100–6297) into 96 well plates. We included one minus RT control per plate, containing 5 μL of lysis mix and 1.25 μL of RNase free water. Reverse Transcription cycling conditions were 25ºC for 5 min, 42ºC for 30 min and 85ºC for 5 min.

Pre-amplification. Pre-amplification was performed according to Fluidigm instruction manual: for every nano-fluidic chip, a pooled primer mix was prepared by adding 1 μL of primer stock (for every target gene to be tested on the chip) to water up to a final volume of 100 μL. Every primer stock contained both reverse and forward primers at a concentration of 50 μM each. A pre-amplification mix was prepared containing for each sample: 1 μL of

PreAmp Master mix (Fluidigm PN 100–5744), 0.5 μL of pooled primer mix and 2.25 μL of nuclease free water. 3.75 μL of pre-amplification mix was then aliquoted in a 96 well-plate. 1.25 μL of cDNA was then added in each well. The samples were mixed by quick vortexing and centrifuged. Pre amplification conditions were the following: 95°C for 2 min, 10 cycles of denaturation at 95°C for 15 s followed by annealing/extension at 60°C for 4 min.

Exo I treatment and sample dilution. To remove unincorporated primers, 2 μL of Exonuclease I mix was added to each pre-amplification reaction. The Exonuclease I mix contained 0.2 μL of Exonuclease I reaction buffer (New England BioLabs), 0.4 μL Exonuclease I at 20 Units/μL (New England BioLabs), and 1.4 μL of nuclease free water. The samples were incubated at 37°C for 30 min followed by 15 min at 80°C. The samples were finally diluted 1:5 by adding 18 μL of DNA suspension buffer (10 mM Tris, 0.1 mM EDTA, pH = 8.0, TEKnova PN-T0021).

Assay Mix preparation. For every pair of primers to be tested on the Fluidigm nano-fluidic chip, an assay mix was individually prepared on a 384 well PCR plate (for easier transfer to the Fluidigm nano-fluidic chips), typically the day before the experiment. Each assay mix (for 36 samples) contained 6.25 μL of 2X Assay loading reagent (Fluidigm PN 100–5359), 5 μL of DNA suspension buffer (10 mM Tris, 0.1 mM EDTA, pH = 8.0, TEKnova PN T0021), and 1.25 μL of primer stock (reverse and forward primers at a concentration of 50 μM each). Assay mixes were vortexed during 30 s minimum on a thermoblock set up at 4 °C and centrifuged for 30 s minimum. 3 μL of each assay mix were loaded onto Flex Six Gene Expression IFC chips (Fluidigm PN 100–6308).

Sample Mix preparation. The samples mixes were prepared at the day of the experiment. 1.8 μL of diluted PreAmp and Exo I treated samples were added to a sample mix containing 2 μL of 2X SsoFast EvaGreen Supermix with Low ROX (Bio-Rad, PN 172–5211) and 0.2 μL of Flex Six Delta Gene Sample Reagent (Fluidigm PN 100–7673). 3 μL of each sample mix was loaded onto Flex Six IFC chips.

Biomark Run and data clean-up. Assay and sample mixes of Flex Six IFCs were loaded using a HX IFC controller (Fluidigm). The nano-fluidic chips were then run on a Biomark HD using the FlexSix Fast PCR+melt protocols. After the run, the data from every well on the plate was checked and cleaned up as following: samples for which all PCRs failed were eliminated. Any well, in which the melting peak temperature of a particular pair of primers was not as expected, was eliminated. It would happen occasionally, presumably when pairs of primers form dimers when target gene concentrations are very low, or from interactions of target primers with other primers in the pooled primer mix. Ct values were then normalized to the average of housekeeping genes and relative mRNA expression levels were calculated using the delta Ct method.

Determination of "Gold Standard" stable and variable transcripts. To validate our single-worm high throughput qRT-PCR method to monitor inter-individual variability in gene expression, we measured the coefficient of variation CV (CV = standard deviation/mean) for fluorescent transcriptional reporters of a stable gene MOC92 *bicIs10(hsp-1p*::*tagRFP*::*unc-54 3'UTR)* and of two variable transgenes MOC119 *bicls12(ttr-45p*::*tagRFP*::*ttr45 3'UTR)* (medium variable) and IG274 *frIs7(nlp-29p*::*GFP; col-12p*::*DsRed)* (highly variable). We verified that it matches the coefficient of variation calculated from normalized Ct values of endogenous transcripts *hsp-1*, *ttr-45* and *nlp-29* measured in our high-throughput single worm qPCR assay. Synchronized MOC92 and MOC119 transgenic worms were immobilized in M9 containing 3 mM Levamisole and imaged on a Nikon SMZ18 stereo epi-fluorescence microscope, while synchronized IG274 transgenic animals were mounted in 3 mM levamisole on a 2% agarose pad and imaged on a Nikon Ti Eclipse inverted microscope, as the fluorescence levels of the *nlp-29* reporter in IG274 were too low to be imaged on the Nikon SMZ18. The

fluorescence of each individual transgenic worm was quantified using Fiji software, by subtracting the background measurement from fluorescence measurements. The coefficient of variation was determined for synchronized population of day 2 animals (day 2 of adulthood: 74h post L1 plating at 20˚C) for *nlp-29* and *ttr-45* reporters, while it was determined in day 1 synchronized animals (50h post L1 plating at 20˚C) for *hsp-1* reporter. The coefficient of variation is measured as follows:

- *bicIs10(hsp-1p*::*tagRFP*::*unc-54 3'UTR)*: 0.09< CV <0.14 (3 biological replicates)
- *bicls12(ttr-45p*::*tagRFP*::*ttr45 3'UTR)*: 0.31<CV<0.45 (3 biological replicates)
- *frIs7(nlp-29p*::*GFP; col-12p*::*DsRed)*: CV = 1.0 (1 biological replicate)

We observed a good correlation between the coefficient of variation for *hsp-1*, *ttr-45* and *nlp-29* transgenic reporters and the coefficient of variation for endogenous transcripts *hsp-1*, *ttr-45* and *nlp-29* measured by single worm qRT-PCR (S1F Fig).

Supporting information

S1 Fig. Comparison of expression levels and inter-individual variability of multi-copy $P_{hsp\text{-}6\ mtHSP70}$*gfp (zcIs13)* and single-copy integrated $P_{hsp\text{-}6\ mtHSP70}$*gfp (bcSi9)* transgenes. **(A)** Brightfield (upper panel) and fluorescence images (lower panel) of L4 larvae expressing $P_{hsp\text{-}6}$*gfp (zcIs13)* in wild type (+/+), *spg-7(ad2249)*, *fzo-1(tm1133) or drp-1(tm1108)*. Scale bar: 200 μm. **(B)** Brightfield (upper panel) and fluorescence images (lower panel) of L4 larvae expressing $P_{hsp\text{-}6}$*gfp (bcSi9)* in wild type (+/+), *spg-7(ad2249)*, *fzo-1(tm1133)* or *drp-1(tm1108)*. Scale bar: 200 μm. **(C)** Quantifications of fluorescence images of panel A ($P_{hsp\text{-}6}$*gfp (zcIs13)*) are shown. Each dot represents quantification of 15–20 L4 larvae. Values indicate means ± SD of ≥5 independent measurements. **(D)** Quantifications of fluorescence images of panel B ($P_{hsp\text{-}6}$*gfp (bcSi9)*) are shown. Each dot represents quantification of 15–20 L4 larvae. Values indicate means ± SD of ≥4 independent measurements. **(E)** Quantifications of western blot analysis of endogenous HSP-6 levels in wild-type (+/+), *spg-7(ad2249)*, *fzo-1(tm1133)* or *drp-1 (tm1108)* using anti-HSP-6 antibodies. For each genotype, 100 L4 larvae were harvested per experiment for western blot analysis. Values indicate means of relative HSP-6 expression (HSP-6/TUB) ± SD, n = 2. **(F)** Inter-individual variability in gene expression of target genes in *bcSi9* and *zcIs13* in both wild type (+/+) and *fzo-1(tm1133)*. To estimate inter-individual variability in gene expression, the coefficient of variation was calculated from individual mRNA levels obtained from normalized Ct values using the delta Ct method. Inter-individual variability values were normalized such that variability values for *nlp-29* in wild type = 1 *(bcSi9* or *zcIs13)*. Number of individual worms: n = 35 *(bcSi9)*, n = 32 (*bcSi9; fzo-1(tm1133))*, n = 31 *(zcIs13)*, n = 31 *(zcIs13; fzo-1(tm1133)*).
(TIF)

S2 Fig. RNAi against *vps-4*^{VPS4} and *vps-20*^{CHMP6} suppresses expression of *bcSi9* and induces autophagy in wild type (+/+). **(A)** L4 larvae were subjected to *control(RNAi)*, *atfs-1 (RNAi)*, *vps-4(RNAi)* or *vps-20(RNAi)* and the F1 generation was imaged. Each dot represents the quantification of fluorescence intensity of 15–20 L4 larvae. Values indicate means ± SD of 5 independent experiments in duplicates. $^{*}P<0.05$, $^{***}P<0.001$ using one-way ANOVA with Dunnett's multiple comparison test to *control(RNAi)*. **(B)** $P_{lgg\text{-}1}$*gfp*::*lgg-1* expression of L4 larvae in hypodermal seam cells and intestinal cells upon *control(RNAi)*, *vps-4(RNAi)* or *vps-20 (RNAi)*. Representative images of >30 animals from two independent biological replicates are shown. Scale bar hypodermal seam cells: 5 μm. Scale bar intestinal cells: 20 μm.
(TIF)

S3 Fig. Knock-down of ESCRT components in body wall muscle cells of wild type and intestinal cells in *fzo-1(tm1133)* does not change mitochondrial morphology. (A) Fluorescence images of L4 larvae expressing $P_{myo-3}gfp^{mt}$ in wild type (+/+). L4 larvae were subjected to *control(RNAi)*, *atfs-1(RNAi)*, *vps-4(RNAi)*, *vps-20(RNAi)* or *let-363(RNAi)* and the F1 generation was imaged. Scale bar: 10 μm. **(B)** Fluorescence images of L4 larvae expressing $P_{let-858}gfp^{mt}$ in wild type (+/+) or *fzo-1(tm1133)*. L4 larvae were subjected to *control(RNAi)*, *atfs-1 (RNAi)*, *vps-4(RNAi)*, *vps-20(RNAi)* or *let-363(RNAi)* and the F1 generation was imaged. Scale bar: 10 μm.
(TIF)

S4 Fig. Image segmentation and intensity measurement workflow. A raw 16-bit image (1) is converted to 8-bit, followed by a background subtraction using the rolling ball algorithm (2). This is followed by the successive application of a minimum (3) and average filter (4). The ImageJ Tubeness plugin generates an image with object curvature scores (5), after which the IsoData autothresholding is applied to generate the binary mask (6). Noise is removed by filtering out particles below a certain size (7) and the final mask is used to define the area in which intensity measurements are obtained (8). Scale bar: 5 μm.
(TIF)

S5 Fig. Thrashing assay in wild-type and *fzo-1(tm1133)* animals upon induction of autophagy. Thrashing rate was analyzed by counting body bends of animals swimming for 1 minute in M9 buffer in 3 independent experiments. Each dot represents one L4 larvae. **(A)** Thrashing rates of wild-type (+/+) or *fzo-1(tm1133)* L4 larvae. $^{****}P<0.0001$ using unpaired two-tailed t-test. n = 30. **(B)** Thrashing rates in wild-type animals upon induction of autophagy. L4 larvae were subjected to *control(RNAi)*, *vps-4(RNAi)*, *vps-20(RNAi)*, *let-363(RNAi)* or *hars-1(RNAi)* and the F1 generation was analyzed. ns: not significant, $^{****}P<0.0001$ using Kruskal-Wallis test with Dunn's multiple comparison test to *control(RNAi)*. n = 30. **(C)** Thrashing rates in *fzo-1(tm1133)* animals upon induction of autophagy. L4 larvae were subjected to *control(RNAi)*, *vps-4(RNAi)*, *vps-20(RNAi)*, *let-363(RNAi)* or *hars-1(RNAi)* and the F1 generation was analyzed. ns: not significant, $^{***}P<0.001$ using Kruskal-Wallis test with Dunn's multiple comparison test to *control(RNAi)*. n = 30.
(TIF)

S6 Fig. RNAi against *vps-4*^{VPS4} and *vps-20*^{CHMP6} does not suppress *fzo-1(tm1133)*-induced UPR^{mt} when diluted with *control(RNAi)* or carried out in one generation from L2 to L4 larvae. (A) Quantifications of fluorescence images of L4 larvae expressing $P_{hsp-6}gfp$ *(bcSi9)* in *fzo-1(tm1133)*. Each *ESCRT(RNAi)* was diluted 1:1 with *control(RNAi)*. After subtracting the mean fluorescence intensity of wild type (+/+) on *control(RNAi)*, the values were normalized to *fzo-1(tm1133)* on *control(RNAi)*. Each dot represents the quantification of fluorescence intensity of 15–20 L4 larvae. Values indicate means ± SD of 3 independent experiments in duplicates. ns: not significant, using one-way ANOVA with Dunnett's multiple comparison test to *control(RNAi)*. **(B)** Quantifications of fluorescence images of L4 larvae expressing $P_{hsp-6}gfp$ *(bcSi9)* in *fzo-1(tm1133)*. L2 larvae were subjected to *control(RNAi)*, *atfs-1(RNAi)*, *vps-4 (RNAi)* or *vps-20(RNAi)* and the same animals were imaged in L4 stage. After subtracting the mean fluorescence intensity of wild type (+/+) on *control(RNAi)*, the values were normalized to *fzo-1(tm1133)* on *control(RNAi)*. Each dot represents the quantification of fluorescence intensity of 15–20 L4 larvae. Values indicate means ± SD of 4 independent experiments in duplicates. ns: not significant, $^{**}P<0.01$ using Kruskal-Wallis test with Dunn's multiple comparison test to *control(RNAi)*. **(C)** $P_{lgg-1}gfp$::*lgg-1* expression of *fzo-1(tm1133)* L4 larvae in

hypodermal seam cells and intestinal cells. L2 larvae were subjected to *control(RNAi)*, *vps-4 (RNAi)* or *vps-20(RNAi)* and the same animals were imaged in L4 stage. Representative images of >60 animals from two independent biological replicates are shown. Scale bar hypodermal seam cells: 5 μm. Scale bar intestinal cells: 20 μm. **(D)** Quantifications of fluorescence images of L4 larvae expressing P_{hsp-6}*gfp (bcSi9)* in *fzo-1(tm1133) rrf-3(pk1426)*. L2 larvae were subjected to *control(RNAi)*, *atfs-1(RNAi)*, *vps-4(RNAi)* or *vps-20(RNAi)* and the same animals were imaged in L4 stage. After subtracting the mean fluorescence intensity of wild type (+/+) on *control(RNAi)*, the values were normalized to *fzo-1(tm1133)* on *control(RNAi)*. Each dot represents the quantification of fluorescence intensity of 15–20 L4 larvae. Values indicate means ± SD of 4 independent experiments in duplicates. ns: not significant, $^{****}P<0.0001$ using one-way ANOVA with Dunnett's multiple comparison test to *control(RNAi)*.
(TIF)

S7 Fig. Autophagy is induced in *spg-7(ad2249)* animals. (A) P_{lgg-1}*gfp*::*lgg-1* expression in hypodermal seam cells of wild type (+/+) or *spg-7(ad2249)* L4 larvae. Scale bar: 5 μm. **(B)** Quantification of GFP::LGG-1 foci in hypodermal seam cells from panel A. Each dot represents the average amount of GFP::LGG-1 foci counted from 2–5 seam cells in one animal. n≥18 for each genotype; values indicate means ± SD; $^{**}P<0.01$ using unpaired two-tailed t-test with Welch's correction. **(C)** Nomarski and fluorescent images of the P_{sqst-1}*sqst-1*::*gfp* translational reporter in embryos of wild type (+/+) and *spg-7(ad2249)* animals. As a positive control for a block in autophagy, *unc-51(e369)* was used. Representative images of >60 embryos are shown. Scale bar: 10 μm.
(TIF)

S8 Fig. Defects in mitochondrial homeostasis lead to major changes in lipid metabolism. (A) Venn diagrams showing the overlap of lipids up- or downregulated in *fzo-1(tm1133)*, *drp-1(tm1108)* and *spg-7(ad2249)* in comparison to wild type (+/+). **(B)** Total amount of TGs in wild type (+/+), *fzo-1(tm1133)*, *drp-1(tm1108)* and *spg-7(ad2249)* backgrounds. Means ± SD are shown; ns: not significant, $^{*}P<0.05$, $^{****}P<0.0001$ using Welch test. **(C)** Scatterplot indicating the distribution and changes in the levels of TG species in the different mutants in comparison to wild type (+/+). **(D))** Scatterplot indicating the overlap of the changes in the levels of TG species of *fzo-1(tm1133)* and *drp-1(tm1108)* mutants in comparison to wild type (+/+). **(C)** and **(D)** The x-axis labels the number of carbons (# of C) and the y-axis the number of double bonds (DB) in the acyl sidechains. The size of a dot indicates the number of detected isomers for a specific sum composition. Grey dots represent all detected TGs species and blue and red dots indicate down- (blue) or upregulation (red).
(TIF)

S9 Fig. Induction of autophagy upon *cogc-2(RNAi)* changes the levels of specific TGs in *fzo-1(tm1133)* mutants. (A) Scatterplot indicating the distribution and changes in the level of TG species in *fzo-1(tm1133)* mutants in comparison to wild type (+/+). The x-axis labels the number of carbons (# of C) and the y-axis the number of double bonds (DB) in the acyl sidechains. The size of a dot indicates the number of detected isomers for a specific sum composition. Grey dots represent all detected TGs species and blue and red dots indicate down- (blue) or upregulation (red). **(B)** Venn diagram indicating the overlap of TG species downregulated (left panel) or upregulated (right panel) in *fzo-1(tm1133)* and downregulated upon *vps-4 (RNAi)* or *cogc-2(RNAi)*.
(TIF)

S1 Table. List of genes that suppress *fzo-1(lf)*-induced UPR^{mt} and induce autophagy in wild-type animals upon knock-down. Candidate genes were identified in the primary RNAi-

screen using *fzo-1(tm1133)*, subsequently knocked-down and tested for induction of autophagy and re-screened for UPR^{mt} suppression in two different mutant backgrounds: *drp-1 (tm1108)* and *spg-7(ad2249)*.
(XLSX)

S2 Table. Numerical data of lipidomic experiments. Significantly up- or downregulated lipids in *fzo-1(tm1133)*, *drp-1(tm1108)* or *spg-7(ad2249)* mutants (Sheet 1), significantly up- or downregulated TGs in *fzo-1(tm1133)*, *drp-1(tm1108)* or *spg-7(ad2249)* mutants (Sheet 2) and significantly up- or downregulated TGs in *fzo-1(tm1133)* upon induction of autophagy by *vps-4(RNAi)* or *cogc-2(RNAi)* (Sheet 3). MS^1 annotations, *P*-values and fold change are indicated.
(XLSX)

S3 Table. List of qRT-PCR primers. Primers used for qRT-PCR including PCR efficiency and coefficient of determination (R^2).
(XLSX)

Acknowledgments

We thank Eric Lambie, Dejana Mokranjac, the 'Mito Club' and members of the Conradt lab for discussion and comments on the manuscript. We thank M. Bauer, L. Jocham, N. Lebedeva and M. Schwarz for excellent technical support and S. Mitani (National BioResource Project, Tokyo, Japan) for *fzo-1*(*tm1133*), *drp-1(tm1108)* and *atfs-1(tm4525)*. We thank Keith Nehrke and Vincent Galy for *fndc-1(rny-14)*. Some strains were provided by the CGC, which is funded by NIH Office of Research Infrastructure Programs (P40 OD010440).

Author Contributions

Conceptualization: Simon Haeussler, Fabian Köhler, Michael Witting, Stéphane G. Rolland, Laetitia Chauve, Olivia Casanueva, Barbara Conradt.

Data curation: Simon Haeussler, Fabian Köhler, Michael Witting.

Formal analysis: Simon Haeussler, Fabian Köhler, Michael Witting, Madeleine F. Premm, Christian Fischer, Laetitia Chauve.

Funding acquisition: Barbara Conradt.

Investigation: Simon Haeussler, Fabian Köhler.

Methodology: Simon Haeussler, Fabian Köhler, Michael Witting.

Project administration: Barbara Conradt.

Resources: Simon Haeussler, Fabian Köhler, Michael Witting.

Software: Christian Fischer.

Validation: Simon Haeussler, Fabian Köhler, Madeleine F. Premm.

Visualization: Simon Haeussler, Fabian Köhler, Michael Witting, Christian Fischer, Laetitia Chauve.

Writing – original draft: Simon Haeussler, Fabian Köhler, Michael Witting, Barbara Conradt.

Writing – review & editing: Simon Haeussler, Fabian Köhler, Michael Witting, Barbara Conradt.

References

1. Youle RJ, van der Bliek AM. Mitochondrial fission, fusion, and stress. Science (New York, NY). 2012; 337(6098):1062–5.
2. van der Bliek AM, Shen Q, Kawajiri S. Mechanisms of Mitochondrial Fission and Fusion. Cold Spring Harbor Perspectives in Biology. 2013;5(6).
3. Labrousse AM, Zappaterra MD, Rube DA, van der Bliek AM. *C. elegans* Dynamin-Related Protein DRP-1 Controls Severing of the Mitochondrial Outer Membrane. Molecular cell. 1999; 4(5):815–26. https://doi.org/10.1016/s1097-2765(00)80391-3 PMID: 10619028
4. Ingerman E, Perkins EM, Marino M, Mears JA, McCaffery JM, Hinshaw JE, et al. Dnm1 forms spirals that are structurally tailored to fit mitochondria. The Journal of cell biology. 2005; 170(7):1021–7. https://doi.org/10.1083/jcb.200506078 PMID: 16186251
5. Ichishita R, Tanaka K, Sugiura Y, Sayano T, Mihara K, Oka T. An RNAi Screen for Mitochondrial Proteins Required to Maintain the Morphology of the Organelle in *Caenorhabditis elegans*. The Journal of Biochemistry. 2008; 143(4):449–54. https://doi.org/10.1093/jb/mvm245 PMID: 18174190
6. Kanazawa T, Zappaterra MD, Hasegawa A, Wright AP, Newman-Smith ED, Buttle KF, et al. The *C. elegans* Opa1 Homologue EAT-3 Is Essential for Resistance to Free Radicals. PLoS genetics. 2008; 4 (2):e1000022. https://doi.org/10.1371/journal.pgen.1000022 PMID: 18454199
7. Kim S, Sieburth D. Sphingosine Kinase Activates the Mitochondrial Unfolded Protein Response and Is Targeted to Mitochondria by Stress. Cell reports. 2018; 24(11):2932–45.e4. https://doi.org/10.1016/j.celrep.2018.08.037 PMID: 30208318
8. Zhang Q, Wu X, Chen P, Liu L, Xin N, Tian Y, et al. The Mitochondrial Unfolded Protein Response Is Mediated Cell-Non-autonomously by Retromer-Dependent Wnt Signaling. Cell. 2018; 174(4):870–83. e17. https://doi.org/10.1016/j.cell.2018.06.029 PMID: 30057120
9. Haynes CM, Yang Y, Blais SP, Neubert TA, Ron D. The matrix peptide exporter HAF-1 signals a mitochondrial UPR by activating the transcription factor ZC376.7 in *C. elegans*. Molecular cell. 2010; 37 (4):529–40. https://doi.org/10.1016/j.molcel.2010.01.015 PMID: 20188671
10. Rolland SG, Schneid S, Schwarz M, Rackles E, Fischer C, Haeussler S, et al. Compromised Mitochondrial Protein Import Acts as a Signal for UPR^{mt}. Cell reports. 2019; 28(7):1659–69.e5. https://doi.org/10.1016/j.celrep.2019.07.049 PMID: 31412237
11. Nargund AM, Pellegrino MW, Fiorese CJ, Baker BM, Haynes CM. Mitochondrial import efficiency of ATFS-1 regulates mitochondrial UPR activation. Science (New York, NY). 2012; 337(6094):587–90. https://doi.org/10.1126/science.1223560 PMID: 22700657
12. Benedetti C, Haynes CM, Yang Y, Harding HP, Ron D. Ubiquitin-like protein 5 positively regulates chaperone gene expression in the mitochondrial unfolded protein response. Genetics. 2006; 174 (1):229–39. https://doi.org/10.1534/genetics.106.061580 PMID: 16816413
13. Haynes CM, Petrova K, Benedetti C, Yang Y, Ron D. ClpP mediates activation of a mitochondrial unfolded protein response in *C. elegans*. Developmental cell. 2007; 13(4):467–80. https://doi.org/10.1016/j.devcel.2007.07.016 PMID: 17925224
14. Yoneda T, Benedetti C, Urano F, Clark SG, Harding HP, Ron D. Compartment-specific perturbation of protein handling activates genes encoding mitochondrial chaperones. Journal of cell science. 2004; 117(Pt 18):4055–66.
15. Levine B, Klionsky DJ. Development by Self-Digestion. Developmental cell. 2004; 6(4):463–77. https://doi.org/10.1016/s1534-5807(04)00099-1 PMID: 15068787
16. Mizushima N. Autophagy: process and function. Genes Dev. 2007; 21(22):2861–73. https://doi.org/10.1101/gad.1599207 PMID: 18006683
17. Feng Y, He D, Yao Z, Klionsky DJ. The machinery of macroautophagy. Cell Res. 2014; 24(1):24–41. https://doi.org/10.1038/cr.2013.168 PMID: 24366339
18. Nakatogawa H, Suzuki K, Kamada Y, Ohsumi Y. Dynamics and diversity in autophagy mechanisms: lessons from yeast. Nature reviews Molecular cell biology. 2009; 10(7):458–67. https://doi.org/10.1038/nrm2708 PMID: 19491929
19. Long X, Spycher C, Han ZS, Rose AM, Müller F, Avruch J. TOR Deficiency in *C. elegans* Causes Developmental Arrest and Intestinal Atrophy by Inhibition of mRNA Translation. Current Biology. 2002; 12(17):1448–61. https://doi.org/10.1016/s0960-9822(02)01091-6 PMID: 12225660
20. Hansen M, Chandra A, Mitic LL, Onken B, Driscoll M, Kenyon C. A role for autophagy in the extension of lifespan by dietary restriction in *C. elegans*. PLoS genetics. 2008; 4(2):e24. https://doi.org/10.1371/journal.pgen.0040024 PMID: 18282106

21. Jia K, Chen D, Riddle DL. The TOR pathway interacts with the insulin signaling pathway to regulate *C. elegans* larval development, metabolism and life span. Development. 2004; 131(16):3897–906. https://doi.org/10.1242/dev.01255 PMID: 15253933

22. Kuroyanagi H, Yan J, Seki N, Yamanouchi Y, Suzuki Y, Takano T, et al. Human ULK1, a novel serine/threonine kinase related to UNC-51 kinase of *Caenorhabditis elegans*: cDNA cloning, expression, and chromosomal assignment. Genomics. 1998; 51(1):76–85. https://doi.org/10.1006/geno.1998.5340 PMID: 9693035

23. Ogura K, Wicky C, Magnenat L, Tobler H, Mori I, Müller F, et al. *Caenorhabditis elegans* unc-51 gene required for axonal elongation encodes a novel serine/threonine kinase. Genes & Development. 1994; 8(20):2389–400.

24. Wullschleger S, Loewith R, Hall MN. TOR signaling in growth and metabolism. Cell. 2006; 124 (3):471–84. https://doi.org/10.1016/j.cell.2006.01.016 PMID: 16469695

25. Tsukada M, Ohsumi Y. Isolation and characterization of autophagy-defective mutants of *Saccharomyces cerevisiae*. FEBS Letters. 1993; 333(1–2):169–74. https://doi.org/10.1016/0014-5793(93)80398-e PMID: 8224160

26. Sato M, Sato K. Degradation of Paternal Mitochondria by Fertilization-Triggered Autophagy in *C. elegans* Embryos. Science (New York, NY). 2011; 334(6059):1141–4.

27. Christ L, Raiborg C, Wenzel EM, Campsteijn C, Stenmark H. Cellular Functions and Molecular Mechanisms of the ESCRT Membrane-Scission Machinery. Trends in biochemical sciences. 2017; 42 (1):42–56. https://doi.org/10.1016/j.tibs.2016.08.016 PMID: 27669649

28. Katzmann DJ, Babst M, Emr SD. Ubiquitin-Dependent Sorting into the Multivesicular Body Pathway Requires the Function of a Conserved Endosomal Protein Sorting Complex, ESCRT-I. Cell. 2001; 106 (2):145–55. https://doi.org/10.1016/s0092-8674(01)00434-2 PMID: 11511343

29. Raiborg C, Bache KG, Gillooly DJ, Madshus IH, Stang E, Stenmark H. Hrs sorts ubiquitinated proteins into clathrin-coated microdomains of early endosomes. Nature cell biology. 2002; 4(5):394–8. https://doi.org/10.1038/ncb791 PMID: 11988743

30. Sachse M, Urbe S, Oorschot V, Strous GJ, Klumperman J. Bilayered clathrin coats on endosomal vacuoles are involved in protein sorting toward lysosomes. Mol Biol Cell. 2002; 13(4):1313–28. https://doi.org/10.1091/mbc.01-10-0525 PMID: 11950941

31. Amit I, Yakir L, Katz M, Zwang Y, Marmor MD, Citri A, et al. Tal, a Tsg101-specific E3 ubiquitin ligase, regulates receptor endocytosis and retrovirus budding. Genes Dev. 2004; 18(14):1737–52. https://doi.org/10.1101/gad.294904 PMID: 15256501

32. Carlton JG, Martin-Serrano J. Parallels between cytokinesis and retroviral budding: a role for the ESCRT machinery. Science (New York, NY). 2007; 316(5833):1908–12.

33. Filimonenko M, Stuffers S, Raiborg C, Yamamoto A, Malerod L, Fisher EM, et al. Functional multivesicular bodies are required for autophagic clearance of protein aggregates associated with neurodegenerative disease. The Journal of cell biology. 2007; 179(3):485–500. https://doi.org/10.1083/jcb.200702115 PMID: 17984323

34. Lee JA, Beigneux A, Ahmad ST, Young SG, Gao FB. ESCRT-III dysfunction causes autophagosome accumulation and neurodegeneration. Curr Biol. 2007; 17(18):1561–7. https://doi.org/10.1016/j.cub.2007.07.029 PMID: 17683935

35. Rusten TE, Vaccari T, Lindmo K, Rodahl LM, Nezis IP, Sem-Jacobsen C, et al. ESCRTs and *Fab1* regulate distinct steps of autophagy. Curr Biol. 2007; 17(20):1817–25. https://doi.org/10.1016/j.cub.2007.09.032 PMID: 17935992

36. Tamai K, Tanaka N, Nara A, Yamamoto A, Nakagawa I, Yoshimori T, et al. Role of Hrs in maturation of autophagosomes in mammalian cells. Biochem Biophys Res Commun. 2007; 360(4):721–7. https://doi.org/10.1016/j.bbrc.2007.06.105 PMID: 17624298

37. Takahashi Y, He H, Tang Z, Hattori T, Liu Y, Young MM, et al. An autophagy assay reveals the ESCRT-III component CHMP2A as a regulator of phagophore closure. Nature communications. 2018; 9(1):2855. https://doi.org/10.1038/s41467-018-05254-w PMID: 30030437

38. Zhou F, Wu Z, Zhao M, Murtazina R, Cai J, Zhang A, et al. Rab5-dependent autophagosome closure by ESCRT. The Journal of cell biology. 2019; 218(6):1908–27. https://doi.org/10.1083/jcb.201811173 PMID: 31010855

39. Djeddi A, Michelet X, Culetto E, Alberti A, Barois N, Legouis R. Induction of autophagy in ESCRT mutants is an adaptive response for cell survival in *C. elegans*. Journal of cell science. 2012; 125 (3):685–94.

40. Guo B, Huang X, Zhang P, Qi L, Liang Q, Zhang X, et al. Genome-wide screen identifies signaling pathways that regulate autophagy during *Caenorhabditis elegans* development. EMBO reports. 2014; 15(6):705–13. https://doi.org/10.1002/embr.201338310 PMID: 24764321

41. Zubovych IO, Straud S, Roth MG, Newmeyer DD. Mitochondrial Dysfunction Confers Resistance to Multiple Drugs in *Caenorhabditis elegans*. Molecular Biology of the Cell. 2010; 21(6):956–69. https://doi.org/10.1091/mbc.E09-08-0673 PMID: 20089839

42. Köhler F, Müller-Rischart AK, Conradt B, Rolland SG. The loss of *LRPPRC* function induces the mitochondrial unfolded protein response. Aging. 2015; 7(9):701–12. https://doi.org/10.18632/aging.100812 PMID: 26412102

43. Liu Y, Samuel BS, Breen PC, Ruvkun G. *Caenorhabditis elegans* pathways that surveil and defend mitochondria. Nature. 2014; 508(7496):406–10. https://doi.org/10.1038/nature13204 PMID: 24695221

44. Runkel ED, Liu S, Baumeister R, Schulze E. Surveillance-activated defenses block the ROS-induced mitochondrial unfolded protein response. PLoS genetics. 2013; 9(3):e1003346. https://doi.org/10.1371/journal.pgen.1003346 PMID: 23516373

45. Kamath RS, Ahringer J. Genome-wide RNAi screening in *Caenorhabditis elegans*. Methods (San Diego, Calif). 2003; 30(4):313–21.

46. Rolland SG, Motori E, Memar N, Hench J, Frank S, Winklhofer KF, et al. Impaired complex IV activity in response to loss of LRPPRC function can be compensated by mitochondrial hyperfusion. Proceedings of the National Academy of Sciences of the United States of America. 2013; 110(32):E2967–76. https://doi.org/10.1073/pnas.1303872110 PMID: 23878239

47. Loew LM, Tuft RA, Carrington W, Fay FS. Imaging in five dimensions: time-dependent membrane potentials in individual mitochondria. Biophysical Journal. 1993; 65(6):2396–407. https://doi.org/10.1016/S0006-3495(93)81318-3 PMID: 8312478

48. Chen Y, Scarcelli V, Legouis R. Approaches for Studying Autophagy in *Caenorhabditis elegans*. Cells. 2017; 6(3).

49. Jenzer C, Simionato E, Legouis R. Tools and methods to analyze autophagy in *C. elegans*. Methods (San Diego, Calif). 2015; 75:162–71.

50. Klionsky DJ, Abdelmohsen K, Abe A, Abedin MJ, Abeliovich H, Acevedo Arozena A, et al. Guidelines for the use and interpretation of assays for monitoring autophagy (3rd edition). Autophagy. 2016; 12(1):1–222. https://doi.org/10.1080/15548627.2015.1100356 PMID: 26799652

51. Tian Y, Li Z, Hu W, Ren H, Tian E, Zhao Y, et al. *C. elegans* Screen Identifies Autophagy Genes Specific to Multicellular Organisms. Cell. 2010; 141(6):1042–55. https://doi.org/10.1016/j.cell.2010.04.034 PMID: 20550938

52. Zhang H, Chang JT, Guo B, Hansen M, Jia K, Kovacs AL, et al. Guidelines for monitoring autophagy in *Caenorhabditis elegans*. Autophagy. 2015; 11(1):9–27. https://doi.org/10.1080/15548627.2014.1003478 PMID: 25569839

53. Chapin HC, Okada M, Merz AJ, Miller DL. Tissue-specific autophagy responses to aging and stress in *C. elegans*. Aging (Albany NY). 2015; 7(6):419–34.

54. Mizushima N, Yoshimori T, Levine B. Methods in Mammalian Autophagy Research. Cell. 2010; 140(3):313–26. https://doi.org/10.1016/j.cell.2010.01.028 PMID: 20144757

55. Homma K, Suzuki K, Sugawara H. The Autophagy Database: an all-inclusive information resource on autophagy that provides nourishment for research. Nucleic Acids Research. 2011; 39(suppl_1):D986–D90.

56. Lipinski MM, Hoffman G, Ng A, Zhou W, Py BF, Hsu E, et al. A genome-wide siRNA screen reveals multiple mTORC1 independent signaling pathways regulating autophagy under normal nutritional conditions. Developmental cell. 2010; 18(6):1041–52. https://doi.org/10.1016/j.devcel.2010.05.005 PMID: 20627085

57. Strohecker AM, Joshi S, Possemato R, Abraham RT, Sabatini DM, White E. Identification of 6-phosphofructo-2-kinase/fructose-2,6-bisphosphatase as a novel autophagy regulator by high content shRNA screening. Oncogene. 2015; 34(45):5662–76. https://doi.org/10.1038/onc.2015.23 PMID: 25772235

58. Dayalan Naidu S, Dikovskaya D, Gaurilcikaite E, Knatko EV, Healy ZR, Mohan H, et al. Transcription factors NRF2 and HSF1 have opposing functions in autophagy. Sci Rep. 2017; 7(1):11023. https://doi.org/10.1038/s41598-017-11262-5 PMID: 28887499

59. Demishtein A, Fraiberg M, Berko D, Tirosh B, Elazar Z, Navon A. SQSTM1/p62-mediated autophagy compensates for loss of proteasome polyubiquitin recruiting capacity. Autophagy. 2017; 13(10):1697–708. https://doi.org/10.1080/15548627.2017.1356549 PMID: 28792301

60. Dokladny K, Zuhl MN, Mandell M, Bhattacharya D, Schneider S, Deretic V, et al. Regulatory coordination between two major intracellular homeostatic systems: heat shock response and autophagy. The Journal of biological chemistry. 2013; 288(21):14959–72. https://doi.org/10.1074/jbc.M113.462408 PMID: 23576438

61. Hu G, McQuiston T, Bernard A, Park YD, Qiu J, Vural A, et al. A conserved mechanism of TOR-dependent RCK-mediated mRNA degradation regulates autophagy. Nature cell biology. 2015; 17(7):930–42. https://doi.org/10.1038/ncb3189 PMID: 26098573

62. Hwang DW, So KS, Kim SC, Park KM, Lee YJ, Kim SW, et al. Autophagy Induced by CX-4945, a Casein Kinase 2 Inhibitor, Enhances Apoptosis in Pancreatic Cancer Cell Lines. Pancreas. 2017; 46 (4):575–81. https://doi.org/10.1097/MPA.0000000000000780 PMID: 28196025

63. Keith SA, Maddux SK, Zhong Y, Chinchankar MN, Ferguson AA, Ghazi A, et al. Graded Proteasome Dysfunction in *Caenorhabditis elegans* Activates an Adaptive Response Involving the Conserved SKN-1 and ELT-2 Transcription Factors and the Autophagy-Lysosome Pathway. PLoS genetics. 2016; 12(2):e1005823. https://doi.org/10.1371/journal.pgen.1005823 PMID: 26828939

64. Kumsta C, Chang JT, Schmalz J, Hansen M. Hormetic heat stress and HSF-1 induce autophagy to improve survival and proteostasis in *C. elegans*. Nature communications. 2017; 8:14337. https://doi.org/10.1038/ncomms14337 PMID: 28198373

65. Lee SW, Song YS, Lee SY, Yoon YG, Lee SH, Park BS, et al. Downregulation of protein kinase CK2 activity facilitates tumor necrosis factor-alpha-mediated chondrocyte death through apoptosis and autophagy. PloS one. 2011; 6(4):e19163. https://doi.org/10.1371/journal.pone.0019163 PMID: 21559479

66. Meléndez A, Tallóczy Z, Seaman M, Eskelinen E-L, Hall DH, Levine B. Autophagy Genes Are Essential for Dauer Development and Life-Span Extension in *C. elegans*. Science (New York, NY). 2003; 301(5638):1387–91.

67. Menzies FM, Garcia-Arencibia M, Imarisio S, O'Sullivan NC, Ricketts T, Kent BA, et al. Calpain inhibition mediates autophagy-dependent protection against polyglutamine toxicity. Cell death and differentiation. 2015; 22(3):433–44. https://doi.org/10.1038/cdd.2014.151 PMID: 25257175

68. Murphy CT, McCarroll SA, Bargmann CI, Fraser A, Kamath RS, Ahringer J, et al. Genes that act downstream of DAF-16 to influence the lifespan of *Caenorhabditis elegans*. Nature. 2003; 424:277. https://doi.org/10.1038/nature01789 PMID: 12845331

69. Pierce SB, Costa M, Wisotzkey R, Devadhar S, Homburger SA, Buchman AR, et al. Regulation of DAF-2 receptor signaling by human insulin and ins-1, a member of the unusually large and diverse C. elegans insulin gene family. Genes & Development. 2001; 15(6):672–86.

70. Putker M, Madl T, Vos Harmjan R, de Ruiter H, Visscher M, van den Berg Maaike CW, et al. Redox-Dependent Control of FOXO/DAF-16 by Transportin-1. Molecular cell. 2013; 49(4):730–42. https://doi.org/10.1016/j.molcel.2012.12.014 PMID: 23333309

71. Sheaffer KL, Updike DL, Mango SE. The Target of Rapamycin pathway antagonizes *pha-4/FoxA* to control development and aging. Curr Biol. 2008; 18(18):1355–64. https://doi.org/10.1016/j.cub.2008.07.097 PMID: 18804378

72. Tang L, Fares H, Zhao X, Du W, Liu BF. Different endocytic functions of AGEF-1 in *C. elegans* coelomocytes. Biochimica et biophysica acta. 2012; 1820(7):829–40. https://doi.org/10.1016/j.bbagen.2012.03.004 PMID: 22446376

73. Yang D, Li L, Liu H, Wu L, Luo Z, Li H, et al. Induction of autophagy and senescence by knockdown of ROC1 E3 ubiquitin ligase to suppress the growth of liver cancer cells. Cell death and differentiation. 2013; 20(2):235–47. https://doi.org/10.1038/cdd.2012.113 PMID: 22935614

74. Zhao Y, Yang J, Liao W, Liu X, Zhang H, Wang S, et al. Cytosolic FoxO1 is essential for the induction of autophagy and tumour suppressor activity. Nature cell biology. 2010; 12:665. https://doi.org/10.1038/ncb2069 PMID: 20543840

75. Nawa M, Kage-Nakadai E, Aiso S, Okamoto K, Mitani S, Matsuoka M. Reduced expression of BTBD10, an Akt activator, leads to motor neuron death. Cell Death & Differentiation. 2012; 19 (8):1398–407.

76. Nawa M, Matsuoka M. The Method of the Body Bending Assay Using Caenorhabditis elegans. Bio Protoc. 2012; 2(17):e253.

77. Johnson D, Nehrke K. Mitochondrial Fragmentation Leads to Intracellular Acidification in Caenorhabditis elegans and Mammalian Cells. Molecular Biology of the Cell. 2010; 21(13):2191–201. https://doi.org/10.1091/mbc.E09-10-0874 PMID: 20444981

78. Lim Y, Rubio-Peña K, Sobraske PJ, Molina PA, Brookes PS, Galy V, et al. Fndc-1 contributes to paternal mitochondria elimination in C. elegans. Developmental Biology. 2019; 454(1):15–20. https://doi.org/10.1016/j.ydbio.2019.06.016 PMID: 31233739

79. Palikaras K, Lionaki E, Tavernarakis N. Coordination of mitophagy and mitochondrial biogenesis during ageing in *C. elegans*. Nature. 2015.

80. Rauthan M, Ranji P, Aguilera Pradenas N, Pitot C, Pilon M. The mitochondrial unfolded protein response activator ATFS-1 protects cells from inhibition of the mevalonate pathway. Proceedings of

the National Academy of Sciences of the United States of America. 2013; 110(15):5981–6. https://doi.org/10.1073/pnas.1218778110 PMID: 23530189

81. Bennett CF, Vander Wende H, Simko M, Klum S, Barfield S, Choi H, et al. Activation of the mitochondrial unfolded protein response does not predict longevity in *Caenorhabditis elegans*. Nature communications. 2014; 5:3483. https://doi.org/10.1038/ncomms4483 PMID: 24662282

82. Buis A, Bellemin S, Goudeau J, Monnier L, Loiseau N, Guillou H, et al. Coelomocytes Regulate Starvation-Induced Fat Catabolism and Lifespan Extension through the Lipase LIPL-5 in Caenorhabditis elegans. Cell reports. 2019; 28(4):1041–9.e4. https://doi.org/10.1016/j.celrep.2019.06.064 PMID: 31340142

83. Harvald EB, Sprenger RR, Dall KB, Ejsing CS, Nielsen R, Mandrup S, et al. Multi-omics Analyses of Starvation Responses Reveal a Central Role for Lipoprotein Metabolism in Acute Starvation Survival in *C.elegans*. Cell Systems. 2017; 5(1):38–52.e4. https://doi.org/10.1016/j.cels.2017.06.004 PMID: 28734827

84. Vrablik TL, Petyuk VA, Larson EM, Smith RD, Watts JL. Lipidomic and proteomic analysis of Caenorhabditis elegans lipid droplets and identification of ACS-4 as a lipid droplet-associated protein. Biochimica et Biophysica Acta (BBA)—Molecular and Cell Biology of Lipids. 2015; 1851(10):1337–45.

85. Benador IY, Veliova M, Mahdaviani K, Petcherski A, Wikstrom JD, Assali EA, et al. Mitochondria Bound to Lipid Droplets Have Unique Bioenergetics, Composition, and Dynamics that Support Lipid Droplet Expansion. Cell metabolism. 2018; 27(4):869–85.e6. https://doi.org/10.1016/j.cmet.2018.03.003 PMID: 29617645

86. Rambold Angelika S, Cohen S, Lippincott-Schwartz J. Fatty Acid Trafficking in Starved Cells: Regulation by Lipid Droplet Lipolysis, Autophagy, and Mitochondrial Fusion Dynamics. Developmental cell. 2015; 32(6):678–92. https://doi.org/10.1016/j.devcel.2015.01.029 PMID: 25752962

87. Singh R, Kaushik S, Wang Y, Xiang Y, Novak I, Komatsu M, et al. Autophagy regulates lipid metabolism. Nature. 2009; 458:1131. https://doi.org/10.1038/nature07976 PMID: 19339967

88. Saito T, Kuma A, Sugiura Y, Ichimura Y, Obata M, Kitamura H, et al. Autophagy regulates lipid metabolism through selective turnover of NCoR1. Nature communications. 2019; 10(1):1567. https://doi.org/10.1038/s41467-019-08829-3 PMID: 30952864

89. Pellegrino MW, Nargund AM, Haynes CM. Signaling the mitochondrial unfolded protein response. Biochimica et Biophysica Acta (BBA)—Molecular Cell Research. 2013; 1833(2):410–6.

90. Honjoh S, Yamamoto T, Uno M, Nishida E. Signalling through RHEB-1 mediates intermittent fasting-induced longevity in *C. elegans*. Nature. 2008; 457:726. https://doi.org/10.1038/nature07583 PMID: 19079239

91. Cooper JF, Machiela E, Dues DJ, Spielbauer KK, Senchuk MM, Van Raamsdonk JM. Activation of the mitochondrial unfolded protein response promotes longevity and dopamine neuron survival in Parkinson's disease models. Scientific Reports. 2017; 7(1):16441. https://doi.org/10.1038/s41598-017-16637-2 PMID: 29180793

92. Kim KH, Lee M-S. Autophagy—a key player in cellular and body metabolism. Nature Reviews Endocrinology. 2014; 10:322. https://doi.org/10.1038/nrendo.2014.35 PMID: 24663220

93. Rabinowitz JD, White E. Autophagy and Metabolism. Science (New York, NY). 2010; 330 (6009):1344–8.

94. Lin Y-F, Haynes CM. Metabolism and the UPR^{mt}. Molecular cell. 2016; 61(5):677–82. https://doi.org/10.1016/j.molcel.2016.02.004 PMID: 26942672

95. Mouysset J, Kähler C, Hoppe T. A conserved role of *Caenorhabditis elegans* CDC-48 in ER-associated protein degradation. Journal of Structural Biology. 2006; 156(1):41–9. https://doi.org/10.1016/j.jsb.2006.02.015 PMID: 16647269

96. Takahashi M, Iwasaki H, Inoue H, Takahashi K. Reverse Genetic Analysis of the *Caenorhabditis elegans* 26S Proteasome Subunits by RNA Interference. Biological Chemistry2002. p. 1263. https://doi.org/10.1515/BC.2002.140 PMID: 12437114

97. Baker BM, Nargund AM, Sun T, Haynes CM. Protective coupling of mitochondrial function and protein synthesis via the eIF2alpha kinase GCN-2. PLoS genetics. 2012; 8(6):e1002760. https://doi.org/10.1371/journal.pgen.1002760 PMID: 22719267

98. Brenner S. The Genetics of *Caenorhabditis Elegans*. Genetics. 1974; 77(1):71–94. PMID: 4366476

99. Simmer F, Tijsterman M, Parrish S, Koushika SP, Nonet ML, Fire A, et al. Loss of the Putative RNA-Directed RNA Polymerase RRF-3 Makes *C. elegans* Hypersensitive to RNAi. Current Biology. 2002; 12(15):1317–9. https://doi.org/10.1016/s0960-9822(02)01041-2 PMID: 12176360

100. Springer W, Hoppe T, Schmidt E, Baumeister R. A *Caenorhabditis elegans* Parkin mutant with altered solubility couples α-synuclein aggregation to proteotoxic stress. Human Molecular Genetics. 2005; 14 (22):3407–23. https://doi.org/10.1093/hmg/ddi371 PMID: 16204351

101. Pujol N, Cypowyj S, Ziegler K, Millet A, Astrain A, Goncharov A, et al. Distinct Innate Immune Responses to Infection and Wounding in the *C. elegans* Epidermis. Current Biology. 2008; 18(7):481–9. https://doi.org/10.1016/j.cub.2008.02.079 PMID: 18394898

102. Kang C, You Y-j, Avery L. Dual roles of autophagy in the survival of *Caenorhabditis elegans* during starvation. Genes & Development. 2007; 21(17):2161–71.

103. Urano F, Calfon M, Yoneda T, Yun C, Kiraly M, Clark SG, et al. A survival pathway for Caenorhabditis elegans with a blocked unfolded protein response. The Journal of cell biology. 2002; 158(4):639–46. https://doi.org/10.1083/jcb.200203086 PMID: 12186849

104. Mariol M-C, Walter L, Bellemin S, Gieseler K. A rapid protocol for integrating extrachromosomal arrays with high transmission rate into the *C. elegans* genome. Journal of visualized experiments: JoVE. 2013(82):e50773–e. https://doi.org/10.3791/50773 PMID: 24379027

105. Frøkjær-Jensen C, Wayne Davis M, Hopkins CE, Newman BJ, Thummel JM, Olesen S-P, et al. Single-copy insertion of transgenes in *Caenorhabditis elegans*. Nature Genetics. 2008; 40:1375. https://doi.org/10.1038/ng.248 PMID: 18953339

106. Frøkjær-Jensen C, Davis MW, Sarov M, Taylor J, Flibotte S, LaBella M, et al. Random and targeted transgene insertion in *Caenorhabditis elegans* using a modified Mos1 transposon. Nature Methods. 2014; 11:529. https://doi.org/10.1038/nmeth.2889 PMID: 24820376

107. Gibson DG, Young L, Chuang R-Y, Venter JC, Hutchison Iii CA, Smith HO. Enzymatic assembly of DNA molecules up to several hundred kilobases. Nature Methods. 2009; 6:343. https://doi.org/10.1038/nmeth.1318 PMID: 19363495

108. Frøkjær-Jensen C, Davis MW, Ailion M, Jorgensen EM. Improved Mos1-mediated transgenesis in *C. elegans*. Nature Methods. 2012; 9:117. https://doi.org/10.1038/nmeth.1865 PMID: 22290181

109. Jagasia R, Grote P, Westermann B, Conradt B. DRP-1-mediated mitochondrial fragmentation during EGL-1-induced cell death in C. elegans. Nature. 2005; 433(7027):754–60. https://doi.org/10.1038/nature03316 PMID: 15716954

110. Sternberg SR. Biomedical Image Processing. Computer. 1983; 16(1):22–34.

111. Sato Y, Nakajima S, Shiraga N, Atsumi H, Yoshida S, Koller T, et al. Three-dimensional multi-scale line filter for segmentation and visualization of curvilinear structures in medical images. Medical Image Analysis. 1998; 2(2):143–68. https://doi.org/10.1016/s1361-8415(98)80009-1 PMID: 10646760

112. Xiao R, Chun L, Ronan Elizabeth A, Friedman David I, Liu J, Xu XZS. RNAi Interrogation of Dietary Modulation of Development, Metabolism, Behavior, and Aging in *C. elegans*. Cell reports. 2015; 11(7):1123–33. https://doi.org/10.1016/j.celrep.2015.04.024 PMID: 25959815

113. Löfgren L, Forsberg G-B, Ståhlman M. The BUME method: a new rapid and simple chloroform-free method for total lipid extraction of animal tissue. Scientific Reports. 2016; 6(1):27688.

114. Witting M, Maier TV, Garvis S, Schmitt-Kopplin P. Optimizing a ultrahigh pressure liquid chromatography-time of flight-mass spectrometry approach using a novel sub-2μm core–shell particle for in depth lipidomic profiling of Caenorhabditis elegans. Journal of Chromatography A. 2014; 1359:91–9. https://doi.org/10.1016/j.chroma.2014.07.021 PMID: 25074420

115. O'Donnell VB, Dennis EA, Wakelam MJO, Subramaniam S. LIPID MAPS: Serving the next generation of lipid researchers with tools, resources, data, and training. Science Signaling. 2019; 12(563):eaaw2964. https://doi.org/10.1126/scisignal.aaw2964 PMID: 30622195

116. Kind T, Liu K-H, Lee DY, DeFelice B, Meissen JK, Fiehn O. LipidBlast in silico tandem mass spectrometry database for lipid identification. Nature Methods. 2013; 10(8):755–8. https://doi.org/10.1038/nmeth.2551 PMID: 23817071

117. Mok DZL, Sternberg PW, Inoue T. Morphologically defined sub-stages of *C. elegans* vulval development in the fourth larval stage. BMC developmental biology. 2015; 15:26–. https://doi.org/10.1186/s12861-015-0076-7 PMID: 26066484

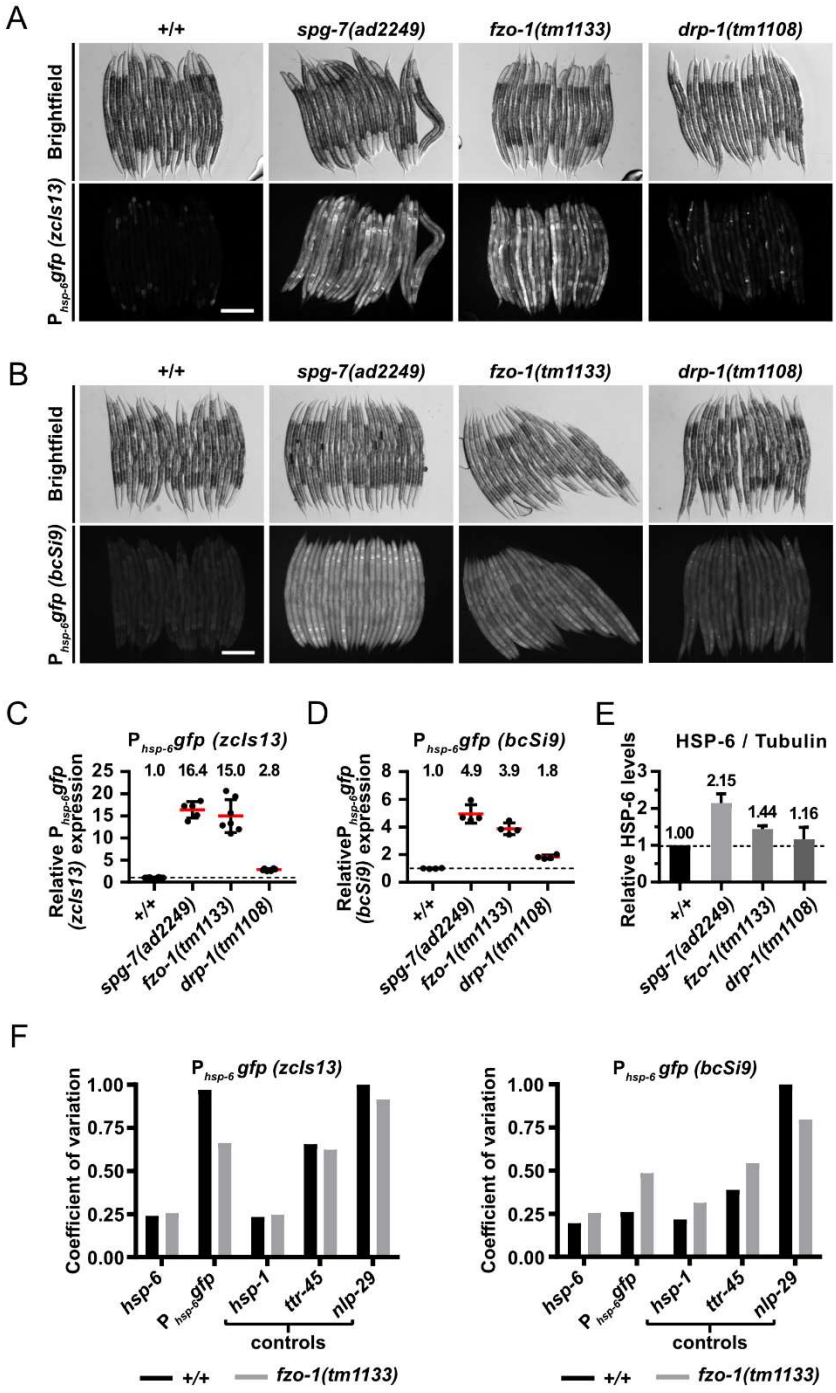

S1 Fig: Comparison of expression levels and inter-individual variability of multi-copy P*hsp-6* mtHSP70*gfp (zcIs13)* and single-copy integrated P*hsp-6* mtHSP70*gfp (bcSi9)* transgenes. (A) Brightfield (upper panel) and fluorescence images (lower panel) of L4 larvae expressing P*hsp-6gfp (zcIs13)* in wild type (+/+), *spg-7(ad2249), fzo-1(tm1133) or drp-1(tm1108)*. Scale bar: 200 µm. **(B)** Brightfield (upper panel) and fluorescence images (lower panel) of L4 larvae expressing P*hsp-6gfp (bcSi9)* in wild type (+/+), *spg-7(ad2249), fzo-1(tm1133)* or *drp-1(tm1108)*. Scale bar: 200 µm. **(C)** Quantifications of fluorescence images of panel A (P*hsp-6gfp*

(zcIs13)) are shown. Each dot represents quantification of 15-20 L4 larvae. Values indicate means ± SD of ≥5 independent measurements. **(D)** Quantifications of fluorescence images of panel B (P_{hsp-6}*gfp (bcSi9)*) are shown. Each dot represents quantification of 15-20 L4 larvae. Values indicate means ± SD of ≥4 independent measurements. **(E)** Quantifications of western blot analysis of endogenous HSP-6 levels in wild-type (+/+), *spg-7(ad2249), fzo-1(tm1133)* or *drp-1(tm1108)* using anti-HSP-6 antibodies. For each genotype, 100 L4 larvae were harvested per experiment for western blot analysis. Values indicate means of relative HSP-6 expression (HSP-6/TUB) ± SD, n = 2. **(F)** Inter-individual variability in gene expression of target genes in *bcSi9* and *zcIs13* in both wild type (+/+) and *fzo-1(tm1133)*. To estimate inter-individual variability in gene expression, the coefficient of variation was calculated from individual mRNA levels obtained from normalized Ct values using the delta Ct method. Inter-individual variability values were normalized such that variability values for *nlp-29* in wild type = 1 *(bcSi9* or *zcIs13)*. Number of individual worms: n=35 *(bcSi9)*, n=32 (*bcSi9; fzo-1(tm1133))*, n=31 *(zcIs13)*, n=31 *(zcIs13; fzo-1(tm1133)*).

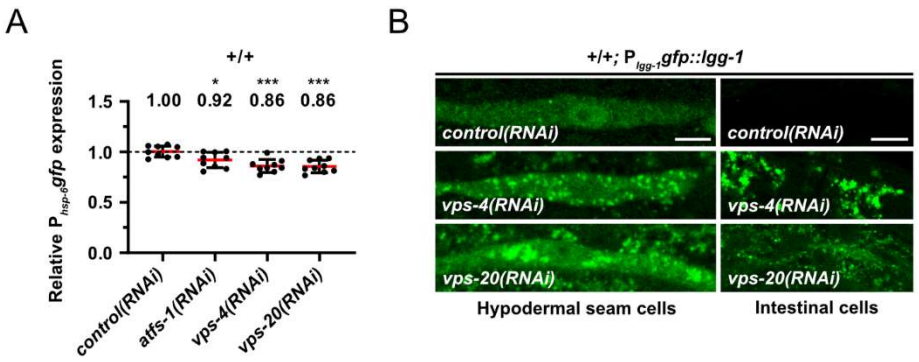

S2 Fig: RNAi against *vps-4*^{VPS4} and *vps-20*^{CHMP6} suppresses expression of *bcSi9* and induces autophagy in wild type (+/+). (A) L4 larvae were subjected to *control(RNAi)*, *atfs-1(RNAi), vps-4(RNAi)* or *vps-20(RNAi)* and the F1 generation was imaged. Each dot represents the quantification of fluorescence intensity of 15-20 L4 larvae. Values indicate means ± SD of 5 independent experiments in duplicates. **P*<0.05, ****P*<0.001 using one-way ANOVA with Dunnett's multiple comparison test to *control(RNAi)*. **(B)** P_{lgg-1}*gfp::lgg-1* expression of L4 larvae in hypodermal seam cells and intestinal cells upon *control(RNAi)*, *vps-4(RNAi)* or *vps-20(RNAi).* Representative images of >30 animals from two independent biological replicates are shown. Scale bar hypodermal seam cells: 5 µm. Scale bar intestinal cells: 20 µm.

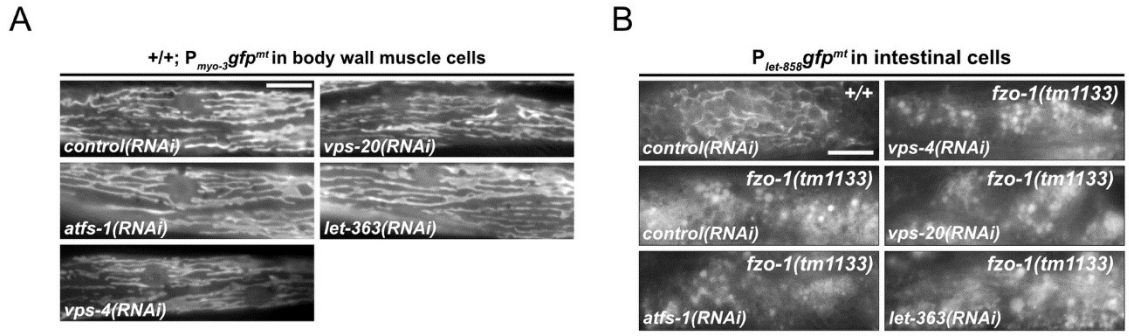

S3 Fig: Knock-down of ESCRT components in body wall muscle cells of wild type and intestinal cells in *fzo-1(tm1133)* does not change mitochondrial morphology. (A) Fluorescence images of L4 larvae expressing $P_{myo\text{-}3}gfp^{mt}$ in wild type (+/+). L4 larvae were subjected to *control(RNAi)*, *atfs-1(RNAi)*, *vps-4(RNAi)*, *vps-20(RNAi)* or *let-363(RNAi)* and the F1 generation was imaged. Scale bar: 10 µm. **(B)** Fluorescence images of L4 larvae expressing $P_{let\text{-}858}gfp^{mt}$ in wild type (+/+) or *fzo-1(tm1133)*. L4 larvae were subjected to *control(RNAi)*, *atfs-1(RNAi)*, *vps-4(RNAi)*, *vps-20(RNAi)* or *let-363(RNAi)* and the F1 generation was imaged. Scale bar: 10 µm.

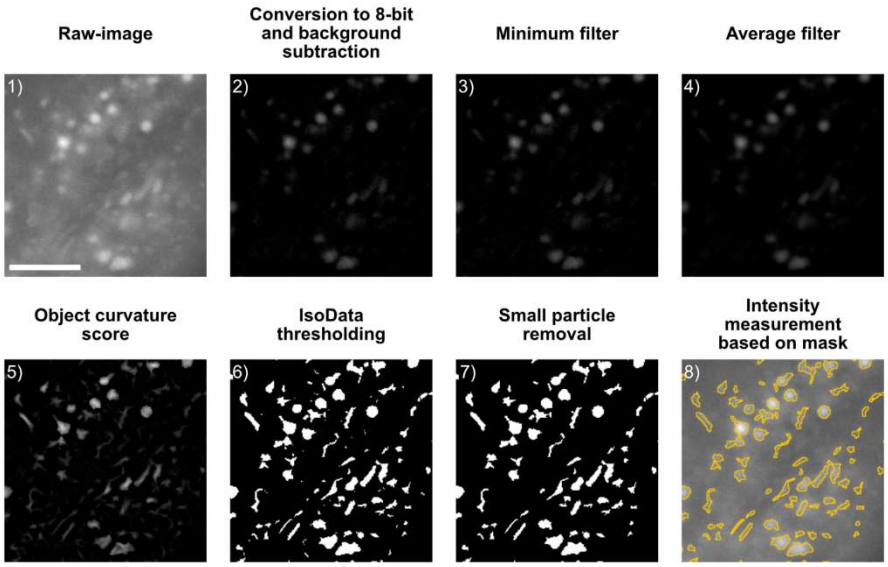

S4 Fig: Image segmentation and intensity measurement workflow. A raw 16-bit image (1) is converted to 8-bit, followed by a background subtraction using the rolling ball algorithm (2). This is followed by the successive application of a minimum (3) and maximum filter (4). The ImageJ Tubeness plugin generates an image with object curvature scores (5), after which the IsoData autothresholding is applied to generate the binary mask (6). Noise is removed by filtering out particles below a certain size (7) and the final mask is used to define the area in which intensity measurements are obtained (8). Scale bar: 5 µm.

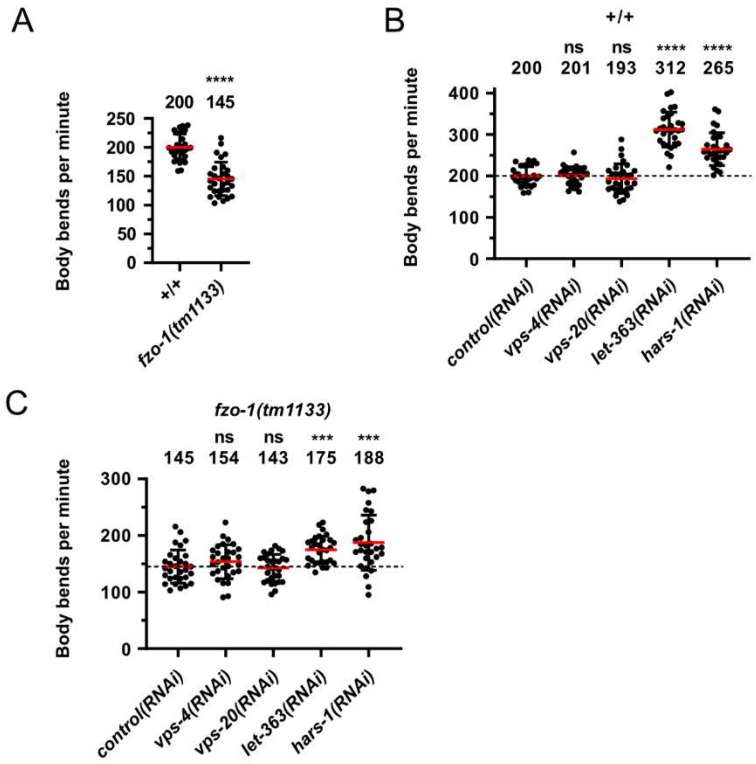

S5 Fig: Thrashing assay in wild-type and *fzo-1(tm1133)* animals upon induction of autophagy. Thrashing rate was analyzed by counting body bends of animals swimming for 1 minute in M9 buffer in 3 independent experiments. Each dot represents one L4 larvae. **(A)** Thrashing rates of wild-type (+/+) or *fzo-1(tm1133)* L4 larvae. ****P<0.0001 using unpaired two-tailed t-test. n=30. **(B)** Thrashing rates in wild-type animals upon induction of autophagy. L4 larvae were subjected to *control(RNAi)*, *vps-4(RNAi)*, *vps-20(RNAi)*, *let-363(RNAi)* or *hars-1(RNAi)* and the F1 generation was analyzed. ns: not significant, ****P<0.0001 using Kruskal-Wallis test with Dunn's multiple comparison test to *control(RNAi)*. n=30. **(C)** Thrashing rates in *fzo-1(tm1133)* animals upon induction of autophagy. L4 larvae were subjected to *control(RNAi)*, *vps-4(RNAi)*, *vps-20(RNAi)*, *let-363(RNAi)* or *hars-1(RNAi)* and the F1 generation was analyzed. ns: not significant, ***P<0.001 using Kruskal-Wallis test with Dunn's multiple comparison test to *control(RNAi)*. n=30.

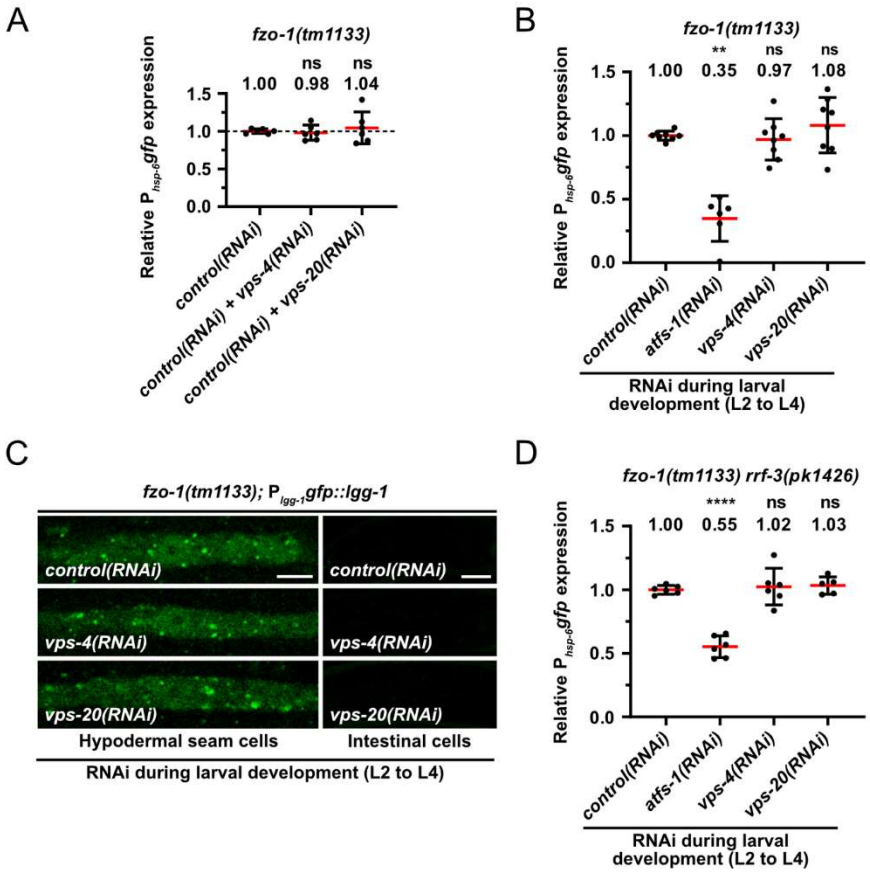

S6 Fig: RNAi against *vps-4*^{VPS4} and *vps-20*^{CHMP6} does not suppress *fzo-1(tm1133)*-induced UPR^{mt} when diluted with *control(RNAi)* or carried out in one generation from L2 to L4 larvae. (A) Quantifications of fluorescence images of L4 larvae expressing P*hsp-6*gfp *(bcSi9)* in *fzo-1(tm1133)*. After subtracting the mean fluorescence intensity of wild type (+/+) on *control(RNAi)*, the values were normalized to *fzo-1(tm1133)* on *control(RNAi)*. Each dot represents the quantification of fluorescence intensity of 15-20 L4 larvae. Values indicate means ± SD of 3 independent experiments in duplicates. ns: not significant, using one-way ANOVA with Dunnett's multiple comparison test to *control(RNAi)*. **(B)** Quantifications of fluorescence images of L4 larvae expressing P*hsp-6*gfp *(bcSi9)* in *fzo-1(tm1133)*. L2 larvae were subjected to *control(RNAi)*, *atfs-1(RNAi)*, *vps-4(RNAi)* or *vps-20(RNAi)* and the same animals were imaged in L4 stage. After subtracting the mean fluorescence intensity of wild type (+/+) on *control(RNAi)*, the values were normalized to *fzo-1(tm1133)* on *control(RNAi)*. Each dot represents the quantification of fluorescence intensity of 15-20 L4 larvae. Values indicate means ± SD of 4 independent experiments in duplicates. ns: not significant, $^{**}P<0.01$ using Kruskal-Wallis test with Dunn's multiple comparison test to *control(RNAi)*. **(C)** P*lgg-1*gfp::lgg-*1* expression of *fzo-1(tm1133)* L4 larvae in hypodermal seam cells and intestinal cells. L2 larvae were subjected to *control(RNAi)*, *vps-4(RNAi)* or *vps-20(RNAi)* and the same animals

were imaged in L4 stage. Representative images of >60 animals from two independent biological replicates are shown. Scale bar hypodermal seam cells: 5 µm. Scale bar intestinal cells: 20 µm. **(D)** Quantifications of fluorescence images of L4 larvae expressing $P_{hsp\text{-}6}$*gfp (bcSi9)* in *fzo-1(tm1133) rrf-3(pk1426)*. L2 larvae were subjected to *control(RNAi)*, *atfs-1(RNAi)*, *vps-4(RNAi)* or *vps-20(RNAi)* and the same animals were imaged in L4 stage. After subtracting the mean fluorescence intensity of wild type (+/+) on *control(RNAi)*, the values were normalized to *fzo-1(tm1133)* on *control(RNAi)*. Each dot represents the quantification of fluorescence intensity of 15-20 L4 larvae. Values indicate means ± SD of 4 independent experiments in duplicates. ns: not significant, ****P<0.0001 using one-way ANOVA with Dunnett's multiple comparison test to *control(RNAi)*.

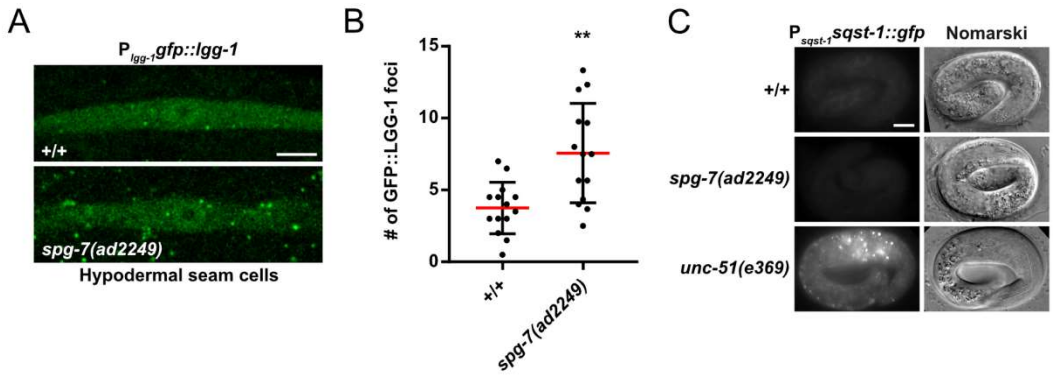

S7 Fig: Autophagy is induced in *spg-7(ad2249)* animals. (A) $P_{lgg\text{-}1}$*gfp::lgg-1* expression in hypodermal seam cells of wild type (+/+) or *spg-7(ad2249)* L4 larvae. Scale bar: 5 µm. **(B)** Quantification of GFP::LGG-1 foci in hypodermal seam cells from panel A. Each dot represents the average amount of GFP::LGG-1 foci counted from 2 – 5 seam cells in one animal. n≥18 for each genotype; values indicate means ± SD; **P<0.01 using unpaired two-tailed t-test with Welch's correction. **(C)** Nomarski and fluorescent images of the $P_{sqst\text{-}1}$*sqst-1::gfp* translational reporter in embryos of wild type (+/+) and *spg-7(ad2249)* animals. As a positive control for a block in autophagy, *unc-51(e369)* was used. Representative images of >60 embryos are shown. Scale bar: 10 µm.

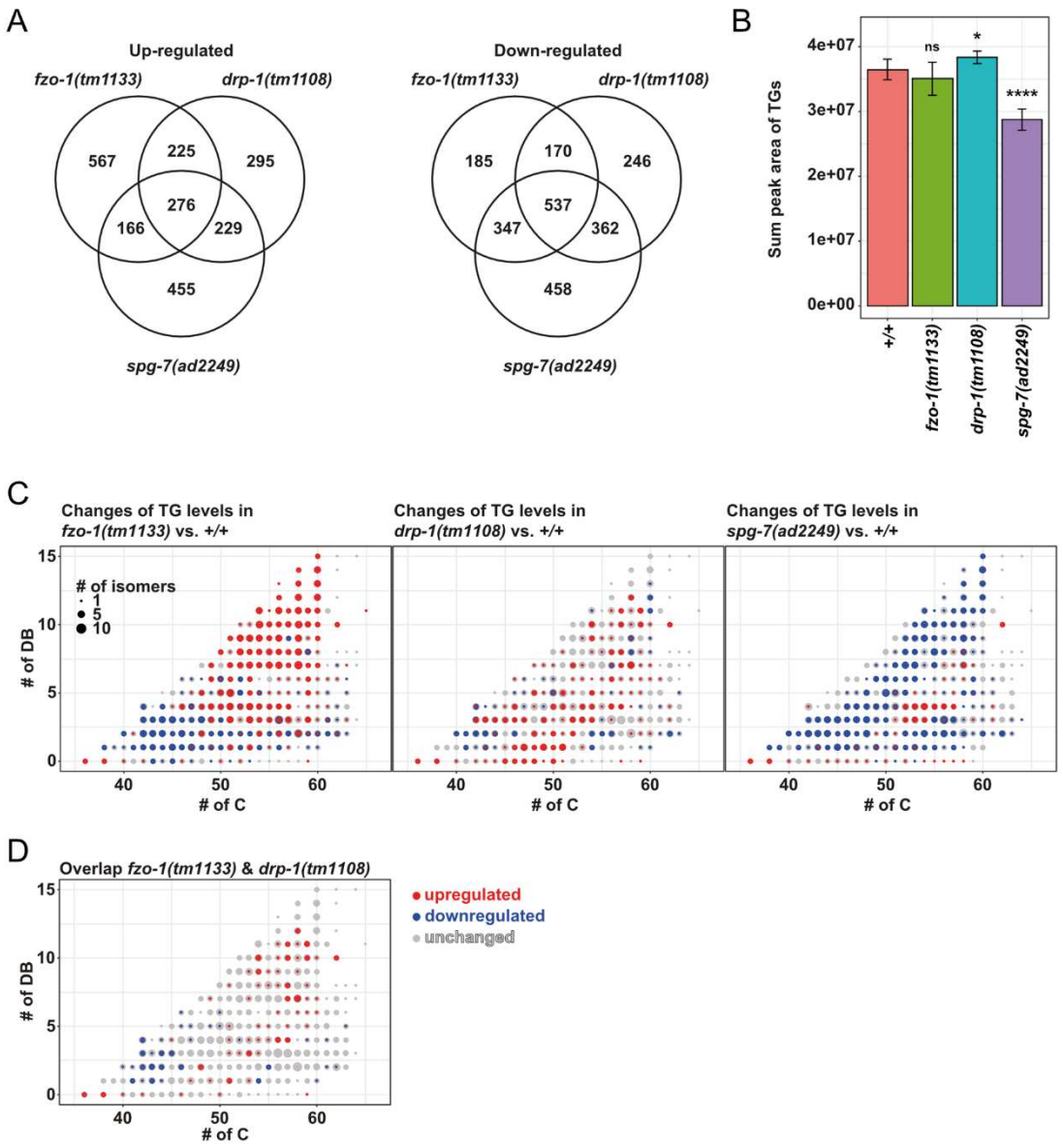

S8 Fig: Defects in mitochondrial homeostasis lead to major changes in lipid metabolism. **(A)** Venn diagrams showing the overlap of lipids up- or downregulated in *fzo-1(tm1133)*, *drp-1(tm1108)* and *spg-7(ad2249)* in comparison to wild type (+/+). **(B)** Total amount of TGs in wild type (+/+), *fzo-1(tm1133)*, *drp-1(tm1108)* and *spg-7(ad2249)* backgrounds. Means ± SD are shown; ns: not significant, **P*<0.05, *****P*<0.0001 using Welch test. **(C)** Scatterplot indicating the distribution and changes in the levels of TG species in the different mutants in comparison to wild type (+/+). **(D)** Scatterplot indicating the overlap of the changes in the levels of TG species of *fzo-1(tm1133)* and *drp-1(tm1108)* mutants in comparison to wild type (+/+). **(C)** and **(D)** The x-axis labels the number of carbons (C) and the y-axis the number of double bonds (DB) in the acyl sidechains. The size of a dot indicates the number of detected isomers for a specific sum composition. Grey dots represent all detected TGs species and blue and red dots indicate down- (blue) or upregulation (red).

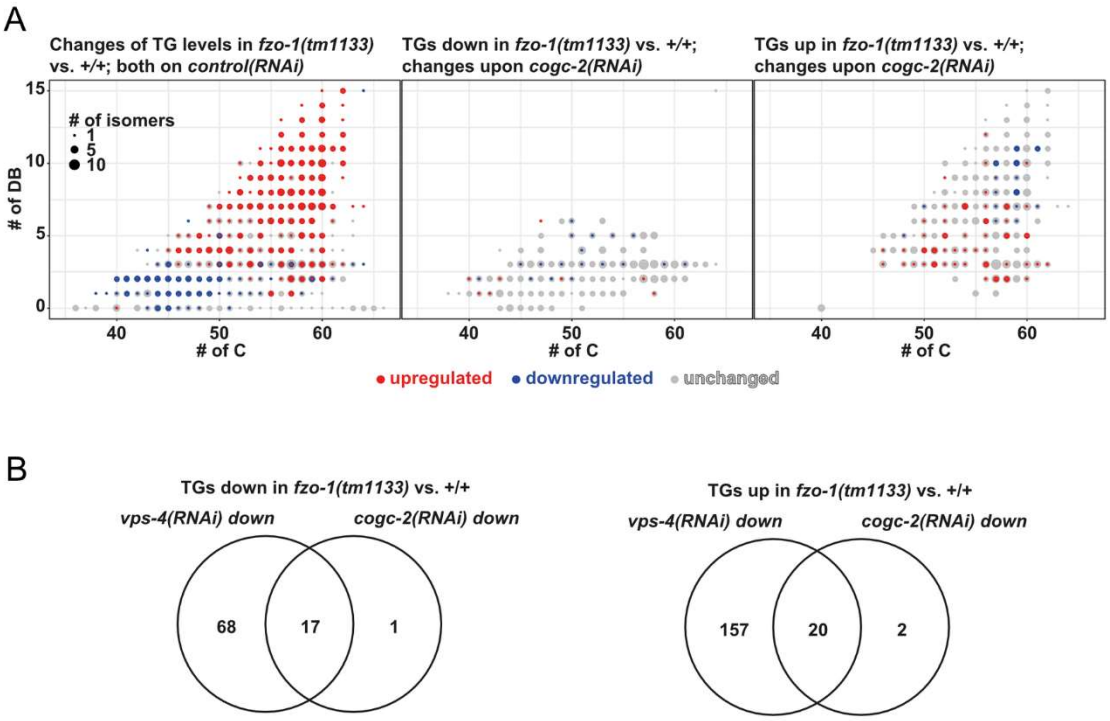

S9 Fig: Induction of autophagy upon *cogc-2(RNAi)* changes the levels of specific TGs in *fzo-1(tm1133)* mutants. (A) Scatterplot indicating the distribution and changes in the level of TG species in *fzo-1(tm1133)* mutants in comparison to wild type (+/+). The x-axis labels the number of carbons (C) and the y-axis the number of double bonds (DB) in the acyl sidechains. The size of a dot indicates the number of detected isomers for a specific sum composition. Grey dots represent all detected TGs species and blue and red dots indicate down- (blue) or upregulation (red). **(B)** Venn diagram indicating the overlap of TG species downregulated (left panel) or upregulated (right panel) in *fzo-1(tm1133)* and either up- or downregulated upon *vps-4(RNAi)* or *cogc-2(RNAi)*.

S1 Table: List of genes that suppress *fzo-1(lf)*-induced UPR^{mt} and induce autophagy in wild-type animals upon knock-down. Candidate genes were identified in the primary RNAi-screen using *fzo-1(tm1133),* subsequently knocked-down and tested for induction of autophagy and re-screened for UPR^{mt} suppression in two different mutant backgrounds: *drp-1(tm1108)* and *spg-7(ad2249)*.

Category	Sequence	Gene name	Human ortholog	*fzo-1(lf)*	*drp-1(lf)*	*spg-7(lf)*
Cell Architecture	K07C5.1	*arx-2*	*ACTR2*			
	D2024.6	*cap-1*	*CAPZA1,2*			
	M106.5	*cap-2*	*CAPZB*			
	C53A5.6	*C53A5.6*	*IPP*			
	C17H12.1	*dyci-1*	*DYNC1I1,2*			
Cell Signaling	W03H9.4	*cacn-1*	*CACTIN*			
	H25P06.2	*cdk-9*	*CDK9*			
	C24H11.7	*gbf-1**	*GBF1*			
	T01G9.6	*kin-10**	*CSNK2B*			
	C27H6.2	*ruvb-1**	*RUVBL1*			
Cellular Trafficking	C06G3.10	*cogc-2**	*COG2*			
	Y51H7C.6	*cogc-4**	*COG4*			
	F23F1.5	*F23F1.5*	*SNUPN*			
	F38A1.8	*F38A1.8*	*SRPRA*			
	F32E10.4	*ima-3*	*KPNA3,4*			
	C53D5.6	*imb-3*	*IPO5, RANBP6*			
	Y59E9AL.7	*nbet-1*	*BET1*			
	Y77E11A.13	*npp-20*	*SEC13*			
	H15N14.2	*nsf-1**	*NSF*			
	R186.3	*R186.3*	*SRPRB*			
	F20G4.1	*smgl-1**	*NBAS*			
	F55C5.8	*srpa-68*	*SRP68*			
	T10H9.3	*syx-18*	*STX18*			
	Y63D3A.5	*tfg-1*	*TFG*			
	Y34D9A.10	*vps-4**	*VPS4A,B*			
	Y65B4A.3	*vps-20**	*CHMP6*			
	CD4.4	*vps-37**	*VPS37B,C*			
	Y48G1A.5	*xpo-2/imb-5*	*CSE1L*			
Chromatin Structure	ZK1251.1	*htas-1*	*H2AFY, H2AFY2*			
	F26F12.7	*let-418*	*CHD4*			
	F55A3.3	*spt-16*	*SUPT16H*			
Metabolism	C33H5.18	*cdgs-1*	*CDS2*			
	C06E4.6	*C06E4.6*	*HSD17B14*			
	F25B4.6	*hmgs-1*	*HMGCS1,2*			
	H37A05.1	*lpin-1*	*LPIN1,2,3*			
	W09B6.1	*pod-2*	*ACACB*			
	C47E12.4	*pyp-1*	*PPA1,2*			
PTM	T17E9.2	*nmt-1*	*NMT1,2*			
	W02A11.4	*uba-2*	*UBA2*			
Proteostasis	T21B10.7	*cct-2*	*CCT2*			
	C04A2.7	*dnj-5*	*DNAJC14*			
	C56C10.8	*icd-1*	*BTF3,L4*			
	F21C3.5	*pfd-6*	*PFDN6*			
	F54C9.2	*stc-1*	*HSPA13*			
	F19B6.2	*ufd-1**	*UFD1L*			

RNA Processing	B0511.6	*B0511.6*	*DDX18*			
	C14A4.4	*crn-3*	*EXOSC10*			
	C55B7.8	*dbr-1*	*DBR1*			
	F42H10.7	*ess-2*	*ESS2*			
	F59C6.4	*exos-3*	*EXOSC3*			
	F10B5.8	*F10B5.8*	*INTS11*			
	C17E4.5	*pabp-2*	*PABPN1*			
	C06E1.10	*rha-2*	*DHX37*			
	C47E12.7	*rrp-1*	*RRP1B, RRP1*			
	Y116A8C.32	*sfa-1*	*SF1*			
	T28D9.10	*snr-3*	*SNRPD1*			
	Y49E10.15	*snr-6*	*SNRPE*			
	K02F2.3	*teg-4*	*SF3B3*			
	W04A4.5	*W04A4.5*	*INTS4*			
Transcription	B0261.1	*B0261.1*	*BDP1*			
	F10E9.4	*F10E9.4*	*TWISTNB*			
	C48E7.2	*let-611*	*POLR3C*			
	Y113G7B.18	*mdt-17*	*MED17*			
	F28F8.5	*mdt-28*	*MED28*			
	F58A4.9	*rpac-19*	*POLR1D*			
	H43I07.2	*rpac-40*	*POLR1C*			
	C42D4.8	*rpc-1*	*POLR3A*			
	F09F7.3	*rpc-2*	*POLR3B*			
	ZK856.10	*rpc-25*	*POLR3H*			
	R119.6	*taf-4*	*TAF4B, TAF4*			
	F30F8.8	*taf-5*	*TAF5*			
	ZK1320.12	*taf-8*	*TAF8*			
	K03B4.3	*taf-10*	*TAF10*			
	Y50D7A.2	*xpd-1*	*ERCC2*			
Miscellaneous	W07B3.2	*gei-4*	*n.a.*			
	Y46G5A.6	*phi-3*	*n.a.*			
	ZK637.8	*unc-32*	*ATP6V0A1,4*			
Uncharacterized	C23G10.8	*C23G10.8*	*n.a.*			
	K02E2.7	*K02E2.7*	*n.a.*			
	K10G6.5	*K10G6.5*	*n.a.*			
	K10H10.4	*K10H10.4*	*n.a.*			
	Y82E9BR.13	*pals-17*	*n.a.*			
	E02H1.1	*E02H1.1*	*DIMT1*			
	T01C3.7	*fib-1*	*FBLL1*			
	K12H4.3	*K12H4.3*	*BRIX1*			
	R13A5.12	*lpd-7*	*PES1*			
	T07A9.9	*nog-1**	*GTPBP4*			
	R151.3	*rpl-6*	*RPL6*			
	F53G12.10	*rpl-7*	*RPL7*			
	Y24D9A.4	*rpl-7A*	*RPL7A*			
	JC8.3	*rpl-12*	*RPL12*			
	C04F12.4	*rpl-14*	*RPL14*			
	Y45F10D.12	*rpl-18*	*RPL18*			
	E04A4.8	*rpl-20*	*RPL18A*			

Ribosome Biogenesis	C14B9.7	*rpl-21*	*RPL21*			
	C27A2.2	*rpl-22*	*RPL22*			
	B0336.10	*rpl-23*	*RPL23*			
	F28C6.7	*rpl-26*	*RPL26*			
	C53H9.1	*rpl-27*	*RPL27*			
	W09C5.6	*rpl-31*	*RPL31*			
	ZK652.4	*rpl-35*	*RPL35*			
	B0393.1	*rps-0*	*RPSA*			
	C23G10.3	*rps-3*	*RPS3*			
	Y71A12B.1	*rps-6*	*RPS6*			
	F40F11.1	*rps-11*	*RPS11*			
	Y41D4B.5	*rps-28*	*RPS28*			
	F10G7.1	*tag-151*	*TSR1*			
Translation	F17C11.9	*eef-1G*	*EEF1G*			
	H06H21.3	*eif-1.A*	*EIF1AX,Y*			
	F11A3.2	*eif-2B δ*	*EIF2B4*			
	D2085.3	*eif-2B ε*	*EIF2B5*			
	Y54E2A.11	*eif-3.B*	*EIF3B*			
	B0511.10	*eif-3.E*	*EIF3E*			
	H19N07.1	*erfa-3*	*GSPT1,2*			
	F28H1.3	*aars-2*	*AARS*			
	T08B2.9	*fars-1*	*FARSA*			
	T10F2.1	*gars-1*	*GARS*			
	T11G6.1	*hars-1**	*HARS, HARS2*			
	R11A8.6	*iars-1**	*IARS*			
	F22D6.3	*nars-1*	*NARS*			
	Y41E3.4	*qars-1*	*QARS*			
	F26F4.10	*rars-1**	*RARS*			
	C47D12.6	*tars-1**	*TARS, TARS2,2L*			
	Y80D3A.1	*wars-1*	*WARS*			
	R08D7.4	*R08D7.4*	*EEF2KMT, FAM86B1,2*			
	Y65B4A.6	*Y65B4A.6*	*EIF4A3*			

* Genes that are already implemented in Fig 4A

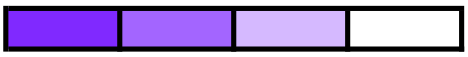

from the strongest to no GFP suppression

Candidate genes were screened for UPR^{mt} suppression three times in technical duplicates with the same reporter *(zcIs13)* in two different mutant backgrounds: *drp-1(tm1108)* and *spg-7(ad2249)* . Fluorescence intensity was scored and classified from very strong suppression to weak suppression (gradual violet coloring) or no suppression (white).

PTM: Post-translational modification.

S3 Table: Design of qRT-PCR primers. Primers sets were designed to quantify *C. elegans* postspliced transcripts. Primer sets were designed to span exon-exon junctions using NCBI Primer Blast software and subsequently blasted against the *C. elegans* genome to test for off-target complementarity. The list of qRT-PCR primers used with their PCR efficiency and coefficient of determination (R2) is shown.

Gene	Sequence Forward Primer	Sequence Reverse Primer	PCR Efficiency (%)	R^2
cdc-42	TCCACAGACCGACGTGTTTC	AGGCACCCATTTTTCTCGGA	100.3	0.99
gfp	TGTTCCATGGCCAACACTTG	CCTGTACATAACCTTCGGGCA	99.1	0.99
hsp-1	CACTGTTTTCGATGCCAAACG	TCCTTCGGCAGAGATGACCT	107.8	0.99
hsp-6	GATTGGATAAGGACGCTGGAGA	CCGTTGGTGGACTTGACCTC	101	0.99
hsp-60	CCAAGGACGTCAAGTTCGGA	TCACGTTTCTTCCTTTTGGGC	106	0.99
ire-1	TACTTGCCACCACGGAGACC	CGTTGCCATCGTCATCATTG	110.3	0.99
nlp-29	AGGATATGGAAGAGGATATGGAGG	CTCCGTACATTCCACGTCCA	114.8	0.99
pmp-3	GTTCCCGTGTTCATCACTCAT	ACACCGTCGAGAAGCTGTAGA	109.3	0.99
ttr-45	CGACGGGCAAGGAATGTTCA	CGGAGTCCTGGCTTCAACTT	114.2	0.99

Chapter IV

MitoSegNet: easy to use deep learning segmentation for analysing mitochondrial morphology

Christian A. Fischer, Laura Besora-Casals, Stéphane G. Rolland, Simon Haeussler, Kritarth Singh, Michael Duchen, Barbara Conradt, Carsten Marr

Published: September 22, 2020. iScience 23(10): https://doi.org/10.1016/j.isci.2020.101601

Article

MitoSegNet: Easy-to-use Deep Learning Segmentation for Analyzing Mitochondrial Morphology

Christian A. Fischer,[1,2,3] Laura Besora-Casals,[1] Stéphane G. Rolland,[1] Simon Haeussler,[1] Kritarth Singh,[4] Michael Duchen,[4] Barbara Conradt,[1,2,4,*] and Carsten Marr[3,5,*]

SUMMARY

While the analysis of mitochondrial morphology has emerged as a key tool in the study of mitochondrial function, efficient quantification of mitochondrial microscopy images presents a challenging task and bottleneck for statistically robust conclusions. Here, we present Mitochondrial Segmentation Network (MitoSegNet), a pretrained deep learning segmentation model that enables researchers to easily exploit the power of deep learning for the quantification of mitochondrial morphology. We tested the performance of MitoSegNet against three feature-based segmentation algorithms and the machine-learning segmentation tool Ilastik. MitoSegNet outperformed all other methods in both pixelwise and morphological segmentation accuracy. We successfully applied MitoSegNet to unseen fluorescence microscopy images of mitoGFP expressing mitochondria in wild-type and *catp-6*^{ATP13A2} mutant *C. elegans* adults. Additionally, MitoSegNet was capable of accurately segmenting mitochondria in HeLa cells treated with fragmentation inducing reagents. We provide MitoSegNet in a toolbox for Windows and Linux operating systems that combines segmentation with morphological analysis.

INTRODUCTION

Cellular organelles are integral to eukaryotic cells and their functions. One organelle that has always been of particular interest is the mitochondrion, which plays an essential role in several metabolic pathways including that of Adenosine triphosphate (ATP). Mitochondria are often represented as static, bean-shaped organelles but actually form highly dynamic 'tubular' networks that often undergo changes in distribution and morphology (Tilokani et al., 2018; Chan, 2020). The steady-state morphology of mitochondria in a cell is a result of a balance between two opposing processes, mitochondrial fusion and fission. Changes in this balance result in changes in mitochondrial morphology. It has been shown that changes in morphology allow mitochondria to respond to metabolic or environmental stresses, while maintaining homeostasis (Tondera et al., 2009; Rolland et al., 2013; Wai and Langer, 2016). While partially damaged mitochondria can be rescued by exchanging their contents with functional mitochondria through mitochondrial fusion, mitochondrial fission enables the removal of damaged mitochondria and can also facilitate apoptosis during increased levels of cellular stress (Pernas and Scorrano, 2016). Mitochondrial fusion and fission are regulated by a conserved family of dynamin-related GTPases and have been well studied in *Caenorhabditis* elegans (van der Bliek et al., 2017). In *C. elegans*, the membrane anchored dynamin-related GTPases FZO-1^{MFN} and EAT-3^{OPA1} are required for the fusion of the outer- and inner mitochondrial membranes, respectively. The loss of function of either of these two proteins results in mitochondria with a 'fragmented' morphology (Breckenridge et al., 2008; Ichishita et al., 2008; Kanazawa et al., 2008; Tan et al., 2008; Rolland et al., 2009).

Mitochondrial fission in *C. elegans* is mediated by DRP-1^{DRP-1}, a cytosolic dynamin-related GTPase. Depletion of DRP-1 has been shown to result in mitochondria with an 'elongated' morphology (Labrousse et al., 1999). Mutations in the human orthologs of the genes encoding these proteins have been associated with several diseases, including neurodegenerative diseases (Chan, 2020). For this reason, understanding mitochondrial fusion and fission is not only an important basic biological question but is critical for our ability to understand the pathology of these diseases and to develop novel therapeutics to treat them. However, such studies have been hindered by the fact that is difficult to assess mitochondrial morphology in different genetic backgrounds or physiological

[1]Fakultät für Biologie, Ludwig-Maximilians-Universität Munich, Planegg-Martinsried, Munich, 82152 Bavaria, Germany

[2]Centre for Integrated Protein Science, Ludwig-Maximilians-University, Planegg-Martinsried, Munich, 82152 Bavaria, Germany

[3]Institute of Computational Biology, Helmholtz Zentrum München – German Research Center for Environmental Health, Ingolstädter Landstr. 1, 85764 Neuherberg, Germany

[4]Department of Cell and Developmental Biology, Division of Biosciences, University College London, London WC1E 6AP, UK

[5]Lead Contact

*Correspondence: b.conradt@ucl.ac.uk (B.C.), carsten.marr@helmholtz-muenchen.de (C.M.)

https://doi.org/10.1016/j.isci.2020.101601

conditions in an unbiased and quantitative manner. Specifically, the diversity of shapes among mitochondria (elongated, fragmented, tubular, as well as 'mixed' morphologies) poses a challenge to the automated quantification of mitochondrial morphology. For this reason, researchers often resorted to the use of a simple qualitative assessment of mitochondrial morphology. As a result, subtle differences in morphology and, hence, phenotypes are often not detected. To analyze mitochondrial morphology, for example, in *C. elegans*, mitochondria are labeled using either a mitochondria-specific fluorescent dye (such as TMRE) or a transgene expressing a mitochondrial-targeted GFP (mitoGFP) (Regmi and Rolland, 2017) and a fluorescent microscopy image is acquired. In order to quantify the mitochondrial morphology in an automated and unbiased manner, the next critical step is to segment the objects in the fluorescent image. The simplest form of image segmentation is thresholding, which is only successful if features are well separated and their intensities vary considerably from the background (Torborg and Feller, 2004). These requirements are seldom met in live cell imaging due to autofluorescence, noise or fluctuating intensities. Thresholding segmentation can be improved through the prior application of feature enhancement algorithms based on intensity derived features, such as the Difference-of-Gaussians (DoG), Determinant of Hessian (Sato et al., 1998) or Laplacian-of-Gaussian (LoG), which are also known as blob detectors. DoG is used to enhance the visibility of edges by removing high frequency information but at the cost of reducing the overall image contrast, while LoG is useful for detecting edges that appear at different image scales or degrees of focus (Marr and Hildreth, 1980; Lindeberg, 1994). Curvilinear structures (such as nerve fibers or blood vessels) can be segmented using the eigenvalues of a Hessian matrix, with which one can calculate the object curvature. There are a many other methods available used in segmentation workflows, such as morphological filtering (dilation, erosion, etc.), region accumulation (watershed transform), deformable model fitting (active contour model) and machine learning (k-means clustering, random forest, etc.) (Meijering, 2012). Most of these methods can now be implemented by biologists through free and opensource tools such as Fiji (Schindelin et al., 2012), CellProfiler (McQuin et al., 2018) or Ilastik (Berg et al., 2019).

All of these segmentation methods have shown varying degrees of success depending on the images they were supposed to segment (de Boer et al., 2015; Li et al., 2015; Akram et al., 2017; Berg et al., 2019). However, with rising image complexity as well as a decreased signal-to-noise ratio, most of the methods perform poorly. For such cases, the only option in the past was manual segmentation, which is highly laborious and introduces a varying degree of bias on each labeled image. With the recent emergence of deep learning and in particular the development of convolutional neural networks (CNNs) (LeCun et al., 1989; Krizhevsky et al., 2012) automated approaches that perform these tasks with human accuracy have become available. CNNs were inspired by the research of Hubel and Wiesel on the primary visual cortex of cats (Wiesel and Hubel, 1963). CNN's can classify data based on convolution and pooling operations. Convolution describes the extraction of features from an image by sliding filters across the image and generating feature maps. Pooling reduces the dimensionality of each feature map, while retaining the most important information. It also reduces the number of network parameters, prevents overfitting, and makes the network invariant to small distortions in the input image (Scherer et al., 2010). Through the successive and repetitive application of convolution and pooling, CNNs are capable of classifying highly complex images with great accuracy (Szegedy et al., 2014). To perform semantic segmentation, which is the assignment of a class label to each pixel, one must use a fully convolutional neural network (FCNN) (Long et al., 2014). A popular FCNN in the biological community is the U-Net that was specifically developed for biomedical image segmentation (Ronneberger et al., 2015). It has been successfully applied to many different biomedical image segmentation tasks and yields good results with only a few hand-segmented images (Chlebus et al., 2018; De Fauw et al., 2018; Stember et al., 2018).

In this study, we trained a U-Net, which we named Mitochondrial Segmentation Network (MitoSegNet), to learn how to segment mitochondria in adult *C. elegans* body wall muscle cells, compared its performance and tested its generalizability in biologically relevant applications that demonstrate *C. elegans* animals carrying a loss-of-function mutation in the gene *catp-6*^{ATP13A2} exhibit a previously unreported mitochondrial morphology phenotype. We also show that MitoSegNet can be successfully used to analyze mitochondrial morphology in HeLa cells.

RESULTS

The MitoSegNet Model

The MitoSegNet model was generated by training a modified U-Net with a training set of 12 1300 × 1030 pixel fluorescent microscopy, maximum-intensity projection images, depicting mitochondria in body wall muscle cells of adult *C. elegans* worms (mitochondria were visualized using a transgene expressing mitochondrial matrix-targeted GFP under the control of a body wall muscle-specific promoter (P_{myo3}::*mitoGFP*))

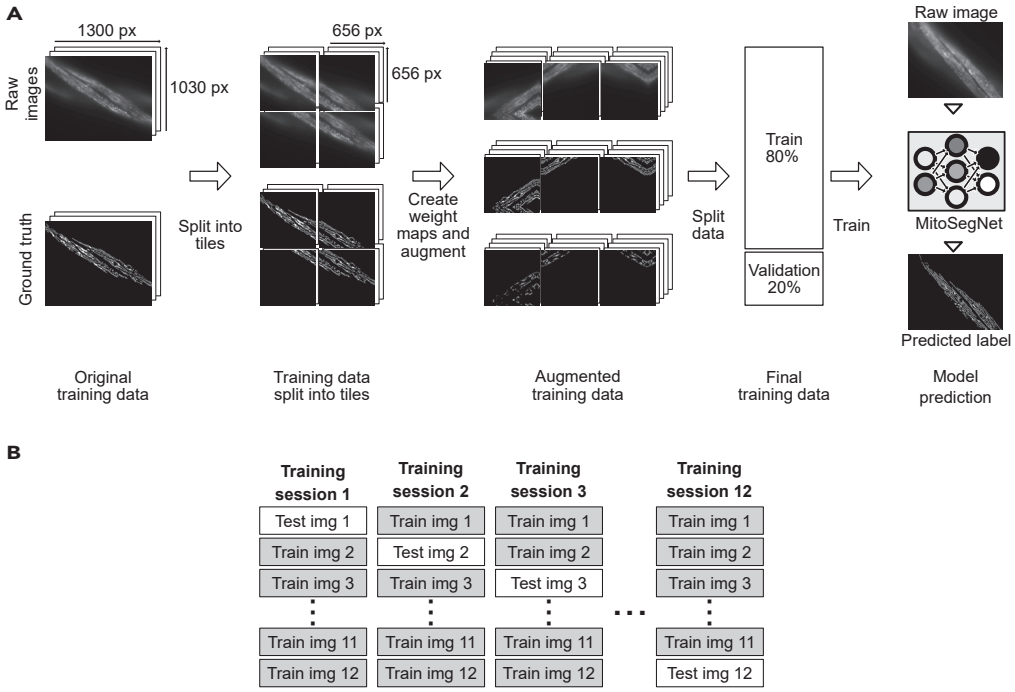

Figure 1. Training the MitoSegNet Model and Using It with the MitoS Tool

(A) The original training data is comprised 12 raw images and the appendant hand-generated ground truth images. Each image is split into 4 overlapping tiles of equal length. For each tile, a weight map is generated and subsequently all three set of tiles (raw images, ground truth, and weight maps) are augmented 80 times, increasing the size of the training data to 3,840 image tiles. Prior to training, the augmented training data is split into training (80%) and validation data (20%). The pretrained MitoSegNet model can now be used to segment new images of mitochondria.

(B) We performed a cross validation for which 12 separate MitoSegNet models were trained each with 11 images, excluding one image that was later used to test the prediction accuracy against other segmentation methods.

(Figure 1A and Methods). Our U-Net modification entails the removal of dropout layers at the end of the contracting pathway and instead placing batch normalization layers after every convolutional layer prior to ReLU activation in the contracting pathway. This modification decreased the amount of necessary training time. Each image was split into 4 overlapping tiles. For each tile, 80 augmented copies were generated for training the model. A cross validation was performed to estimate the performance of the MitoSegNet on an unseen test set and to compare it against other segmentation methods (Figure 1B).

Visual Comparison of Segmentation Performance

To qualitatively evaluate the performance of the MitoSegNet, we compared the predicted segmentations against manually segmented ground truth in an unseen test set. The same procedure was repeated for four other segmentation methods. We considered three classical feature enhancement methods (Gaussian, Hessian, and Laplacian) followed by different thresholding algorithms, all implemented in ImageJ/Fiji. The fourth method is the machine-learning segmentation tool Ilastik (Kreshuk and Zhang, 2019). The Gaussian, Hessian, Laplacian, and Ilastik methods failed to consistently prevent false positive and/or false negative segmentation on all phenotypes (Figure 2). The Gaussian segmentation produced large sections of false positive predictions in the mixed and tubular phenotype (indicated by yellow arrows). The Hessian and Laplacian segmentation largely avoided false positive predictions but instead often failed to recognize mitochondria, resulting in false negative segmentations in the elongated, mixed, and tubular phenotype (and fragmented for the Laplacian segmentation) (Figure 2). The Ilastik-based segmentation produced only very little false negative predictions but like the Gaussian segmentation, predicted large amounts of false positives in all but the fragmented phenotype. The MitoSegNet segmentation drastically reduces the amount of false negative or false positive segmentation when compared to the other methods and yielded consistent results across all different phenotypes (Figure 2).

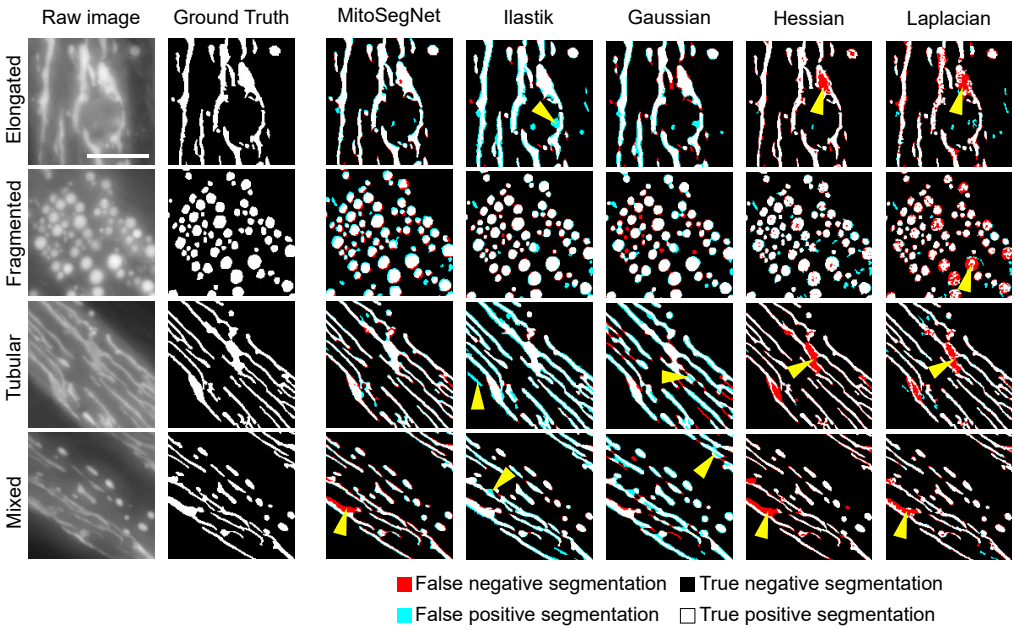

Figure 2. MitoSegNet Visually Outperforms Feature-Based Segmentation Approaches

On the left side, four images of elongated, fragmented, tubular, and mixed *C. elegans* mitochondria and their respective ground truth are shown. The masks on the right show the results of MitoSegNet and the four segmentation methods applied to each image, displaying the false negative segmentation in red, the false positive segmentation in turquoise, the true negative segmentation as black, and the true positive segmentation as white. The yellow arrows indicate areas in which false segmentation occured. The scale bar is 5 μm.

Quantitative Comparison of Segmentation Performance

To compare the methods' performance more quantitatively, we evaluated the pixelwise segmentation accuracy using the dice coefficient (Taha and Hanbury, 2015). The MitoSegNet outperforms the feature-based and Ilastik-generated segmentations (Figure 3A) with a median dice coefficient of 0.89 and a lower and upper 95% confidence interval of 0.87 and 0.91 (N = 12) significantly ($p = 5.11*10^{-5}$, Kruskal-Wallis test). However, pixelwise accuracy as measured by the dice coefficient does not necessarily guarantee correct prediction of morphology (Figure 3B). Because segmented images in biology are often used for morphological quantification (de Boer et al., 2015; Abdolhoseini et al., 2019; Orozco-Fuentes et al., 2019), we assessed the morphological accuracy with two other approaches. The single object shape deviation per object was measured for five shape descriptors (area, eccentricity, aspect ratio, perimeter, and solidity) and averaged over 12 images (Figure 3C). The MitoSegNet with a median average fold deviation of 1.09 and a lower and upper 95% confidence interval of 1.07 and 1.12 (N = 60) outperforms all other methods in the accurate prediction of single object morphology ($p = 7.4*10^{-10}$, Kruskal-Wallis test) (Figure 3D). Because the single object shape deviation method does not consider false negative predictions, we also compared all segmented objects in ground truth and prediction. For each image and each of the five object descriptors, the energy distance between the ground truth and predicted distributions was calculated (Figure 3E). Due to the different value ranges among the descriptors the values were normalized prior statistical analysis. The MitoSegNet segmentation achieves a median normalized energy distance of 0.20 with a lower and upper 95% confidence interval of 0.16 and 0.23 (N = 60) and again statistically outperforms all other non-deep learning segmentation methods ($p = 3.3*10^{-18}$, Kruskal-Wallis test) (Figure 3F).

Comparison of Mitochondrial Morphology between *Catp-6*^{ATP13A2} Mutant and Wild-type

To evaluate the applicability of the MitoSegNet on a different, unseen set of images, we decided to use the MitoSegNet to determine whether a loss-of-function mutation of the gene *catp-6*^{ATP13A2}, *ok3473* (hereafter referred to as *catp-6*(lf)), causes a mitochondrial morphology phenotype. *catp-6*^{ATP13A2} encodes a member of the family of P-type ATPases, which transport various compounds across membranes using ATP hydrolysis as energy source (Moller et al., 1996; Lambie et al., 2013; Anand et al., 2020). In addition, *catp-6*^{ATP13A2}

iScience
Article

CellPress
OPEN ACCESS

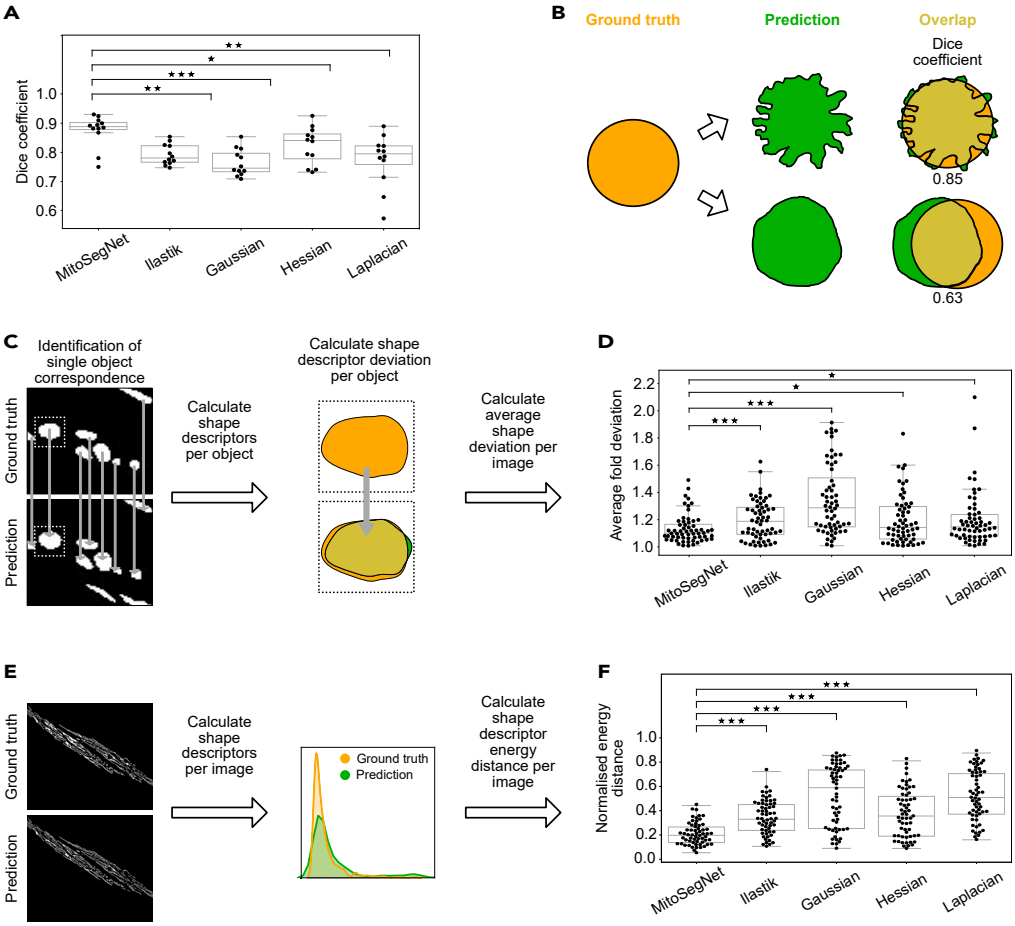

Figure 3. MitoSegNet's Pixelwise Accuracy Outperforms Non-Deep Learning Segmentation Methods

(A) The average dice coefficient achieved with the MitoSegNet is significantly higher than with the four other segmentation approaches. The data was statistically evaluated by using the Kruskal-Wallis test followed by a Dunn's multiple comparisons test.

(B) The dice coefficient is limited as a predictor of morphological segmentation performance: A dice coefficient close to 1.0 does not guarantee correct prediction of morphology. Contrary, a low dice coefficient does not rule out an accurate shape prediction. Ground truth segmentation is shown in orange, and the predicted segmentation in green.

(C) To gain insight into how accurately the shape of ground truth objects is predicted, five object shape descriptors (area, eccentricity, aspect ratio, perimeter, and solidity) are compared by calculating the fold deviation. Predicted objects that correspond to more than one ground truth object (or vice versa) are excluded from this analysis.

(D) The MitoSegNet shows the lowest average fold deviation between predicted and ground truth object shape descriptors. The data were statistically evaluated by first testing for normality using D'Agostino's K-squared test and then subsequently using the Kruskal-Wallis test followed by a Dunn's multiple comparisons test. N = 60.

(E) To determine the total morphological prediction accuracy, the same five shape descriptors were measured for each image. The descriptor distributions in the ground truth and predicted images were statistically evaluated for differences by calculating the energy distances between predicted and ground truth distribution. The energy distances for each shape descriptor and image were normalized prior to statistical analysis.

(F) The MitoSegNet shows the lowest normalized energy distance, statistically outperforming all other segmentation approaches. The data were first tested for normality using the D'Agostino's K-squared. After determining that all distributions were non-parametric, a Kruskal-Wallis test was used followed by a Dunn's multiple comparisons test. N = 60.

*p < 0.05, **0.001 < p < 0.01, ***p < 0.001 for (A), (D) and (F).

is the human ortholog of ATP13A2, mutations of which leads to Kufor-Rakeb syndrome, a form of inherited juvenile-onset Parkinsons disease (Ramirez et al., 2006; Di Fonzo, Chien et al., 2007). No abnormal differences in mitochondrial morphology has so far been reported for the *catp-6*(lf). Consistent with this, upon brief visual inspection, no obvious differences in mitochondrial morphology are noticeable (Figure 4A). We applied the MitoSegNet (Figures 4A) to 19 fluorescence microscopy images of each genotype

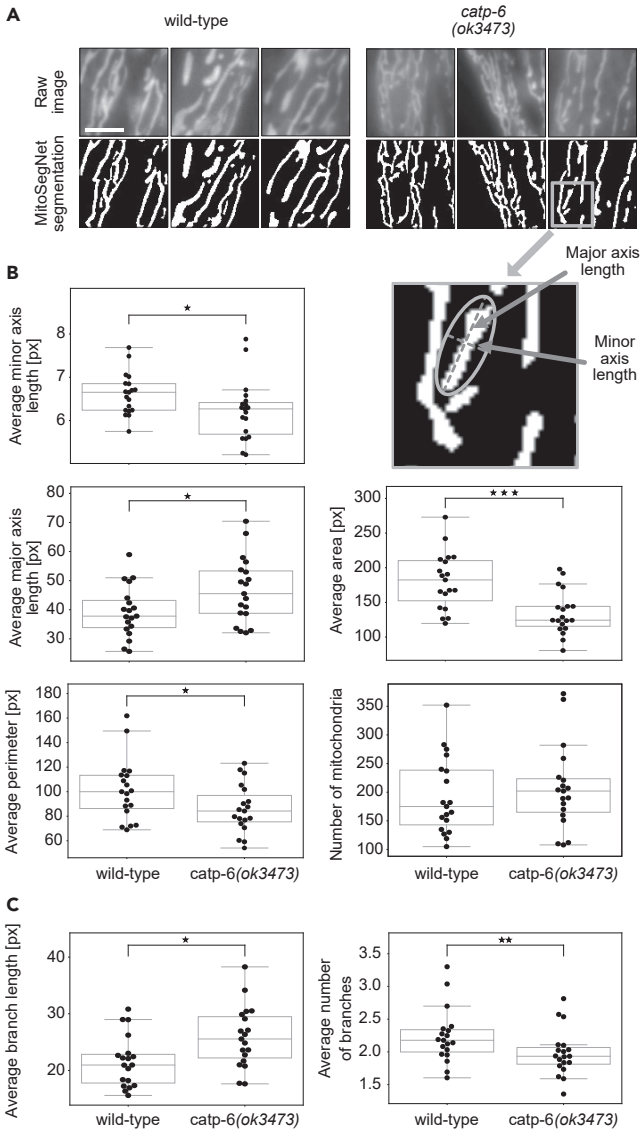

Figure 4. Wild-type and *Catp-6* Mutant Mitochondria Show Significant Morphological Differences

(A) Visual comparison of *catp-6* mutant and wild-type mitochondrial morphology. Raw images are at the top and MitoSegNet model segmentations at the bottom. The scale bar is 3 μm.

(B) Mitochondrial shape descriptor comparison.

(C) Mitochondrial branch descriptor comparison. Average area, minor and major axis length (see scheme for explanation), perimeter, number of mitochondria, average branch length, and number of branches were measured in segmented images of wild-type and *catp-6* mutant mitochondria. *$p < 0.05$, **$0.001 < p < 0.01$, ***$p < 0.001$ using the Mann-Whitney U test. N = 19.

and subsequently analyzed the data with the MitoA tool (Figure 4B). Segmentation masks (Figure 4A) visually matched the raw images closely and subsequent quantification revealed a statistically significant morphological difference between mitochondria in wild-type and *catp-6*(lf) mutants. Compared to wild-type, mitochondria are significantly thinner and longer in *catp-6*(lf) mutants, as determined by the average minor ($p = 0.047$, independent two-sample t test) and major axis length ($p = 0.029$, independent two-sample t test) (Figure 4B). Furthermore, the average mitochondrial area is larger ($p = 0.00039$, independent two-sample t test) and the perimeter is longer ($p = 0.043$, independent two-sample t test) in wild-type compared to *catp-6*(lf) mutants (Figure 5B). Excessive mitochondrial fission (i.e. mitochondrial fragmentation) as a cause for these observations can be excluded since the numbers of mitochondria in wild-type and *catp-6*(lf) mutants are similar ($p = 0.56$, independent two-sample t test) (Figure 4B). Differences were also found

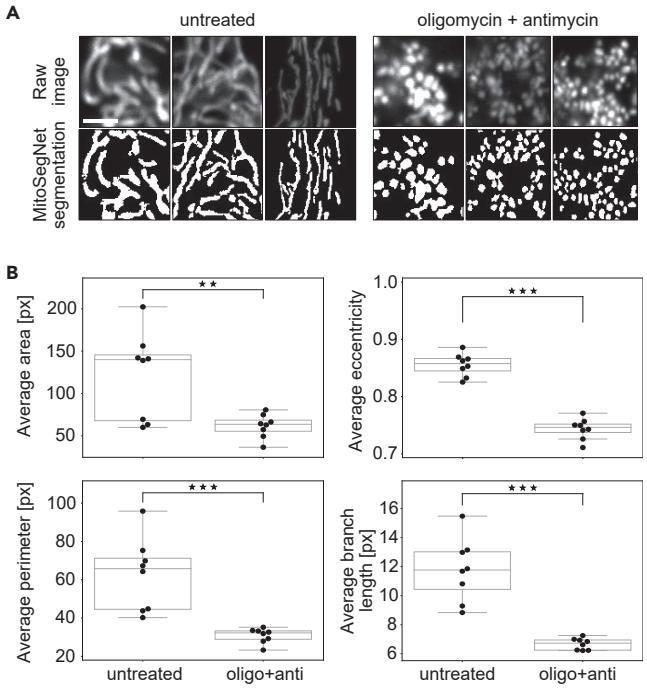

Figure 5. MitoSegNet Model Segmentation and Morphological Quantification Can Be Applied to Mitochondria of Mammalian Cells

Comparing untreated HeLa cells and HeLa cells treated with oligomycin or antimycin for a duration of 3 h.

(A) Visual comparison of untreated and treated mitochondrial morphology. Raw images are at the top and MitoSegNet model segmentations at the bottom. The scale bar is 2.5 μm.

(B) Average area, eccentricity, perimeter, and branch length of mitochondria were measured in segmented images of treated and untreated mitochondria. *$p < 0.05$, ***$p < 0.001$ using an independent two-sample t test. N = 8.

in terms of mitochondrial branch morphology (Figure 4C). While the average mitochondrial branch length in *catp-6*(lf) mutants is larger than in wild-type ($p = 0.01$, independent two-sample t test), the average number of mitochondrial branches was found to be significantly smaller in *catp-6*(lf) mutants ($p = 0.009$, Mann-Whitney U test). Altogether these results indicate that *catp-6(ok3473)* causes a previously unreported mitochondrial morphology phenotype that cannot be detected by simple visual inspection.

MitoSegNet Segmentation of Mitochondria in HeLa Cells

To test the generalizability of our model even further, we applied the MitoSegNet to segment 8 confocal microscopy images depicting mitochondria in HeLa cells (Figure 5A). The fragmentation of mitochondria in HeLa cells treated with oligomycin and antimycin for 3 hr was captured in the segmentation both visually and quantitatively. As expected, the average mitochondrial area is significantly larger in untreated cells compared to treated HeLa cells ($p = 0.0068$, independent two-sample t test) (Figure 5B). The average eccentricity is lower for the fragmented mitochondria compared to the untreated mitochondria, indicating a more circular shape ($p = 1.32*10^{-8}$, independent two-sample t test) (Figure 5B). The average perimeter distribution reflects a similar pattern as found for the area, showing the fragmented mitochondria to have a smaller perimeter on average ($p = 0.00037$, independent two-sample t test) (Figure 5B). The average branch length is also significantly smaller in the treated mitochondria compared to the untreated mitochondria ($p = 1.30*10^{-5}$, independent two-sample t test) (Figure 5B).

The MitoS Segmentation and MitoA Analysis Tool

To enable non-experts, we implemented the MitoSegNet in an easy-to-use tool, the MitoS segmentation tool, a Python-based, standalone executable. MitoS can be executed in a basic mode, which utilizes the pretrained MitoSegNet for segmentation of mitochondria and allows us to easily apply the model without prior deep learning experience (Figure 1). We applied the MitoS image segmentation using the pretrained

MitoSegNet on two different systems. For all cases 10 images of each 1300 × 1030 px size (8-bit) were segmented. The MitoS GPU segmentation was run using an NVIDIA GeForce GTX 960M and NVIDIA TITAN X and segmentation took 65 and 15 s, respectively. Segmentation using the MitoS CPU version was performed on an Intel(R) Core(TM) i7-6700HQ CPU and a system using four Intel(R) Xeon(R) CPU E5-2680 v4 processors and lasted 7.5 min and 65 s, respectively. The basic mode also includes a fine-tuning module, which allows us to optimize the pretrained on new images (Figure S1A). The MitoS advanced mode can be used if other structures besides mitochondria should be segmented or if the user wishes to build a self-configured deep learning segmentation model (Figure S1B). The MitoA analyzer is a separate Python-based, standalone executable tool that can be run after successful segmentation for quantification and visualization of potential morphological differences (Figure S3). It measures ten different morphological and three intensity-based features for each object and summary statistics for all object features per image are generated. The tables of two or multiple samples containing these summary statistics can then be subjected to hypothesis testing, visualization, and correlation analysis. The MitoS and MitoA tools require no installation and no prerequisite installations (such as frameworks), and they are available for both Windows and Linux.

DISCUSSION

We present MitoSegNet, a segmentation model that exploits the power of deep learning to address the challenging problem of accurate mitochondria segmentation. We show that the MitoSegNet outperforms feature-based, non-deep learning-based algorithms and that it is generalizable to unseen images from *C. elegans* and mammalian cells.

MitoSegNet Model Segmentation Performance

While the superior visual and quantitative performance of the MitoSegNet model segmentation might not come as a surprise to researchers acquainted with the capabilities of deep learning-based segmentation, we believe these results to be interesting to researchers who commonly use feature-based segmentation methods. For accuracy evaluation, we did not rely only on pixel-based accuracy, as we found this to be an insufficient measure of morphological accuracy but extended our analysis. Our single object shape comparison as well as the calculation of energy distances for five different feature descriptors per image demonstrate that the MitoSegNet model segmentation yields the best morphological accuracy compared with commonly applied segmentation methods.

Comparison of Mitochondrial Morphology between *Catp-6*^{ATP13A2} Mutants and Wild-type

The visual comparison of mitochondrial morphology in wild type and *catp-6*(lf) mutants did not reveal any obvious differences in morphology. In both cases, mitochondria appeared to be largely tubular. However, the quantitative analysis using the MitoSegNet revealed that average area, perimeter, and minor axis length of mitochondria in *catp-6*(lf) mutants are smaller than in wild-type. Since the average number of mitochondria per cell is the same as in wild-type, we concluded that *catp-6*(lf) causes a reduction in overall mitochondrial mass. This is consistent with observations of Anand et al., who found that oxygen consumption is lower in *C. elegans catp-6*(lf) mutants than in wild type (Anand et al., 2020). In mammalian cells, mutation of *ATP13A2* has been found to cause impairment of mitochondrial function and induce mitochondrial fragmentation (Gusdon et al., 2012; Ramonet et al., 2012). However, this is associated with increased mitochondrial mass due to inefficient autophagic clearance (Grünewald et al., 2012). The differences between the mutant phenotypes observed in *C. elegans* and mammalian cells is likely to reflect the multiple roles of ATP13A2 and CATP-6 transport substrates (polyamines) in maintaining mitochondrial function (van Veen et al., 2020). Further research on properties of *catp-6* deficient mitochondria, such as membrane potential or levels of reactive oxygen species, might uncover the cause for the observed differences in mitochondrial morphology.

Application of the MitoSegNet to Mitochondria in HeLa Cells

Although the pretrained model was generated with standard fluorescence microscopy images, depicting mitoGFP-labeled mitochondria in *C. elegans*, the same pretrained model was able to generate visually accurate segmentations of mitoRFP labeled mitochondria in HeLa cells using a laser scanning confocal microscope. This demonstrates the high robustness and generalization capabilities of our pretrained MitoSegNet model and that it can be used for segmentation of mitochondria in organisms other than *C. elegans*. Furthermore, our MitoSegNet Analysis tool quantitatively confirmed the morphological differences of mitochondria between untreated HeLa cells and HeLa cells treated with oligomycin or antimycin.

MitoSegNet Model Architecture

Although the MitoSegNet architecture is largely based on the U-Net, through testing various changes in the original architecture, we found that the validation dice coefficient as well as the validation loss improved upon removing the dropout layers and instead placing a batch normalization layer (Ioffe and Szegedy, 2015) after every convolution layer in the contracting pathway. Interestingly, a recent study found that the combined usage of batch normalization followed by dropout (forming an independent component layer) stabilized the training process, increased convergence speed, and improved the convergence limit (Chen et al., 2019). It would require further testing to find out if the usage of an independent component layer would improve the current MitoSegNet performance even further.

MitoS and MitoA Tools

Most deep learning applications in the field of biological image segmentation were created for the purpose of 2D cell segmentation (Chen et al., 2017; Al-Kofahi et al., 2018; Falk et al., 2019; Kusumoto and Yuasa, 2019), while organelle-specific deep learning applications are scarce. Although most tools allow the user to retrain available 2D cell segmentation models to segment other biological structures of interest, this often requires computer science-related skills, such as familiarity with programming languages, shell interaction or knowledge on how to install various deep learning frameworks. One of the main motivations behind MitoSegNet and the MitoS and MitoA toolbox was to make deep learning segmentation accessible to researchers that do not have an extensive background in computer science or deep learning. The MitoS tool can be run without installation. The simple graphical user interface allows users to quickly navigate the MitoS and MitoA tools. The MitoS basic mode also comes with a fine-tuning module that allows researchers that would like to segment other organelles or images taken under different conditions than those used for training the MitoSegNet model. Since the subsequent step after segmentation is usually the analysis, we included the MitoA tool to save researchers the time to look up appropriate analysis tools and instead be able to quickly obtain potentially interesting insights.

Conclusion

The MitoSegNet has been shown to outperform both conventional feature-based and machine-learning-based segmentation of mitochondria. The pretrained model can be easily applied to new 2D microscopy images of mitochondria through the usage of the MitoS tool, which is available for both standard and high-end Windows and Linux systems. Successfully segmented images of mitochondria can be subjected to quantification, statistical testing, and visualization with the MitoA tool.

Limitations of the Study

The MitoSegNet model used for segmentation of images depicting fluorescently labeled mitochondria in *C. elegans* and HeLa cells was trained with 12 pairs of raw images and the appendant hand-labeled ground truth images. Although both the visual and quantitative segmentation accuracy was shown to be high in this study, there remains a bias which is based on the two annotators who generated 6 ground truth images each. To reduce the ground truth bias and increase the generalizability of the MitoSegNet model, more images labeled by different annotators can be added. Furthermore, image sections in which single mitochondria were not clearly distinguishable due to optical constraints of the microscope used to generate the image, made it difficult for the annotator to create labeled images that accurately represent the ground truth. This uncertainty introduced to the MitoSegNet model can be decreased by adding images recorded with higher resolution, thus reducing the sections in which such visually indistinguishable mitochondria exist.

Resource Availability

Lead Contact

Further information and requests for resources should be directed to and will be fulfilled by the Lead Contact, Carsten Marr (carsten.marr@helmholtz-muenchen.de).

Materials Availability

Images used for training and testing the model are available upon request.

Data and Code Availability

The software documentation for the MitoS and MitoA tool can be found at https://github.com/mitosegnet. The MitoSegNet segmentation model, the MitoA analysis and MitoS segmentation tool (GPU/CPU) for

Linux and Windows are available at https://zenodo.org/search?page=1&size=20&q=mitosegnet. The Python code used for generating the figures displayed in the manuscript is available at https://github.com/MitoSegNet/MitoSegNet_AccuracyTesting_Manuscript.

METHODS

All methods can be found in the accompanying Transparent Methods supplemental file.

SUPPLEMENTAL INFORMATION

Supplemental Information can be found online at https://doi.org/10.1016/j.isci.2020.101601.

ACKNOWLEDGMENTS

We thank E. Lambie, H. Hartz and members of the Conradt and Marr lab for comments on the project development, the manuscript, and testing the MitoS and MitoA tools. We also thank Iva Dzhilyanova for testing the MitoS tool on multiple systems. This work was supported by the Deutsche Forschungsgemeinschaft (Center for Integrated Protein Science Munich [CIPSM; EXC 114], CO204/6-1 and CO204/9-1). C.M. has received funding from the European Research Council (ERC) under the European Union's Horizon 2020 research and innovation program (Grant agreement No. 866411). Some strains were provided by the CGC, which is funded by NIH Office of Research Infrastructure Programs (P40 OD010440).

AUTHOR CONTRIBUTIONS

C.A.F. designed and conducted the computational experiments, performed the data analysis, and wrote the paper. B.C. designed the biological experiments and wrote the paper. C.M. designed the computational experiments and wrote the paper. S.G.R., S.H., L.B.C., M.D. and K.S. designed and conducted the biological experiments.

DECLARATION OF INTERESTS

None.

Received: February 7, 2020
Revised: August 18, 2020
Accepted: September 17, 2020
Published: October 23, 2020

REFERENCES

Abdolhoseini, M., Kluge, M.G., Walker, F.R., and Johnson, S.J. (2019). Segmentation, tracing, and quantification of microglial cells from 3D image stacks. Sci. Rep. *9*, 8557.

Akram, F., Garcia, M.A., and Puig, D. (2017). Active contours driven by difference of Gaussians. Sci. Rep. *7*, 14984.

Al-Kofahi, Y., Zaltsman, A., Graves, R., Marshall, W., and Rusu, M. (2018). A deep learning-based algorithm for 2-D cell segmentation in microscopy images. BMC Bioinformatics *19*, 365.

Anand, N., Holcom, A., Broussalian, M., Schmidt, M., Chinta, S.J., Lithgow, G.J., Andersen, J.K., and Chamoli, M. (2020). Dysregulated iron metabolism in C. elegans catp-6/ATP13A2 mutant impairs mitochondrial function. Neurobiol. Dis. *139*, 104786.

Berg, S., Kutra, D., Kroeger, T., Straehle, C.N., Kausler, B.X., Haubold, C., Schiegg, M., Ales, J., Beier, T., Rudy, M., et al. (2019). Ilastik: interactive machine learning for (bio)image analysis. Nat. Methods *16*, 1226–1232.

van der Bliek, A.M., Sedensky, M.M., and Morgan, P.G. (2017). Cell biology of the mitochondrion. Genetics *207*, 843–871.

de Boer, R., Smith, R.L., De Vos, W.H., Manders, E.M., Brul, S., and van der Spek, H. (2015). Caenorhabditis elegans as a model system for studying drug induced mitochondrial toxicity. PLoS One *10*, e0126220.

Breckenridge, D.G., Kang, B.-H., Kokel, D., Mitani, S., Staehelin, L.A., and Xue, D. (2008). Caenorhabditis elegans drp-1 and fis-2 regulate distinct cell-death execution pathways downstream of ced-3 and independent of ced-9. Mol. Cell *31*, 586–597.

Chan, D.C. (2020). Mitochondrial dynamics and its involvement in disease. Annu. Rev. Pathol. Mech. Dis. *15*, 235–259.

Chen, M., Dai, W., Sun, S.Y., Jonasch, D., He, C.Y., Schmid, M.F., Chiu, W., and Ludtke, S.J. (2017). Convolutional neural networks for automated annotation of cellular cryo-electron tomograms. Nat. Methods *14*, 983–985.

Chen, G., Chen, P., Shi, Y., Hsieh, C.Y., Liao, B., and Zhang, B. (2019). Rethinking the usage of batch normalization and dropout in the training of deep neural networks. arXiv, arxiv:1905.05928.

Chlebus, G., Schenk, A., Moltz, J.H., van Ginneken, B., Hahn, H.K., and Meine, H. (2018). Automatic liver tumor segmentation in CT with fully convolutional neural networks and object-based postprocessing. Sci. Rep. *8*, 15497.

Falk, T., Mai, D., Bensch, R., Cicek, O., Abdulkadir, A., Marrakchi, Y., Bohm, A., Deubner, J., Jackel, Z., Seiwald, K., et al. (2019). U-Net: deep learning for cell counting, detection, and morphometry. Nat. Methods *16*, 67–70.

De Fauw, J., Ledsam, J.R., Romera-Paredes, B., Nikolov, S., Tomasev, N., Blackwell, S., Askham, H., Glorot, X., O'Donoghue, B., Visentin, D., et al. (2018). Clinically applicable deep learning for diagnosis and referral in retinal disease. Nat. Med. *24*, 1342–1350.

Di Fonzo, A., Chien, H.F., Socal, M., Giraudo, S., Tassorelli, C., Iliceto, G., Fabbrini, G., Marconi, R., Fincati, E., Abbruzzese, G., et al. (2007). ATP13A2 missense mutations in juvenile parkinsonism and

young onset Parkinson disease. Neurology *68*, 1557–1562.

Grünewald, A., Arns, B., Seibler, P., Rakovic, A., Münchau, A., Ramirez, A., Sue, C.M., and Klein, C. (2012). ATP13A2 mutations impair mitochondrial function in fibroblasts from patients with Kufor-Rakeb syndrome. Neurobiol. Aging *33*, 1843.e1–1843.e7.

Gusdon, A.M., Zhu, J., Van Houten, B., and Chu, C.T. (2012). ATP13A2 regulates mitochondrial bioenergetics through macroautophagy. Neurobiol. Dis. *45*, 962–972.

Ichishita, R., Tanaka, K., Sugiura, Y., Sayano, T., Mihara, K., and Oka, T. (2008). An RNAi screen for mitochondrial proteins required to maintain the morphology of the organelle in Caenorhabditis elegans. J. Biochem. *143*, 449–454.

Ioffe, S., and Szegedy, C. (2015). Batch normalization: accelerating deep network training by reducing internal covariate shift. In Proceedings of the 32nd International Conference on International Conference on Machine Learning - Volume 37Proceedings of the 32nd International Conference on International Conference on Machine Learning - Volume 37, pp. 448–456.

Kanazawa, T., Zappaterra, M.D., Hasegawa, A., Wright, A.P., Newman-Smith, E.D., Buttle, K.F., McDonald, K., Mannella, C.A., and van der Bliek, A.M. (2008). The C. elegans Opa1 homologue EAT-3 is essential for resistance to free radicals. PLoS Genet. *4*, e1000022.

Kreshuk, A., and Zhang, C. (2019). Machine learning: advanced image segmentation using ilastik. Methods Mol. Biol. *2040*, 449–463.

Krizhevsky, A., Sutskever, I., and Hinton, G.E. (2012). ImageNet classification with deep convolutional neural networks. In Proceedings of the 25th International Conference on Neural Information Processing Systems - Volume 1Proceedings of the 25th International Conference on Neural Information Processing Systems - Volume 1 (Curran Associates Inc.), pp. 1097–1105.

Kusumoto, D., and Yuasa, S. (2019). The application of convolutional neural network to stem cell biology. Inflamm. Regen. *39*, 14.

Labrousse, A.M., Zappaterra, M.D., Rube, D.A., and van der Bliek, A.M. (1999). C. elegans dynamin-related protein DRP-1 controls severing of the mitochondrial outer membrane. Mol. Cell *4*, 815–826.

Lambie, E.J., Tieu, P.J., Lebedeva, N., Church, D.L., and Conradt, B. (2013). CATP-6, a C. elegans ortholog of ATP13A2 PARK9, positively regulates GEM-1, an SLC16A transporter. PLoS One *8*, e77202.

LeCun, Y., Boser, B., Denker, J.S., Henderson, D., Howard, R.E., Hubbard, W., and Jackel, L.D. (1989). Backpropagation applied to handwritten zip code recognition. Neural Comput. *1*, 541–551.

Li, Y., Gong, H., Wu, W., Liu, G., and Chen, G. (2015). An automated method using hessian matrix and random walks for retinal blood vessel segmentation. 2015 8th International Congress on Image and Signal Processing (CISP).

Lindeberg, T. (1994). Scale-space theory: a basic tool for analysing structures at different scales. J. Appl. Stat. *21*, 225–270.

Long, J., Shelhamer, E., and Darrell, T. (2014). Fully convolutional networks for semantic segmentation. arXiv, arxiv:1411.4038.

Marr, D., and Hildreth, E. (1980). Theory of edge detection. Proc. R. Soc. Lond. B Biol. Sci. *207*, 187–217.

McQuin, C., Goodman, A., Chernyshev, V., Kamentsky, L., Cimini, B.A., Karhohs, K.W., Doan, M., Ding, L., Rafelski, S.M., Thirstrup, D., et al. (2018). CellProfiler 3.0: next-generation image processing for biology. PLoS Biol. *16*, e2005970.

Meijering, E. (2012). Cell segmentation: 50 Years down the road [life sciences]. IEEE Signal Process. Mag. *29*, 140–145.

Moller, J.V., Juul, B., and le Maire, M. (1996). Structural organization, ion transport, and energy transduction of P-type ATPases. Biochim. Biophys. Acta *1286*, 1–51.

Orozco-Fuentes, S., Neganova, I., Wadkin, L.E., Baggaley, A.W., Barrio, R.A., Lako, M., Shukurov, A., and Parker, N.G. (2019). Quantification of the morphological characteristics of hESC colonies. Sci. Rep. *9*, 17569.

Pernas, L., and Scorrano, L. (2016). Mito-morphosis: mitochondrial fusion, fission, and cristae remodeling as key mediators of cellular function. Annu. Rev. Physiol. *78*, 505–531.

Ramirez, A., Heimbach, A., Grundemann, J., Stiller, B., Hampshire, D., Cid, L.P., Goebel, I., Mubaidin, A.F., Wriekat, A.L., Roeper, J., et al. (2006). Hereditary parkinsonism with dementia is caused by mutations in ATP13A2, encoding a lysosomal type 5 P-type ATPase. Nat. Genet. *38*, 1184–1191.

Ramonet, D., Podhajska, A., Stafa, K., Sonnay, S., Trancikova, A., Tsika, E., Pletnikova, O., Troncoso, J.C., Glauser, L., and Moore, D.J. (2012). PARK9-associated ATP13A2 localizes to intracellular acidic vesicles and regulates cation homeostasis and neuronal integrity. Hum. Mol. Genet. *21*, 1725–1743.

Regmi, S.G., and Rolland, S.G. (2017). New imaging tools to analyze mitochondrial morphology in Caenorhabditis elegans. Methods Mol. Biol. *1567*, 255–272.

Rolland, S.G., Lu, Y., David, C.N., and Conradt, B. (2009). The BCL-2-like protein CED-9 of C. elegans promotes FZO-1/Mfn1,2- and EAT-3/Opa1-dependent mitochondrial fusion. J. Cell Biol. *186*, 525–540.

Rolland, S.G., Motori, E., Memar, N., Hench, J., Frank, S., Winklhofer, K.F., and Conradt, B. (2013). Impaired complex IV activity in response to loss of LRPPRC function can be compensated by mitochondrial hyperfusion. Proc. Natl. Acad. Sci. U S A *110*, E2967–E2976.

Ronneberger, O., Fischer, P., and Brox, T. (2015). U-net: Convolutional Networks for Biomedical Image Segmentation, Cham (Springer International Publishing).

Sato, Y., Nakajima, S., Shiraga, N., Atsumi, H., Yoshida, S., Koller, T., Gerig, G., and Kikinis, R. (1998). Three-dimensional multi-scale line filter for segmentation and visualization of curvilinear structures in medical images. Med. Image Anal. *2*, 143–168.

Scherer, D., Müller, A., and Behnke, S. (2010). Evaluation of Pooling Operations in Convolutional Architectures for Object Recognition (Springer Berlin Heidelberg).

Schindelin, J., Arganda-Carreras, I., Frise, E., Kaynig, V., Longair, M., Pietzsch, T., Preibisch, S., Rueden, C., Saalfeld, S., Schmid, B., et al. (2012). Fiji: an open-source platform for biological-image analysis. Nat. Methods *9*, 676–682.

Stember, J.N., Chang, P., Stember, D.M., Liu, M., Grinband, J., Filippi, C.G., Meyers, P., and Jambawalikar, S. (2018). Convolutional neural networks for the detection and measurement of cerebral aneurysms on magnetic resonance angiography. J. Digit. Imaging *32*, 808–815.

Szegedy, C., Liu, W., Jia, Y., Sermanet, P., Reed, S.E., Anguelov, D., Erhan, D., Vanhoucke, V., and Rabinovich, A. (2014). Going deeper with convolutions. arXiv, arxiv:1409.4842.

Taha, A.A., and Hanbury, A. (2015). Metrics for evaluating 3D medical image segmentation: analysis, selection, and tool. BMC Med. Imaging *15*, 29.

Tan, F.J., Husain, M., Manlandro, C.M., Koppenol, M., Fire, A.Z., and Hill, R.B. (2008). CED-9 and mitochondrial homeostasis in C. elegans muscle. J. Cell Sci. *121*, 3373–3382.

Tilokani, L., Nagashima, S., Paupe, V., and Prudent, J. (2018). Mitochondrial dynamics: overview of molecular mechanisms. Essays Biochem. *62*, 341–360.

Tondera, D., Grandemange, S., Jourdain, A., Karbowski, M., Mattenberger, Y., Herzig, S., Da Cruz, S., Clerc, P., Raschke, I., Merkwirth, C., et al. (2009). SLP-2 is required for stress-induced mitochondrial hyperfusion. EMBO J. *28*, 1589–1600.

Torborg, C.L., and Feller, M.B. (2004). Unbiased analysis of bulk axonal segregation patterns. J. Neurosci. Methods *135*, 17–26.

van Veen, S., Martin, S., Van den Haute, C., Benoy, V., Lyons, J., Vanhoutte, R., Kahler, J.P., Decuypere, J.-P., Gelders, G., Lambie, E., et al. (2020). ATP13A2 deficiency disrupts lysosomal polyamine export. Nature *578*, 419–424.

Wai, T., and Langer, T. (2016). Mitochondrial dynamics and metabolic regulation. Trends Endocrinol. Metab. *27*, 105–117.

Wiesel, T.N., and Hubel, D.H. (1963). Single-cell responses in striate cortex of kittens deprived of vision in one eye. J. Neurophysiol. *26*, 1003–1017.

Figure S1

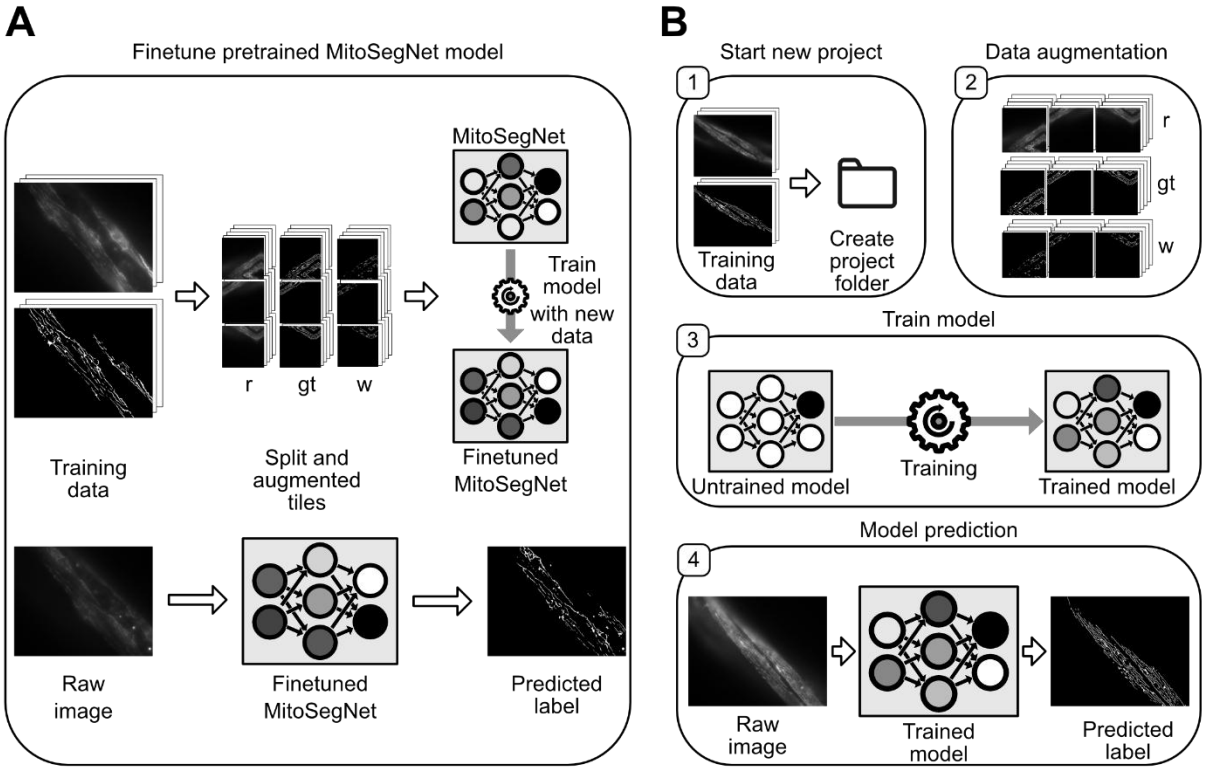

Figure S1: MitoS segmentation tool finetuning module and advanced mode workflow, Related to Figure 1 **(A)** The finetuning module enables the user to add new training data to finetune the existing MitoSegNet. This function automatically splits the new training data into tiles, performs augmentation (r: raw images, gt: ground truth images, w: weight map images) and the augmented data is then used to train the pretrained MitoSegNet. After completion of training, the finetuned MitoSegNet can be used for segmentation of new images using the prediction function. **(B)** The advanced mode allows the user to create a new deep learning segmentation model by adjusting network parameters. [1] Generation of a new project folder, in which all subsequent advanced functions will be carried out. [2] Data augmentation parameters can be specified and users can decide whether weight maps should be generated. [3] Model training allows the user to set the learning rate, batch size, class balance weight factor and if weight maps should be used. [4] Once the model has been trained the prediction function of the MitoS tool can be used to predict the segmentation on previously unseen images.

Figure S2

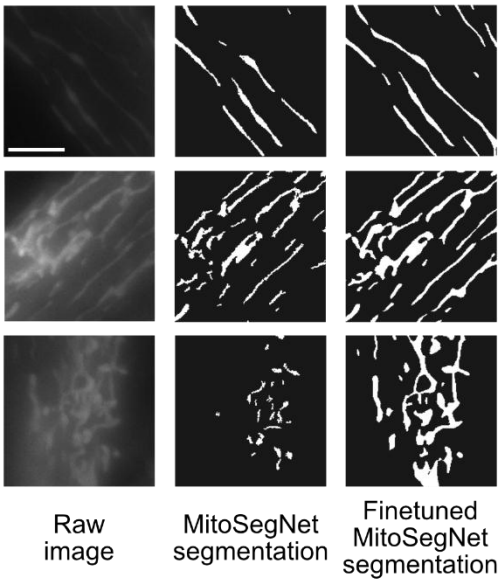

Figure S2: Finetuning MitoSegNet improves visual segmentation results, Related to Figure 2. Due to the usage of a non-integrated P_{myo-3}::mitoGFP reporter, the intensity of fluorescently labelled mitochondria appeared weaker and hence the MitoSegNet model failed to accurately segment these images. The input images are shown on the left, in the middle are the binary masks before finetuning and to the right the same masks after finetuning. By segmenting one image by hand and finetuning the pretrained segmentation model for 10 epochs, the visual segmentation results could be largely improved. The scale bar is 5µm.

Figure S3

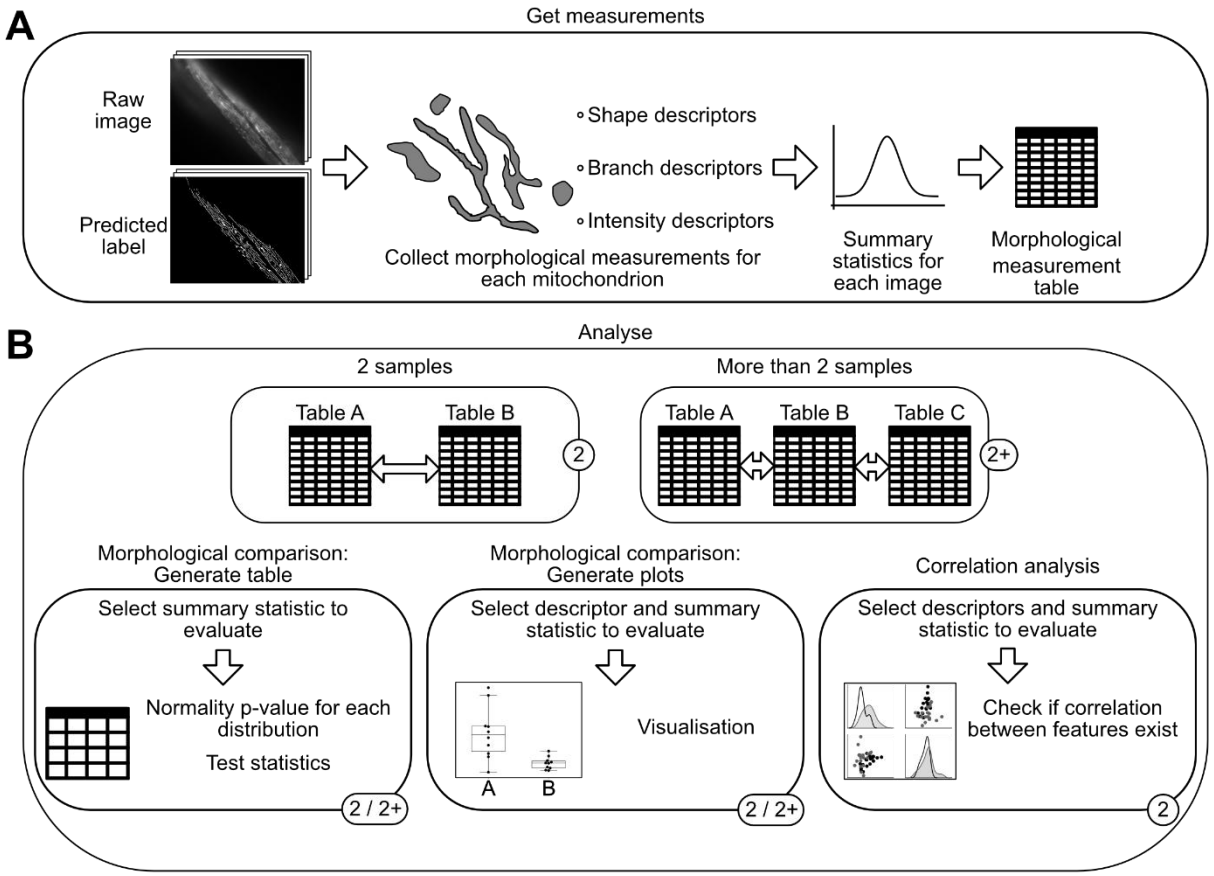

Figure S3: MitoA analyser tool workflow, Related to Figure 4 and 5. The two main functions of the MitoA tool are to get measurements or to analyse. To analyse images of interest, one has to first get the relevant measurements. **(A)** The "Get measurements" function uses images and their predicted labels to measure 6 different shape descriptors, 4 branch descriptors and the mean, maximum and minimum fluorescence intensity for each segmented object. The summary statistics are then saved to a measurements table. **(B)** Analysis can either be performed on only two samples (2) or more than two samples (2+). Subsequent statistical analysis and visualisation can be used in both cases but the correlation analysis is currently only implemented for the two sample comparison. The generate table function allows the user to select a summary statistic to evaluate (such as average, median or standard deviation) after which a table is generated in which sample distribution normality is tested and an appropriate statistical test is selected. The generate plots function lets the user select a feature descriptor and summary statistic to display as a boxplot. With the correlation analysis, up to 4 different feature descriptors from two samples can be visualised as scatterplots, including the display of the correlation coefficients.

Figure S4

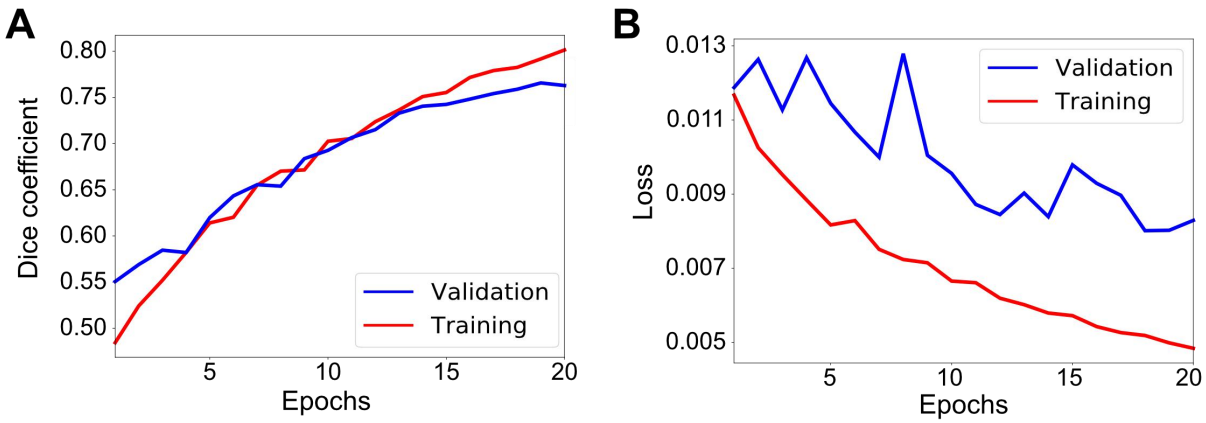

Figure S4: Training performance of final MitoSegNet trained on 12 images, related to Figure 1. (A) Training (red) and validation (blue) dice coefficient increase much like during cross validation and after epoch 15 discrepancy between training and validation dice coefficient begins to increase. **(B)** Training and validation loss decrease and reaches its minimum of 0.008 at 18 epochs.

Figure S5

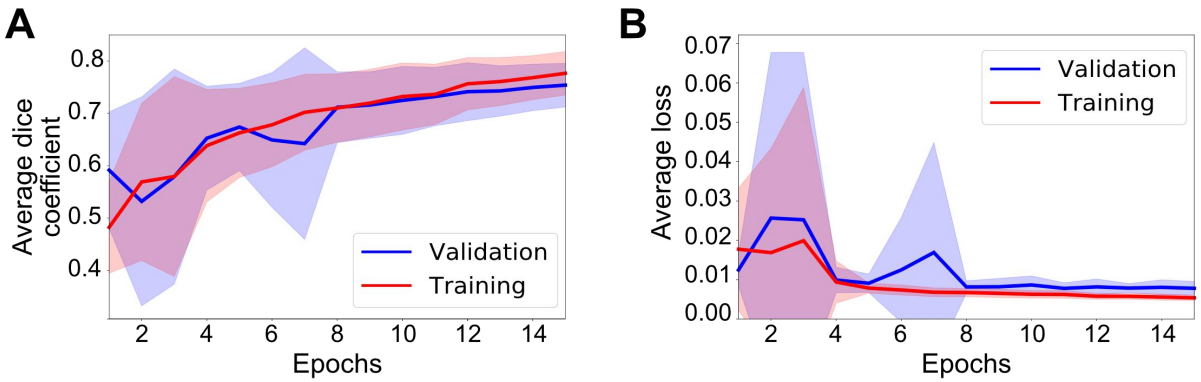

Figure S5: Average training performance of 12 different MitoSegNet models trained on 11 images for cross validation, Related to Figure 1. (A) Average validation (blue) and training (red) dice coefficient steadily increases over 15 epochs of training. **(B)** Average training loss decreases as expected, while validation loss enters a plateau after 8 epochs. Blue and red areas indicate the standard deviation added (upper border) or subtracted (lower border) from the average of the validation and training metric respectively.

4. Discussion

4.1 Genome-wide RNAi-screen for suppressors and enhancers of *fzo-1(tm1133)*-induced UPR^{mt}

In a genome-wide RNAi screen, we identified a complex network of 385 candidate genes that either suppress or enhance *fzo-1(tm1133)*-induced UPR^{mt}. Interestingly, we find that 90% of these genes are conserved in humans (Consortium, 2018; Hunt *et al.*, 2018; Kriventseva *et al.*, 2018; Harris *et al.*, 2019; The Alliance of Genome Resources, 2019), one third of which are implicated in human disease (Amberger *et al.*, 2018). Our dataset includes many genes, which have not previously been found or implicated in the modulation of UPR^{mt} upon depletion. Previous screens were carried out using different genetic backgrounds (an uncharacterized mutation (*zc32*)) or drug treatments (antimycin, paraquat) in order to induce the UPR^{mt} response (Haynes *et al.*, 2007; Runkel *et al.*, 2013; Bennett *et al.*, 2014; Liu *et al.*, 2014), which could potentially have led to the observed differences in the datasets. Moreover, variability of RNAi efficiency plays an important role in the reproducibility of phenotypes, especially in RNAi-screens. Simmer and colleagues estimated false negatives to vary between 10%-30% in RNAi experiments, even when performed by the same people in the same laboratory (Simmer *et al.*, 2003). Taken together, we identified a highly conserved set of genes that, upon depletion, influences mitochondrial homeostasis in mutants with defects in mitochondrial fusion.

4.2 Genes with functions in development, receptor-mediated endocytosis and metabolism modulate UPR^{mt} signaling

Using gene ontology (GO) enrichment analysis, we identified various processes in our dataset that modulate UPR^{mt} signaling (Figure 10). We found several GO-terms related to nematode development to be enriched both among the suppressors and enhancers of *fzo-1(tm1133)*-induced UPR^{mt}. Interestingly, reducing mitochondrial respiration by depletion of ETC components in the nervous system at a specific time point during *C. elegans* development, has previously been shown to result in a systemic UPR^{mt} response throughout adult life and to lead to increased lifespan (Dillin *et al.*, 2002; Rea *et al.*, 2007; Durieux *et al.*, 2011). Thus, many cellular processes and pathways, such as mitochondrial metabolism and -chaperone expression, are adjusted at a certain level during development, which are then maintained throughout life. This may then in turn affect processes, such as ageing. Consistent with this notion, we

additionally identified the GO-term ‘determination of lifespan’ to be enriched among the suppressors and speculate that there are several other genes among our candidates that have previously not been associated with a role in lifespan extension.

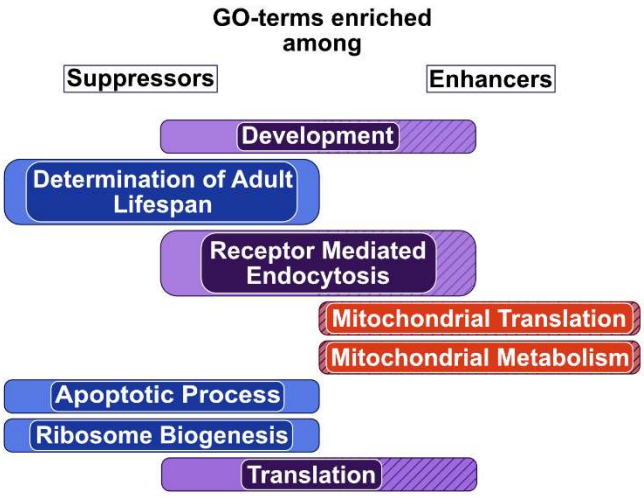

Figure 10: Overview of all enriched gene ontology (GO) terms among suppressors and enhancers of *fzo-1(tm1133)*-induced UPR^{mt}.

Among the enhancers, GO-terms related to mitochondrial translation and -metabolism are highly enriched. This is in line with previous reports where disruption of these processes has been found to induce UPR^{mt}, also under non-stressed conditions (Durieux *et al.*, 2011; Houtkooper *et al.*, 2013). Thus, reducing mitochondrial function robustly induces UPR^{mt}. In addition, ‘receptor-mediated endocytosis’ is enriched in the GO analysis among the enhancers. Analysis of this subset of candidates revealed that many mitochondrial ribosomal subunits and genes involved in mitochondrial translation are misannotated with this term, leading to its enrichment in our statistical analysis.

Among the suppressors, the GO-term ‘apoptotic process’ and ‘receptor mediated endocytosis’ are enriched. While misannotation of ribosomal subunits most likely led to the enrichment of the GO-term ‘apoptotic process’, the GO-term ‘receptor mediated endocytosis’ contains 101 candidate genes, many of which have roles in vesicular trafficking and vesicle budding. Previously, we showed that around half of these (53), negatively regulate autophagy (chapter III (Haeussler *et al.*, 2020)). Moreover, we detected specific changes in the levels of certain triacylglycerols (TGs) upon induction of autophagy in *fzo-1(tm1133)* mutants. We speculated that these changes in lipid metabolism upon autophagy induction may in turn suppress UPR^{mt} in these animals. In line with this notion, a previous study for essential genes that influence mitochondrial morphology in yeast identified many genes with roles in vesicular trafficking

(Altmann and Westermann, 2005). The authors proposed that the observed changes in mitochondrial morphology may result from changes in organellar contact sites and, as a consequence, altered lipid transfer into mitochondria. Moreover, endocytosis plays an important role in several cellular signaling pathways, which originate at the plasma membrane, such as signaling via G-protein-coupled receptors (GPCR) or receptor-mediated tyrosine kinases (Sorkin and von Zastrow, 2009; Di Fiore and von Zastrow, 2014). Thus, the disruption of endocytosis may either influence mitochondrial homeostasis through metabolic changes or directly influence cell non-autonomous UPR^{mt} signaling.

Moreover, the GO-terms related to 'ribosome biogenesis' and 'translation' are highly enriched in our statistical GO analysis, as well as the GO-terms of transcription- and RNA-related processes. We found the highest overlap between our list of candidates and the dataset of the Baumeister group (Runkel *et al.*, 2013), who also identified many ribosomal subunits or genes that are implicated in cytosolic translation to suppress paraquat-induced UPR^{mt}. Knock-down of these genes may lead to reduced biosynthesis of the *gfp* reporter and, thus, may be unspecific to the UPR^{mt} response. Runkel and colleagues therefore tested the ability of *ife-2*^{EIF4E} mutants, which have reduced cytosolic translation, to express the P$_{hsp\text{-}6\ mtHSP70}$*gfp* reporter upon paraquat treatment and surprisingly, detected increased levels of the reporter (Runkel *et al.*, 2013). However, in our experiments, reducing the levels of a cytosolic tRNA synthetase HARS-1^{HARS}, and the concomitant decrease in translation efficiency, led to attenuated biosynthesis of an unrelated GFP reporter, which is expressed in the same tissue as the P$_{hsp\text{-}6\ mtHSP70}$*gfp* reporter (chapter III (Haeussler *et al.*, 2020)). Thus, the candidates related to the functional groups 'transcription', 'RNA processing', 'ribosome biogenesis' and 'translation' may, to some extent, affect expression of the *gfp* reporter.

In contrast, attenuation of cytosolic translation has previously been suggested to be an ATFS-1^{ATF4,5}-independent arm of the UPR^{mt} pathway in animals that lack *clk-1*^{COQ7} function (Baker *et al.*, 2012). In these mutants, Baker and colleagues showed that attenuation of cytosolic translation by depletion of GCN-2^{EIF2AK4} leads to suppression of UPR^{mt}. The suggested model predicted that mitochondrial stress (by excessive ROS production, decreased mitochondrial translation and/or function) leads to stochiometric imbalance of mitochondrial and nuclear encoded subunits of the multi-subunit complexes of the ETC (Baker *et al.*, 2012; Houtkooper *et al.*, 2013). The nuclear encoded subunits would in turn accumulate in the mitochondrial matrix, overload mitochondrial chaperone capacity and subsequently induce UPR^{mt}. Therefore, decreasing cytosolic translation would counteract this so-called 'mito-nuclear' imbalance.

However, conflicting with this model, we recently showed that UPR^{mt} is activated upon knock-down of complex II subunits, which exclusively are encoded by the nuclear genome and therefore cannot lead to a 'mito-nuclear' imbalance. Thus, we proposed that the MTS of ATFS-1^{ATF4,5} acts as a sensor for any decrease in mitochondrial membrane potential (chapter II (Rolland *et al.*, 2019)). Even though we predict a different model for the activation of UPR^{mt}, the two models are not mutually exclusive. Accumulation of subunits of, for example, the respiratory chain complexes upon mitochondrial stress may further perturb mitochondrial homeostasis under these conditions. Thus, mitochondrial import and the biosynthesis of mitochondrial precursors in the cytosol need to be balanced in order to maintain homeostasis.

The importance of a balance between cytosolic translation and mitochondrial import is further highlighted by the existence of numerous stress pathways, which coordinate cytosolic translation and the removal of precursors from the OMM in situations when mitochondrial import is impaired. These are the 'mitochondrial compromised protein import response' (mitoCPR), the 'unfolded protein response activated by mistargeting of proteins' (UPR^{am}) and the 'mitochondrial precursor over-accumulation stress' (mPOS) (Wang and Chen, 2015; Wrobel *et al.*, 2015; Weidberg and Amon, 2018). In chapter III we show that mitochondrial membrane potential and, hence, mitochondrial import is reduced in *fzo-1(tm1133)* mutants (Haeussler *et al.*, 2020). Thus, mitochondrial proteins that are encoded in the nuclear genome may accumulate on the OMM of *fzo-1(tm1133)* mutants, thereby exerting stress both to the cytosolic and mitochondrial compartments. The knock-down of ribosomal subunits and other genes with roles in transcription, RNA-processing and translation may therefore be beneficial for mitochondrial and ultimately cellular homeostasis in mutants with attenuated mitochondrial import. In this scenario, mitochondrial proteins, which are specifically upregulated upon UPR^{mt} induction, may be imported more efficiently into mitochondria in order to mitigate mitochondrial stress. However, as stated above, we cannot exclude that compromising transcription, RNA processing and cytosolic translation interferes with *gfp* reporter expression *per se*. Thus, further testing of these candidates using an, to the UPR^{mt} unrelated, *gfp* reporter may help to identify their exact role in the suppression of UPR^{mt}.

In summary, for the majority of our candidates we identified a role in development and propose that disruption of certain processes at specific time points during development leads to the adjustment of many cellular processes, which are persistent throughout life and have an influence, for example, on ageing. Furthermore, our GO analysis revealed that disruption of receptor-mediated endocytosis suppresses UPR^{mt} and we speculate that this is the result either

of altered cell non-autonomous signaling or changes in metabolism. Further experiments are required in order to find out if attenuation of cytosolic translation specifically suppresses UPR^{mt} in mutants with a block in mitochondrial fusion. Finally, we identify the reduction of mitochondrial metabolism and translation as processes that robustly induce UPR^{mt} when disrupted.

4.3 Defects in mitochondrial fusion and fission are suppressed and enhanced by the same pathways

The secondary screens in *drp-1(tm1108)*, *eat-3(ad426)* and *spg-7(ad2249)* mutant backgrounds revealed a certain specificity of the identified candidates. We found most of the suppressors reproducing in all mitochondrial dynamics mutants and around half to influence UPR^{mt} signaling in general since they reproduced also in *spg-7(ad2249)* mutants (Figure 11).

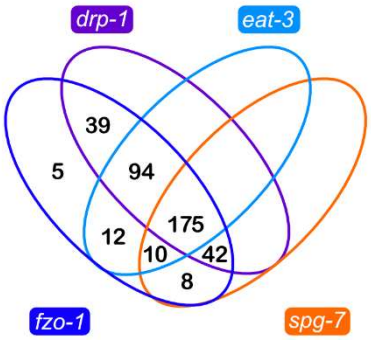

Figure 11: Venn diagram showing the number of candidates reproducing in each of the mutant backgrounds tested in the secondary screens (*drp-1(tm1108)*, *eat-3(ad426)*, *spg-7(ad2249)*). The overlap between the datasets was identified using Oliveros, J.C. (2007-2015) Venny; An interactive tool for comparing lists with Venn's diagrams. https://bioinfogp.cnb.csic.es/tools/venny/index.html.

We identified the suppressors, which generally suppress UPR^{mt} independent of the genetic background, to be assigned to the functional groups 'ribosome biogenesis', 'RNA processing' and 'translation'. Thus, we speculate that decreased mitochondrial membrane potential may also be a consequence of the defects in *drp-1(tm1108)* and *eat-3(ad426)* mutants and therefore, attenuation of mitochondrial translation may specifically lead to suppression of UPR^{mt} in these animals. This may also apply for *spg-7(ad2249)* mutants, since we detected reduced mitochondrial membrane potential in these animals (chapter II, (Rolland *et al.*, 2019)). However, as previously discussed, GFP synthesis may be affected upon knock-down of these genes, leading to the observed reduction in GFP signal intensity in these experiments. In addition, we found an inverse correlation in the results of the secondary screens between the

number of candidates reproducing and the level of reporter expression in the genetic backgrounds tested. Thus, the number of false negatives among both the suppressors and the enhancers may be higher in *spg-7(ad2249)* as compared to *drp-1(tm1108)* mutants.

Interestingly, we identified a subset of 22 genes in the secondary screens that either suppress *fzo-1(tm1133)*-induced UPR^{mt} and enhance UPR^{mt} in one or more of the other genetic backgrounds, or which were initially identified as enhancers in *fzo-1(tm1133)* mutants and reproduced as suppressors in the secondary screens. For example, we identified *icd-1*$^{\beta NAC}$ among the suppressors in all mitochondrial dynamics related backgrounds, while it enhances *spg-7(ad2249)*-induced UPR^{mt}. Knock-down of *icd-1*$^{\beta NAC}$ in mutants with defects in mitochondrial dynamics may therefore rescue some aspect and has adverse effects in *spg-7(ad2249)* mutants. The role of *icd-1*$^{\beta NAC}$ as a cytosolic stress sensor (Kirstein-Miles *et al.*, 2013) or the fact that depletion of *icd-1*$^{\beta NAC}$ also induces UPR^{ER} in wild-type embryos (Arsenovic *et al.*, 2012) may be important in this context. Moreover, we previously identified the knock-down of *icd-1*$^{\beta NAC}$ to induce autophagy, which leads to suppression of UPR^{mt} in *fzo-1(tm1133)* and *drp-1(tm1108)* mutants through increased metabolic activity. Therefore, we propose that UPR^{mt} may also be suppressed by this mechanism in *eat-3(ad426)* mutant and speculate that the enhancement of UPR^{mt} upon *icd-1(RNAi)* in *spg-7(ad2249)* mutants is independent of the induction of autophagy. In addition to the perturbations in mitochondrial homeostasis, *spg-7(ad2249)* mutants might as well have defects in cytosolic homeostasis, which are normally compensated for by ICD-1$^{\beta NAC}$. Thus, depletion of ICD-1$^{\beta NAC}$ may increase cytosolic stress and in turn further impair homeostasis both in the cytosol and in mitochondria and therefore enhance UPR^{mt} in *spg-7(ad2249)* mutants. Another interesting candidate, which we found to enhance UPR^{mt} in *fzo-1(tm1133)* and suppress *spg-7(ad2249)*-induced UPR^{mt}, while having no effect on P$_{hsp\text{-}6\ \mathrm{mtHSP70}}$*gfp* expression in *drp-1(tm1108)* and *eat-3(ad426)*, is *moma-1*^{APOO,APOOL}. MOMA-1^{APOO,APOOL} has been shown to localize to the OMM and to lead to altered mitochondrial morphology and cristae structure when mutated (Head *et al.*, 2011). Therefore, MOMA-1^{APOO,APOOL} may take over some function of FZO-1^{MFN1,2} in its absence, leading to increased mitochondrial stress and enhancement of UPR^{mt} upon depletion. Moreover, we propose that the defects in mitochondrial morphology, which have been observed upon *spg-7(RNAi)* (Haynes *et al.*, 2007), are also present in *spg-7(ad2249)* mutants and speculate that RNAi against *moma-1*^{APOO,APOOL} may have an effect on mitochondrial shape and distribution in these mutants, thereby suppressing UPR^{mt}. Thus, analyzing mitochondrial morphology upon knock-down of *moma-1*^{APOO,APOOL} both in *fzo-1(tm1133)* and *spg-7(ad2249)*

mutants may give further insights into the underlying mechanism of UPR^{mt} modulation. Taken together, we identified a subset of 22 genes in our dataset with opposing UPR^{mt} phenotypes in one or more genetic backgrounds of the secondary screens. These candidates may be interesting for further studies in *fzo-1(tm1133)*, *drp-1(tm1108)*, *eat-3(ad426)* and *spg-7(ad2249)* mutants due to their specific phenotypes in these mutants. Moreover, we identified the majority of suppressors reproducing in all mitochondrial dynamics related mutant backgrounds, which suggests that common pathways exist that can compensate for the defects in these mutants. Furthermore, we identified the disruption of mitochondrial function by depletion of mitochondrial translation and metabolism to robustly induce UPR^{mt} in all mutant backgrounds. However, only around half of the enhancers reproduced in *drp-1(tm1108)*, *eat-3(ad426)* and *spg-7(ad2249)* mutants, while almost all induced UPR^{mt} in a wild-type background. Therefore, we speculate that the baseline expression of P$_{hsp\text{-}6\ \mathrm{mtHSP70}}$*gfp* in the mutants may interfere with the identification of enhancers in these mutants.

4.4 Mitochondrial fitness balances cellular homeostasis

The majority (88%) of enhancers of *fzo-1(tm1133)*-induced UPR^{mt} have been shown to localize to mitochondria or are predicted to do so, according to our MTS analysis. In contrast, we also identified ten non-mitochondrial inducers of UPR^{mt}. Among these, Y61A9LA.11 may be targeted to mitochondria since the prediction of its MTS is just below our cut-off value. Thus, Y61A9LA.11 may also have a mitochondrial function. Furthermore, Y61A9LA.11, as well as C25H3.10 and F29B9.8 are so far uncharacterized in *C. elegans* and lack obvious orthologs in yeast, flies or mammals and may therefore be interesting for further studies specifically in *C. elegans*. The remaining seven non-mitochondrial enhancers are PLC-1^{PLCE1}, SRH-40, CPNA-3^{CPNE5,8,9}, NHR-209^{ESRRG}, ORC-1^{ORC1}, F25H9.6^{PPCDC} and COPD-1^{ARCN1} (Figure 12), the latter two of which do not induce UPR^{mt} upon depletion in the absence of mitochondrial stress. F25H9.6^{PPCDC} is orthologous to mammalian phosphorpantothenoylcysteine decarboxylase (PPCDC), which synthesizes precursors for coenzyme A (coA) production (Daugherty *et al.*, 2002). Therefore, depletion of F25H9.6^{PPCDC} may limit availability of certain substrates required for biosynthetic and metabolic pathways, thereby enhancing UPR^{mt} in *fzo-1(tm1133)* and we speculate that depletion of F25H9.6^{PPCDC} may be compensated for in wild-type animals.

The orthologs of COPD-1^{ARCN1} have been shown to be involved in the formation of coat complex I (COPI) vesicles both in yeast and humans. COPI vesicles transport many ER resident

proteins and lipids from the Golgi apparatus back to the ER (Lee *et al.*, 2004; Beck *et al.*, 2009). Moreover, most of the non-mitochondrial and non-peroxisomal transmembrane proteins are targeted to their final destination by the secretory pathway (Farhan and Rabouille, 2011). Some of these proteins play important roles in intra- and intercellular signaling pathways, such as signaling via GPCRs and receptor tyrosine kinases. Furthermore, intracellular signaling pathways, such as Ras and TOR, receive signals from the secretory pathway (Farhan and Rabouille, 2011). In addition, knock-down of ARCN1, the ortholog of COPD-1^{ARCN1} in humans, and other coatomer components in yeast have been shown to lead to secretion of ER chaperones and the induction of UPR^{ER} (Aguilera-Romero *et al.*, 2008; Izumi *et al.*, 2016). Thus, knock-down of *copd-1*^{ARCN1} may interfere with inter- and/or intracellular signaling pathways, which could lead to enhancement of UPR^{mt} in *fzo-1(tm1133)*. In line with this notion, depletion of phospholipase C (PLC-1^{PLCE1}), a GPCR associated enzyme, and SRH-40 (Serpentine Receptor class H), a predicted GPCR, also enhances UPR^{mt} in *fzo-1(tm1133)* mutants.

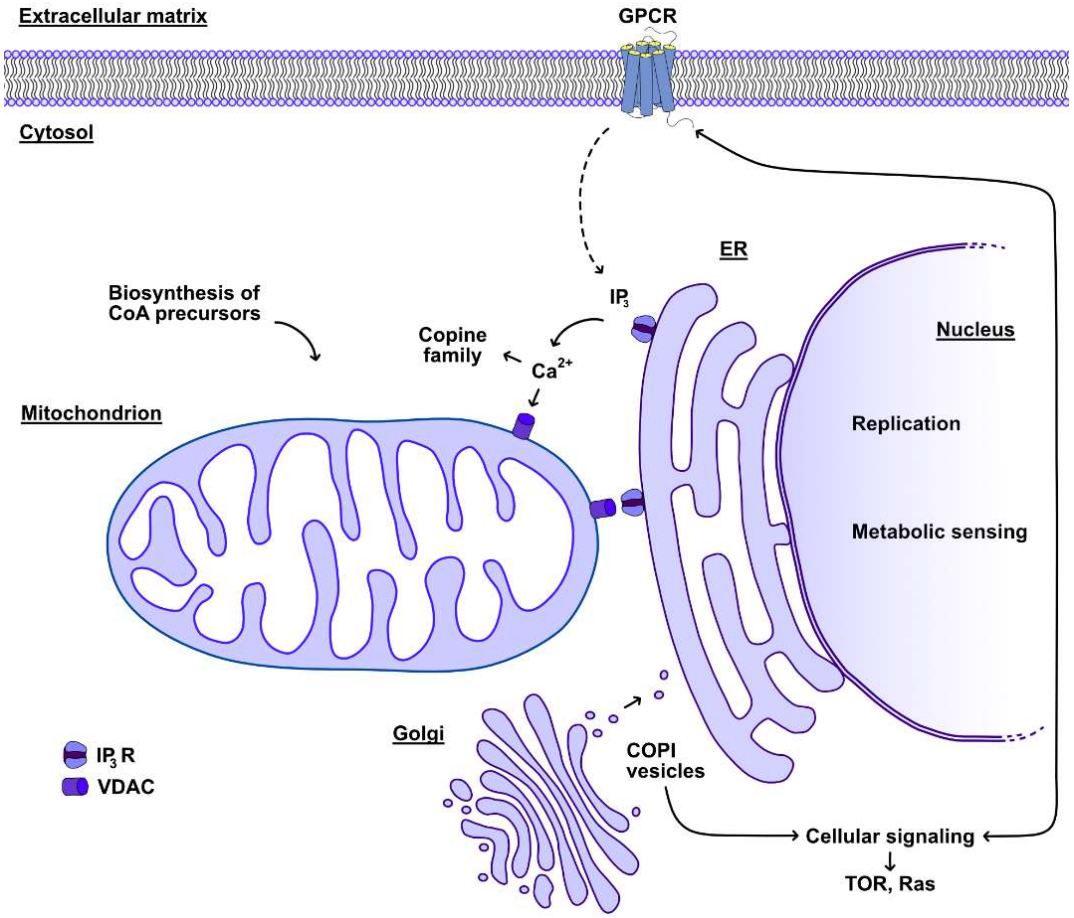

Figure 12: Schematic showing non-mitochondrial processes that, when disrupted, lead to induction of UPR^{mt} in *fzo-1(tm1133)*. GPCR: G-protein-coupled receptor, ER: Endoplasmic reticulum, IP_3(R): Inositol triphosphate (receptor), CoA: Acetyl coenzyme A, Ca^{2+}: Calcium ion, COPI: Coat complex I. VDAC: Voltage-dependent anion channel.

Depletion of ORC-1^{ORC1}, a component of the origin recognition complex (Gavin *et al.*, 1995; Ohta *et al.*, 2003; Tatsumi *et al.*, 2003), presumably leads to defects in DNA-replication and the cell cycle. This in turn may affect development, thereby disrupting mitochondrial homeostasis and enhancing UPR^{mt}. Moreover, we identified NHR-209^{HNF4A,G} among the non-mitochondrial enhancers, which is the *C. elegans* ortholog of Hepatocyte Nuclear Factor 4α and γ (HNF4A,G). The superfamily of nuclear hormone receptors (NHRs) are dependent on co-factors and ligands for their transcriptional activity and regulate diverse cellular processes (Aranda and Pascual, 2001; Bolotin *et al.*, 2010). Interestingly, HNF4A binds long-chain fatty acids and has been shown to activate or repress the transcription of its targets, depending on the chain length and saturation status of its ligands (Hertz *et al.*, 1998; Dhe-Paganon *et al.*, 2002; Wisely *et al.*, 2002; Duda *et al.*, 2004). In accordance with this, HNF4A has been shown to regulate FAO both in mice and *D. melanogaster* (Palanker *et al.*, 2009; Chen *et al.*, 2020). Therefore, we speculate that NHR-209^{HNF4A,G} may act as a metabolic sensor also in *C. elegans* and, thus, enhances UPR^{mt} upon depletion. In addition, we found a copine family member, CPNA-3^{CPNE5,8,9}, among the non-mitochondrial enhancers. Members of this family are calcium-dependent phospholipid binding proteins, which are implicated in intracellular signaling and membrane trafficking (Creutz *et al.*, 1998; Tomsig *et al.*, 2003; Tomsig *et al.*, 2004; Ramsey *et al.*, 2008). Interestingly, *gem-4*^{CPNE8}, which is orthologous to mammalian copine 8 (CPNE8), has been shown to be upregulated upon mitochondrial stress induced by *spg-7(RNAi)*, but this upregulation was independent of ATFS-1^{ATF4,5} (Nargund *et al.*, 2012). Thus, UPR^{mt} signaling may be dependent on members of the copine family. In summary, we identified the majority of enhancers of UPR^{mt} to localize to mitochondria but additionally found several processes outside of mitochondria to enhance UPR^{mt} when disrupted (Figure 12). Some of the above-mentioned non-mitochondrial enhancers may directly be required for UPR^{mt} signaling, while others regulate metabolism and, thus, influence mitochondrial function and homeostasis.

Furthermore, our analysis revealed that only ~5% of the suppressors localize to mitochondria. Among these are *tfg-1*^{TFG} and *gbf-1*^{GBF1}, both of which associate with contact sites between the ER and mitochondria. GBF-1^{GBF1} is a guanine nucleotide exchange factor for ARF-1.2^{ARF1,3} and is required for the localization of ARF-1.2^{ARF1,3} to ER-mitochondria contact sites (ERMCs) (Ackema *et al.*, 2014). Furthermore, *gbf-1(RNAi)* has been shown to lead to altered mitochondrial morphology, which is comparable to that upon depletion of MIRO-1^{MIRO1} and VDAC-1^{VDAC}, two other proteins residing at contact sites between the ER and mitochondria.

Moreover, epistasis experiments showed that mitochondrial morphology in animals lacking *fzo-1*^{MFN1,2} function is not further altered upon *gbf-1(RNAi)* or *arf-1.2(RNAi)* (Ackema *et al.*, 2014). From this data, we conclude that *gbf-1(RNAi)* in *fzo-1(tm1133)* mutants leads to altered ER-mitochondria contact sites rather than a rescue in mitochondrial morphology. Furthermore, we speculate that the changes in contact sites between these two organelles influences mitochondrial metabolism and consequently mitochondrial function, thereby leading to suppression of UPR^{mt} in *fzo-1(tm1133)* animals (Figure 13).

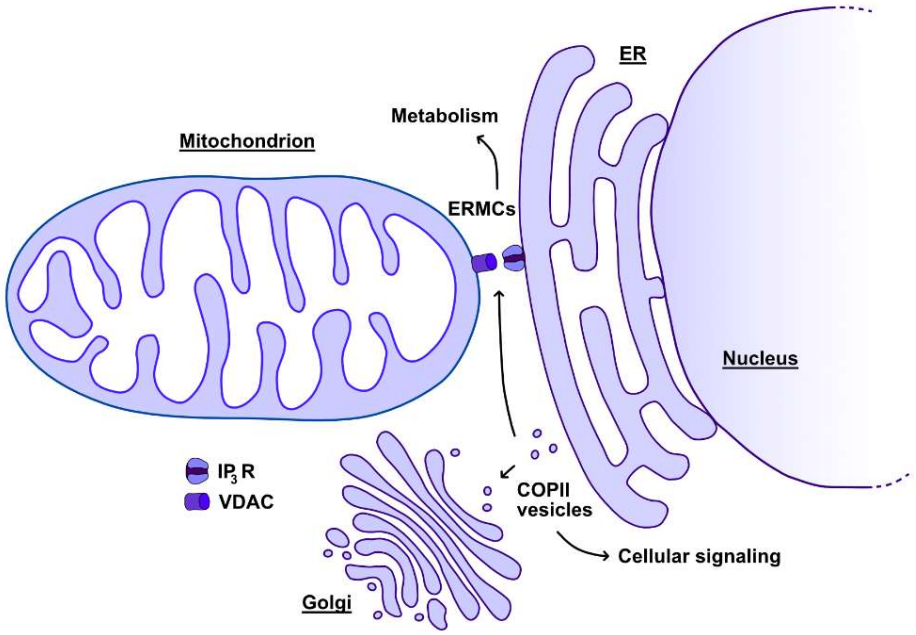

Figure 13: Schematic showing processes that affect mitochondria when disrupted, leading to suppression of UPR^{mt} in *fzo-1(tm1133)*. ER: Endoplasmic reticulum, ERMCs: ER-mitochondria contact sites, COPII: Coat complex II, IP_3R: Inositol triphosphate receptor, VDAC: Voltage-dependent anion channel.

Moreover, we identified a component of the secretory pathway, TFG-1^{TFG}, as a non-mitochondrial suppressor of UPR^{mt} in *fzo-1(tm1133)*. TFG-1^{TFG} is implicated in COPII vesicle transport and localizes to ER-exit sites (ERES) (Witte *et al.*, 2011). ERES are specialized ER zones that stay in close contact to the Golgi apparatus where lipids as well as newly synthesized proteins are loaded into COPII vesicles for their transport to the Golgi apparatus (Budnik and Stephens, 2009; Kurokawa and Nakano, 2018). As previously discussed for COPD-1^{ARCN1}, we propose that the disruption of the secretory pathway may affect cellular signaling and contact sites between the ER and mitochondria, thereby influencing mitochondrial function and consequently UPR^{mt} (Figure 13). Furthermore, we speculate that, depending on the context, disruption of the secretory pathway can both suppress or enhance UPR^{mt}. Taken together, these results suggest a role for contact sites, especially between mitochondria and the ER, to influence mitochondrial homeostasis and, hence, UPR^{mt} signaling. Furthermore, we

demonstrate that disrupting the secretory pathway can challenge or improve mitochondrial homeostasis under certain circumstances. Apart from these non-mitochondrial candidates that enhance UPR^{mt} signaling in *fzo-1(tm1133)* mutants, we find that mitochondrial homeostasis is primarily affected when processes within mitochondria are disrupted. Conversely, we primarily identified non-mitochondrial suppressors, suggesting that mitochondrial function plays a vital role in cellular homeostasis since many processes outside of mitochondria can compensate for mitochondrial dysfunction.

4.5 Transcription factor enrichment analysis identifies factors with roles in development, metabolism and oxidative stress response

The identification of transcription factors (TFs) that specifically bind to the promotors of the identified candidate genes in our dataset revealed additional potential regulators of UPR^{mt} signaling. Using this approach, we identified several TFs that play a role in development, metabolism and oxidative stress response. As previously discussed, the level of UPR^{mt} signaling has been shown to be adjusted during development (Dillin *et al.*, 2002; Rea *et al.*, 2007; Durieux *et al.*, 2011). Therefore, we speculate that the identified TFs may play a role in this process during development. Moreover, we previously demonstrated that induction of autophagy leads to alterations in cellular metabolism and, hence, can influence UPR^{mt} signaling in *fzo-1(tm1133)* (Haeussler *et al.*, 2020). Consistent with this notion, we identified two TFs (HLH-11^{TFAP4}, HLH-29) in our analysis, which are known to regulate metabolic gene expression and energy homeostasis (McMiller *et al.*, 2007; Quach *et al.*, 2013; Watson *et al.*, 2013). Therefore, we propose that UPR^{mt} is induced to compensate for metabolic defects in *fzo-1(tm1133)* animals, which may require HLH-11^{TFAP4} and HLH-29. Finally, we identified three TFs (SKN-1^{NFE2,NFE2L1,2,3}, ELT-3^{GATA3,4}, HLH-29), which are known to regulate the response to oxidative stress (An and Blackwell, 2003; An *et al.*, 2005; Inoue *et al.*, 2005; Quach *et al.*, 2013; Hu *et al.*, 2017). The expression of ROS detoxifying genes has previously been shown to be part of the transcriptional program, which is expressed upon activation of UPR^{mt} in an ATFS-1^{ATF4,5} and SKN-1^{NFE2,NFE2L1,2,3} -dependent manner (Nargund *et al.*, 2012; Nargund *et al.*, 2015; Wu *et al.*, 2018). Thus, we propose that additional TFs may be required for the expression of the oxidative response upon UPR^{mt} activation and speculate that ELT-3^{GATA3,4}, HLH-29 may play a role in this process. In summary, we identified several TFs that may play

a role in UPR^{mt} signaling and speculate that some of them are generally required for UPR^{mt} signaling.

4.6 Interactome analysis reveals potential new regulators of UPR^{mt}

In the interactome analysis, we identified many potential new regulators of the UPR^{mt} response in *fzo-1(tm1133)*, some of which may regulate UPR^{mt} in general. For example, we identified four interactors (GTF-2F2^{GTF2F2}, LIN-54^{LIN54}, SPR-2^{SET}, TBP-1^{TBP}) of the master regulator of UPR^{mt}, ATFS-1^{ATF4,5}, that localize to the nucleus (Sopta *et al.*, 1989; Lichtsteiner and Tjian, 1993; Wen *et al.*, 2000; Thomas *et al.*, 2003; Harrison *et al.*, 2006; Tabuchi *et al.*, 2011) and therefore may generally be involved in activation of the transcriptional program of the UPR^{mt} response. Moreover, we identified the E2 SUMO conjugating enzyme UBC-9^{UBE2I}, a suppressor of *fzo-1(tm1133)*-induced UPR^{mt} interacting with known players of the UPR^{mt} pathway POP-1^{LEF1,TCF7,TCF7L2} and DVE-1^{SATB1}. Conflicting with our results of the secondary screens where *ubc-9(RNAi)* suppresses UPR^{mt} exclusively in mutants with defects in mitochondrial membrane fusion, while having no effects in *drp-1(tm1108)* and *spg-7(ad2249)* mutants, *ubc-9(RNAi)* has previously been shown to further enhance antimycin and *spg-7(RNAi)*-induced UPR^{mt} (Gao *et al.*, 2019). This may be explained by the different experimental approaches used since Gao and colleagues first depleted *ubc-9*^{UBE2I} before inducing mitochondrial stress while in our experiments mitochondrial stress is persistent. Further validation of these results would be required to determine the role of UBC-9^{SATB1} in UPR^{mt} signaling. In addition, we identified three splicing factors (PQBP-1.2^{PQBP1}, SFA-1^{SF1}, SNR-3^{SNRPD1}) among our dataset that interact with UBL-5^{UBL5}. Interestingly, a study in *Saccharomyces pombe* previously reported a function of HUB1, the ortholog of UBL-5^{UBL5} in budding yeast, in pre-mRNA splicing. Depletion of HUB1 resulted in accumulation of unspliced RNAs of various genes (Wilkinson *et al.*, 2004). In contrast, *ubl-5(RNAi)* has previously been reported not to result in the accumulation of unspliced RNAs in *C. elegans* (Haynes *et al.*, 2007). Therefore, we propose that we identified a potential link between pre-mRNA splicing and activation of UPR^{mt} via UBL-5^{UBL5}. Taken together, we identified several candidates among our dataset that may directly act in the UPR^{mt} pathway through interaction with known players of the response.

4.7 Interactome analysis reveals involvement of IP_3 signaling pathway in UPR^{mt} regulation in *fzo-1(tm1133)*

The interactome analysis also revealed an interaction between phospholipase C (*plc-1*^{PLCE}) and *bar-1*$^{\beta\text{-catenin}}$ (Byrne *et al.*, 2007), which previously has been shown to be required for cell non-autonomous regulation of UPR^{mt} in *C. elegans* (Zhang *et al.*, 2018). This interaction drew our attention to the IP_3 signaling pathway, which could potentially also have a role in cell non-autonomous regulation of UPR^{mt} in *fzo-1(tm1133)* mutants. Interestingly, we found three more suppressors in our dataset that also act in the IP_3 signaling pathway. We identified the enzyme cytidine biphosphate-diacylglycerol (CDP-DAG) synthase, which is required for phosphatidylinositol (PI) production (Wu *et al.*, 1995; Vance, 1998). In humans, PI4-kinase phosphorylates PI to form PI 4-phosphate (PI4P) and has been shown to be targeted to the plasma membrane by EFR3B (Nakatsu *et al.*, 2012), which is orthologous to one of the candidates in our dataset, EFR-3^{EFR3B}. Thus, it would be interesting to test whether depletion of the PI 4-kinase PIFK-1^{PI4KB} can also suppress UPR^{mt} in *fzo-1(tm1133)* animals. This gene has been identified in another screen before (Runkel *et al.*, 2013), but was later withdrawn from the dataset by the authors. PI4P is further phosphorylated by the sole type I PIP kinase in *C. elegans* (Weinkove *et al.*, 2008), PPK-1^{PIP5K1A}, which is among our candidates, thereby forming PI(4,5)P2 (Ishihara *et al.*, 1996; Loijens and Anderson, 1996). Upon activation via GPCRs, PLC-1^{PLCE} hydrolyzes $PI(4,5)P_2$, thereby generating IP_3 and DAG. These two second messengers are powerful signaling molecules that are known for their role in the regulation of cellular calcium levels (Clandinin *et al.*, 1998; Kariya *et al.*, 2004; Kovacevic *et al.*, 2013). While we identified depletion of PLC-1^{PLCE} to enhance UPR^{mt}, all other above-mentioned genes were found to suppress UPR^{mt} in *fzo-1(tm1133)* upon knock-down. Furthermore, Liu and colleagues identified ITR-1^{ITPR1}, the IP_3 receptor at the ER, to suppress antimycin-induced UPR^{mt} (Liu *et al.*, 2014). Taken together, we propose that IP_3 signaling and the interrelated regulation of cellular calcium may influence mitochondrial homeostasis and UPR^{mt} signaling in *fzo-1(tm1133)*. In contrast, we previously did not find a role for mitochondrial calcium signaling in a screen for inducers of UPR^{mt} (chapter II (Rolland *et al.*, 2019)). Furthermore, we speculate that we identified this previously unknown signaling cascade to have an influence on UPR^{mt} specifically in *fzo-1(tm1133)* mutants since ER-mitochondria contact sites, known to serve as hubs for the exchange of calcium between the ER and mitochondria, may be disrupted in these mutants. Of note, MFN2 has previously been shown to be involved in the regulation

of these contact sites (de Brito and Scorrano, 2008; Cosson *et al.*, 2012; Filadi *et al.*, 2015, 2016; Leal *et al.*, 2016; Naon *et al.*, 2016; Basso *et al.*, 2018).

4.8 Compromised mitochondrial protein import acts as a signal for UPR^{mt}

In a genome-wide RNAi screen for inducers of UPR^{mt} (chapter II) we found that dysregulation of almost all mitochondrial processes induces UPR^{mt}, except for the disruption of mitochondrial calcium signaling and mitophagy. In total, 171 candidates were identified to induce the expression of the P$_{hsp\text{-}6\ mt\text{HSP70}}$*gfp* reporter when knocked-down in wild-type animals. Previously, it has been proposed that UPR^{mt} is induced when unfolded or misfolded proteins accumulate in the mitochondrial matrix (Yoneda *et al.*, 2004), similar to the induction of the unfolded protein response in the ER (UPR^{ER}) (Walter and Ron, 2011). Since many mitochondrial proteins are multi-subunit complexes, which are encoded both in the mitochondrial and the nuclear genomes, the accepted model in the field predicted that nuclear encoded subunits would accumulate if the protein folding environment in mitochondria is disturbed (Haynes *et al.*, 2007; Haynes *et al.*, 2010; Houtkooper *et al.*, 2013). However, this model does not fit with many of the identified candidates in our dataset since disruption of the ETC, the TCA cycle or mitochondrial lipid metabolism does not result in accumulation of unfolded or misfolded proteins in the mitochondrial matrix. Instead, we propose that a decrease in mitochondrial membrane potential acts as the signal for UPR^{mt} induction (Figure 14). We analyzed the net charge of several MTS's of mitochondrial proteins acting in the UPR^{mt} pathway. Consistent with our hypothesis, we found that the major regulator of the response, ATFS-1^{ATF4,5}, has a weak MTS as compared to some of the UPR^{mt} effectors, such as HSP60^{HSPA1} and SPG-7^{AFG3L2}. Additionally, we found that a chimeric ATFS-1^{ATF4,5} protein, containing a strong MTS, induces UPR^{mt} in a mitochondrial membrane dependent manner. Hence, situations of high mitochondrial membrane potential would allow for ATFS-1^{ATF4,5} import into mitochondria and its subsequent degradation. Conversely, any reduction in mitochondrial membrane potential would lead to decreased import of ATFS-1^{ATF4,5} into mitochondria and consequently to its import into the nucleus (Figure 14), since ATFS-1^{ATF4,5} additionally contains an NLS at its C-terminus (Nargund *et al.*, 2012). Thus, we propose that the MTS of ATFS-1^{ATF4,5} acts as a sensor for mitochondrial membrane potential, which is the signal for UPR^{mt} induction.

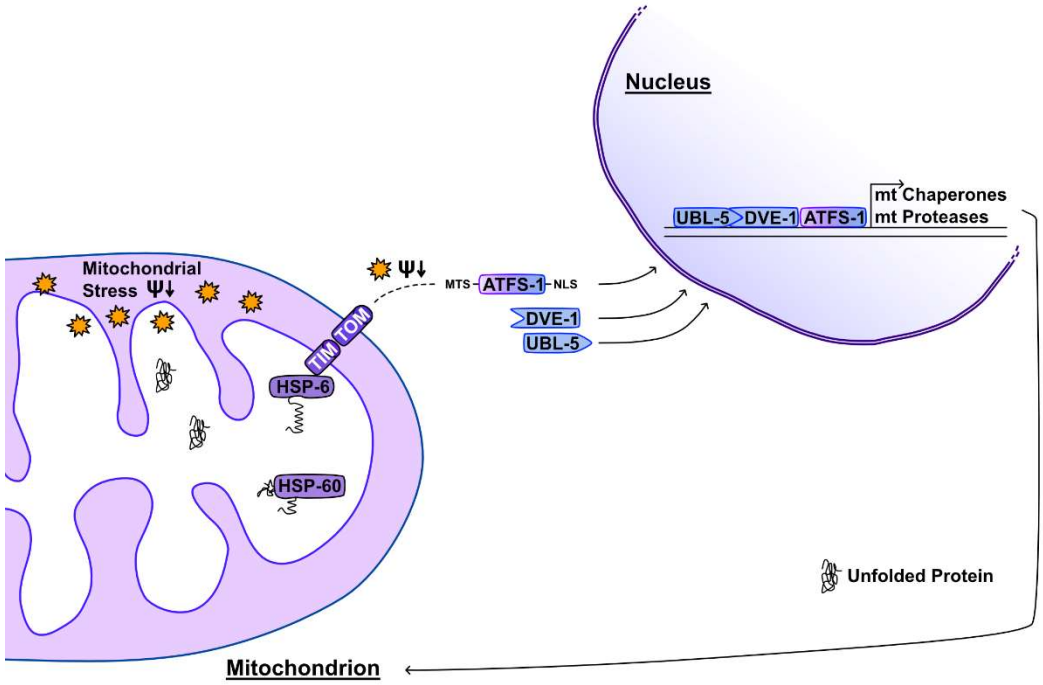

Figure 14: Revised UPR^{mt} model according to (Rolland *et al.*, 2019). The comparably weak MTS of ATFS-1^{ATF4,5} acts as a stress sensor since it is sensitive to subtle changes in mitochondrial membrane potential (ψ). If mitochondrial homeostasis is perturbed, mitochondrial membrane potential decreases leading to less efficient import of ATFS-1^{ATF4,5} into mitochondria. This in turn leads to import of ATFS-1^{ATF4,5} into the nucleus where it activates its transcriptional program (UPR^{mt}). Schematic adapted from (Jovaisaite *et al.*, 2014).

4.9 Induction of autophagy suppresses UPR^{mt} in *fzo-1(tm1133)* mutants by increasing mitochondrial membrane potential

Among the 299 suppressors of *fzo-1(tm1133)*-induced UPR^{mt}, we identified 143 genes that negatively regulate autophagy. Depletion of these negative regulators of autophagy does not result in altered steady-state mitochondrial morphology but instead, to an increase in mitochondrial membrane potential. Thus, some aspect of mitochondrial homeostasis, which is perturbed in *fzo-1(tm1133)* mutants leading to decreased mitochondrial membrane potential, is partially restored by the induction of autophagy. As shown in chapter II, we found that ATFS-1^{ATF4,5}, the master regulator of the UPR^{mt} response, is sensitive to changes in mitochondrial membrane potential. Consequently, the observed increase in mitochondrial membrane potential upon autophagy induction leads to suppression of UPR^{mt}. To further test this hypothesis, we wanted to show that knock-down of ESCRT components, which are among the negative regulators of autophagy, would still suppress UPR^{mt} in *fzo-1(tm1133)* mutants when, in parallel, autophagy is blocked. However, *fzo-1(tm1133); unc-51(e369)* mutants, which are

unable to induce autophagy, died during embryogenesis upon *ESCRT(RNAi)*. Djeddi *et al.* previously showed that induction of autophagy in ESCRT depleted animals is a compensatory mechanism for the defects in the endosomal pathway (Djeddi *et al.*, 2012). Furthermore, we did not find any evidence for *pdr-1*^{parkin}- or *fndc-1*^{FNDC}-dependent mitophagy in the suppression of UPR^{mt} in *fzo-1(tm1133)* mutants upon ESCRT depletion. Therefore, we conclude that induction of autophagy rather than mitophagy plays a role in suppression of UPR^{mt} in *fzo-1(tm1133)* mutants.

4.10 Defects in mitochondrial dynamics can be compensated for by the induction of autophagy

Knock-down of 97% of the identified negative regulators of autophagy also suppress UPR^{mt} in *drp-1(tm1108)*, while only 63% suppress in *spg-7(ad2249)*. Thus, the induction of autophagy may not suppress UPR^{mt} in general but rather compensate for defects in mitochondrial dynamics. This hypothesis is supported by the finding that *let-363(RNAi)* does not suppress UPR^{mt} in *spg-7(ad2249)*. Using lipidomics, we detected changes in the levels of certain TGs in both *fzo-1(tm1133)* and *drp-1(tm1108)* mutants, as compared to wild type, which were not detectable in *spg-7(ad2249)* mutants. Additionally, we found that the induction of autophagy in *fzo-1(tm1133)* animals reverted some of the observed changes in the levels of these TGs.

Interestingly, autophagy has been shown to play a role in the breakdown of TGs from lipid droplets, which are closely associated with mitochondria to ensure a constant fatty acid supply for FAO (Singh *et al.*, 2009). Additionally, lipid droplets play an important role in the delivery of building blocks for the synthesis of fatty acids and TGs. These fatty acids typically have lower chain length and a high degree of saturation (Benador *et al.*, 2018), which we see to be decreased in mitochondrial dynamics mutants. Furthermore, disruption of mitochondrial dynamics by deletions in *Opa1* or *Mfn1* in mouse embryonic fibroblasts (MEFs) has been shown to affect fatty acid transfer from lipid droplets to mitochondria (Rambold *et al.*, 2015). Moreover, MFN2 has been shown to be enriched in contact sites between lipid droplets and mitochondria (Benador *et al.*, 2018). In addition, the master regulator of lipid metabolism, PPARα, which affects expression of key enzymes of the FAO pathway by transcriptional repression, has been shown to be degraded by autophagy (Saito *et al.*, 2019). Therefore, we hypothesize that the disruption of mitochondrial dynamics leads to alterations in contact sites

between mitochondria and lipid droplets. Furthermore, we speculate that the induction of autophagy mobilizes lipids that are stored in lipid droplets for oxidation in mitochondria with altered morphology and -distribution (Figure 15), as it has recently been shown in yeast upon glucose starvation (Seo *et al.*, 2017; Weber *et al.*, 2020). Thus, in mutants with defects in mitochondrial dynamics, the induction of autophagy fuels mitochondria with fatty acids for FAO and OXPHOS, leading to increased metabolic activity and consequently mitochondrial membrane potential and in turn to suppression of UPR^{mt}.

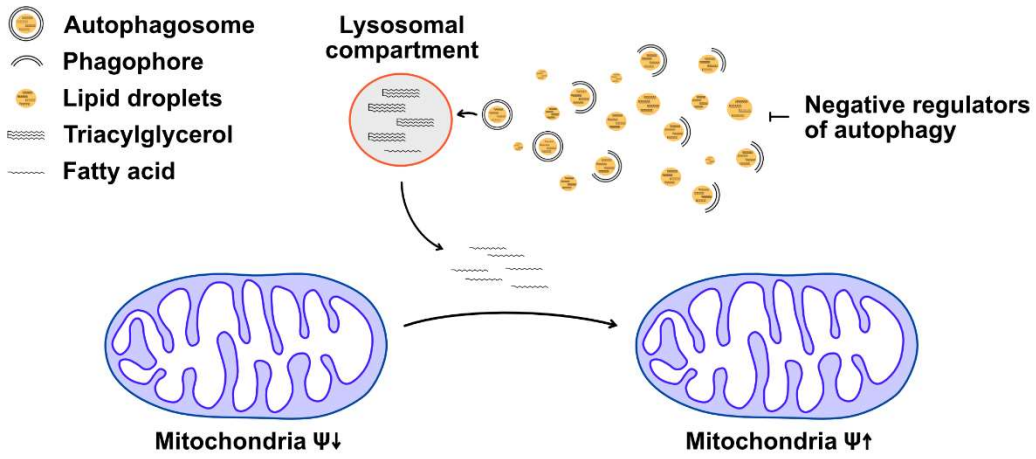

Figure 15: Lipid droplets containing triacylglycerols are degraded in the lysosomal compartment by the induction of autophagy. Fatty acids derived from these lipid droplets fuel mitochondrial metabolism leading to increased membrane potential (ψ).

On the other hand, we do see a very similar trend in the results of the secondary screens in *drp-1(tm1108)* and *spg-7(ad2249)* mutants for the 156 suppressors, which do not negatively regulate autophagy. Altogether, 96% of the suppressors reproduced in *drp-1(tm1108)*, while 59% reproduced in *spg-7(ad2249)* (see chapter I). Moreover, 78% of the candidates negatively regulating autophagy reproduced in *eat-3(ad426)* mutants, while overall 81% of the suppressors reproduced in this background. As discussed earlier, we find the number of candidates reproducing to negatively correlate with the expression level of the P$_{hsp\text{-}6\ mt\text{HSP70}}$*gfp* reporter. Consequently, the expression level of the reporter may influence the ability of a certain candidate to reproduce in a specific genetic background. These results allow for two alternative conclusions. First, the induction of autophagy can exclusively compensate for defects in mitochondrial dynamics induced by *fzo-1(tm1133)* and *drp-1(tm1108)*, since *eat-3(ad426)*-induced UPR^{mt} is not suppressed by all of the identified negative regulators of autophagy. Second, the induction of autophagy may generally fuel mitochondria with substrates for respiration in mutants with defects in mitochondrial homeostasis that also have reduced membrane potential, thereby increasing metabolic activity and mitochondrial

membrane potential. Thus, UPR^{mt} may also be suppressed under these conditions but the suppression of UPR^{mt} in *eat-3(ad426)* and *spg-7(ad2249)* mutants may be harder to detect due to the high GFP expression of the reporter in these mutants. Consequently, this requires further experiments to test if mitochondrial membrane potential is increased in *drp-1(tm1108)* and *spg-7(ad2249)* mutants upon autophagy induction. Furthermore, it would be interesting to analyze the lipid profiles of these mutants and to compare them upon induction of autophagy to see how TGs behave in these genetic backgrounds.

4.11 Functional interactions of autophagy and UPR^{mt}

The functional interaction of different cellular quality control mechanisms has previously been proposed (Pellegrino *et al.*, 2013) and this idea has been supported by several different studies in recent years. Haynes and colleagues, pioneers in the field of UPR^{mt} research in *C. elegans*, found *rheb-1*^{RHEB}, a positive regulator of mTOR (Honjoh *et al.*, 2008), as a suppressor of UPR^{mt}. The authors did not study the mechanistic details at the time but concentrated on describing the UPR^{mt} pathway itself (Haynes *et al.*, 2007). More recently, it has been shown that certain mitochondrial stresses (e.g. *spg-7(RNAi)*) upregulate both UPR^{mt} and autophagy in *C. elegans* (Guo *et al.*, 2014), which we also show for *fzo-1(tm1133)* and *spg-7(ad2249)* mutants. The functional connection between blocking mitophagy and the consequences in respect to UPR^{mt} induction also has been tested in two independent studies before. However, conflicting results were published since one study found that UPR^{mt} is induced when mitophagy is blocked (Cooper *et al.*, 2017) while the other study could not detect an upregulation of the UPR^{mt} reporter (Kim and Sieburth, 2018). We tested the functional interaction of autophagy and UPR^{mt} and found that a block in autophagy using *unc-51(e369)* mutants induces UPR^{mt} in the absence of mitochondrial stress while UPR^{mt} is not further increased in *fzo-1(tm1133)*. The role of autophagy in cellular metabolism has been shown to be diverse and, hence, also influences mitochondrial homeostasis (Rabinowitz and White, 2010; Kim and Lee, 2014). Therefore, we conclude that a block in autophagy results in decreased supply of substrates for respiration into mitochondria, which may lead to a decrease in mitochondrial membrane potential, increased UPR^{mt} and a concomitant metabolic switch towards glycolysis (Lin and Haynes, 2016). Furthermore, we speculate that if UPR^{mt} is already activated, as in *fzo-1(tm1133)* mutants, a block in autophagy does not further influence UPR^{mt} signaling since this metabolic shift already occurred. Moreover, we found that neither blocking

nor activating UPR^{mt} constitutively influences autophagic flux in the absence of mitochondrial stress. Thus, from our results, we conclude that alterations in autophagic flux can influence UPR^{mt} signaling but changes in UPR^{mt} do not have an impact on autophagy. Therefore, our data contradicts previous reports where induction of UPR^{mt} and autophagy was found to be dependent on ATFS-1^{ATF4,5} (Guo *et al.*, 2014). Taken together, we show that the interaction between the autophagic pathway and UPR^{mt} is unidirectional. In addition, we speculate that blocking autophagy limits substrate supply into mitochondria and, hence, the interaction of these pathways is indirect.

4.12 Genome-wide RNAi screen identifies a new autophagy network

Among our dataset of 299 suppressors of *fzo-1(tm1133)*-induced UPR^{mt}, we identified 143 genes that negatively regulate UPR^{mt}, 94% of which are conserved in humans. In addition to the ESCRT components, we found several other genes involved in cellular trafficking, which play roles in nuclear import and -export, respectively (*imb-2*^{TNPO1,2}, *imb-3*^{IPO5,RANBP6}, *ima-3*^{KPNA3,4}, *xpo-2/imb-5*^{CSE1L}). Interestingly, *imb-2*^{TNPO1,2}, a regulator of the nuclear transport of DAF-16^{FOXO} (Putker *et al.*, 2013), has previously been implicated in the regulation of autophagy (Zhao *et al.*, 2010). Moreover, loss of components of the ubiquitin-proteasome system has previously been shown to result in increased autophagic flux (Takahashi *et al.*, 2002; Mouysset *et al.*, 2006; Yang *et al.*, 2013) and we identified several of these components in our screen (*rpt-3*^{PSMC4}, *rpn-13*^{ADRM1}, *ufd-1*^{UFD1}, *rbx-1*^{RBX1}, *cul-1*^{CUL1}). In addition, we identified a gene of the TOR pathway, *ruvb-1*^{RUVBL1}, in our dataset (Sheaffer *et al.*, 2008). Furthermore, we identified approximately one third of the genes in our autophagy network to have roles in translation or ribosome biogenesis. Interestingly, translation inhibition is often accompanied by the induction of autophagy in cancer (Acevo-Rodríguez *et al.*, 2020) and therefore may be a general cellular mechanism. In summary, we identified many different cellular components that negatively regulate autophagy. Moreover, we propose that the induction of autophagy upon knock-down of these genes is a secondary effect in order to maintain cellular homeostasis.

4.13 MitoSegNet: a deep learning segmentation tool for the analysis of mitochondrial morphology

Mitochondrial morphology and mitochondrial function are closely linked but determination of abnormal mitochondrial morphology by visual examination has proven difficult. Segmentation and subsequent quantification of microscopic images helps to determine even subtle differences that are present in mitochondrial morphology. We developed a deep learning segmentation tool called MitoSegNet and found that it outperforms currently available threshold algorithms in ImageJ/Fiji, as well as another machine-learning segmentation tool currently available (Kreshuk and Zhang, 2019). MitoSegNet provides more accuracy in single object comparison as well as in the calculation for five different feature descriptors (area, eccentricity, aspect ratio, perimeter and solidity). Taken together, we provide a deep learning tool for the automated segmentation of mitochondrial morphology and subsequent statistical analysis with high accuracy, which can be used in *C. elegans*, as well as in other organisms.

4.14 Conclusions

In summary, we identified a highly conserved dataset that influences mitochondrial homeostasis and therefore modulates UPR^{mt} signaling in *fzo-1(tm1133)* mutants. The majority of suppressors do not localize to mitochondria, suggesting that non-mitochondrial processes exist that can compensate for disrupted mitochondrial dynamics. We identified autophagy to be one of these non-mitochondrial processes, which, upon activation, fuels mitochondria of mitochondrial dynamics defective mutants with lipids to elevate mitochondrial metabolism, thereby leading to suppression of UPR^{mt} (Figure 16). Furthermore, we find that contact sites between organelles, especially between mitochondria and the ER, to be of importance to mitochondrial homeostasis and propose a role for IP_3 signaling in the UPR^{mt} pathway. Moreover, we find that disruption of primarily mitochondrial processes to induce UPR^{mt} signaling, which further highlights the importance of mitochondrial homeostasis in a cellular context. In line with this notion, we identified a role for the mitochondrial membrane potential, which is sensed by the MTS of ATFS-1^{ATF4,5}, in UPR^{mt} activation. Finally, we found a so far uncharacterized gene (*miga-1*) in *C. elegans*, which may have a role in mitochondrial dynamics and which induces UPR^{mt} when knocked-down or mutated. Therefore, we propose that mutants with defective mitochondrial morphology and -distribution may either activate UPR^{mt} due to

reduced mitochondrial quality control or the secondary effects resulting from the altered mitochondrial morphology. Future experiments using *drp-1(tm1108); fzo-1(tm1133)* double mutants in which mitochondrial morphology is partially restored (Weir *et al.*, 2017) may help to explain how UPR^{mt} is induced in mutants with defects in mitochondrial dynamics.

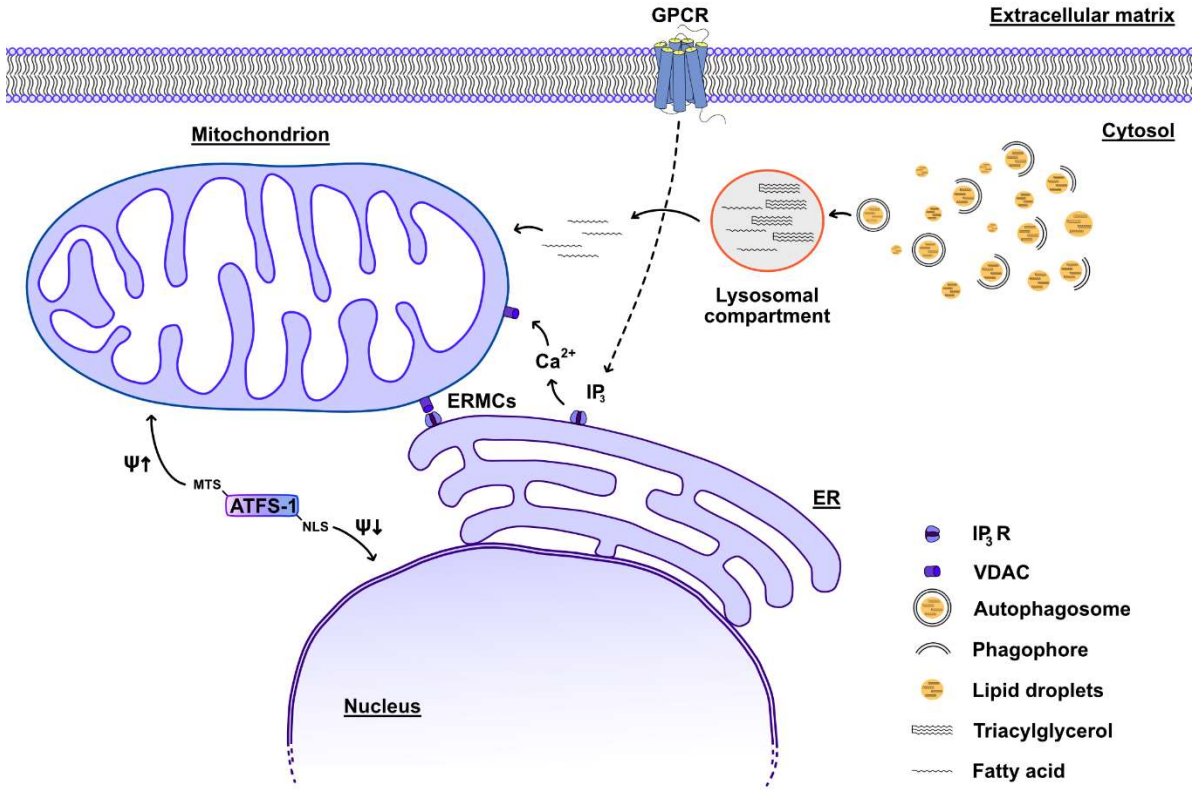

Figure 16: The majority of the identified suppressors have roles outside of mitochondria. The induction of autophagy, alterations in ER-mitochondria contact sites (ERMCs) and the inositol triphosphate (IP_3) signaling pathway were identified to influence UPR^{mt} signaling. UPR^{mt} signaling is dependent on the import efficiency of its master regulator ATFS-1^{ATF4,5}. GPCR: G-protein-coupled receptor, Ca^{2+}: Calcium ion, ER: Endoplasmic reticulum, VDAC: Voltage-dependent anion channel.

5. References

Abrisch, R.G., Gumbin, S.C., Wisniewski, B.T., Lackner, L.L., and Voeltz, G.K. (2020). Fission and fusion machineries converge at ER contact sites to regulate mitochondrial morphology. Journal of Cell Biology *219*.

Acevo-Rodríguez, P.S., Maldonado, G., Castro-Obregón, S., and Hernández, G. (2020). Autophagy Regulation by the Translation Machinery and Its Implications in Cancer. Frontiers in oncology *10*, 322-322.

Ackema, K.B., Hench, J., Böckler, S., Wang, S.C., Sauder, U.*, et al.* (2014). The small GTPase Arf1 modulates mitochondrial morphology and function. The EMBO journal *33*, 2659-2675.

Aguilera-Romero , A., Kaminska , J., Spang , A., Riezman , H., and Muñiz , M. (2008). The yeast p24 complex is required for the formation of COPI retrograde transport vesicles from the Golgi apparatus. Journal of Cell Biology *180*, 713-720.

Akram, M. (2014). Citric Acid Cycle and Role of its Intermediates in Metabolism. Cell Biochemistry and Biophysics *68*, 475-478.

Allen, G.F.G., Toth, R., James, J., and Ganley, I.G. (2013). Loss of iron triggers PINK1/ Parkin-independent mitophagy. EMBO reports *14*, 1127-1135.

Altmann, K., and Westermann, B. (2005). Role of Essential Genes in Mitochondrial Morphogenesis in Saccharomyces cerevisiae. Molecular Biology of the Cell *16*, 5410-5417.

Amberger, J.S., Bocchini, C.A., Scott, A.F., and Hamosh, A. (2018). OMIM.org: leveraging knowledge across phenotype–gene relationships. Nucleic Acids Research *47*, D1038-D1043.

An, J.H., and Blackwell, T.K. (2003). SKN-1 links C. elegans mesendodermal specification to a conserved oxidative stress response. Genes & Development *17*, 1882-1893.

An, J.H., Vranas, K., Lucke, M., Inoue, H., Hisamoto, N.*, et al.* (2005). Regulation of the *Caenorhabditis elegans* oxidative stress defense protein SKN-1 by glycogen synthase kinase-3. Proceedings of the National Academy of Sciences of the United States of America *102*, 16275.

Anand, R., Wai, T., Baker, M.J., Kladt, N., Schauss, A.C.*, et al.* (2014). The i-AAA protease YME1L and OMA1 cleave OPA1 to balance mitochondrial fusion and fission. Journal of Cell Biology *204*, 919-929.

Anderson, N.M., Mucka, P., Kern, J.G., and Feng, H. (2018). The emerging role and targetability of the TCA cycle in cancer metabolism. Protein & Cell *9*, 216-237.

References

Anding, A.L., and Baehrecke, E.H. (2017). Cleaning House: Selective Autophagy of Organelles. Developmental cell *41*, 10-22.

Aranda, A., and Pascual, A. (2001). Nuclear Hormone Receptors and Gene Expression. Physiological Reviews *81*, 1269-1304.

Arsenovic, P.T., Maldonado, A.T., Colleluori, V.D., and Bloss, T.A. (2012). Depletion of the C. elegans NAC Engages the Unfolded Protein Response, Resulting in Increased Chaperone Expression and Apoptosis. PloS one *7*, e44038.

Avery, L. (1993). The genetics of feeding in Caenorhabditis elegans. Genetics *133*, 897-917.

Baker, B.M., Nargund, A.M., Sun, T., and Haynes, C.M. (2012). Protective coupling of mitochondrial function and protein synthesis via the eIF2alpha kinase GCN-2. PLoS genetics *8*, e1002760.

Bartlett, K., and Eaton, S. (2004). Mitochondrial β-oxidation. European Journal of Biochemistry *271*, 462-469.

Basso, V., Marchesan, E., Peggion, C., Chakraborty, J., von Stockum, S.*, et al.* (2018). Regulation of ER-mitochondria contacts by Parkin via Mfn2. Pharmacological Research *138*, 43-56.

Beck, R., Ravet, M., Wieland, F.T., and Cassel, D. (2009). The COPI system: Molecular mechanisms and function. FEBS Letters *583*, 2701-2709.

Becker, T., Böttinger, L., and Pfanner, N. (2012). Mitochondrial protein import: from transport pathways to an integrated network. Trends in biochemical sciences *37*, 85-91.

Becker, T., Pfannschmidt, S., Guiard, B., Stojanovski, D., Milenkovic, D.*, et al.* (2008). Biogenesis of the Mitochondrial TOM Complex: Mim1 promotes insertion and assembly of signal-anchored receptors. Journal of Biological Chemistry *283*, 120-127.

Benador, I.Y., Veliova, M., Mahdaviani, K., Petcherski, A., Wikstrom, J.D.*, et al.* (2018). Mitochondria Bound to Lipid Droplets Have Unique Bioenergetics, Composition, and Dynamics that Support Lipid Droplet Expansion. Cell metabolism *27*, 869-885.e866.

Benedetti, C., Haynes, C.M., Yang, Y., Harding, H.P., and Ron, D. (2006). Ubiquitin-like protein 5 positively regulates chaperone gene expression in the mitochondrial unfolded protein response. Genetics *174*, 229-239.

Bennett, C.F., Vander Wende, H., Simko, M., Klum, S., Barfield, S.*, et al.* (2014). Activation of the mitochondrial unfolded protein response does not predict longevity in *Caenorhabditis elegans*. Nature communications *5*, 3483.

References

Berendzen, K.M., Durieux, J., Shao, L.-W., Tian, Y., Kim, H.-e., *et al.* (2016). Neuroendocrine Coordination of Mitochondrial Stress Signaling and Proteostasis. Cell *166*, 1553-1563.e1510.

Berridge, M.J. (2009). Inositol trisphosphate and calcium signalling mechanisms. Biochimica et Biophysica Acta (BBA) - Molecular Cell Research *1793*, 933-940.

Bhujabal, Z., Birgisdottir, Å.B., Sjøttem, E., Brenne, H.B., Øvervatn, A., *et al.* (2017). FKBP8 recruits LC3A to mediate Parkin-independent mitophagy. EMBO reports *18*, 947-961.

Bleazard, W., McCaffery, J.M., King, E.J., Bale, S., Mozdy, A., *et al.* (1999). The dynamin-related GTPase Dnm1 regulates mitochondrial fission in yeast. Nature cell biology *1*, 298-304.

Bolotin, E., Liao, H., Ta, T.C., Yang, C., Hwang-Verslues, W., *et al.* (2010). Integrated approach for the identification of human hepatocyte nuclear factor 4α target genes using protein binding microarrays. Hepatology *51*, 642-653.

Boye, E., and Grallert, B. (2020). eIF2α phosphorylation and the regulation of translation. Current Genetics *66*, 293-297.

Brenner, S. (1974). The Genetics of *Caenorhabditis Elegans*. Genetics *77*, 71-94.

Budnik, A., and Stephens, D.J. (2009). ER exit sites – Localization and control of COPII vesicle formation. FEBS Letters *583*, 3796-3803.

Burgoyne, T., Patel, S., and Eden, E.R. (2015). Calcium signaling at ER membrane contact sites. Biochimica et Biophysica Acta (BBA) - Molecular Cell Research *1853*, 2012-2017.

Byrne, A.B., Weirauch, M.T., Wong, V., Koeva, M., Dixon, S.J., *et al.* (2007). A global analysis of genetic interactions in Caenorhabditis elegans. Journal of Biology *6*, 8.

Byrne, J.J., Soh, M.S., Chandhok, G., Vijayaraghavan, T., Teoh, J.-S., *et al.* (2019). Disruption of mitochondrial dynamics affects behaviour and lifespan in Caenorhabditis elegans. Cellular and Molecular Life Sciences *76*, 1967-1985.

Cao, Y.-L., Meng, S., Chen, Y., Feng, J.-X., Gu, D.-D., *et al.* (2017). MFN1 structures reveal nucleotide-triggered dimerization critical for mitochondrial fusion. Nature *542*, 372-376.

Chaban, Y., Boekema, E.J., and Dudkina, N.V. (2014). Structures of mitochondrial oxidative phosphorylation supercomplexes and mechanisms for their stabilisation. Biochimica et Biophysica Acta (BBA) - Bioenergetics *1837*, 418-426.

Chacinska, A., Koehler, C.M., Milenkovic, D., Lithgow, T., and Pfanner, N. (2009). Importing Mitochondrial Proteins: Machineries and Mechanisms. Cell *138*, 628-644.

References

Chacinska, A., Pfannschmidt, S., Wiedemann, N., Kozjak, V., Sanjuán Szklarz, L.K., *et al.* (2004). Essential role of Mia40 in import and assembly of mitochondrial intermembrane space proteins. The EMBO journal *23*, 3735-3746.

Chapin, H.C., Okada, M., Merz, A.J., and Miller, D.L. (2015). Tissue-specific autophagy responses to aging and stress in *C. elegans*. Aging (Albany NY) *7*, 419-434.

Chen, H., Chomyn, A., and Chan, D.C. (2005). Disruption of Fusion Results in Mitochondrial Heterogeneity and Dysfunction. Journal of Biological Chemistry *280*, 26185-26192.

Chen, H., Detmer, S.A., Ewald, A.J., Griffin, E.E., Fraser, S.E., *et al.* (2003). Mitofusins Mfn1 and Mfn2 coordinately regulate mitochondrial fusion and are essential for embryonic development. The Journal of cell biology *160*, 189-200.

Chen, L., Vasoya, R.P., Toke, N.H., Parthasarathy, A., Luo, S., *et al.* (2020). HNF4 Regulates Fatty Acid Oxidation and Is Required for Renewal of Intestinal Stem Cells in Mice. Gastroenterology *158*, 985-999.e989.

Chen, Y., Scarcelli, V., and Legouis, R. (2017). Approaches for Studying Autophagy in *Caenorhabditis elegans*. Cells *6*.

Christ, L., Raiborg, C., Wenzel, E.M., Campsteijn, C., and Stenmark, H. (2017). Cellular Functions and Molecular Mechanisms of the ESCRT Membrane-Scission Machinery. Trends in biochemical sciences *42*, 42-56.

Clandinin, T.R., DeModena, J.A., and Sternberg, P.W. (1998). Inositol Trisphosphate Mediates a RAS-Independent Response to LET-23 Receptor Tyrosine Kinase Activation in C. elegans. Cell *92*, 523-533.

Claros, M.G., and Vincens, P. (1996). Computational Method to Predict Mitochondrially Imported Proteins and their Targeting Sequences. European Journal of Biochemistry *241*, 779-786.

Consortium, T.*C.e.*S. (1998). Genome Sequence of the Nematode C. elegans: A Platform for Investigating Biology. Science (New York, NY) *282*, 2012-2018.

Consortium, T.U. (2018). UniProt: a worldwide hub of protein knowledge. Nucleic Acids Research *47*, D506-D515.

Cooper, J.F., Machiela, E., Dues, D.J., Spielbauer, K.K., Senchuk, M.M., *et al.* (2017). Activation of the mitochondrial unfolded protein response promotes longevity and dopamine neuron survival in Parkinson's disease models. Scientific Reports *7*, 16441.

Cosson, P., Marchetti, A., Ravazzola, M., and Orci, L. (2012). Mitofusin-2 Independent Juxtaposition of Endoplasmic Reticulum and Mitochondria: An Ultrastructural Study. PloS one *7*, e46293.

References

Creutz, C.E., Tomsig, J.L., Snyder, S.L., Gautier, M.C., Skouri, F.*, et al.* (1998). The copines, a novel class of C2 domain-containing, calcium-dependent, phospholipid-binding proteins conserved from Paramecium to humans. The Journal of biological chemistry *273*, 1393-1402.

Curran, S.P., Leuenberger, D., Oppliger, W., and Koehler, C.M. (2002). The Tim9p–Tim10p complex binds to the transmembrane domains of the ADP/ATP carrier. The EMBO journal *21*, 942-953.

Daugherty, M., Polanuyer, B., Farrell, M., Scholle, M., Lykidis, A.*, et al.* (2002). Complete Reconstitution of the Human Coenzyme A Biosynthetic Pathway via Comparative Genomics. Journal of Biological Chemistry *277*, 21431-21439.

de Brito, O.M., and Scorrano, L. (2008). Mitofusin 2 tethers endoplasmic reticulum to mitochondria. Nature *456*, 605.

Decrock, E., De Bock, M., Wang, N., Gadicherla, A.K., Bol, M.*, et al.* (2013). IP3, a small molecule with a powerful message. Biochimica et Biophysica Acta (BBA) - Molecular Cell Research *1833*, 1772-1786.

Dhe-Paganon, S., Duda, K., Iwamoto, M., Chi, Y.-I., and Shoelson, S.E. (2002). Crystal Structure of the HNF4α Ligand Binding Domain in Complex with Endogenous Fatty Acid Ligand. Journal of Biological Chemistry *277*, 37973-37976.

Di Fiore, P.P., and von Zastrow, M. (2014). Endocytosis, signaling, and beyond. Cold Spring Harbor perspectives in biology *6*, a016865.

Di Rita, A., Peschiaroli, A., D′Acunzo, P., Strobbe, D., Hu, Z.*, et al.* (2018). HUWE1 E3 ligase promotes PINK1/PARKIN-independent mitophagy by regulating AMBRA1 activation via IKKα. Nature communications *9*, 3755.

Dillin, A., Hsu, A.-L., Arantes-Oliveira, N., Lehrer-Graiwer, J., Hsin, H.*, et al.* (2002). Rates of Behavior and Aging Specified by Mitochondrial Function During Development. Science (New York, NY) *298*, 2398-2401.

Djeddi, A., Michelet, X., Culetto, E., Alberti, A., Barois, N.*, et al.* (2012). Induction of autophagy in ESCRT mutants is an adaptive response for cell survival in *C. elegans*. Journal of cell science, *125* 685-694.

Dougherty, E.C., Hansen, E.L., Nicholas, W.L., Mollett, J.A., and Yarwood, E.A. (1959). AXENIC CULTIVATION OF CAENORHABDITIS BRIGGSAE (NEMATODA: RHABDITIDAE) WITH UNSUPPLEMENTED AND SUPPLEMENTED CHEMICALLY DEFINED MEDIA*. Annals of the New York Academy of Sciences *77*, 176-217.

Duda, K., Chi, Y.-I., and Shoelson, S.E. (2004). Structural Basis for HNF-4α Activation by Ligand and Coactivator Binding. Journal of Biological Chemistry *279*, 23311-23316.

Durieux, J., Wolff, S., and Dillin, A. (2011). The cell-non-autonomous nature of electron transport chain-mediated longevity. Cell *144*, 79-91.

Duvezin-Caubet, S., Jagasia, R., Wagener, J., Hofmann, S., Trifunovic, A.*, et al.* (2006). Proteolytic Processing of OPA1 Links Mitochondrial Dysfunction to Alterations in Mitochondrial Morphology. Journal of Biological Chemistry *281*, 37972-37979.

Ehses, S., Raschke, I., Mancuso, G., Bernacchia, A., Geimer, S.*, et al.* (2009). Regulation of OPA1 processing and mitochondrial fusion by m-AAA protease isoenzymes and OMA1. Journal of Cell Biology *187*, 1023-1036.

Eisner, V., Lenaers, G., and Hajnóczky, G. (2014). Mitochondrial fusion is frequent in skeletal muscle and supports excitation–contraction coupling. Journal of Cell Biology *205*, 179-195.

Endres, M., Neupert, W., and Brunner, M. (1999). Transport of the ADP/ATP carrier of mitochondria from the TOM complex to the TIM22·54 complex. The EMBO journal *18*, 3214-3221.

Farhan, H., and Rabouille, C. (2011). Signalling to and from the secretory pathway. Journal of cell science *124*, 171-180.

Fatt, H.V., and Dougherty, E.C. (1963). Genetic Control of Differential Heat Tolerance in Two Strains of the Nematode Caenorhabditis elegans. Science (New York, NY) *141*, 266-267.

Feng, Y., He, D., Yao, Z., and Klionsky, D.J. (2014). The machinery of macroautophagy. Cell Res *24*, 24-41.

Filadi, R., Greotti, E., Turacchio, G., Luini, A., Pozzan, T.*, et al.* (2015). Mitofusin 2 ablation increases endoplasmic reticulum–mitochondria coupling. Proceedings of the National Academy of Sciences *112*, E2174-E2181.

Filadi, R., Greotti, E., Turacchio, G., Luini, A., Pozzan, T.*, et al.* (2016). Presenilin 2 Modulates Endoplasmic Reticulum-Mitochondria Coupling by Tuning the Antagonistic Effect of Mitofusin 2. Cell reports *15*, 2226-2238.

Filimonenko, M., Stuffers, S., Raiborg, C., Yamamoto, A., Malerod, L.*, et al.* (2007). Functional multivesicular bodies are required for autophagic clearance of protein aggregates associated with neurodegenerative disease. The Journal of cell biology *179*, 485-500.

Fire, A., Albertson, D., Harrison, S.W., and Moerman, D.G. (1991). Production of antisense RNA leads to effective and specific inhibition of gene expression in C. elegans muscle. Development *113*, 503-514.

Fire, A., Xu, S., Montgomery, M.K., Kostas, S.A., Driver, S.E.*, et al.* (1998). Potent and specific genetic interference by double-stranded RNA in Caenorhabditis elegans. Nature *391*, 806-811.

Fölsch, H., Gaume, B., Brunner, M., Neupert, W., and Stuart, R.A. (1998). C- to N-terminal translocation of preproteins into mitochondria. The EMBO journal *17*, 6508-6515.

Friedman, J.R., Lackner, L.L., West, M., DiBenedetto, J.R., Nunnari, J.*, et al.* (2011). ER Tubules Mark Sites of Mitochondrial Division. Science (New York, NY) *334*, 358-362.

Gabaldón, T., and Huynen, M.A. (2004). Shaping the mitochondrial proteome. Biochimica et Biophysica Acta (BBA) - Bioenergetics *1659*, 212-220.

Gao, K., Li, Y., Hu, S., and Liu, Y. (2019). SUMO peptidase ULP-4 regulates mitochondrial UPR-mediated innate immunity and lifespan extension. eLife *8*, e41792.

Gavin, K.A., Hidaka, M., and Stillman, B. (1995). Conserved initiator proteins in eukaryotes. Science (New York, NY) *270*, 1667-1671.

Griparic , L., Kanazawa , T., and van der Bliek , A.M. (2007). Regulation of the mitochondrial dynamin-like protein Opa1 by proteolytic cleavage. Journal of Cell Biology *178*, 757-764.

Guo, B., Huang, X., Zhang, P., Qi, L., Liang, Q.*, et al.* (2014). Genome-wide screen identifies signaling pathways that regulate autophagy during *Caenorhabditis elegans* development. EMBO reports *15*, 705-713.

Guo, S., and Kemphues, K.J. (1995). par-1, a gene required for establishing polarity in C. elegans embryos, encodes a putative Ser/Thr kinase that is asymmetrically distributed. Cell *81*, 611-620.

Haeussler, S., Köhler, F., Witting, M., Premm, M.F., Rolland, S.G.*, et al.* (2020). Autophagy compensates for defects in mitochondrial dynamics. PLoS genetics *16*, e1008638.

Hales, K.G., and Fuller, M.T. (1997). Developmentally regulated mitochondrial fusion mediated by a conserved, novel, predicted GTPase. Cell *90*, 121-129.

Hanna, R.A., Quinsay, M.N., Orogo, A.M., Giang, K., Rikka, S.*, et al.* (2012). Microtubule-associated Protein 1 Light Chain 3 (LC3) Interacts with Bnip3 Protein to Selectively Remove Endoplasmic Reticulum and Mitochondria via Autophagy. Journal of Biological Chemistry *287*, 19094-19104.

Harbauer, Angelika B., Zahedi, René P., Sickmann, A., Pfanner, N., and Meisinger, C. (2014). The Protein Import Machinery of Mitochondria—A Regulatory Hub in Metabolism, Stress, and Disease. Cell metabolism *19*, 357-372.

Harris, T.W., Arnaboldi, V., Cain, S., Chan, J., Chen, W.J.*, et al.* (2019). WormBase: a modern Model Organism Information Resource. Nucleic Acids Research *48*, D762-D767.

Harrison, M.M., Ceol, C.J., Lu, X., and Horvitz, H.R. (2006). Some *C. elegans* class B synthetic multivulva proteins encode a conserved LIN-35 Rb-containing complex distinct from a NuRD-like complex. Proceedings of the National Academy of Sciences *103*, 16782-16787.

Hawlitschek, G., Schneider, H., Schmidt, B., Tropschug, M., Hartl, F.-U.*, et al.* (1988). Mitochondrial protein import: Identification of processing peptidase and of PEP, a processing enhancing protein. Cell *53*, 795-806.

Haynes, C.M., Petrova, K., Benedetti, C., Yang, Y., and Ron, D. (2007). ClpP mediates activation of a mitochondrial unfolded protein response in *C. elegans*. Developmental cell *13*, 467-480.

Haynes, C.M., Yang, Y., Blais, S.P., Neubert, T.A., and Ron, D. (2010). The matrix peptide exporter HAF-1 signals a mitochondrial UPR by activating the transcription factor ZC376.7 in *C. elegans*. Molecular cell *37*, 529-540.

Head, B., Griparic, L., Amiri, M., Gandre-Babbe, S., and van der Bliek, A.M. (2009). Inducible proteolytic inactivation of OPA1 mediated by the OMA1 protease in mammalian cells. Journal of Cell Biology *187*, 959-966.

Head, B.P., Zulaika, M., Ryazantsev, S., and van der Bliek, A.M. (2011). A novel mitochondrial outer membrane protein, MOMA-1, that affects cristae morphology in Caenorhabditis elegans. Molecular Biology of the Cell *22*, 831-841.

Hell, K., Neupert, W., and Stuart, R.A. (2001). Oxa1p acts as a general membrane insertion machinery for proteins encoded by mitochondrial DNA. The EMBO journal *20*, 1281-1288.

Herlan, M., Bornhövd, C., Hell, K., Neupert, W., and Reichert, A.S. (2004). Alternative topogenesis of Mgm1 and mitochondrial morphology depend on ATP and a functional import motor. Journal of Cell Biology *165*, 167-173.

Herlan, M., Vogel, F., Bornhövd, C., Neupert, W., and Reichert, A.S. (2003). Processing of Mgm1 by the Rhomboid-type Protease Pcp1 Is Required for Maintenance of Mitochondrial Morphology and of Mitochondrial DNA. Journal of Biological Chemistry *278*, 27781-27788.

Hermann, G.J., Thatcher, J.W., Mills, J.P., Hales, K.G., Fuller, M.T.*, et al.* (1998). Mitochondrial Fusion in Yeast Requires the Transmembrane GTPase Fzo1p. Journal of Cell Biology *143*, 359-373.

Hertz, R., Magenheim, J., Berman, I., and Bar-Tana, J. (1998). Fatty acyl-CoA thioesters are ligands of hepatic nuclear factor-4α. Nature *392*, 512-516.

Hillier, L.W., Coulson, A., Murray, J.I., Bao, Z., Sulston, J.E.*, et al.* (2005). Genomics in *C. elegans*: So many genes, such a little worm. Genome Research *15*, 1651-1660.

Honjoh, S., Yamamoto, T., Uno, M., and Nishida, E. (2008). Signalling through RHEB-1 mediates intermittent fasting-induced longevity in *C. elegans*. Nature *457*, 726.

Houtkooper, R.H., Mouchiroud, L., Ryu, D., Moullan, N., Katsyuba, E.*, et al.* (2013). Mitonuclear protein imbalance as a conserved longevity mechanism. Nature *497*, 451-457.

Hu, Q., D'Amora, D.R., MacNeil, L.T., Walhout, A.J.M., and Kubiseski, T.J. (2017). The Oxidative Stress Response in *Caenorhabditis elegans* Requires the GATA Transcription Factor ELT-3 and SKN-1/Nrf2. Genetics *206*, 1909.

Hulett, J.M., Lueder, F., Chan, N.C., Perry, A.J., Wolynec, P.*, et al.* (2008). The Transmembrane Segment of Tom20 Is Recognized by Mim1 for Docking to the Mitochondrial TOM Complex. Journal of Molecular Biology *376*, 694-704.

Hunt, S.E., McLaren, W., Gil, L., Thormann, A., Schuilenburg, H.*, et al.* (2018). Ensembl variation resources. Database *2018*.

Ichishita, R., Tanaka, K., Sugiura, Y., Sayano, T., Mihara, K.*, et al.* (2008). An RNAi Screen for Mitochondrial Proteins Required to Maintain the Morphology of the Organelle in Caenorhabditis elegans. The Journal of Biochemistry *143*, 449-454.

Ingerman, E., Perkins, E.M., Marino, M., Mears, J.A., McCaffery, J.M.*, et al.* (2005). Dnm1 forms spirals that are structurally tailored to fit mitochondria. The Journal of cell biology *170*, 1021-1027.

Inoue, H., Hisamoto, N., An, J.H., Oliveira, R.P., Nishida, E.*, et al.* (2005). The C. elegans p38 MAPK pathway regulates nuclear localization of the transcription factor SKN-1 in oxidative stress response. Genes & Development *19*, 2278-2283.

International Human Genome Sequencing, C. (2004). Finishing the euchromatic sequence of the human genome. Nature *431*, 931-945.

Ishihara, H., Shibasaki, Y., Kizuki, N., Katagiri, H., Yazaki, Y.*, et al.* (1996). Cloning of cDNAs Encoding Two Isoforms of 68-kDa Type I Phosphatidylinositol4-phosphate 5-Kinase. Journal of Biological Chemistry *271*, 23611-23614.

Ishihara, N., Fujita, Y., Oka, T., and Mihara, K. (2006). Regulation of mitochondrial morphology through proteolytic cleavage of OPA1. The EMBO journal *25*, 2966-2977.

Izumi, K., Brett, M., Nishi, E., Drunat, S., Tan, E.-S.*, et al.* (2016). ARCN1 Mutations Cause a Recognizable Craniofacial Syndrome Due to COPI-Mediated Transport Defects. Am J Hum Genet *99*, 451-459.

Jenzer, C., Simionato, E., and Legouis, R. (2015). Tools and methods to analyze autophagy in *C. elegans*. Methods (San Diego, Calif) *75*, 162-171.

Ji, W.-K., Chakrabarti, R., Fan, X., Schoenfeld, L., Strack, S., *et al.* (2017). Receptor-mediated Drp1 oligomerization on endoplasmic reticulum. Journal of Cell Biology *216*, 4123-4139.

Ji, W.-k., Hatch, A.L., Merrill, R.A., Strack, S., and Higgs, H.N. (2015). Actin filaments target the oligomeric maturation of the dynamin GTPase Drp1 to mitochondrial fission sites. eLife *4*, e11553.

Jiang, H.-C., Hsu, J.-M., Yen, C.-P., Chao, C.-C., Chen, R.-H., *et al.* (2015). Neural activity and CaMKII protect mitochondria from fragmentation in aging *Caenorhabditis elegans* neurons. Proceedings of the National Academy of Sciences *112*, 8768-8773.

Jing, K., and Lim, K. (2012). Why is autophagy important in human diseases? Exp Mol Med *44*, 69-72.

Johnson, D., and Nehrke, K. (2010). Mitochondrial Fragmentation Leads to Intracellular Acidification in Caenorhabditis elegans and Mammalian Cells. Molecular Biology of the Cell *21*, 2191-2201.

Jores, T., Klinger, A., Groß, L.E., Kawano, S., Flinner, N., *et al.* (2016). Characterization of the targeting signal in mitochondrial β-barrel proteins. Nature communications *7*, 12036.

Jovaisaite, V., Mouchiroud, L., and Auwerx, J. (2014). The mitochondrial unfolded protein response, a conserved stress response pathway with implications in health and disease. The Journal of Experimental Biology *217*, 137-143.

Kamath, R.S., and Ahringer, J. (2003). Genome-wide RNAi screening in *Caenorhabditis elegans*. Methods (San Diego, Calif) *30*, 313-321.

Kamath, R.S., Martinez-Campos, M., Zipperlen, P., Fraser, A.G., and Ahringer, J. (2000). Effectiveness of specific RNA-mediated interference through ingested double-stranded RNA in Caenorhabditis elegans. Genome Biol *2*.

Kanazawa, T., Zappaterra, M.D., Hasegawa, A., Wright, A.P., Newman-Smith, E.D., *et al.* (2008). The *C. elegans* Opa1 Homologue EAT-3 Is Essential for Resistance to Free Radicals. PLoS genetics *4*, e1000022.

Kang, P.-J., Ostermann, J., Shilling, J., Neupert, W., Craig, E.A., *et al.* (1990). Requirement for hsp70 in the mitochondrial matrix for translocation and folding of precursor proteins. Nature *348*, 137-

Kania, E., Roest, G., Vervliet, T., Parys, J.B., and Bultynck, G. (2017). IP3 Receptor-Mediated Calcium Signaling and Its Role in Autophagy in Cancer. Frontiers in Oncology *7*.

Kariya, K.-i., Kim Bui, Y., Gao, X., Sternberg, P.W., and Kataoka, T. (2004). Phospholipase Cε regulates ovulation in Caenorhabditis elegans. Developmental Biology *274*, 201-210.

Kim, K.H., and Lee, M.-S. (2014). Autophagy—a key player in cellular and body metabolism.

Nature Reviews Endocrinology *10*, 322.

Kim, S., and Sieburth, D. (2018). Sphingosine Kinase Activates the Mitochondrial Unfolded Protein Response and Is Targeted to Mitochondria by Stress. Cell reports *24*, 2932-2945.e2934.

Kim, S., and Sieburth, D. (2020). FSHR-1/GPCR Regulates the Mitochondrial Unfolded Protein Response in *Caenorhabditis elegans*. Genetics *214*, 409-418.

Kim, W., Underwood, R.S., Greenwald, I., and Shaye, D.D. (2018). OrthoList 2: A New Comparative Genomic Analysis of Human and *Caenorhabditis elegans* Genes. Genetics *210*, 445-461.

Kirstein-Miles, J., Scior, A., Deuerling, E., and Morimoto, R.I. (2013). The nascent polypeptide-associated complex is a key regulator of proteostasis. The EMBO journal *32*, 1451-1468.

Klein, A., Israel, L., Lackey, S.W.K., Nargang, F.E., Imhof, A.*, et al.* (2012). Characterization of the insertase for β-barrel proteins of the outer mitochondrial membrane. Journal of Cell Biology *199*, 599-611.

Klionsky, D.J., Abdelmohsen, K., Abe, A., Abedin, M.J., Abeliovich, H.*, et al.* (2016). Guidelines for the use and interpretation of assays for monitoring autophagy (3rd edition). Autophagy *12*, 1-222.

Korobova, F., Gauvin, Timothy J., and Higgs, Henry N. (2014). A Role for Myosin II in Mammalian Mitochondrial Fission. Current Biology *24*, 409-414.

Korobova, F., Ramabhadran, V., and Higgs, H.N. (2013). An Actin-Dependent Step in Mitochondrial Fission Mediated by the ER-Associated Formin INF2. Science (New York, NY) *339*, 464-467.

Koshiba, T., Detmer, S.A., Kaiser, J.T., Chen, H., McCaffery, J.M.*, et al.* (2004). Structural Basis of Mitochondrial Tethering by Mitofusin Complexes. Science (New York, NY) *305*, 858.

Kovacevic, I., Orozco, J.M., and Cram, E.J. (2013). Filamin and Phospholipase C-ε Are Required for Calcium Signaling in the Caenorhabditis elegans Spermatheca. PLoS genetics *9*, e1003510.

Koyano, F., Okatsu, K., Kosako, H., Tamura, Y., Go, E.*, et al.* (2014). Ubiquitin is phosphorylated by PINK1 to activate parkin. Nature *510*, 162-166.

Kreshuk, A., and Zhang, C. (2019). Machine Learning: Advanced Image Segmentation Using ilastik. In Computer Optimized Microscopy: Methods and Protocols, E. Rebollo, and M. Bosch, eds. (New York, NY: Springer New York), pp. 449-463.

Kriventseva, E.V., Kuznetsov, D., Tegenfeldt, F., Manni, M., Dias, R.*, et al.* (2018). OrthoDB v10: sampling the diversity of animal, plant, fungal, protist, bacterial and viral genomes for evolutionary and functional annotations of orthologs. Nucleic Acids Research *47*, D807-D811.

Kurokawa, K., and Nakano, A. (2018). The ER exit sites are specialized ER zones for the transport of cargo proteins from the ER to the Golgi apparatus. The Journal of Biochemistry *165*, 109-114.

Labrousse, A.M., Zappaterra, M.D., Rube, D.A., and van der Bliek, A.M. (1999). *C. elegans* Dynamin-Related Protein DRP-1 Controls Severing of the Mitochondrial Outer Membrane. Molecular cell *4*, 815-826.

Lazarou, M., Sliter, D.A., Kane, L.A., Sarraf, S.A., Wang, C.*, et al.* (2015). The ubiquitin kinase PINK1 recruits autophagy receptors to induce mitophagy. Nature *524*, 309-314.

Leal, N.S., Schreiner, B., Pinho, C.M., Filadi, R., Wiehager, B.*, et al.* (2016). Mitofusin-2 knockdown increases ER–mitochondria contact and decreases amyloid β-peptide production. Journal of Cellular and Molecular Medicine *20*, 1686-1695.

Lee, J.A., Beigneux, A., Ahmad, S.T., Young, S.G., and Gao, F.B. (2007). ESCRT-III dysfunction causes autophagosome accumulation and neurodegeneration. Curr Biol *17*, 1561-1567.

Lee, M.C.S., Miller, E.A., Goldberg, J., Orci, L., and Schekman, R. (2004). Bi-directional protein transport between the ER and Golgi. Annual Review of Cell and Developmental Biology *20*, 87-123.

Lefebvre, C., Legouis, R., and Culetto, E. (2018). ESCRT and autophagies: Endosomal functions and beyond. Semin Cell Dev Biol *74*, 21-28.

Letts, J.A., and Sazanov, L.A. (2017). Clarifying the supercomplex: the higher-order organization of the mitochondrial electron transport chain. Nature structural & molecular biology *24*, 800-808.

Levine, B., and Klionsky, D.J. (2004). Development by Self-Digestion. Developmental cell *6*, 463-477.

Li, S., Xu, S., Roelofs, B.A., Boyman, L., Lederer, W.J.*, et al.* (2014). Transient assembly of F-actin on the outer mitochondrial membrane contributes to mitochondrial fission. Journal of Cell Biology *208*, 109-123.

Lichtsteiner, S., and Tjian, R. (1993). Cloning and properties of the Caenorhabditis elegans TATA-box-binding protein. Proceedings of the National Academy of Sciences *90*, 9673-9677.

Lim, Y., Rubio-Peña, K., Sobraske, P.J., Molina, P.A., Brookes, P.S.*, et al.* (2019). Fndc-1 contributes to paternal mitochondria elimination in C. elegans. Developmental Biology *454*, 15-20.

Lin, Y.-F., and Haynes, C.M. (2016). Metabolism and the UPR^{mt}. Molecular cell *61*, 677-682.

Liu, L., Feng, D., Chen, G., Chen, M., Zheng, Q.*, et al.* (2012). Mitochondrial outer-membrane protein FUNDC1 mediates hypoxia-induced mitophagy in mammalian cells. Nature cell biology *14*, 177-185.

Liu, Y., Samuel, B.S., Breen, P.C., and Ruvkun, G. (2014). *Caenorhabditis elegans* pathways that surveil and defend mitochondria. Nature *508*, 406-410.

Loijens, J.C., and Anderson, R.A. (1996). Type I Phosphatidylinositol-4-phosphate 5-Kinases Are Distinct Members of This Novel Lipid Kinase Family. Journal of Biological Chemistry *271*, 32937-32943.

Luz, A.L., Rooney, J.P., Kubik, L.L., Gonzalez, C.P., Song, D.H., *et al.* (2015). Mitochondrial Morphology and Fundamental Parameters of the Mitochondrial Respiratory Chain Are Altered in Caenorhabditis elegans Strains Deficient in Mitochondrial Dynamics and Homeostasis Processes. PloS one *10*, e0130940.

Machiela, E., Liontis, T., Dues, D.J., Rudich, P.D., Traa, A., *et al.* (2020). Disruption of mitochondrial dynamics increases stress resistance through activation of multiple stress response pathways. The FASEB Journal *34*, 8475-8492.

Manor, U., Bartholomew, S., Golani, G., Christenson, E., Kozlov, M., *et al.* (2015). A mitochondria-anchored isoform of the actin-nucleating spire protein regulates mitochondrial division. eLife *4*, e08828.

Marchi, S., Patergnani, S., and Pinton, P. (2014). The endoplasmic reticulum–mitochondria connection: One touch, multiple functions. Biochimica et Biophysica Acta (BBA) - Bioenergetics *1837*, 461-469.

Martin, J., Mahlke, K., and Pfanner, N. (1991). Role of an energized inner membrane in mitochondrial protein import. Delta psi drives the movement of presequences. Journal of Biological Chemistry *266*, 18051-18057.

Martínez-Reyes, I., and Chandel, N.S. (2020). Mitochondrial TCA cycle metabolites control physiology and disease. Nature communications *11*, 102.

Martinus, R.D., Garth, G.P., Webster, T.L., Cartwright, P., Naylor, D.J., *et al.* (1996). Selective Induction of Mitochondrial Chaperones in Response to Loss of the Mitochondrial Genome. European Journal of Biochemistry *240*, 98-103.

Matsuda, N., Sato, S., Shiba, K., Okatsu, K., Saisho, K., *et al.* (2010). PINK1 stabilized by mitochondrial depolarization recruits Parkin to damaged mitochondria and activates latent Parkin for mitophagy. Journal of Cell Biology *189*, 211-221.

Mattie, S., Riemer, J., Wideman, J.G., and McBride, H.M. (2017). A new mitofusin topology places the redox-regulated C terminus in the mitochondrial intermembrane space. Journal of Cell Biology *217*, 507-515.

Maupas, É. (1899). La mue et l'enkystement chez les nématodes. Arch Zool Exp Gen *7*, 563-628.

Maupas, É. (1900). Modes et formes de reprodution des nematodes. Archives de Zoologie Experimentale et Generale *8*, 463-624.

McBride, H.M., Neuspiel, M., and Wasiak, S. (2006). Mitochondria: More Than Just a Powerhouse. Current Biology *16*, R551-R560.

McGarry, J.D., and Brown, N.F. (1997). The Mitochondrial Carnitine Palmitoyltransferase System — From Concept to Molecular Analysis. European Journal of Biochemistry *244*, 1-14.

McMiller, T.L., Sims, D., Lee, T., Williams, T., and Johnson, C.M. (2007). Molecular characterization of the Caenorhabditis elegans REF-1 family member, hlh-29/hlh-28. Biochimica et Biophysica Acta (BBA) - Gene Structure and Expression *1769*, 5-19.

McQuibban, G.A., Saurya, S., and Freeman, M. (2003). Mitochondrial membrane remodelling regulated by a conserved rhomboid protease. Nature *423*, 537-541.

Meeusen, S., DeVay, R., Block, J., Cassidy-Stone, A., Wayson, S.*, et al.* (2006). Mitochondrial Inner-Membrane Fusion and Crista Maintenance Requires the Dynamin-Related GTPase Mgm1. Cell *127*, 383-395.

Meeusen, S., McCaffery, J.M., and Nunnari, J. (2004). Mitochondrial Fusion Intermediates Revealed in Vitro. Science (New York, NY) *305*, 1747-1752.

Merkwirth, C., Jovaisaite, V., Durieux, J., Matilainen, O., Jordan, Sabine D.*, et al.* (2016). Two Conserved Histone Demethylases Regulate Mitochondrial Stress-Induced Longevity. Cell *165*, 1209-1223.

Mesecke, N., Terziyska, N., Kozany, C., Baumann, F., Neupert, W.*, et al.* (2005). A Disulfide Relay System in the Intermembrane Space of Mitochondria that Mediates Protein Import. Cell *121*, 1059-1069.

Michelet, X., Djeddi, A., and Legouis, R. (2010). Developmental and cellular functions of the ESCRT machinery in pluricellular organisms. Biology of the Cell *102*, 191-202.

Michelet, X., and Legouis, R. (2012). Autophagy in endosomal mutants: Desperately seeking to survive. Worm *1*, 216-220.

Mizushima, N. (2007). Autophagy: process and function. Genes Dev *21*, 2861-2873.

Mizushima, N., Yoshimori, T., and Levine, B. (2010). Methods in Mammalian Autophagy Research. Cell *140*, 313-326.

Mokranjac, D., and Neupert, W. (2015). Architecture of a protein entry gate. Nature *528*, 201-202.

Mouysset, J., Kähler, C., and Hoppe, T. (2006). A conserved role of *Caenorhabditis elegans* CDC-48 in ER-associated protein degradation. Journal of Structural Biology *156*, 41-49.

Muthye, V., and Lavrov, D.V. (2020). Causes and consequences of mitochondrial proteome size variation in animals. Mitochondrion *52*, 100-107.

Nakada, K., Inoue, K., Ono, T., Isobe, K., Ogura, A.*, et al.* (2001). Inter-mitochondrial complementation: Mitochondria-specific system preventing mice from expression of disease phenotypes by mutant mtDNA. Nature Medicine *7*, 934-940.

Nakatsu, F., Baskin, J.M., Chung, J., Tanner, L.B., Shui, G.*, et al.* (2012). PtdIns4P synthesis by PI4KIIIα at the plasma membrane and its impact on plasma membrane identity. The Journal of cell biology *199*, 1003-1016.

Naon, D., Zaninello, M., Giacomello, M., Varanita, T., Grespi, F.*, et al.* (2016). Critical reappraisal confirms that Mitofusin 2 is an endoplasmic reticulum–mitochondria tether. Proceedings of the National Academy of Sciences *113*, 11249-11254.

Narendra , D., Tanaka , A., Suen , D.-F., and Youle , R.J. (2008). Parkin is recruited selectively to impaired mitochondria and promotes their autophagy. Journal of Cell Biology *183*, 795-803.

Narendra, D.P., Jin, S.M., Tanaka, A., Suen, D.-F., Gautier, C.A.*, et al.* (2010). PINK1 Is Selectively Stabilized on Impaired Mitochondria to Activate Parkin. PLOS Biology *8*, e1000298.

Nargund, Amrita M., Fiorese, Christopher J., Pellegrino, Mark W., Deng, P., and Haynes, Cole M. (2015). Mitochondrial and Nuclear Accumulation of the Transcription Factor ATFS-1 Promotes OXPHOS Recovery during the UPRmt. Molecular cell *58*, 123-133.

Nargund, A.M., Pellegrino, M.W., Fiorese, C.J., Baker, B.M., and Haynes, C.M. (2012). Mitochondrial Import Efficiency of ATFS-1 Regulates Mitochondrial UPR Activation. Science (New York, NY) *337*, 587-590.

Neupert, W., and Herrmann, J.M. (2007). Translocation of Proteins into Mitochondria. Annual review of biochemistry *76*, 723-749.

Nigon, V., and Dougherty, E.C. (1949). Reproductive patterns and attempts at reciprocal crossing of Rhabditis elegans maupas, 1900, and Rhabditis briggsae Dougherty and nigon, 1949 (Nematoda: Rhabditidae). Journal of Experimental Zoology *112*, 485-503.

Nigon, V.M. (1943). Le déterminisme du sexe chez un nématode libre hermaphrodite (Rhabditis elegans Maupas). C R Soc Biol *137*, 40-41.

Novak, I., Kirkin, V., McEwan, D.G., Zhang, J., Wild, P.*, et al.* (2010). Nix is a selective autophagy receptor for mitochondrial clearance. EMBO reports *11*, 45-51.

Nsiah-Sefaa, A., and McKenzie, M. (2016). Combined defects in oxidative phosphorylation and fatty acid β-oxidation in mitochondrial disease. Bioscience Reports *36*.

Ohta, S., Tatsumi, Y., Fujita, M., Tsurimoto, T., and Obuse, C. (2003). The ORC1 cycle in human cells: II. Dynamic changes in the human ORC complex during the cell cycle. The Journal of biological chemistry *278*, 41535-41540.

Oks, O., Lewin, S., Goncalves, I.L., and Sapir, A. (2018). The UPR^{mt} Protects *Caenorhabditis elegans* from Mitochondrial Dysfunction by Upregulating Specific Enzymes of the Mevalonate Pathway. Genetics *209*, 457-473.

Olichon, A., Emorine, L.J., Descoins, E., Pelloquin, L., Brichese, L.*, et al.* (2002). The human dynamin-related protein OPA1 is anchored to the mitochondrial inner membrane facing the inter-membrane space. FEBS Letters *523*, 171-176.

Ono, T., Isobe, K., Nakada, K., and Hayashi, J.-I. (2001). Human cells are protected from mitochondrial dysfunction by complementation of DNA products in fused mitochondria. Nature Genetics *28*, 272-275.

Otsuga, D., Keegan, B.R., Brisch, E., Thatcher, J.W., Hermann, G.J.*, et al.* (1998). The Dynamin-related GTPase, Dnm1p, Controls Mitochondrial Morphology in Yeast. Journal of Cell Biology *143*, 333-349.

Palanker, L., Tennessen, J.M., Lam, G., and Thummel, C.S. (2009). Drosophila HNF4 Regulates Lipid Mobilization and β-Oxidation. Cell metabolism *9*, 228-239.

Palikaras, K., Lionaki, E., and Tavernarakis, N. (2015). Coordination of mitophagy and mitochondrial biogenesis during ageing in *C. elegans*. Nature.

Palmisano, N.J., and Meléndez, A. (2016). Detection of Autophagy in Caenorhabditis elegans Using GFP::LGG-1 as an Autophagy Marker. Cold Spring Harbor Protocols *2016*, pdb.prot086496.

Palmisano, N.J., and Meléndez, A. (2019). Autophagy in C. elegans development. Developmental Biology *447*, 103-125.

Paschen, S.A., Waizenegger, T., Stan, T., Preuss, M., Cyrklaff, M.*, et al.* (2003). Evolutionary conservation of biogenesis of β-barrel membrane proteins. Nature *426*, 862-866.

Pellegrino, M.W., Nargund, A.M., and Haynes, C.M. (2013). Signaling the mitochondrial unfolded protein response. Biochimica et Biophysica Acta (BBA) - Molecular Cell Research *1833*, 410-416.

Popov-Čeleketić, J., Waizenegger, T., and Rapaport, D. (2008). Mim1 Functions in an Oligomeric Form to Facilitate the Integration of Tom20 into the Mitochondrial Outer Membrane. Journal of Molecular Biology *376*, 671-680.

Putker, M., Madl, T., Vos, Harmjan R., de Ruiter, H., Visscher, M.*, et al.* (2013). Redox-Dependent Control of FOXO/DAF-16 by Transportin-1. Molecular cell *49*, 730-742.

Qi, Y., Yan, L., Yu, C., Guo, X., Zhou, X., *et al.* (2016). Structures of human mitofusin 1 provide insight into mitochondrial tethering. Journal of Cell Biology *215*, 621-629.

Quach, T.K., Chou, H.T., Wang, K., Milledge, G.Z., and Johnson, C.M. (2013). Genome-Wide Microarrray Analysis Reveals Roles for the REF-1 Family Member HLH-29 in Ferritin Synthesis and Peroxide Stress Response. PloS one *8*, e59719.

Rabinowitz, J.D., and White, E. (2010). Autophagy and Metabolism. Science (New York, NY) *330*, 1344-1348.

Rambold, Angelika S., Cohen, S., and Lippincott-Schwartz, J. (2015). Fatty Acid Trafficking in Starved Cells: Regulation by Lipid Droplet Lipolysis, Autophagy, and Mitochondrial Fusion Dynamics. Developmental cell *32*, 678-692.

Ramsey, C.S., Yeung, F., Stoddard, P.B., Li, D., Creutz, C.E., *et al.* (2008). Copine-I represses NF-kappaB transcription by endoproteolysis of p65. Oncogene *27*, 3516-3526.

Ranji, P., Rauthan, M., Pitot, C., and Pilon, M. (2014). Loss of HMG-CoA Reductase in C. elegans Causes Defects in Protein Prenylation and Muscle Mitochondria. PloS one *9*, e100033.

Rapaport, D., Brunner, M., Neupert, W., and Westermann, B. (1998). Fzo1p Is a Mitochondrial Outer Membrane Protein Essential for the Biogenesis of Functional Mitochondria in Saccharomyces cerevisiae. Journal of Biological Chemistry *273*, 20150-20155.

Raturi, A., and Simmen, T. (2013). Where the endoplasmic reticulum and the mitochondrion tie the knot: The mitochondria-associated membrane (MAM). Biochimica et Biophysica Acta (BBA) - Molecular Cell Researc *1833*, 213-224.

Rea, S.L., Ventura, N., and Johnson, T.E. (2007). Relationship Between Mitochondrial Electron Transport Chain Dysfunction, Development, and Life Extension in Caenorhabditis elegans. PLOS Biology *5*, e259.

Regmi, S.G., Rolland, S.G., and Conradt, B. (2014). Age-dependent changes in mitochondrial morphology and volume are not predictors of lifespan. Aging *6*, 118-130.

Rehling, P., Model, K., Brandner, K., Kovermann, P., Sickmann, A., *et al.* (2003). Protein Insertion into the Mitochondrial Inner Membrane by a Twin-Pore Translocase. Science (New York, NY) *299*, 1747.

Rissler, M., Wiedemann, N., Pfannschmidt, S., Gabriel, K., Guiard, B., *et al.* (2005). The Essential Mitochondrial Protein Erv1 Cooperates with Mia40 in Biogenesis of Intermembrane Space Proteins. Journal of Molecular Biology *353*, 485-492.

Roise, D., Horvath, S.J., Tomich, J.M., Richards, J.H., and Schatz, G. (1986). A chemically synthesized pre-sequence of an imported mitochondrial protein can form an amphiphilic helix and perturb natural and artificial phospholipid bilayers. The EMBO journal *5*, 1327-1334.

Rojo, M., Legros, F., Chateau, D., and Lombès, A. (2002). Membrane topology and mitochondrial targeting of mitofusins, ubiquitous mammalian homologs of the transmembrane GTPase Fzo. Journal of cell science *115*, 1663-1674.

Rolland, S.G., Motori, E., Memar, N., Hench, J., Frank, S.*, et al.* (2013). Impaired complex IV activity in response to loss of LRPPRC function can be compensated by mitochondrial hyperfusion. Proceedings of the National Academy of Sciences of the United States of America *110*, E2967-2976.

Rolland, S.G., Schneid, S., Schwarz, M., Rackles, E., Fischer, C.*, et al.* (2019). Compromised Mitochondrial Protein Import Acts as a Signal for UPR^{mt}. Cell reports *28*, 1659-1669.e1655.

Rual, J.-F., Ceron, J., Koreth, J., Hao, T., Nicot, A.-S.*, et al.* (2004). Toward Improving Caenorhabditis elegans Phenome Mapping With an ORFeome-Based RNAi Library. Genome Research *14*, 2162-2168.

Runkel, E.D., Liu, S., Baumeister, R., and Schulze, E. (2013). Surveillance-activated defenses block the ROS-induced mitochondrial unfolded protein response. PLoS genetics *9*, e1003346.

Rusten, T.E., Vaccari, T., Lindmo, K., Rodahl, L.M., Nezis, I.P.*, et al.* (2007). ESCRTs and *Fab1* regulate distinct steps of autophagy. Curr Biol *17*, 1817-1825.

Saito, T., Kuma, A., Sugiura, Y., Ichimura, Y., Obata, M.*, et al.* (2019). Autophagy regulates lipid metabolism through selective turnover of NCoR1. Nature communications *10*, 1567.

Santel, A., Frank, S., Gaume, B., Herrler, M., Youle, R.J.*, et al.* (2003). Mitofusin-1 protein is a generally expressed mediator of mitochondrial fusion in mammalian cells. Journal of cell science *116*, 2763-2774.

Santel, A., and Fuller, M.T. (2001). Control of mitochondrial morphology by a human mitofusin. Journal of cell science *114*, 867-874.

Seo, A.Y., Lau, P.-W., Feliciano, D., Sengupta, P., Gros, M.A.L.*, et al.* (2017). AMPK and vacuole-associated Atg14p orchestrate μ-lipophagy for energy production and long-term survival under glucose starvation. eLife *6*, e21690.

Sesaki, H., Southard, S.M., Yaffe, M.P., and Jensen, R.E. (2003). Mgm1p, a Dynamin-related GTPase, Is Essential for Fusion of the Mitochondrial Outer Membrane. Molecular Biology of the Cell *14*, 2342-2356.

Shao, L.-W., Niu, R., and Liu, Y. (2016). Neuropeptide signals cell non-autonomous mitochondrial unfolded protein response. Cell Research *26*, 1182-1196.

Shaye, D.D., and Greenwald, I. (2011). OrthoList: A Compendium of C. elegans Genes with Human Orthologs. PloS one *6*, e20085.

Sheaffer, K.L., Updike, D.L., and Mango, S.E. (2008). The Target of Rapamycin pathway antagonizes *pha-4/FoxA* to control development and aging. Curr Biol *18*, 1355-1364.

Shepard, K.A., and Yaffe, M.P. (1999). The Yeast Dynamin-like Protein, Mgm1p, Functions on the Mitochondrial Outer Membrane to Mediate Mitochondrial Inheritance. Journal of Cell Biology *144*, 711-720.

Signes, A., and Fernandez-Vizarra, E. (2018). Assembly of mammalian oxidative phosphorylation complexes I–V and supercomplexes. Essays in Biochemistry *62*, 255-270.

Simmer, F., Moorman, C., van der Linden, A.M., Kuijk, E., van den Berghe, P.V.E.*, et al.* (2003). Genome-Wide RNAi of C. elegans Using the Hypersensitive rrf-3 Strain Reveals Novel Gene Functions. PLOS Biology *1*, e12.

Singh, R., Kaushik, S., Wang, Y., Xiang, Y., Novak, I.*, et al.* (2009). Autophagy regulates lipid metabolism. Nature *458*, 1131.

Smirnova, E., Shurland, D.-L., Ryazantsev, S.N., and van der Bliek, A.M. (1998). A Human Dynamin-related Protein Controls the Distribution of Mitochondria. Journal of Cell Biology *143*, 351-358.

Smith, A.C., and Robinson, A.J. (2015). MitoMiner v3.1, an update on the mitochondrial proteomics database. Nucleic Acids Research *44*, D1258-D1261.

Song , Z., Chen , H., Fiket , M., Alexander , C., and Chan , D.C. (2007). OPA1 processing controls mitochondrial fusion and is regulated by mRNA splicing, membrane potential, and Yme1L. Journal of Cell Biology *178*, 749-755.

Sopta, M., Burton, Z.F., and Greenblatt, J. (1989). Structure and associated DNA-helicase activity of a general transcription initiation factor that binds to RNA polymerase II. Nature *341*, 410-414.

Sorkin, A., and von Zastrow, M. (2009). Endocytosis and signalling: intertwining molecular networks. Nature reviews Molecular cell biology *10*, 609-622.

Sousa, J.S., D'Imprima, E., and Vonck, J. (2018). Mitochondrial Respiratory Chain Complexes. In Membrane Protein Complexes: Structure and Function, J.R. Harris, and E.J. Boekema, eds. (Singapore: Springer Singapore), pp. 167-227.

Spinelli, J.B., and Haigis, M.C. (2018). The multifaceted contributions of mitochondria to cellular metabolism. Nature cell biology *20*, 745-754.

Springer, W., Hoppe, T., Schmidt, E., and Baumeister, R. (2005). A Caenorhabditis elegans Parkin mutant with altered solubility couples α-synuclein aggregation to proteotoxic stress. Human Molecular Genetics *14*, 3407-3423.

Sulston, J.E., and Brenner, S. (1974). The DNA of *Caenorhabditis elegans*. Genetics *77*, 95-104.

Tabara, H., Grishok, A., and Mello, C.C. (1998). RNAi in *C. elegans*: Soaking in the Genome Sequence. Science (New York, NY) *282*, 430-431.

Tabuchi, T.M., Deplancke, B., Osato, N., Zhu, L.J., Barrasa, M.I.*, et al.* (2011). Chromosome-Biased Binding and Gene Regulation by the Caenorhabditis elegans DRM Complex. PLoS genetics *7*, e1002074.

Takahashi, M., Iwasaki, H., Inoue, H., and Takahashi, K. (2002). Reverse Genetic Analysis of the *Caenorhabditis elegans* 26S Proteasome Subunits by RNA Interference. In Biological Chemistry, pp. 1263.

Takahashi, Y., He, H., Tang, Z., Hattori, T., Liu, Y.*, et al.* (2018). An autophagy assay reveals the ESCRT-III component CHMP2A as a regulator of phagophore closure. Nature communications *9*, 2855.

Tamai, K., Tanaka, N., Nara, A., Yamamoto, A., Nakagawa, I.*, et al.* (2007). Role of Hrs in maturation of autophagosomes in mammalian cells. Biochem Biophys Res Commun *360*, 721-727.

Tatsumi, Y., Ohta, S., Kimura, H., Tsurimoto, T., and Obuse, C. (2003). The ORC1 cycle in human cells: I. cell cycle-regulated oscillation of human ORC1. The Journal of biological chemistry *278*, 41528-41534.

The Alliance of Genome Resources, C. (2019). Alliance of Genome Resources Portal: unified model organism research platform. Nucleic Acids Research *48*, D650-D658.

Thomas, J.H., Ceol, C.J., Schwartz, H.T., and Horvitz, H.R. (2003). New Genes That Interact With *lin-35* Rb to Negatively Regulate the *let-60 ras* Pathway in *Caenorhabditis elegans*. Genetics *164*, 135-151.

Tian, Y., Garcia, G., Bian, Q., Steffen, Kristan K., Joe, L.*, et al.* (2016). Mitochondrial Stress Induces Chromatin Reorganization to Promote Longevity and UPRmt. Cell *165*, 1197-1208.

Tian, Y., Li, Z., Hu, W., Ren, H., Tian, E.*, et al.* (2010). *C. elegans* Screen Identifies Autophagy Genes Specific to Multicellular Organisms. Cell *141*, 1042-1055.

Timmis, J.N., Ayliffe, M.A., Huang, C.Y., and Martin, W. (2004). Endosymbiotic gene transfer: organelle genomes forge eukaryotic chromosomes. Nature Reviews Genetics *5*, 123-135.

Timmons, L., and Fire, A. (1998). Specific interference by ingested dsRNA. Nature *395*, 854-854.

Tomsig, J.L., Snyder, S.L., and Creutz, C.E. (2003). Identification of targets for calcium signaling through the copine family of proteins. Characterization of a coiled-coil copine-binding motif. The Journal of biological chemistry *278*, 10048-10054.

Tomsig, J.L., Sohma, H., and Creutz, C.E. (2004). Calcium-dependent regulation of tumour necrosis factor-alpha receptor signalling by copine. Biochem J *378*, 1089-1094.

Tondera, D., Grandemange, S., Jourdain, A., Karbowski, M., Mattenberger, Y.*, et al.* (2009). SLP-2 is required for stress-induced mitochondrial hyperfusion. The EMBO journal *28*, 1589-1600.

Truscott, K.N., Kovermann, P., Geissler, A., Merlin, A., Meijer, M.*, et al.* (2001). A presequence- and voltage-sensitive channel of the mitochondrial preprotein translocase formed by Tim23. Nature Structural Biology *8*, 1074-1082.

Twig, G., Elorza, A., Molina, A.J.A., Mohamed, H., Wikstrom, J.D.*, et al.* (2008). Fission and selective fusion govern mitochondrial segregation and elimination by autophagy. The EMBO journal *27*, 433-446.

van der Bliek, A.M., Sedensky, M.M., and Morgan, P.G. (2017). Cell Biology of the Mitochondrion. Genetics *207*, 843-871.

van der Laan, M., Meinecke, M., Dudek, J., Hutu, D.P., Lind, M.*, et al.* (2007). Motor-free mitochondrial presequence translocase drives membrane integration of preproteins. Nature cell biology *9*, 1152-1159.

Vance, J.E. (1998). Eukaryotic lipid-biosynthetic enzymes: the same but not the same. Trends in biochemical sciences *23*, 423-428.

Villa, E., Proïcs, E., Rubio-Patiño, C., Obba, S., Zunino, B.*, et al.* (2017). Parkin-Independent Mitophagy Controls Chemotherapeutic Response in Cancer Cells. Cell reports *20*, 2846-2859.

Vives-Bauza, C., Zhou, C., Huang, Y., Cui, M., de Vries, R.L.A.*, et al.* (2010). PINK1-dependent recruitment of Parkin to mitochondria in mitophagy. Proceedings of the National Academy of Sciences *107*, 378-383.

Vögtle, F.N., Wortelkamp, S., Zahedi, R.P., Becker, D., Leidhold, C.*, et al.* (2009). Global Analysis of the Mitochondrial N-Proteome Identifies a Processing Peptidase Critical for Protein Stability. Cell *139*, 428-439.

Walter, P., and Ron, D. (2011). The Unfolded Protein Response: From Stress Pathway to Homeostatic Regulation. Science (New York, NY) *334*, 1081-1086.

Walther, D.M., and Rapaport, D. (2009). Biogenesis of mitochondrial outer membrane proteins. Biochimica et Biophysica Acta (BBA) - Molecular Cell Research *1793*, 42-51.

Wanders, R.J.A., Ruiter, J.P.N., Ijlst, L., Waterham, H.R., and Houten, S.M. (2010). The enzymology of mitochondrial fatty acid beta-oxidation and its application to follow-up analysis of positive neonatal screening results. J Inherit Metab Dis *33*, 479-494.

Wang, X., and Chen, X.J. (2015). A cytosolic network suppressing mitochondria-mediated proteostatic stress and cell death. Nature *524*, 481-484.

Watson, E., MacNeil, Lesley T., Arda, H.E., Zhu, Lihua J., and Walhout, Albertha J.M. (2013). Integration of Metabolic and Gene Regulatory Networks Modulates the C. elegans Dietary Response. Cell *153*, 253-266.

Weber, C.A., Sekar, K., Tang, J.H., Warmer, P., Sauer, U.*, et al.* (2020). β-Oxidation and autophagy are critical energy providers during acute glucose depletion in *Saccharomyces cerevisiae*. Proceedings of the National Academy of Sciences *117*, 12239-12248.

Weidberg, H., and Amon, A. (2018). MitoCPR—A surveillance pathway that protects mitochondria in response to protein import stress. Science (New York, NY) *360*, eaan4146.

Weinkove, D., Bastiani, M., Chessa, T.A.M., Joshi, D., Hauth, L.*, et al.* (2008). Overexpression of PPK-1, the Caenorhabditis elegans Type I PIP kinase, inhibits growth cone collapse in the developing nervous system and causes axonal degeneration in adults. Developmental Biology *313*, 384-397.

Weir, H.J., Yao, P., Huynh, F.K., Escoubas, C.C., Goncalves, R.L.*, et al.* (2017). Dietary Restriction and AMPK Increase Lifespan via Mitochondrial Network and Peroxisome Remodeling. Cell metabolism *26*, 884-896.e885.

Wen, C., Levitan, D., Li, X., and Greenwald, I. (2000). *spr-2*, a suppressor of the egg-laying defect caused by loss of *sel-12* presenilin in *Caenorhabditis elegans*, is a member of the SET protein subfamily. Proceedings of the National Academy of Sciences *97*, 14524-14529.

Wiedemann, N., Kozjak, V., Chacinska, A., Schönfisch, B., Rospert, S.*, et al.* (2003). Machinery for protein sorting and assembly in the mitochondrial outer membrane. Nature *424*, 565-571.

Wiedemann, N., and Pfanner, N. (2017). Mitochondrial Machineries for Protein Import and Assembly. Annual review of biochemistry *86*, 685-714.

Wilkinson, C.R.M., Dittmar, G.A.G., Ohi, M.D., Uetz, P., Jones, N.*, et al.* (2004). Ubiquitin-like Protein Hub1 Is Required for Pre-mRNA Splicing and Localization of an Essential Splicing Factor in Fission Yeast. Current Biology *14*, 2283-2288.

Wisely, G.B., Miller, A.B., Davis, R.G., Thornquest, A.D., Johnson, R.*, et al.* (2002). Hepatocyte Nuclear Factor 4 Is a Transcription Factor that Constitutively Binds Fatty Acids. Structure *10*, 1225-1234.

Witte, K., Schuh, A.L., Hegermann, J., Sarkeshik, A., Mayers, J.R., *et al.* (2011). TFG-1 function in protein secretion and oncogenesis. Nature cell biology *13*, 550-558.

Wong, E.D., Wagner, J.A., Gorsich, S.W., McCaffery, J.M., Shaw, J.M., *et al.* (2000). The Dynamin-Related Gtpase, Mgm1p, Is an Intermembrane Space Protein Required for Maintenance of Fusion Competent Mitochondria. Journal of Cell Biology *151*, 341-352.

Wong, E.D., Wagner, J.A., Scott, S.V., Okreglak, V., Holewinske, T.J., *et al.* (2003). The intramitochondrial dynamin-related GTPase, Mgm1p, is a component of a protein complex that mediates mitochondrial fusion. Journal of Cell Biology *160*, 303-311.

Wood, W.B., Herman, R.K., Emmons, S.W., White, J., Sulston, J., *et al.* (1988). The Nematode *Caenorhabditis elegans* (Cold Spring Harbor Laboratory Press).

Wrobel, L., Topf, U., Bragoszewski, P., Wiese, S., Sztolsztener, M.E., *et al.* (2015). Mistargeted mitochondrial proteins activate a proteostatic response in the cytosol. Nature *524*, 485-488.

Wu, L., Niemeyer, B., Colley, N., Socolich, M., and Zuker, C.S. (1995). Regulation of PLC-mediated signalling in vivo by CDP-diacylglycerol synthase. Nature *373*, 216-222.

Wu, Z., Senchuk, M.M., Dues, D.J., Johnson, B.K., Cooper, J.F., *et al.* (2018). Mitochondrial unfolded protein response transcription factor ATFS-1 promotes longevity in a long-lived mitochondrial mutant through activation of stress response pathways. BMC Biology *16*, 147.

Yang, D., Li, L., Liu, H., Wu, L., Luo, Z., *et al.* (2013). Induction of autophagy and senescence by knockdown of ROC1 E3 ubiquitin ligase to suppress the growth of liver cancer cells. Cell death and differentiation *20*, 235-247.

Yoneda, M., Miyatake, T., and Attardi, G. (1994). Complementation of mutant and wild-type human mitochondrial DNAs coexisting since the mutation event and lack of complementation of DNAs introduced separately into a cell within distinct organelles. Molecular and Cellular Biology *14*, 2699-2712.

Yoneda, T., Benedetti, C., Urano, F., Clark, S.G., Harding, H.P., *et al.* (2004). Compartment-specific perturbation of protein handling activates genes encoding mitochondrial chaperones. Journal of cell science *117*, 4055-4066.

Youle, R.J., and van der Bliek, A.M. (2012). Mitochondrial fission, fusion, and stress. Science (New York, NY) *337*, 1062-1065.

Zhang, H., Chang, J.T., Guo, B., Hansen, M., Jia, K., *et al.* (2015). Guidelines for monitoring autophagy in *Caenorhabditis elegans*. Autophagy *11*, 9-27.

Zhang, J., and Ney, P. (2008). NIX induces mitochondrial autophagy in reticulocytes. Autophagy *4*, 354-356.

Zhang, J., and Ney, P.A. (2009). Role of BNIP3 and NIX in cell death, autophagy, and mitophagy. Cell Death & Differentiation *16*, 939-946.

Zhang, Q., Wu, X., Chen, P., Liu, L., Xin, N.*, et al.* (2018). The Mitochondrial Unfolded Protein Response Is Mediated Cell-Non-autonomously by Retromer-Dependent Wnt Signaling. Cell *174*, 870-883.e817.

Zhao, Q., Wang, J., Levichkin, I.V., Stasinopoulos, S., Ryan, M.T.*, et al.* (2002). A mitochondrial specific stress response in mammalian cells. The EMBO journal *21*, 4411-4419.

Zhao, Y., Yang, J., Liao, W., Liu, X., Zhang, H.*, et al.* (2010). Cytosolic FoxO1 is essential for the induction of autophagy and tumour suppressor activity. Nature cell biology *12*, 665.

Zhou, F., Wu, Z., Zhao, M., Murtazina, R., Cai, J.*, et al.* (2019). Rab5-dependent autophagosome closure by ESCRT. The Journal of cell biology *218*, 1908-1927.

Zhu, T., Chen, J.-L., Wang, Q., Shao, W., and Qi, B. (2018). Modulation of Mitochondrial Dynamics in Neurodegenerative Diseases: An Insight Into Prion Diseases. Frontiers in Aging Neuroscience *10*.

Zick, M., Duvezin-Caubet, S., Schäfer, A., Vogel, F., Neupert, W.*, et al.* (2009). Distinct roles of the two isoforms of the dynamin-like GTPase Mgm1 in mitochondrial fusion. FEBS Letters *583*, 2237-2243.

Appendices

Acknowledgements

The people who ever met me in person for more than two minutes know that I am a guy of many words and almost endless stories. For the sake of our time, I'll try my best to keep these acknowledgments rather short.

First of all, I thank Barbara for providing me a position in her lab. After running out of resources in my previous lab, you gave me the opportunity to grow as a researcher while growing a lot of worms in your lab - I even got to choose my own project. I don't know if you expected me to stay that long when you initially told me that I won't have to worry about financing anymore, but in the end, I think it was worth it and this was a fruitful time. I always appreciated most that you gave me the chance to develop my own ideas, even though sometimes this needed some persuasion. Thanks for your trust in me!

Special thanks to Stéphane, my mentor in lab. You taught me almost everything in lab and your endless patience made learning an easy job. In many ways you became an inspiration for me. Also, thanks for all the fun times we had along the way (even for the really silly jokes, especially on Friday afternoons) and for showing so much interest in me.

Thank you, Eric, for nice discussions during lab meetings and for spicing up our manuscripts with your talent for putting complex connections into simple sentences. Thank you Nadja, Linda, Melanie, Michaela, Tatjana and Sylvia for excellent technical support. Thanks to Sebastian and Christian for all the help with my datasets, you guys made my life a lot easier with your programming skills. Thanks to my collaborators Michael, Assa and Laetitia, it was a pleasure working with you. Thanks also to the 'Mito-Club' for a lot of support and helpful suggestions. Thanks to the students Anna, Emin and Madeleine for all your help. Thanks to inspiring scientists on campus and on conferences: Bill, Christof, Wolfgang, Walter, Richard, Angelika, Dejana and Kai.

Many thanks also to the best lab on campus! The Conradt lab (of course including the Lambie, Mikeladze-Dvali, Zanin and Wagener labs!) was a great mix of people from all over the world - a bucket full of joy (if I may remind you about Campusfest 2019). We had lots of fun together, both in- and outside of the lab. I found a lot of friends here. Special thanks go to my dear friend

and companion in this lab, Fabian. Sharing the autophagy project with you was the best time I had so far in a lab (‘you may sing ‘IIIIII haaaad theee tiiime oooof myyyy liiiiife’ now!). We had a lot of work but it was always nice (and this may almost sound a bit cheesy) to have you by my side and to discuss our project. Thanks for giving me the certainty that, if a lab day was too annoying long, we would go out for a beer or two afterwards. Thanks also to my ‘sun’ Nikhil, your warm smile always welcomed me in the morning when coming to the lab. Thank you, Jeff, for many good conversations over the years, I could always count on your judgement. Many thanks to Elisabeth. We became good friends, especially in recent years. Initially attracted by your incredible baking skills, I soon realized what a kind person you are. Thanks to Anna, we had really good times together. Thank you, Hai. I can imagine sitting next to me at the scope for the first year or so was sometimes annoying for you because I just kept talking all the time, but I really enjoyed your company and we became friends after all. Thank you, Rodina. Even though your time in our lab was rather short we became good friends and I really like our endless conversations. Thanks to Adi, you gave our already flourishing social life another boost when joining the lab and I really like that we are still in contact. Thank you, Laura, for spicing up our lab with your temperament. Thanks to Sayantan. We had a lot of fun pulling each other’s and other people’s legs. Thanks also to Saroj. You helped me with ideas in the beginning and taught me a few things about the most interesting organelles, which ‘constantly fuse and divide’. Thanks also to all the people I shared the office with over all these years: Marion, Ryan, Carina, Marion, Lisa and Yanwen. Special thanks also to the people of the lab who are not mentioned by their names. We had a lot of great times together, which I will never forget!

Vielen lieben Dank auch an all die lieben Freundinnen und Freunde außerhalb des Labors, die mich über die letzten Jahre begleitet, unterstützt und mir diese Zeit versüßt haben. Danke an meine Mitbewohner Clemens, Ioannis und Orkan für die viele Geduld mit mir. Das Pirkheim mit euch zu teilen war mir eine riesen große Freude. Danke, dass ihr mich durch all die Höhen und Tiefen begleitet habt, ich konnte immer auf euch zählen! Danke dir Philippe. Du bist ein besonders treuer Freund und das schätze ich sehr. Danke an Taipari für die vielen tiefen Gespräche, die mein Bewusstsein erweitert haben. Danke an die Boulderbande. Mit euch zusammen den Affen an der Wand rauszulassen tat mir immer sehr gut. Danke Flo, für dein Vertrauen in mich, du bist ein treuer Freund. Danke an Laura und Yanis, ihr begleitet mich schon so viele Jahre und ich bin froh euch beide in meinem Leben zu haben. Danke an Lukas, auch für die vielen Tipps während der Vorbereitung meiner Radtour. Danke dir Max. Du

wohnst schon lange weit weg aber unsere Freundschaft hat nie unter dieser Entfernung gelitten. Danke an die Allgäuer Feieranten und den vielen Menschen mit denen ich die ein oder andere Runde getanzt habe. Danke an die Berchtesgadener Jungs. Alex deine Musik ist genial und ich hoffe noch vieles von dir zu hören. Danke auch an ‘Die freshe Gruppe’, ihr habt mich über die Jahre oft erheitert.

Meine besondere Dankbarkeit gilt meiner Schwester und meinen Eltern. Eure Förderung hat eine fast unendliche Neugier in mir geweckt, die mich befähigt bis hierher und hoffentlich noch viel weiter zu kommen. Ihr habt immer alles in eurer Macht stehende für mich getan und an mich geglaubt, wodurch ich mit Leichtigkeit durchs Leben schreite. Danke für das freundschaftliche und sehr liebevolle Verhältnis.

Publications

Simon Haeussler, Assa Yeroslaviz, Stéphane G. Rolland, Sebastian Luehr, Eric Lambie and Barbara Conradt. Genome-wide RNAi-screen for regulators of UPR^{mt} in *Caenorhabditis elegans* mutants with defects in mitochondrial fusion. *Unpublished manuscript*

Christian A. Fischer, Laura Besora-Casals, Stéphane G. Rolland, **Simon Haeussler**, Kritarth Singh, Michael Duchen, Barbara Conradt, Carsten Marr **(2020)**. MitoSegNet: easy to use deep learning segmentation for analysing mitochondrial morphology. iScience 23(10). https://doi.org/10.1016/j.isci.2020.101601

Simon Haeussler, Fabian Köhler, Michael Witting, Madeleine F. Premm, Stéphane G. Rolland, Christian Fischer, Laetitia Chauve, Olivia Casanueva, Barbara Conradt **(2020)**. Autophagy compensates for defects in mitochondrial dynamics. PLOS Genetics 16(3). https://doi.org/10.1371/journal.pgen.1008638

Stéphane G. Rolland, Sandra Schneid, Melanie Schwarz, Elisabeth Rackles, Christian Fischer, **Simon Haeussler**, Saroj G. Regmi, Assa Yeroslaviz, Bianca Habermann, Dejana Mokranjac, Eric Lambie and Barbara Conradt **(2019)**. Compromised mitochondrial protein import acts as a signal for UPR^{mt}. Cell Reports 28(7). https://doi.org/10.1016/j.celrep.2019.07.049

Astrid Heim, Christina Grimm, Udo Müller, **Simon Häußler**, Mukram M Mackeen, Juliane Merl, Stefanie M Hauck, Benedikt M Kessler, Christopher J Schofield, Alexander Wolf, Angelika Böttger **(2014)**. Jumonji Domain Containing Protein 6 (Jmjd6) Modulates Splicing and Specifically Interacts With Arginine-Serine-Rich (RS) Domains of SR- And SR-like Proteins. Nucleic Acids Research 42(12). doi: 10.1093/nar/gku488.

Trixi Hollweck, Bassil Akra, **Simon Häussler**, Peter Uberfuhr, Christoph Schmitz, Stefan Pfeifer, Markus Eblenkamp, Erich Wintermantel, Günther Eissner **(2011)**. A Novel Pulsatile Bioreactor for Mechanical Stimulation of Tissue Engineered Cardiac Constructs. Journal of Functional Biomaterials 2(3). doi: 10.3390/jfb2030107.